Chemical vapour deposition growth of carbon nanotube forests: kinetics, morphology, composition, and their mechanisms

Phillip Vinten

Thesis submitted to the
Faculty of Graduate and Postdoctoral Studies
In partial fulfillment of the requirements for the degree of
Doctor of Philosophy in Physics

Ottawa-Carleton Institute for Physics
Department of Physics
Faculty of Science
University of Ottawa

© Phillip Vinten, Ottawa, Canada, 2013

Abstract

This thesis analyzes the chemical vapour deposition (CVD) growth of vertically aligned carbon nanotube (CNT) forests in order to understand how CNT forests grow, why they stop growing, and how to control the properties of the synthesized CNTs. *In situ* kinetics data of the growth of CNT forests are gathered by *in situ* optical microscopy. The overall morphology of the forests and the characteristics of the individual CNTs in the forests are investigated using scanning electron microscopy and Raman spectroscopy. The *in situ* data show that forest growth and termination are activated processes (with activation energies on the order of 1 eV), suggesting a possible chemical origin. The activation energy changes at a critical temperature for ethanol CVD (approximately 870°C). These activation energies and critical temperature are also seen in the temperature dependence of several important characteristics of the CNTs, including the defect density as determined by Raman spectroscopy. This observation is seen across several CVD processes and suggests a mechanism of defect healing. The CNT diameter also depends on the growth temperature. In this thesis, a thermodynamic model is proposed. This model predicts a temperature and pressure dependence of the CNT diameter from the thermodynamics of the synthesis reaction and the effect of strain on the enthalpy of formation of CNTs. The forest morphology suggests significant interaction between the constituent CNTs. These interactions may play a role in termination. The morphology, in particular a microscale rippling feature that is capable of diffracting light, suggest a non-uniform growth rate across the forest. A gas phase diffusion model predicts a non-uniform distribution of the source gas. This gas phase diffusion is suggested as a possible explanation for the non-uniform growth rate. The gas phase diffusion is important because growth by acetylene CVD is found to be very efficient (approximately 30% of the acetylene is converted to CNTs). It is seen that multiple mechanisms are active during CNT growth. The results of this thesis provide insight into both the basic understanding of the microscopic processes involved in CVD growth and how to control the properties of the synthesized CNTs.

Statement of originality and collaborations

The author (Phillip Vinten) states that, to the best of his knowledge, this thesis constitutes original research. As this thesis consists of collaborative publications, the specific contributions of each author are as follows:

- All CVD growth of carbon nanotubes and subsequent analysis of that growth was performed by the author.
- All scanning electron microscopy images were acquired by the author.
- Raman spectra in Chapter 2 and Chapter 3 were mostly acquired by the author's research supervisor, Paul Finnie, with some involvement of the author. Raman spectra in subsequent chapters were acquired by the author. The analysis of the Raman spectra was performed by the author with the guidance of Paul Finnie.
- Auger electron spectra were acquired by Terry Quance, with the involvement of the author. Analysis of these spectra was performed by the author with the assistance of Terry Quance.
- Optical diffraction experiments were performed by the author with some technical assistance from Jacques Lefebvre.
- Growth substrates were prepared by personnel of the National Research Council of Canada (NRC): Hue Tran, Mike Denhoff, Philip Chow-Chong, and Boris Lamontange.
- The basic growth procedure and initial CVD optimization were already in place at the beginning of this thesis and involved several people including Jeffery Bond, Paul Marshall, and Paul Finnie. Much of the subsequent optimization and refinement to the procedure were developed by the author.
- All manuscripts (including the text, figures, and tables) were prepared by the author, in consultation with the co-authors, except Chapter 4 (text and several figures), which was prepared by Paul Finnie, based on the work of the author. The thermodynamics model presented in Chapter 8 was originally conceived by Paul Finnie in an unpublished paper.

As is the nature of graduate studies, all of the author's work was done under the supervision of his research supervisor, Paul Finnie.

Acknowledgments

First, I thank my research supervisor, Paul Finnie, who always encouraged me to think critically about my results and really understand why things were happening, for supervising me, being available to discuss results without an appointment, giving me critical feedback on my papers, and teaching me and pointing me in the right direction toward what I needed to know in order to successfully conduct my research.

I thank quite a few other NRC personnel who helped me along the way, either by giving advice, assistance, or performing various measurements, many of which never made it into any published reports. All of the people I have interacted with at NRC were very professional and always treated me as an equal and a colleague. In particular I thank: Jacques Lefebvre who taught me a lot, both about nanotubes and optical methods, provided critical feedback on my papers and performed several measurements for me; Paul Marshall for building and maintaining lab equipment, and for teaching me how to do these tasks by myself; Jeff Fraser for advice and assistance with the SEM and EDX; Kate Kaminska for teaching me how to use the SEM; and Terry Quance for assistance and advice while setting up equipment in the lab, and for not only performing Auger analysis but showing me how to use the instrument in the process. Thanks to Hue Tran, Mike Denhoff, Philip Chow-Chong, Joe McKee, and Boris Lamontagne for preparing the growth substrates that I used. Finally, thanks to the following people for assisting me in various ways (in no particular order): Chris Kingston, Simona Moisa, Xiaohua Wu, Oltion Kodra, Ye Tao, Eric Estwick, Li-Lin Tay, Amy Hrdina, and Jean-Marc Baribeau.

I owe a special thanks to Daniel Pohl who read through my entire thesis and provided feedback. Several of my other classmates and friends also deserve my thanks: Jeffery Bond for performing some preliminary work; Andrew Li-Pook-Than and Catherine Aldous for helpful discussion; and Shane Scott who helped me with the LaTeXthesis template. There are many professors in the Department of Physics at the University of Ottawa who also helped me along the way, whether it was teaching me, encouraging me, writing letters of recommendation, or just generally discussing things with me.

Funding for this research was provided by several organizations over the course of this research: OGS, NRC (GSSSP), NSERC (CGS), NSERC (Paul Finnie's Discovery Grant), the University of Ottawa (admission scholarship and travel grants). Furthermore, I should thank NRC for providing me with lab space, an office, and most importantly for letting me use all of that expensive equipment!

A big thanks to all of my friends, and, finally, thanks to my family for their unconditional and continuing support.

Table of contents

Abstract ii

Statement of originality and collaborations iii

Acknowledgments iv

Table of contents v

List of figures xi

List of tables xv

List of videos xvi

List of abbreviations xvii

List of terms xviii

List of symbols xix

1 Introduction 1

Foreword . . . 2

1.1 Motivation . . . 2

1.2 Carbon nanotubes . . . 4

1.2.1 Bonding in carbon . . . 4

1.2.2 Allotropes of carbon . . . 6

1.2.3 Physical structure of carbon nanotubes . . . 8

1.2.4 Properties of carbon nanotubes . . . 13

1.2.5 Toxicity and safety . . . 15

1.3 Crystal structures and growth . . . 16

1.3.1 Defects in crystal structures . . . 16

Defects on surfaces . . . 17

1.3.2 Crystal growth models . . . 18

1.4 Chemical vapour deposition . . . 21

1.4.1 Overview . . . 21

1.4.2 Growth substrates . . . 24

1.4.3 Experimental setup and procedure . . . 26

1.4.4 Chemistry of CVD growth . . . 28
1.4.5 Growth process at the atomic level . . . 31
1.4.6 The growing forest . . . 34
1.4.7 Termination . . . 35
1.5 Optical microscopy . . . 38
1.6 Raman spectroscopy . . . 40
1.6.1 Theory . . . 40
1.6.2 Raman imaging . . . 43
1.6.3 Experimental setup . . . 43
1.6.4 Spectral features . . . 46
G band . . . 47
D band . . . 48
Radial breathing modes . . . 49
Other features and background noise . . . 53
1.7 Electron microscopy . . . 53
1.7.1 Scanning electron microscopy . . . 54
1.7.2 SEM instrumentation . . . 57
1.7.3 Auger electron spectra and characteristic x-ray spectra . . . 58
1.8 Summary . . . 59
References . . . 61

2 Kinetic critical temperature and optimized chemical vapor deposition growth of carbon nanotubes 68
Foreword . . . 69
Abstract . . . 71
1. Introduction . . . 71
2. Experiment . . . 71
3. Results . . . 72
4. Conclusions . . . 74
Acknowledgements . . . 74
Appendix A. Supplementary material . . . 74
References . . . 74

3 Distinct termination morphologies for vertically aligned carbon nanotube forests 76
Foreword . . . 77
Abstract . . . 79

1. Introduction . . . 79
2. Experimental procedures . . . 79
3. Results and discussion . . . 80
4. Conclusion . . . 84
Acknowledgments . . . 85
References . . . 85

4 Morphological Instabilities and the Dynamics of Carbon Nanotube Forest Growth 86
Foreword . . . 87
Abstract . . . 88
Introduction . . . 88
Experimental . . . 89
Results . . . 90
Discussion . . . 93
Conclusions . . . 96
Acknowledgments . . . 97
References . . . 97

5 Visible iridescence from self-assembled periodic rippling in vertically aligned carbon nanotube forests 98
Foreword . . . 99
Abstract . . . 101
Article . . . 101

6 Origin of periodic rippling during chemical vapor deposition growth of carbon nanotube forests 104
Foreword . . . 105
Abstract . . . 106
1. Introduction . . . 106
2. Experimental procedures . . . 107
3. Results . . . 107
4. Discussion . . . 111
5. Conclusion . . . 113
Acknowledgments . . . 114
Appendix A. Experimental methods . . . 114
Appendix B. Supplementary data . . . 114

References . . . 114

7 Critical role of gas phase diffusion and high efficiency in vertically aligned carbon nanotube forest growth 116

Foreword . . . 117
Abstract . . . 120
1. Introduction . . . 120
2. Experimental procedures . . . 121
3. Results and discussion . . . 122
3.1. Kinetic observations . . . 122
3.2. Gas diffusion observations . . . 126
3.3. Gas diffusion model . . . 129
3.4. Growth rate . . . 133
3.5. CNT density . . . 135
3.6. Termination mechanisms . . . 137
4. Summary . . . 138
Acknowledgments . . . 139
References . . . 139

8 Thermodynamic and Energetic Effects on the Diameter and Defect Density in Single Walled Carbon Nanotube Synthesis 143

Foreword . . . 144
Abstract . . . 146
Introduction . . . 146
Experimental Methods . . . 146
Results and Discussion . . . 147
D/G Ratio . . . 147
CNT Diameters . . . 149
Thermodynamic Model . . . 150
Growth Filters . . . 153
Conclusion . . . 153
Associated Content . . . 154
Author Information . . . 154
Acknowledgments . . . 154
References . . . 154

9 General discussion and conclusions **156**
9.1 Summary of results . . . 157
9.2 General discussion . . . 159
9.2.1 Experimental methods . . . 159
9.2.2 Multiple mechanisms . . . 161
9.2.3 Gas phase diffusion . . . 164
9.2.4 Inter-nanotube interactions . . . 166
9.2.5 Control over diameter distribution and defect density . . . 168
9.3 Conclusions . . . 168
References . . . 170

Appendices **172**

A Supplementary material for: Kinetic critical temperature and optimized chemical vapor deposition growth of carbon nanotubes (Chapter 2) **172**

B Supplementary material for: Distinct termination morphologies for vertically aligned carbon nanotube forests (Chapter 3) **174**
1. Raman Acquisition Parameters . . . 175
2. Figures . . . 176
3. Videos . . . 179

C Supplementary material for: Origin of periodic rippling during chemical vapor deposition growth of carbon nanotube forests (Chapter 6) **180**
Videos . . . 181

D Supplementary material for: Critical role of gas phase diffusion and high efficiency in vertically aligned carbon nanotube forest growth (Chapter 7) **183**
1. Experimental procedures . . . 184
2. Results and discussion . . . 185
2.1. Kinetic observations . . . 185
2.2. SEM observations . . . 187
2.3. Auger electron spectroscopy . . . 188
2.4. Raman spectroscopy . . . 190
2.5. Gas diffusion model . . . 191
2.5.1. Bessel functions . . . 192

2.6. CNT areal density 193

E Supporting Information for: Thermodynamic and Energetic Effects on the Diameter and Defect Density in Single Walled Carbon Nanotube Synthesis (Chapter 8) 195

Experimental Methods 197

Raman Spectra 198

D/G Ratio for Fe CVD 203

D/G Ratio From Peak vs Integrated Intensities 204

Yield 205

Thermodynamic Model 206

List of figures

Chapter 1

1 Molecular diagrams of some simple hydrocarbons. . . . 6
2 Some allotropes of carbon. . . . 7
3 Nanotube chirality. . . . 9
4 Nanotube construction. . . . 10
5 Cut-away diagram of a multi-walled carbon nanotube. . . . 11
6 Carbon nanotube forest. . . . 12
7 Carbon nanotube forest photograph. . . . 12
8 Density of states in a carbon nanotube. . . . 14
9 Defects in crystals and surfaces. . . . 17
10 Stone-Wales defect in a graphene lattice. . . . 18
11 Crystal growth via a screw dislocation. . . . 20
12 Dislocation theory for chirality-selective CNT growth. . . . 21
13 Growth modes for heteroepitaxy. . . . 22
14 CVD reactor. . . . 27
15 CVD gas flow diagram. . . . 28
16 *In situ* optical setup. . . . 29
17 CVD growth processes at the atomic level. . . . 32
18 CVD growth model. . . . 33
19 Energies within forests. . . . 35
20 Interactions between individual nanotubes within a forest. . . . 36
21 Optical diffraction setup. . . . 39
22 Diagrams of Raman scattering. . . . 41
23 Schematic of the Raman spectrometer. . . . 44
24 Typical Raman spectrum for a carbon nanotube forest. . . . 46
25 Schematic diagram of Raman modes in a carbon nanotube. . . . 48
26 Kataura plot. . . . 51
27 Diagram of an SEM. . . . 55
28 Auger electron creation. . . . 56
29 Auger electron spectrum. . . . 59

Chapter 2

1 Kinetic data extracted from *in situ* videos. . . . 72
2 Kinetic parameters vs $1/k_BT$. . . . 72

3 Raman spectra and D/G ratio. 73
4 Raman parameters vs $1/k_BT$. 73

Chapter 3

1 Frames from *in situ* videos. 80
2 Post-growth SEM images. 81
3 Growth curves. 82
4 Kinetic parameters vs $1/k_BT$. 83

Chapter 4

1 Chemical vapor deposition reactor arrangement. 90
2 Morphologies of carbon nanotube forests. 91
3 Optical images of nucleation dynamics. 92
4 SEM images of root morphology. 93
5 Transformations requiring similar energies. 94
6 Balancing adhesion with cohesion. 95
7 Balancing adhesion with strain. 96

Chapter 5

1 Diffraction and rippling pattern. 101
2 Forest being rotated showing a change in color. 102
3 Optical and SEM images of forest. 102

Chapter 6

1 SEM images of rippled forest. 108
2 SEM images of ripples. 109
3 SEM images of rippled forest. 109
4 *In situ* optical images. 110
5 Diffraction grating effect from a forest. 111

Chapter 7

F1 Illustration of rippling mechanism. 117
1 Catalyst pattern and SEM image. 122
2 Growth curves. 123
3 Kinetic parameters. 124
4 Flow rate dependence. 125
5 Non-uniform initial growth rate. 127
6 Island spacing growth curves. 128

7 Gas phase diffusion diagrams and plot. 130
8 Catalyst nanoparticle activity limited by diffusion. 137

Chapter 8

Graphical abstract. 146
1 Raman spectra. 147
2 D/G ratio vs $1/k_BT$. 147
3 Relative SWCNT abundance as a function of T. 149
4 SWCNT diameter as a function of T. 150
5 SWCNT diameter as a function of P. 152
6 SWCNT phase diagram for stability. 152

Chapter 9

1 Schematic of growth filters. 163
2 Forest concavity as a function of T. 164
3 Formation of convex top surface of a forest. 165

Appendix A

S1 Histogram of detected RBMs. 173

Appendix B

S1 Raman spectra and parameters. 176
S2 SEM image of forest concavity. 177
S3 High magnification SEM images. 178

Appendix D

S1 Frames from an *in situ* video. 186
S2 Growth curves for four forests grown simultaneously. 186
S3 SEM image of forests. 187
S4 SEM images of the base of two forests. 187
S5 Auger electron spectroscopy line profiles of Co catalyst island. 189
S6 Raman spectra for 4 different catalyst island sizes. 190
S7 Sketch of the boundary conditions. 191
S8 SEM image of the bottom cross section of a forest. 193

Appendix E

S1 Raman spectra: temperature series. 198
S2 Raman spectra: close-ups. 199
S3 Raman spectra: 700°C and different conditions. 200

S4 Raman spectra: 900°C and different conditions. 201
S5 Raman spectra: pressure series. 202
S6 D/G ratio I_D/I_G vs $1/k_BT$. 203
S7 D/G ratio: peak intensity vs. integrated intensity. 204
S8 Forest height vs growth temperature. 205
S9 Various cases of thermodynamic model. 207

List of tables

Chapter 5

I Grating spacing d measured by white light diffraction. 102

II Grating spacing d measured by laser diffraction. 102

Chapter 7

1 Values of parameters used in generating curves. 134

Chapter 8

1 Observed RBMs. 149

2 Observed G^- peaks. 150

Appendix D

S1 Values used to calculate efficiency. 192

S2 Measured bundle densities for CNT forests. 194

List of videos

This is a list of all of the videos that form part of the appendices of this thesis. These videos are available from the University of Ottawa's thesis repository (uO Research), as well as the respective journal publishers' websites. The file names of these videos are listed here, as well as the hyperlinks to the respective journal publishers' websites. The file names have the format:

`Vinten_Phillip_2013_thesis_video[chapter #][appendix #]S[video #].avi`

Chapter 2/Appendix A (`http://dx.doi.org/10.1016/j.cplett.2008.12.095`)

S1 Growing carbon nanotubes. 173
`Vinten_Phillip_2013_thesis_video2AS1.avi`

Chapter 3/Appendix B (`http://dx.doi.org/10.1088/0957-4484/21/3/035603`)

S1 Forest growth and uniform termination at 900°C. 179
`Vinten_Phillip_2013_thesis_video3BS1.avi`
S2 Forest growth and delamination at 730°C. 179
`Vinten_Phillip_2013_thesis_video3BS2.avi`
S3 Forest growth and cracking at 720°C. 179
`Vinten_Phillip_2013_thesis_video3BS3.avi`
S4 Forest growth on an unpatterned catalyst sample. 179
`Vinten_Phillip_2013_thesis_video3BS4.avi`

Chapter 6/Appendix C (`http://dx.doi.org/10.1016/j.carbon.2011.02.017`)

S1 Iridescence from a forest, as seen *in situ*. 181
`Vinten_Phillip_2013_thesis_video6CS1.avi`
S2 Iridescence from multiple forests, as seen *in situ*. 182
`Vinten_Phillip_2013_thesis_video6CS2.avi`
S3 Iridescence not changing during post-growth cooling. 182
`Vinten_Phillip_2013_thesis_video6CS3.avi`

Chapter 7/Appendix D (`http://dx.doi.org/10.1016/j.carbon.2013.04.007`)

S1 Simultaneous growth from different sized catalyst islands. 185
`Vinten_Phillip_2013_thesis_video7DS1.avi`
S2 Non-uniform initial growth. 185
`Vinten_Phillip_2013_thesis_video7DS2.avi`

List of abbreviations

This list contains the abbreviations used throughout this thesis (and their meanings).

AES – Auger electron spectroscopy/spectrometer/spectra
CNT – carbon nanotube
CVD – chemical vapour deposition
DWCNT/DWNT – double-walled carbon nanotube
EDX – energy dispersive x-ray spectroscopy/spectrometer/spectra
FWHM – full width at half maximum
MWCNT/MWNT – multi-walled carbon nanotube
NP – nanoparticle (usually referring to the catalyst)
RBM – radial breathing mode
sccm – standard cubic centimeters per minute
SEM – scanning electron microscope/microscopy/micrograph
STP – standard temperature and pressure (atmospheric pressure and 0°C)
SWCNT/SWNT – single-walled carbon nanotube
TWCNT/TWNT – triple-walled carbon nanotube

List of terms

This list contains the terms (and their definitions) that are defined with respect to this thesis or terms that have a specific meaning when used within the context of this thesis.

chirality – the angle at which the graphene sheet is "rolled" to make a specific CNT
cracking – the separation of large groups of CNTs in a forest from one another
D band – a Lorentzian peak in the Raman spectra of CNTs at ~ 1350 cm^{-1}
delamination – the (partial) separation of a CNT forest from the substrate
forest – a densely packed vertically aligned array of carbon nanotubes
G band – a Lorentzian peak in the Raman spectra of CNTs at ~ 1590 cm^{-1}
island – the portion of a patterned catalyst deposition where there is catalyst
morphology – the shape and structure, generally used to refer to a forest
rippling – a consistent and synchronized forest morphology like a diffraction grating
termination – the halting of CNT growth

List of symbols

This list contains some mathematical symbols used frequently throughout this thesis (and their meanings). Some symbol have multiple meanings, depending on the context in which they are used.

Carbon nanotube structure

$\vec{a_1}$, $\vec{a_2}$ – lattice vectors
a – lattice constant $a = |\vec{a_1}| = |\vec{a_2}| = 0.25$ nm, C-C bond length $\sim$0.14 nm
$\vec{C_h}$ or (n, m) – chiral vector
d – diameter, usually of a CNT
$\delta = 0.34$ nm is the interlayer spacing in graphite (sometimes denoted by a)
θ – chiral angle of a CNT
Ω – density of carbon in a graphene layer

Growth kinetics

β – initial growth rate
E – activation energy
$H\,(t)$ – height (as a function of growth time)
H_F – final height, from gradual termination
H_T – termination height, sudden
$\mathcal{H}_f$ – projected final height (if sudden termination did not occur)
T – growth temperature
T_c – critical temperature
t – growth time (variable)
τ – time constant, often referring to gradual termination time
τ_T – termination time, sudden

Forest morphology

f_D – fractional defect density
I_D/I_G – D/G (integrated intensity) ratio
λ – linear density of a CNT, wavelength of light or rippling pattern
M or m – masses
n_D – defect (number) density
ν – frequency

ρ – number density

ρ_m – mass density

σ – areal density

ω – Raman Shift

Y – Young's modulus

Gas diffusion

D – diffusion coefficient

ϵ – efficiency of growth

F – volumetric flow rate

I – impingement rate

L - diffusion length

n – concentration or density, order of diffraction or a chemical reaction

P – pressure

τ_d – time constant for C_2H_2 that is not used for growth

τ_g – time constant for C_2H_2 that is used for growth

τ_{eff} – an effective time constant relating τ_d and τ_g

r – radius (position), variable

R – radius, fixed

Thermodynamics

ΔG – change in Gibb's free energy

ΔH – change in enthalpy of formation

k_B or k – Boltzmann constant, k also wave vector

m_j and n_i – stoichiometric coefficients

ΔS – change in entropy

Chapter 1

Introduction

Foreword

This thesis is divided into three principal sections: introductory material, results and analysis in the form of peer reviewed publications, and a general discussion and conclusions section. The introduction contains a brief motivation for this research as well as all of the material needed to understand the analysis: an introduction to nanotubes, chemical vapour deposition, Raman spectroscopy, and scanning electron microscopy. The subsequent chapters are each devoted to a single peer reviewed publication and contain their own introduction, discussion and conclusions, as well as a foreword to create a more continuous monologue and to explain how the publication fits into the thesis (several of these forewords contain references of their own, which are listed at the bottom of the foreword section). Relevant prior research is addressed on a chapter-by-chapter basis. The general discussion ties all of the chapters together and provides a unifying summary and conclusion to the thesis.

Several of the papers that form part of this thesis include supplementary material. All of this material is included in this thesis as appendices, with each appendix corresponding to a different chapter (the appendix corresponding to each chapter is indicated on the first page of each chapter). The printable portion of the supplementary material is directly included in this thesis. The non-printable material (which consists of several videos) is available from the University of Ottawa in the thesis repository (uO Research), as well as the respective journal publishers' websites. A list of videos with file names (for uO Research) and Hyperlinks (to the journal publishers' websites) is included in the front matter of this thesis. Hyperlinks to the publishers' websites are also provided with the papers and the supplementary material. It should be understood that references to "online material" in the papers means the appendices and videos included with this thesis.

1.1 Motivation

Carbon nanotubes (CNTs) are a molecular allotrope of carbon (one of several distinct molecular configurations) with a tube-like structure, a diameter on the order of nanometers [1, 2], and a length up to 10 cm [3], though typical carbon nanotubes are much shorter (on the scale of micrometers to millimeters). Due to their small size, large aspect ratio, and one-dimensional nature, carbon nanotubes have many unique properties that provide an interesting opportunity to study fundamental physics and many opportunities for practical applications [1, 4–6]. There have been many proposals and demonstrations

for various diverse applications, including (but by no means limited to) electronics components such as transistors and interconnects [7], field emission [7–9], display devices [7], solar cells [10], radios [11–13], flexible electronics [14, 15], molecular sensors [16, 17], tags in biological imaging [18, 19], drug delivery [19–21], fighting cancer [19, 21–23], materials reinforcement [7, 16], yarns [24, 25], dry adhesives [26], thermal interfaces [27], and blackness standards [28]. In addition to the above applications, carbon nanotubes are currently being used in some applications, including batteries [7], electrostatic discharge shielding [7], composite materials [7], and atomic force microscope tips [7, 29].

An ensemble of carbon nanotubes is not, in general, a single homogeneous material. Nanotubes vary considerably in length, but also, and more importantly, in diameter [5]. There are two further important parameters. The first is called chirality, which basically describes the angle of the hexagonal carbon nanotube lattice with respect to the carbon nanotube axis [1]. The other parameter is the number of walls a carbon nanotube has [1]. These properties have a large effect on the electronic properties of the carbon nanotubes, which can be either semiconducting or metallic [1].

Many applications of carbon nanotubes require that the nanotubes to be prepared in different ways [25], from large quantities of bulk powders, to solutions of individual nanotubes, to a few precisely placed individual nanotubes in electronic circuits, to carbon nanotube forests (vertically aligned arrays of carbon nanotubes).

Carbon nanotubes can be produced by a variety of methods, one of which is chemical vapour deposition (CVD) [1, 25, 30, 31]. CVD is one of the more versatile methods of synthesizing carbon nanotubes, both in terms of the type of material produced and the quantity [2, 25]. CVD can produce either the precisely placed nanotubes that are required for electronics (while controlling the properties of those nanotubes) or CVD can mass produce nanotubes for many of the other applications that simply require a large volume of material [25].

Although CVD can be used to produce nanotubes, the exact details of how nanotubes grow and how to control their growth are not all well understood [2, 5, 6]. These "exact details" include what happens in the atomic scale processes that occur during growth and what happens to cause the natural termination of growth. The answer to many of these questions can be determined by the careful study of the morphology of the forests and by directly measuring the rate at which they grow and stop growing using *in situ* methods.

In this thesis, scanning electron microscopy, Raman spectroscopy, and *in situ* optical microscopy are used to study carbon nanotube forests grown by CVD and answer some of these questions. In particular, this thesis examines the growth kinetics (growth rate

and termination time–the time it takes for growth to stop) and morphological features (the shape and structure) of carbon nanotube ensembles known as nanotube forests. Further to that, the quality (defect density, diameter distribution, and single-walled carbon nanotube concentration) of the nanotubes is examined. From the analysis of the data collected, physical mechanisms and models are proposed to explain the observations and serve as a basis for future growth optimization procedures. The word optimization should be understood to cover a broad range of conditions due to the different demands of the different applications of nanotubes.

The mechanisms that are identified and the models that are developed allow for a rational approach to synthesis by knowing exactly how each growth parameter affects each aspect of the outcome and the mechanisms that lead to this outcome. The overall goal of carbon nanotube synthesis is to be able to grow application-specific carbon nanotubes with a specific chirality (and hence diameter and electronic type: metal or semiconductor), number of walls, length, crystallinity, and quantity. The results of the research in this thesis make steps towards many of these requirements: in particular, determining why nanotubes stop growing (thus understanding how to make longer nanotubes), how to control the yield, and how to exercise some control over what kind of nanotubes are produced in terms of their diameter and crystallinity.

1.2 Carbon nanotubes

Research into carbon nanotubes took off in the early 1990s, catalyzed by a report by Iijima [32]. Nevertheless, much of the earlier research on carbon fibers from the 1970s and 1980s [33–36] is directly applicable to nanotube research [1, 2], as is research on fullerenes [1, 4] that has occurred since their respective discovery in 1985 [37]. In addition, many important calculations and predictions were done much earlier, in particular the calculation of the band structure of graphite in 1947 [38]. Considering that carbon in the form of diamond and soot has been known since antiquity, nanotubes are a very new material. Much research is still required to fully understand nanotubes and develop them to the point of fulfilling all of their practical technological applications [2].

1.2.1 Bonding in carbon

Carbon is one of the most important elements on the periodic table because its compounds play an integral role in all forms of life as we know them [39]. There are a huge number of unique carbon compounds [39], and the study of these compounds has its

own branch of chemistry: organic chemistry [39, 40]. Carbon is the sixth element in the periodic table and thus has 6 electrons, 4 of which occupy the valence shell: two electrons in the one $2s$ level and two electrons in the three $2p$ levels in the ground state (the electronic configuration of carbon is written as $1s^2 2s^2 2p^2$) [39, 41]. The four valence electrons of carbon allow it to bond in many different ways, forming bonds with 2, 3, or 4 other atoms. These bonding states are described as being hybridized, a mixture between the pure s and p states [1, 39, 40, 42] (hybridization can also occur with d orbitals [39], but carbon does not have any electrons in these states).

In order to form multiple bonds, the electrons in carbon rearrange (the paired $2s$ electrons will not innately form bonds [39, 40]). One of the two electrons in the $2s$ orbital is promoted to a $2p$ orbital [39, 42]; the resulting electronic structure is $1s^2 2s^1 2p^3$ (one electron in the one $2s$ orbital and one electron in each of the three $2p$ orbitals) [39]. These new $2s$ and $2p$ electrons are then combined into new (identical) hybridized orbitals, or a combination of identical hybridized orbitals and p orbitals (always maintaining a total of 4 orbitals) [39, 40]. The extra energy that is required to promote one of the $2s$ electrons to a $2p$ orbital is more than offset by the formation of bonds with other atoms [40, 42].

A carbon atom that bonds with two other atoms will form a linear molecule [1]. In this bonding state, the carbon atom's electrons are described as being in sp hybridized orbitals, which are a combination of one $2s$ and one $2p$ state [1, 39, 40]. An example of sp hybridization is either of the carbon atoms in an acetylene molecule (C_2H_2) [1] (see Fig. 1). A carbon atom that is bonded to 3 other atoms creates a planar molecule in which the bonds are (approximately) evenly spaced by 120° [40]. In this bonding state, the electrons around the central carbon atom are in sp^2 hybridized orbitals, which are a combination of one $2s$ and two $2p$ electron orbitals [1, 39, 40, 42]. An example of sp^2 hybridization is any of the carbon atoms in a benzene molecule (C_6H_6) or an ethylene molecule (C_2H_4) [39], the latter of which is shown in Fig. 1. In a bond with 4 other atoms, the electrons around the central carbon atom are in sp^3 hybridized orbitals (a combination of the one $2s$ and three $2p$ states) [40]. This hybridization state results in a 3 dimensional molecule where all four bonds are approximately evenly spaced in a tetrahedral shape (spaced by 109.5°) [39, 40, 42]. The simplest example of this type of bonding is the carbon atom in methane [39], which is pictured in Fig. 1.

When a carbon atom forms three bonds, each in an sp^2 hybridized state, the 4^{th} electron orbital is perpendicular to the planar molecule (a p orbital) [1, 39, 42]. Similarly, for a linear molecule with sp hybridization, the 3^{rd} and 4^{th} electron orbitals are p orbitals, both perpendicular to each other and the axis of the linear molecule [1, 39]. Unbonded p orbitals in neighbouring bonded atoms can overlap and create indirect π bonds [39,

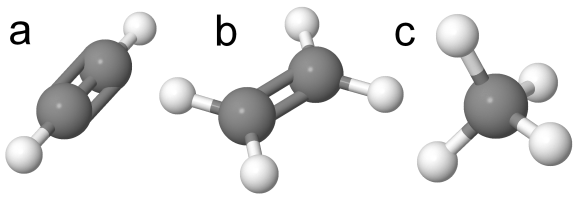


Figure 1: Molecular diagrams of some simple hydrocarbons: (a) acetylene/ethyne (C_2H_2), (b) ethylene/ethene (C_2H_4), and (c) methane (CH_4). Gray atoms are carbon, white atoms are hydrogen.

40, 42]. The direct bonds formed by the hybridized sp^n orbitals between neighbouring atoms are called σ bonds [39, 40]. In molecules that feature double bonds, like ethylene (C_2H_4), one part of the double bond will be a σ bond and the other part will be a π bond [39, 40]. Likewise, for a triple bond, such as in an acetylene molecule (C_2H_2) there is one σ bond and two π bonds [39, 40].

In a molecule such as benzene (C_6H_6), the fourth electron of each carbon atom forms a delocalized type of π bond with the neighbouring carbon atoms [39, 40]. This bond is delocalized over the benzene molecule such that all 6 C-C bonds are identical [39, 40]. The delocalization of a bond makes a molecule more stable [39]. When two benzene rings are placed on top of one another (such that the hexagons are in registry), the electrons in the π bonds on each ring can interact with one another [43]. These π-π interactions are often called π-stacking [44].

The ability to form many bonds is not the only factor that makes carbon very interesting. The other major factor that makes carbon so important in both everyday life and scientific research is its ability to form chains with itself readily (catenation [39]), giving rise to the enormous variety of molecules that fall under the domain of organic chemistry [39, 40].

1.2.2 Allotropes of carbon

Pure carbon has several allotropes (different atomically pure forms with unique molecular structures), some of which are shown in Fig. 2. The most common and well known are diamond, amorphous carbon, and graphite (Fig. 2, left) [40]. Other allotropes of carbon include, graphene (Fig. 2, left), fullerenes (Fig. 2, right), and the subject of this thesis, nanotubes (Fig. 2, center) [40]. Diamond is a 3D crystalline solid composed of pure sp^3 bonded carbon atoms [40] in two interlocking face-centered cubic (FCC) crystal structures [42, 45]. Amorphous carbon is a 3D solid, but lacks any defined crystal structure [40]; the carbon atoms in amorphous carbon can adopt a variety of different bonding states [1]. Graphite is composed of pure sp^2 bonded carbon atoms in 2D layers

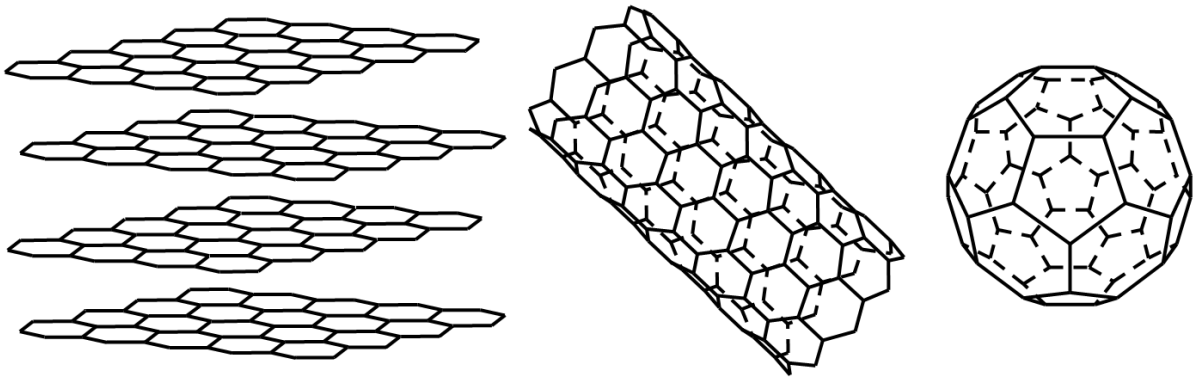


Figure 2: Some allotropes of carbon. From left to right: Graphite (a single layer of which is called graphene), a nanotube, and a fullerene (buckyball/buckminsterfullerene/C_{60}).

(in a hexagonal lattice structure with approximately 0.14 nm edges) that are stacked on top of one another (spaced by 0.34 nm) to form a 3D crystal [1, 40]. The relatively weak van der Waals forces between these layers keep the crystal together [41, 42]. The conductivity of graphite is a result of the delocalization (over the entire crystal) of the fourth electron on each carbon atom [40], similar to the delocalization in a benzene molecule.

A single layer of graphite is called graphene [1]. A graphene sheet can be "rolled up" in a variety of ways. When rolled up in a single dimension to form a hollow tubular structure, the resulting carbon allotrope is called a carbon nanotube [1]. Rolling a graphene sheet in both of its two dimensions results in another carbon allotrope called a fullerene [40]. The most common and basic fullerene is buckminsterfullerene, also known as a buckyball, with a chemical formula C_{60} [40]. Its 0.7 nm diameter spherical structure consists of 12 pentagonal rings of carbon atoms and 20 hexagonal rings, which is the same form as a standard soccer ball [40, 42].

One can think of these allotropes in terms of the number of dimensions they effectively possess. Diamond, amorphous carbon, and graphite, are all extended 3D structures. Graphene is a 2D structure, while nanotubes behave as essentially 1D structures [1], and buckyballs behave as essentially 0D structures [1] due to their small size and high degree of confinement [41]. Buckyballs are made of sp^2 hybridized carbon atoms (which can alternately be described as only sp^2 bonded carbon) that are slightly bent out of their planar shape to the extent that pentagonal rings appear [42] in order to allow for the spherical shape. The extra electrons in the non-hybridized p orbitals on each carbon atom become completely delocalized over the entire molecule [39].

In general, the word "nanotube" can be used to refer to tubular nanostructures made out of a variety of other materials which include both inorganic compounds [46, 47] (in particular boron nitride, which has the same crystal structure as graphene [48]) and

organic molecules [49]. However, throughout this thesis, the word "nanotube" is used exclusively to refer to carbon nanotubes.

1.2.3 Physical structure of carbon nanotubes

Carbon nanotubes can be thought of in two ways (most likely based on the task at hand and the background of the researchers involved): a large molecule composed entirely of carbon atoms or a very small solid state material composed of carbon atoms. Depending on the exact situation one point of view may provide better understanding than the other. This fact is apparent in textbooks as carbon nanotubes are discussed in chemistry text books [39, 40] and solid state physics text books [42, 50]. Furthermore, carbon nanotube research is very interdisciplinary, with research appearing in a wide variety of journals, with general topics ranging from chemistry (such as *Journal of the American Chemical Society*) to chemical physics (such as *Chemical Physics Letters*) to physical chemistry (such as *The Journal of Physical Chemistry*) to physics (such as *Physical Review Letters*), as well as journals dedicated to nanotechnology and carbon.

Carbon nanotubes can have open ends like drinking straws or they can have closed-off ends [1]. These closed ends are called the "caps" of the nanotube [1]. In the simplest description, the caps can be thought of with roughly hemispherical domes of half fullerenes (consisting of six pentagons and several hexagons, with the exact number of hexagons depending on the nanotube diameter), but can also have more complex shapes [1]. One can think of a buckyball as the shortest possible closed nanotube.

When a sheet of graphite is rolled up into a nanotube, the rolling can be done in a variety of ways. This determines the chirality of the nanotube as defined by the chiral vector $\vec{C_h}$ [1], which is depicted in Fig. 3a. This vector can connect any two identical carbon atoms in the graphene lattice (there are two non-identical carbon atoms in the lattice, one at each end of any given bond [1]). When a graphene sheet is rolled up into a nanotube, the chiral vector forms the circumference, and the nanotube is given a chirality (n, m) where n and m are the number of lattice vectors $\vec{a_1}$ and $\vec{a_2}$ used to construct $\vec{C_h}$ [1]. The diameter of the nanotube d is therefore a function of the chiral vector [1]:

$$d = \frac{a}{\pi}\sqrt{n^2 + m^2 + nm} \tag{1.1}$$

where $a = |\vec{a_1}| = |\vec{a_2}| = 0.25$ nm is the lattice constant of graphene.

Typical diameters are in the range of 1 to 10 nm [1], but can be as low as 0.3 nm [51] and as high as ∼20 nm [1]. Although larger diameters may be possible, such structures tend to not be entirely cylindrical [1]. Nanotubes with large inner diameters have a

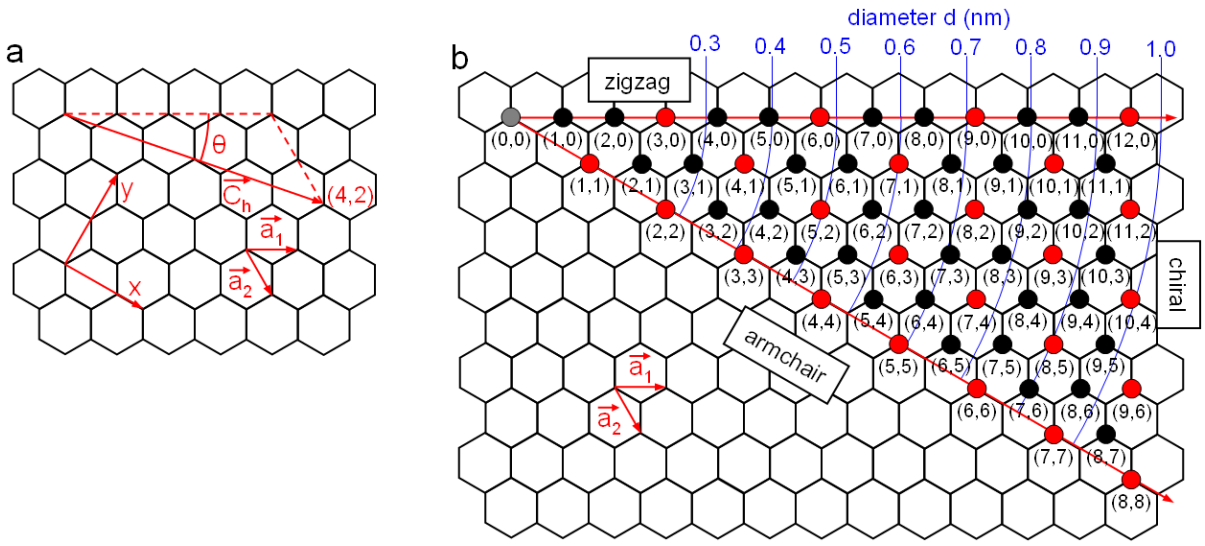


Figure 3: Nanotube chirality. (a) Definitions of vectors $\vec{a_1}$ and $\vec{a_2}$, chiral vector $\vec{C_h}$, and chiral angle θ with respect to the graphene lattice. The chiral vector $(4, 2)$ is presented. (b) Map of small diameter nanotube chiralities. Figures adapted from Reference 1.

tendency to collapse from their tubular structure and flatten out into more ribbon like forms [52]. The length of the nanotubes can be as short as a buckyball, and as long as 10 cm [3], though there is no theoretical limit. The maximum length achieved is more limited by the physical size of the system in which the nanotube was synthesized and the synthesis method employed [3].

The chiral angle θ is the angle between the chiral vector $\vec{C_h}$ and the vector $\vec{a_1}$, as depicted in Fig. 3. From the nanotube chirality (n, m), the chiral angle can be calculated [1]:

$$\cos\theta = \frac{2n + m}{2\sqrt{n^2 + m^2 + nm}} \tag{1.2}$$

The chiral vector is degenerate due to the symmetry of the graphene lattice, with unique chiralities occurring for $0° < \theta < 30°$. This places two conditions on n and m: $n, m>0$ and $n \geq m$. Specific cases of chirality are [1]:

1. $(n, 0)$ with $\theta = 0°$, which is called a "zigzag" nanotube due to the shape of its open end
2. (n, n) with $\theta = 30°$, which is called an "armchair" nanotube due to the shape of its open end
3. All other (n, m) nanotubes are described as "chiral"

These situations are depicted in Fig. 3b and Fig. 4 for a $(9, 0)$ zigzag nanotube (0.72 nm diameter), a $(7, 3)$ chiral nanotube (0.71 nm diameter), and a $(5, 5)$ armchair nanotube (0.69 nm diameter). The left side of the figure shows the respective chiral vectors on the

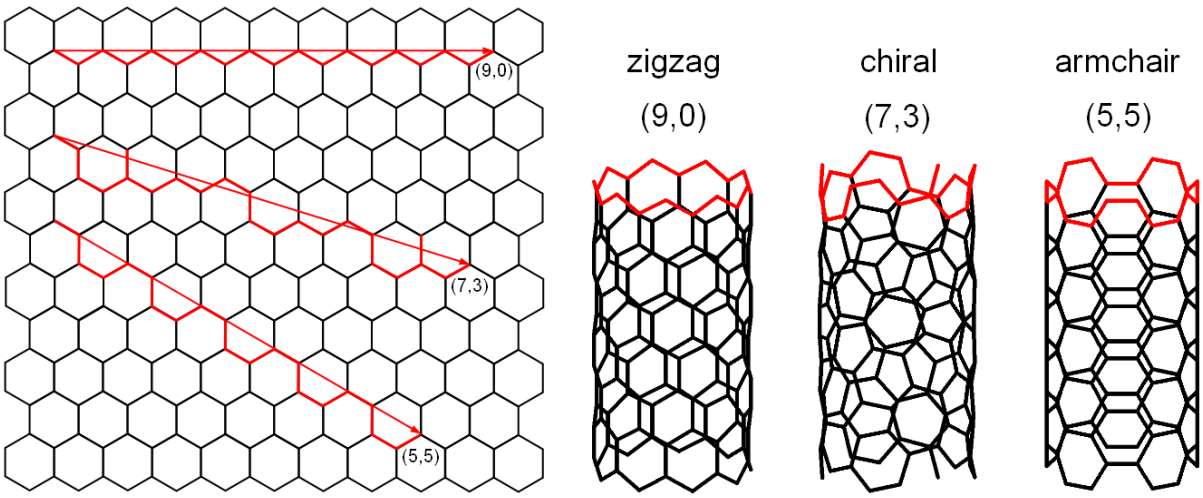


Figure 4: Nanotube construction. Left: chiral vectors and resulting open edge of the nanotube (red). Right: the nanotubes described by these chiral vectors, open edge highlighted (red).

graphene lattice, and the resulting open edge of the nanotube (in red). The nanotubes described by these chiral vectors are shown on the right, with the open edge highlighted (in red).

When a single sheet of graphite is rolled up into a nanotube, that nanotube is described as a single-walled carbon nanotube (SWNT, also written SWCNT) because it only has one circumferential layer [1, 41]. It is possible to roll up more than one graphene sheet and create a multi-layer nanotube with concentric nanotube shells, called a multi-walled carbon nanotube (MWNT, also written MWCNT) [41]. A MWNT is illustrated in Fig. 5. The concentric nanotube walls are spaced by approximately the same amount as layers in graphene, $\sim$0.3 nm [41]. The independent walls are held together by the same van der Waals forces that hold the layers of graphite together [41]. However, the forces between the walls of a MWNT are weaker than the forces between graphite layers because in a MWNT, the adjacent walls are not in perfect registry with one another [1]. Due to the differing diameters of the walls, the chirality of each wall is necessarily different. MWNTs with 2 walls are called double-walled nanotubes (DWNTs) and MWNTs with 3 walls are called triple-walled carbon nanotubes (TWNTs).

It should be noted that nanotubes are not literally made by rolling up pieces of graphene, but are rather synthesized in various self-assembly processes, in which the nanotubes adopt their tubular structure [6]. Details of these processes will be discussed in the following sections.

Because the van der Waals forces between them are quite strong, nanotubes tend to clump together [1] into "bundles". In some applications nanotubes are intentionally bundled together in order to make macroscopic wires or fibers (see for example Reference 53).

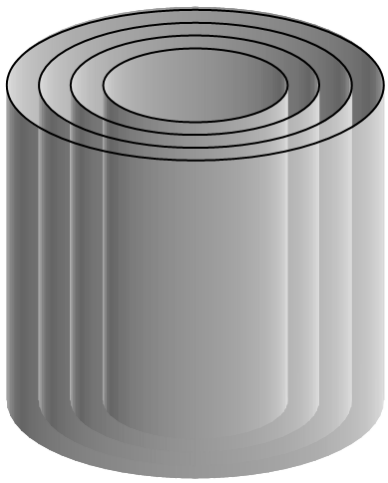


Figure 5: Cut-away diagram of a multi-walled carbon nanotube (MWNT), showing the layer structure. Actual carbon atoms and bonds are omitted for simplicity, but each layer possesses the crystal structure of a single-walled nanotube as illustrated in Fig. 2.

When nanotubes are grown on a (horizontal) surface, the packing can be so dense that they do not lie flat on the surface, but are instead all vertically aligned, perpendicular to the surface upon which they are grown [25], as shown in Fig. 6. This configuration is the main focus of this thesis and is called a "vertically aligned carbon nanotube forest", or simply a "forest" for short. The acronyms VACNT (vertically aligned carbon nanotubes) and VANTA (vertically aligned nanotube array) are synonymous with forest. Nanotube forests are generally composed of small bundles of nanotubes (typically containing on the order of 10 CNTs [54, 55]) that are all roughly parallel, but tend to meander somewhat (see Fig. 6b), due to interactions between them and slightly differing growth rates. These interactions between the constituent nanotubes of the forest (and between the nanotubes and the substrate, the catalyst, and the support) have a direct and significant impact on how these forest structures look and grow and will be discussed in detail in Section 1.4.6 and in later chapters of this thesis, along with the mechanisms that cause the nanotubes to have slightly different growth rates from one another.

Nanotubes forests have a variety of applications and are not simply a means of bulk production (though bulk production can be achieved by growing forests). Carbon nanotube forests have applications in field emission [7–9], dry adhesives [26], thermal interfaces [27], and blackness standards [28]. From a research point of view, one advantage to growing nanotubes in the forest configuration, aside from a high yield of material, is that forests are macroscopically large objects and thus optically visible [56–58]. When grown over a large (5 mm $\times$ 5 mm) area, a nanotube forest that reaches several mm in height is easily visible to the unaided eye (see Fig. 7) as a black layer of increasing thickness (in-

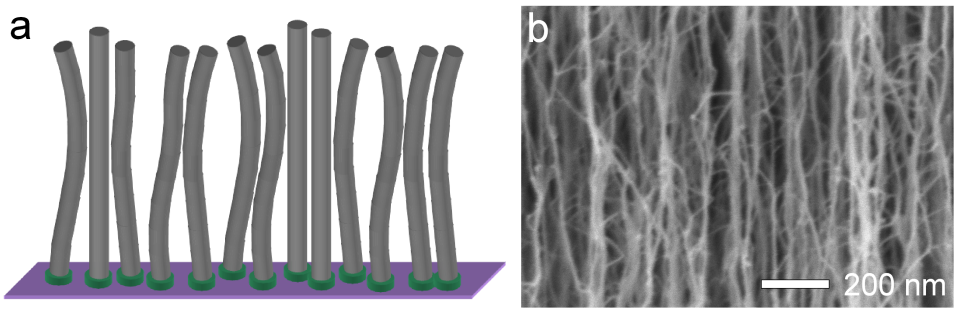


Figure 6: Carbon nanotube forest. (a) Diagram of the forest. Nanotubes are gray, catalyst nanoparticles are green, and substrate is purple. (b) Scanning electron microscope image of an actual forest analyzed in this thesis.

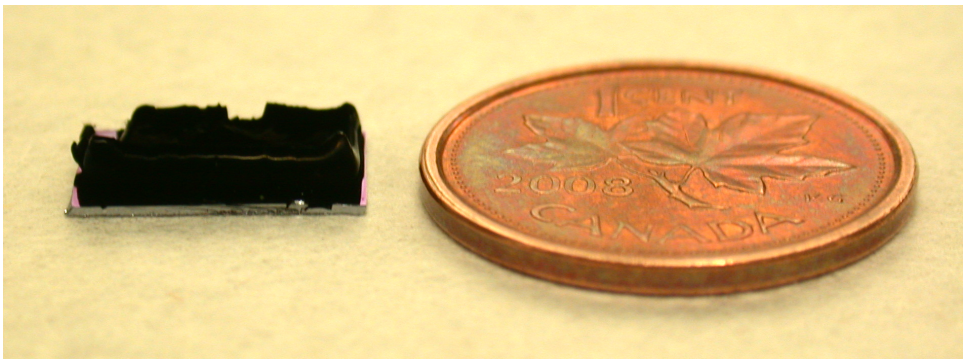


Figure 7: Carbon nanotube forest photograph with a Canadian penny to demonstrate size. Forest grown on ∼12 mm × ∼6 mm silicon substrate (of 0.5 mm thickness), and reaches a height of ∼2 mm.

dividual nanotubes cannot be resolved optically). In particular, forests allow for optical microscopy to be performed *in situ* as the nanotubes are grown [59–63], thus providing a means of extracting *in situ* data of the growth kinetics with a totally non-destructive method. This method is used extensively and further developed in this thesis.

Finally, a brief discussion of carbon fibers is necessary. Compared to nanotubes, carbon fibers are generally much thicker, and lack the well ordered crystal structure of a nanotube [41]. Carbon fibers are often composed of many partially (even significantly) graphitized layers [41]. Although carbon fibers can be hollow [1, 41], an important difference between fibers and carbon nanotubes (aside from the size difference) is that while carbon nanotubes behave in many ways like a 1D material, carbon fibers do not [1]. It is important to consider carbon fibers when discussing carbon nanotubes because much of the early work done on carbon fiber synthesis [33–36] is applicable to research on carbon nanotubes [1, 2].

1.2.4 Properties of carbon nanotubes

Owing to their unique aspect ratio and 1D nature, carbon nanotubes have a number of remarkable properties that give rise to the large number of different applications [1, 5]. Their small diameters give rise to quantum effects, in particular the quantum confinement of electrons and phonons. Although the electronic band structure of carbon nanotubes is not the focus of this thesis, a brief introduction is necessary in order to better explain resonance conditions related to Raman spectroscopy.

The band structure of a nanotube can be calculated using a method called "zone-folding" [1] from the band structure of graphene, which can be calculated using a tight binding model (see for example Reference 1). Graphene is a zero band gap semiconductor with the "gap" occurring at the corner of the Brillouin zone [1, 41]. The effect of rolling up a 2D graphene sheet into a 1D nanotube is that only discrete slices of the graphene band structure are preserved [1]. This is one of the main effects of the chirality: it imposes a periodic boundary condition on the band structure such that the band structure of carbon nanotubes of different chiralities use a different set of evenly spaced "slices" of the graphene band structure.

Depending on their chirality, some nanotubes are metallic in character with no band gap, while others are semiconducting, with a direct band gap at $\vec{k} = 0$ in the center of the Brillouin zone [1]. Because of their direct band gap, semiconducting nanotubes are good light emitters and absorbers [64]. Their ability to absorb light makes them one of the blackest materials available [28].

The division between metals and semiconductors is determined by $\mod((n-m), 3)$: when the modulus is 0, the nanotube is metallic, otherwise the nanotube is a semiconductor [1]. In a large arbitrary sample of nanotubes with randomly distributed chiralities and diameters, 1/3 will be metallic and 2/3 will be semiconducting. In Fig. 3b, the nanotubes whose chiralities correspond to metals are indicated by red points while the black points indicate nanotubes whose chiralities correspond to semiconductors. MWNTs can have some walls that are semiconducting and some that are metallic.

For the semiconducting nanotubes, if one considers a tight binding model as a first approximation of the electronic band structure (as in Reference 1), the band gap can be shown to be inversely proportional to diameter [1]:

$$E_{gap} = \frac{at}{\sqrt{3}d} \tag{1.3}$$

where $a = 0.25$ nm is the lattice constant of graphene, $t = 3.13$ eV is a parameter from the tight binding model used to calculate the band gap, and d is the nanotube diameter.

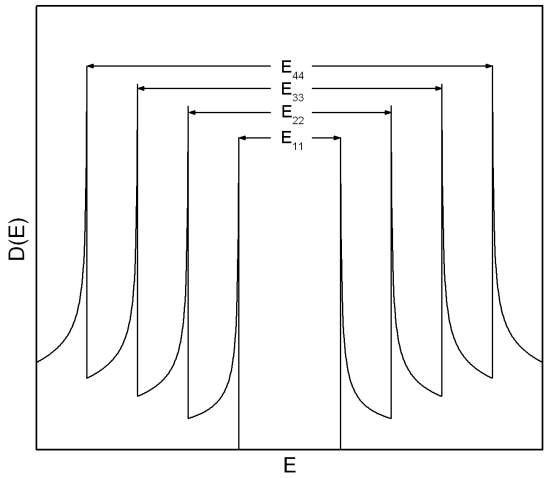


Figure 8: Schematic illustration of the density of states in a semiconducting single-walled carbon nanotube, with energy transitions labeled.

For a nanotube (or indeed any 1D structure), the density of states is characterized by a series of individual asymmetric peaks (1D van Hove singularities) that are symmetric about the band gap (with the peaks being in the conduction band and valence band) [50]. The smallest gap is the band gap and is referred to as the E_{11} transition. Similarly, the next largest symmetric transition is referred to as the E_{22} transition, and so on [64]. The density of states is schematically illustrated in Fig. 8.

A metallic nanotube has very similar density of states, except that the density of states does not go to zero at $E = 0$ [1]. The opposing symmetric van Hove singularities mark the transitions M_{11}, M_{22}, and so on [65, 66].

Mechanically, carbon nanotubes have a very high Young's modulus and tensile strength, particularly for their light weight [1]. This combination of light weight and high strength (that results from strong C-C bonds) is what leads to CNTs being used in material reinforcement.

Chemically, nanotubes are generally inert unless they have been modified and functionalized (the addition of functional chemical groups to the nanotube structure) [16]. When functionalized, nanotubes can be used in both biological applications (with biologically active functional groups) and materials reinforcement (by attaching them to polymer matrices) [7, 16]. The presence of defects makes a nanotube more reactive and easier to functionalize [16]. Functionalization can be as simple as treating the nanotubes with acid to attach various oxygen containing functional groups that can be further used for chemistry. Alternatively, it is possible to use π-stacking interactions to attach aromatic molecules to the carbon nanotubes without altering the structure of the nanotube

[44].

1.2.5 Toxicity and safety

Because of their shape and size, nanotubes can be quite efficient at entering living cells to deliver drugs when properly functionalized [7]. This brings up the issue of toxicity. In terms of human toxicity, there is no definitive answer due to the difficulty of measuring a huge variety of diameters and, especially, lengths [67, 68]. Further complicating the issue of measuring the toxicity of carbon nanotubes is how and where the nanotubes are delivered and whether or not they are in solution, what the solvent is, how bundled they are and whether or not they are functionalized [68–71].

Evidence suggests that inhaling loose powders of carbon nanotubes can be harmful to the lungs, similar to the effects of asbestos exposure [68–71]. Conversely, there is also evidence from *in vivo* animal studies that functionalized nanotubes can be present in the body without significant negative effects and are simply removed by the body [68]. However, there is also evidence that nanotubes might accumulate in certain organs [68]. The long term effects of this accumulation are unknown.

With this potential toxicity in mind, precautions were taken during this research to ensure that the material was handled safely and to avoid (or at least minimize) exposure and contamination. Some of these steps were simply just general safety practices, such as not having food or drink in the lab. Beyond that, gloves were worn when handling samples or potentially contaminated surfaces and proper hand washing was observed. When dusty surfaces were cleaned, it was done with a damp cloth to prevent dust from entering the air. Testing for particulates in the air in the lab indicated that there was no difference between the number of particles in the lab and elsewhere in the building. Because the majority of the samples produced in the lab were bound to silicon substrates, it is unlikely that significant numbers of nanotubes would be able to enter the air.

Regardless, respirator masks with NIOSH 100 particulate filters were worn when handling the material and opening/closing the CVD reactors. Nanotube samples were only manipulated inside a laminar flow bench that prevents material from escaping back into the lab. The bench is exhausted out of the lab through a HEPA (high-efficiency particulate air) filtration system. When carrying samples between the CVD reactor and the laminar flow bench, samples were placed in an enclosed transfer tube. Otherwise, samples were stored in enclosed plastic containers. The Raman spectroscopy system also had a specific sealed container for placing samples in with a very thin glass window to allow optical access.

Overall, common sense and caution were applied to all aspects of the research to ensure that any potentially hazardous material was kept isolated through the use of personal protective equipment (such as gloves and masks) and protocols (such as proper handling and engineering safety measures like the laminar flow bench).

1.3 Crystal structures and growth

A significant amount of research had been done on crystal growth processes, and, in many ways, crystal growth is analogous to carbon nanotube growth (this is one situation where it is useful to think of carbon nanotubes as small individual crystal structures). The general ideas about crystals and crystal growth presented in this section provide insight into the way that carbon nanotubes and forests grow. Additionally, the discussion of defects in crystals is useful for understanding the origin of the D band in Raman spectra of carbon nanotubes.

1.3.1 Defects in crystal structures

Crystal structures, in introductory theories and calculations, are considered to be both infinite and perfectly periodic [50], with each lattice point (of whatever the exact structure may be) occupied by an atom (or ion) of the material. The simplest type of defects in 3D crystals are surfaces and interfaces, both of which are 2D defects that represent breaks in the otherwise ideal infinite crystal structure [50]. Here, "surface" has the meaning of an interface between the bulk crystal and a non-solid material, whereas "interface" specifically means an interface between two different solids, which may even be the same element, but in a different form. In analogy, when discussing nanotubes one talks about the ends of the nanotube.

In addition to the 2D defects, 3D crystals can also have 1D line defects, such as edge dislocations and screw dislocations [42, 45, 50]. An edge dislocation is essentially the result of one atomic plane simply ending in the middle of a crystal. A screw dislocation is the result of part of each atomic plane being offset such that there is, effectively, one continuous atomic plane that spirals around the line defect and creates a 3D crystal, as depicted in Fig. 9. This type of defect is particularly important for crystal growth theories [72].

Another type of defect is a stacking fault [45, 50]. In general, one can consider a crystal structure as a series of layers on top of one another [45]. Each layer will line up with the layer beneath it in a specific way, such the layers appear in a regular order such

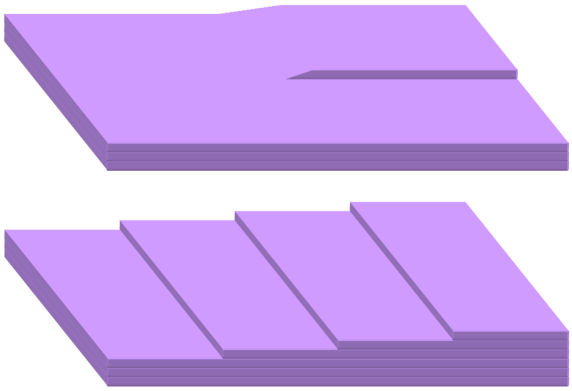


Figure 9: Defects in crystals and surfaces. Top: screw dislocation at the crystal surface, with exposed edge. Bottom: Step edges on a vicinal surface.

as ABCABC where A, B, and C describe the offset of each layer [45]. An edge dislocation will put these layers out of order (such as ABCBABC or ABCBCABC) over a portion of the crystal, creating a stacking fault in the layer structure [45, 50].

Finally, numerous 0D point defects are also possible [50]; these include substitutions, interstitials, and vacancies. Substitutions occur when an atom or ion is replaced by a different atom or ion (which may simply be a different isotope); dopants are generally intentional substitutions [42]. Interstitials are atoms placed in between the lattice points, and vacancies are missing atoms. In addition to single vacancies, double (or higher order) vacancies may also exist.

One particular defect to the graphene lattice is a Stone-Wales defect [73], which is a rotation of a C-C bond, as pictured in Fig. 10. This creates two heptagon-pentagon pairs. The bonds and carbon atoms near the defect are all slightly displaced from their equilibrium positions. Other related defects include pentagons, heptagons, and pentagon-heptagon pairs. Any break in the regular sp^2 bonding structure is a defect, thus the presence of bonds with sp^3 hybridization is also a defect.

Defects on surfaces

In addition to bulk defects, there are also defects specific to surfaces [72]. The most prominent of these are step edges (as shown in Fig. 9), which occur in two situations. The first situation is when a surface is not perfectly cleaved along a crystallographic plane, leaving the exposed edges of the partial planes. This is called a vicinal surface [72]. The second situation is when a screw dislocation (perpendicular to the surface) reaches a surface, leaving an exposed edge of the spiral structure below the surface [72], as depicted in Fig. 9.

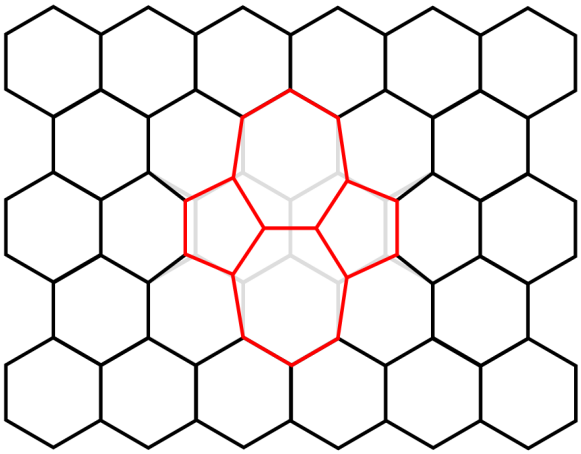


Figure 10: Stone-Wales defect in a graphene lattice. The central bond is rotated 90°, creating two pentagon-heptagon pairs (red) and slightly displacing nearby bonds and carbon atoms.

Other particular surface defects are adsorbed species such as adatoms (adsorbed atoms) [72]. These adsorbed species may be atoms from the solid itself, or may be molecules or atoms captured from the gas phase. Adsorbed species will attach to the surface either physically with van der Waals interactions or bond to the surface chemically [72]. These adsorbed species often have an associated activation energy for the breaking of the bond [72].

1.3.2 Crystal growth models

Crystal growth can be achieved using many different techniques, either forming a bulk crystal [74] or by growing the material layer by layer, which is called "epitaxy" [74]. One method to epitaxially grow crystals is CVD (which will be discussed in detail in Section 1.4), but other processes exist, such as molecular beam epitaxy (MBE) [42, 45, 74]. This section contains a general qualitative description of crystal growth for a monatomic system without referring to the specifics of the method used to grow the crystal.

In a generic epitaxial crystal growth process, a substrate (or seed surface) is used which may or may not be the same material as the layer being deposited [72, 74]. This surface is then exposed to a beam of particles or the vapour phase of the material that is being deposited. The impingement rate of these particles is determined, respectively, by the beam flux and vapour pressure. The impingement rate affects the surface concentration of adatoms [42, 72, 74]. Once adsorbed onto the surface, the adatoms can diffuse across the surface or desorb back into the vapour phase [72]. When the surface density of adatoms is sufficient, collisions between the mobile adatoms may occur [72]. When this happens, the two adatoms will bond together because it is more energetically favourable

than having extra dangling bonds[72]. As collisions increase, islands form, and eventually a solid surface is formed. Subsequent layers are grown by the same means, possible even before the preceding layer is complete [72].

A vicinal surface with step edges allows for much quicker growth than a perfectly smooth surface because it provides an entire edge onto which adatoms can immediately incorporate into the crystal structure (because bonding at the step edge is more energetically favourable due to more bonds being formed) [72]. This kind of growth is quicker than growth on atomically flat surfaces because it does not require a critical density of adatoms and adatom collisions [72].

Similarly, if a surface is intersected by a (perpendicular) screw dislocation, there is a step edge on the surface where growth can occur. One end of this step edge is anchored at the center of the screw dislocation. The whole step edge will propagate along with the growth as more and more atoms are added to the crystal structure [72]. As more and more atoms are added, this edge is continuously added to and propagates around the dislocation. This leads to growth in a spiral pattern, with new atoms continuously being added at the exposed step edge of the screw dislocation [72], as shown schematically in Fig. 11. In a sense, the crystal is just one continuous atomic plane with a screw dislocation.

This spiral growth has been invoked to explain the growth of carbon nanotubes [75], and in particular the possible chiral selectivity of growth. This growth model is inspired by evidence that carbon nanotube chiralities are often skewed toward larger chiral angles [75]. The larger chiral angle nanotubes have more open bonds (not bonded to other carbon atoms in the CNT) that provide energetically favourable locations for new carbon atoms to incorporate, much like the adatoms preferentially incorporating onto step edges as discussed above. This makes the growth of higher chiral angles both more likely and quicker. This is pictured in Fig. 12.

Some evidence for this theory has recently been published [76]. This screw dislocation growth theory of carbon nanotubes is presented here to provide both an overview of theoretical ideas, as well as to show how general crystal growth ideas can be used to explain the growth of carbon nanotubes. Furthermore, this theory is later discussed in Chapter 8 and Chapter 9 as one potential "growth filter".

In epitaxial growth, when the substrate and deposited material are the same, it is called "homoepitaxy"; when they are different materials, it is called "heteroepitaxy" [74]. When dealing with heteroepitaxy, one must consider the lattice constants of the two materials. If there is a significant mismatch between the two materials' lattice constants, this mismatch can introduce a significant amount of strain into the growing layers as they

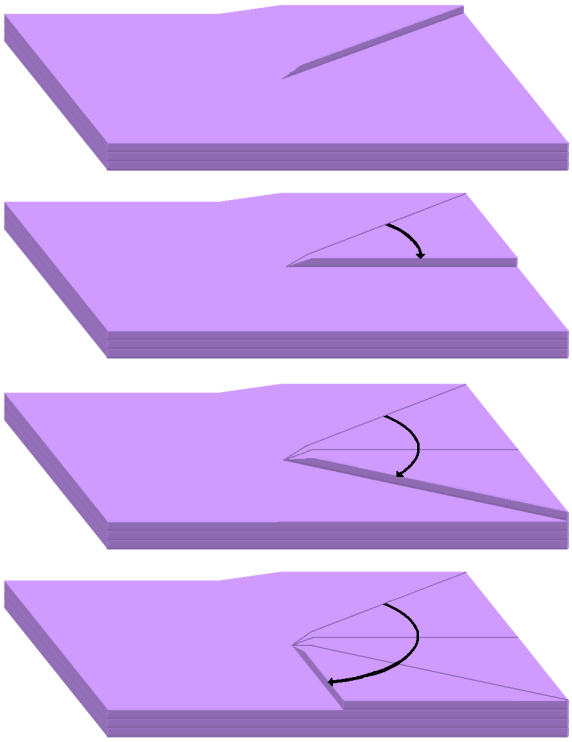


Figure 11: Schematic of crystal growth occurring via a screw dislocation, which proceeds in a characteristic spiral pattern.

are forced to adopt a structure that does not match the ideal, relaxed lattice positions [74]. Above a certain critical thickness, dislocations will appear as the lattice will relax into its preferred spacing [74]. Further growth will yield a surface that corresponds to the ideal spacing of lattice points.

In addition to the effects of lattice mismatch in heteroepitaxy, there are three main growth modes that can occur: Frank-van der Merwe (FM), Volmer-Weber (VW), and Stranski-Krastanov (SK) [45, 74], which are illustrated in Fig. 13. The FM growth mode proceeds layer by layer, with islands forming and coalescing into one uniform layer which is complete before the next layer begins to nucleate. This mode occurs when the atoms of the deposited material stick to the substrate stronger than they stick to one another [74]. The VW growth occurs when subsequent layers nucleate before the previous layers are completed. This leads to the growth of individual islands of material that can later coalesce as they become larger. This growth mode occurs when the deposited material sticks more strongly to itself than to the substrate [74]. The SK growth mode is a combination of the two. It begins with layer by layer growth as in the FM growth mode, but, at a critical number of monolayers (a wetting layer) [74], makes a transition to the island growth seen in the VW growth mode. The critical thickness of this wetting layer is

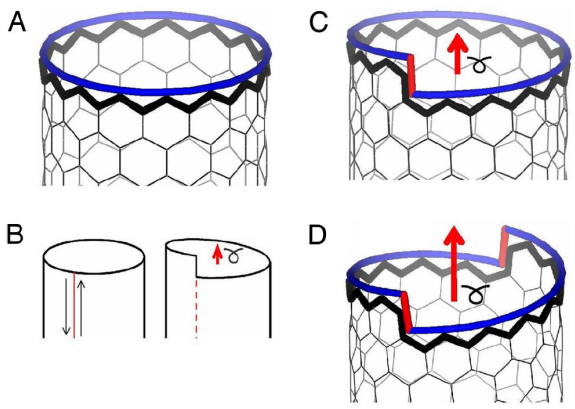


Figure 12: Dislocation theory for chirality selective CNT growth. (a) A zigzag CNT has no "step edges" for preferential incorporation of carbon atoms. (b) Schematic of a screw dislocation in a carbon nanotube, which introduces the equivalent of step edges in a surface. (c,d) Increasing chiral angles have more "step edges" and thus more sites for incorporation, which leads to higher growth rates. Figure reprinted with permission, from: F Ding, A R Harutyunyan, and B I Yakobson. *Proc. Nat. Acad. Sci.*, 106:2506–9, 2009 [75].

different from the critical thickness for the mismatch induced lattice relaxation, however, these two critical thicknesses are often similar [45].

1.4 Chemical vapour deposition

There are many different techniques that can be used to produce carbon nanotubes, including arc discharge, laser ablation, and chemical vapour deposition (CVD) [1, 6, 25, 30]. Of these methods, CVD is amongst the most versatile [2, 25]. The use of CVD to grow nanotubes evolved from the use of CVD to produce carbon fibers [1, 2]. CVD can be scaled up from the laboratory samples used in research to industrial scale production [1, 2, 25]. It can produce bulk nanotube material, films of nanotubes, fibers composed of nanotubes, nanotube forests, or surface nanotubes with specific geometries [2, 25]. Furthermore, nanotubes produced by CVD generally have fewer non-carbon contaminants than other processes [2]. Here, all nanotube samples are prepared by CVD, as described in the following section.

1.4.1 Overview

The basic premise of CVD is contained within its name. It is the deposition of a solid material via the chemical reaction of vapour phase reactants [25, 30, 74]. This deposited material can either be a mass of material not attached to anything, or it can be a uniform layer growing on a pre-existing surface, such as the reactor walls or a growth substrate

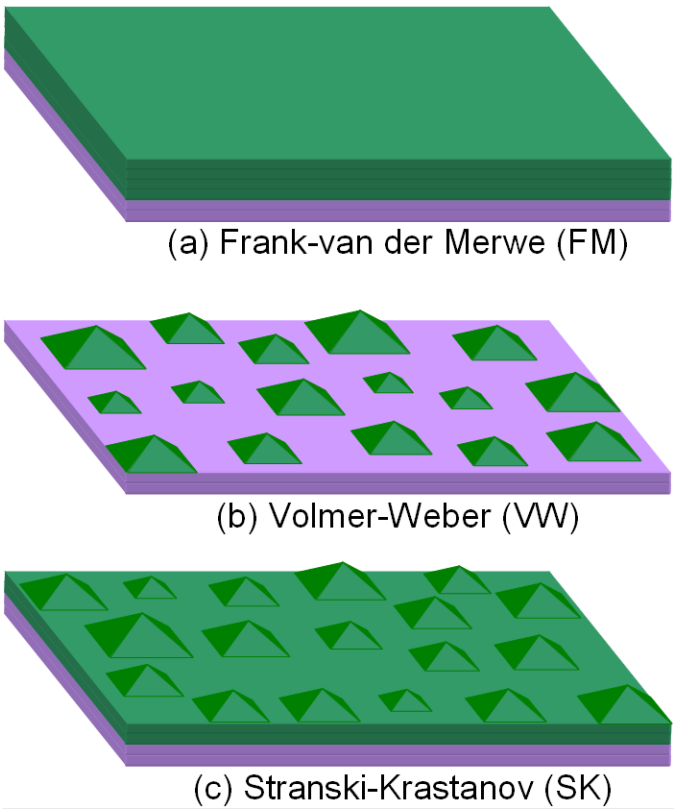


Figure 13: Growth modes for heteroepitaxy. Purple layers represent substrate, green layers represent deposited material.

[2, 25]. CVD is commonly used in the industrial growth of semiconductors (in the form of metal-organic CVD, or MOCVD) [42, 74]. In this thesis CVD is used to grow carbon nanotube forests on a silicon wafer that has layers of catalytic material deposited onto it prior to growth.

The CVD process requires a few basic things: a controlled environment, process gases, energy input, and in many cases a catalyst [2, 25]. In the thermal CVD process used here, the energy input is provided by heating. Thus, the basic control parameters in CVD are the chemistry of the gases and catalyst, the pressures and ratios of these gases, and the temperature [30].

In carbon nanotube growth, the catalyst is typically a transition metal nanoparticle (Fe, Co, Ni, or an alloy), but may also be a nanoparticle of another material [2, 25]. It is thought that a nanoparticle is necessary because the small size of the nanoparticle provides a template over which the nanotubes can form in the appropriate diameter range [2, 77]. Details of the nanoparticle and substrate preparation are given in the next section.

For carbon nanotube growth by CVD, almost any carbon containing molecule can be

used as a source gas [2, 78], although common molecules are methane (CH_4) ethylene (C_2H_4), carbon monoxide (CO) [79], acetylene (C_2H_2), and ethanol vapour (CH_3CH_2OH) [80] (see Fig. 1 for molecular diagrams of some of these molecules). The two latter molecules are used in this thesis. In many cases, growth is performed in the presence of hydrogen gas (H_2) which enhances growth, possibly by acting as a reducing agent that maintains the chemical nature of the catalyst [81]. The presence of oxygen in ethanol, via the hydroxyl (OH) group, is thought to have a significant effect on the growth such that it removes amorphous carbon from the catalyst nanoparticles [2, 80]. Oftentimes, synthesis is performed using water vapour in addition to the process gases [82]. The water (or more specifically the oxygen in it) is thought to remove amorphous carbon from the catalyst nanoparticles [57, 82–84]. It has also proposed that water plays a role in prolonging the growth of carbon nanotubes by inhibiting Ostwald ripening of the nanoparticles [85]. (Ostwald ripening is the growth of larger particles at the expense of the smaller ones due to the diffusion of material between them; more details of this are given in Section 1.4.7). In many CVD processes an inert carrier gas such as helium or argon is used to dilute and transport the source gases.

In the case of ethanol, water, and other vapours, the carrier gas can be passed through a bubbler containing the liquid to obtain a vapour. A bubbler is a closed vessel containing the liquid of the desired vapour with a gas inlet below the surface and an outlet above the surface. The vapour pressure of the liquid maintains a steady concentration of vapour in the bubbler. As the gas passes though the bubbler, gaseous molecules are removed from the bubbler by the outgoing stream of gas. The lost molecules are replenished by further evaporation of the liquid.

In general, a CVD reactor is generally a controlled (closed) environment with an exhaust to the atmosphere for the product gases and unused reactant and carrier gases [86] (though not directly into the lab). The pressure inside the reactor can be controlled by attaching a vacuum pump to the exhaust of the reactor [86], though this is not done in the simple atmospheric pressure system used in this thesis. The amount of gas flowing into the reactor is controlled and the concentration of various process gases is measured, such as measuring water content with a hygrometer.

Heat can be provided by two general methods: hot-walled CVD or cold-walled CVD [86]. In hot-walled CVD, the entire chamber is heated from the outside, such as a quartz tube furnace. A cold-walled CVD reactor has a small heater inside that only locally heats the growth substrate, often using Joule heating. The advantage of hot-walled CVD is a more consistent temperature throughout the reactor, however, this comes with the disadvantage of (often undesired) increased gas phase chemical reactions [87].

The situation is reversed for cold-walled CVD. In either case, it is possible to pre-heat the source gases in order to induce these gas phase reactions [88]. Typical reaction temperatures vary from 600°C to 1000°C [2, 25, 30], although growth outside of this range is possible. Growth of carbon nanotubes at temperatures as low as 350°C has been reported [89].

There are many other forms and variations of CVD, such as plasma enhanced CVD (PECVD, where the energy input requirement for CVD involves a plasma) [2, 25, 30], however, none of these variations are studied here.

1.4.2 Growth substrates

The growth substrates used in this thesis are all 0.5 mm thick silicon wafers with layers deposited onto them by e-beam (electron beam) evaporation using either a mechanical mask (made with a thin piece of metal) or lithographic mask (these processes are described below). The silicon wafers are <100> orientation and either undoped, intrinsic silicon, or are doped with boron, phosphorous, or arsenic. The orientation and doping are unlikely to affect the growth in any way because the catalyst is separated from the silicon wafer by a layer of alumina (Al_2O_3). The silicon wafers have a layer of thermally grown silicon dioxide (SiO_2). Further sample preparation is done in house at the National Research Council of Canada.

All substrates used throughout this thesis consist of two distinct deposited layers. First, a layer of alumina (Al_2O_3) is deposited by e-beam evaporation with a thickness between 10 nm and 250 nm, with the precise thickness depending on the sample. This layer is called the catalyst support and promotes the formation of more dense and consistent catalyst nanoparticles and the growth of carbon nanotube forests [2], though it is possible to grow forests without this layer [90]. If the catalyst nanoparticles are too sparse, forest growth does not take place, and, instead, the nanotubes grow individually on the surface of the silicon wafer.

On top of this support layer of Al_2O_3, the catalyst layer is deposited by e-beam evaporation. Here, it is a thin (0.2 to 2.0 nm) layer of cobalt (or iron). The thickness of the catalyst layer corresponds to approximately 1 to 10 monolayers of cobalt. Upon heating for growth, this thin layer of catalyst breaks up into individual nanoparticles which then act as templates for carbon nanotube growth [91–93]. The size of the nanoparticles is related to the thickness of the deposited catalyst layer. The iron catalyst is only briefly explored in Chapter 8, while the cobalt catalyst is used for most of the research in this thesis. Both catalyst materials (cobalt and iron) function in the same way and differ only

in their chemical composition and reactivity. Both are prepared in the same way and, thus, only cobalt will be discussed in detail.

In e-beam evaporation [94, 95], the silicon wafer is loaded into a vacuum chamber which also contains the solid source for deposition. An electron beam is directed at the source, ablating and ejecting material. The sample is located in the path of this stream of source particles and is thus coated with the desired material. The thickness of the deposited layer is determined by a quartz crystal microbalance.

It is possible to deposit the layers into specific patterns of arbitrary shapes and sizes [82, 96–101]. This is accomplished with a mask that contains holes corresponding to the desired pattern [95]. Without a mask, a uniform layer is deposited across the entire sample. In this thesis, two types of masks are used. The majority of the forests were grown from samples deposited with a mechanical shadow mask. These masks are thin metal sheets that are firmly fitted to the silicon wafer. After the deposition, the mask is simply removed from the wafer, leaving the desired pattern on the wafer, and the excess material on the mask.

Typical masks produced regular patterns of circular catalyst islands. The islands ranged in size from 100 μm diameter to 800 μm diameter. Almost all forests were grown from samples patterned using 4 different masks: (1) a hexagonal array of 700 μm diameter circles, spaced by approximately 500 μm (edge-to-edge); (2) a hexagonal array of 100 μm diameter circles, spaced by approximately 100 μm (edge-to-edge); (3) a widely spaced array of 800 μm diameter circles spaced by approximately 2 mm in a square grid; (4) a pattern of four differently sized circular catalyst islands (100 μm, 200 μm, 400 μm, and 800 μm diameters) that is depicted in Fig. 1a of Chapter 7.

A few forests were grown using patterned substrates prepared with photolithography [102]. In photolithography, the mask is deposited (using a spincoater) as a thin layer of photosensitive resist. When the resist is exposed to light it changes chemically and can be easily dissolved and removed from the substrate [102]. The portion of the resist left behind on the wafer is the mask. The pattern of the mask itself is created by blocking some of the light from reaching the resist, either by using another physical mask placed on the resist or by projecting the image onto the resist [102]. The alumina and cobalt are then e-beam evaporated onto the silicon wafer with the leftover resist acting as a mask. After the e-beam deposition, the remainder of the resist is removed with another developer (a lift-off procedure), and the desired pattern is left behind.

Lithographic masks provide greater resolution for fine details as well as sharper cleaner edges and edge effects (see Appendix D, Section 2.3). However, this process is more time and resource consuming (as it requires significant processing) [102]. For the nature of

the research conducted in this thesis, mechanical shadow masks are more than sufficient for producing high quality substrates that can be easily and quickly fabricated.

In the CVD reactor used in the thesis, nanotubes are typically grown on small pieces of silicon wafer on the order of 5 mm $\times$ 5 mm, though it can handle samples as large as 8 mm $\times$ 13 mm. When a sample is prepared by e-beam evaporation, it is typically much larger (on the order of 4 cm $\times$ 4 cm) and is later cleaved into smaller pieces for CVD growth using a diamond scribe. Not only does this save time in producing growth substrates, but it also greatly improves the uniformity from one growth experiment to the next since all growth substrates from a set of experiments are produced under identical conditions.

1.4.3 Experimental setup and procedure

The CVD reactor used throughout this thesis is pictured in Fig. 14. It was built in house using high vacuum system components, a solid state Joule heater, and 1/4 inch copper or stainless steel pipe. The CVD chamber itself is a cylindrical sealed stainless steel vessel of approximately 10 cm in diameter and 5 cm in length (internal volume). The growth substrate is placed in the reactor chamber; it sits flat on the heater and is held in place with a metallic clip. The entire heater assembly is removable for easy loading and unloading of the samples. The source gases are obtained from cylinders of compressed gas: pure argon, an Ar/H_2 mixture of 2% H_2, and an Ar/C_2H_2 mixture of 0.1% C_2H_2 (the mixtures are delivered pre-mixed). The water and ethanol vapour are obtained from bubblers that were also constructed in house using similar components. The water is purified and de-ionized in house; the ethanol is anhydrous. Either pure argon or Ar/H_2 are passed through the bubbler as a carrier gas. Because pure H_2 and C_2H_2 are both explosive and flammable gases [39, 103], the source gases used in the CVD reactor are diluted with Ar. The concentrations of both are kept below their lower explosive limit [103], which makes them much safer to handle, while not affecting the experiments.

A gas flow diagram of the CVD reactor is shown in Fig. 15. The flow rates of the gases are controlled independently by several rotameters. A rotameter is essentially a vertical inverted conical tube with a ball float and needle valve. The needle valve controls the flow of gas; the faster the flow, the greater the upward force on the ball, and the higher it is lifted (against the downward force of gravity) on the graded measuring scale, thus measuring the flow rate. Flow rates are measured in units of [sccm] (standard cubic centimeters per minute) where "standard" refers to atmospheric pressure and 20°C. The individual gases are combined prior to injection into the CVD chamber through the inlet,

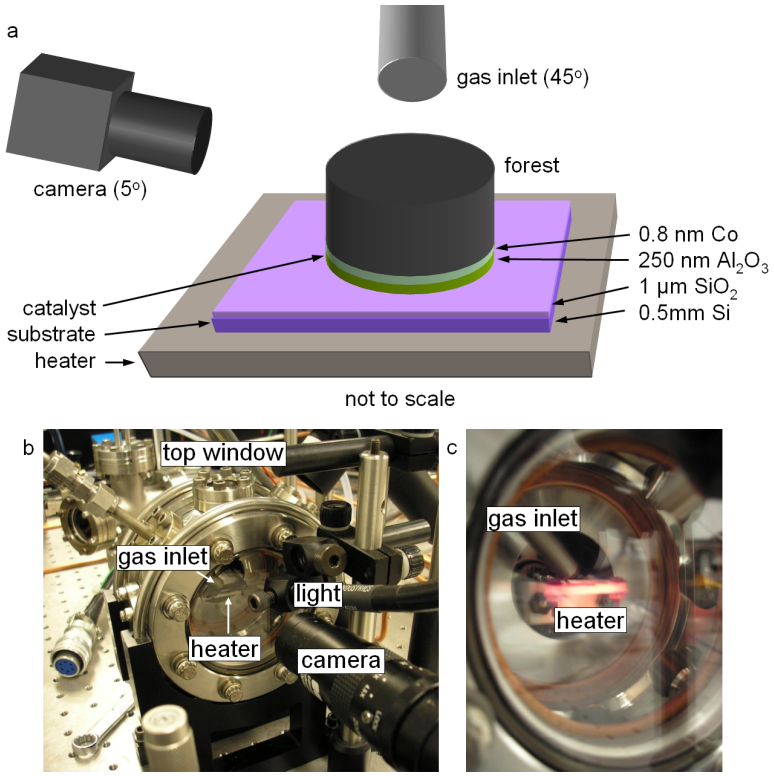


Figure 14: CVD reactor. (a) Schematic diagram of reactor interior with silicon substrate and nanotube forest. (b) Photograph of reactor exterior with several components labeled. (c) Photograph of reactor interior while reactor is in operation. Several components are labeled.

which is directed toward the substrate at a 45° angle to the plane of the substrate at a distance of ∼7 mm from the substrate (see Fig. 14 and Fig. 15). The exhaust is located near the base of the reactor.

The water concentration is measured at the reactor exhaust (see Fig. 15) using a hygrometer (GE Panametrics Moisture Monitor Series 35). By maintaining a constant flow of Ar/H_2 carrier gas, the water concentration can be controlled by passing some of the Ar/H_2 carrier gas through the bubbler and some of it around the bubbler through a bypass. The Ar/H_2 that passes through the bubbler will pick up water vapour, while the gas that passes through the bypass will not. The greater the fraction of Ar/H_2 that passes through the bubbler, the greater the concentration of water vapour.

The reaction chamber has two functional windows to allow optical access to the sample (see Fig. 16). A small window on the top of the reactor provides a plan view of the growth substrate (with the optical path normal to the substrate surface). The window is used to optically measure the temperature using a two-colour infrared pyrometer (Mikron M770/780 Series). There is also a larger window perpendicular to the substrate surface that provides a side view of the forest, thus enabling the direct determination of its

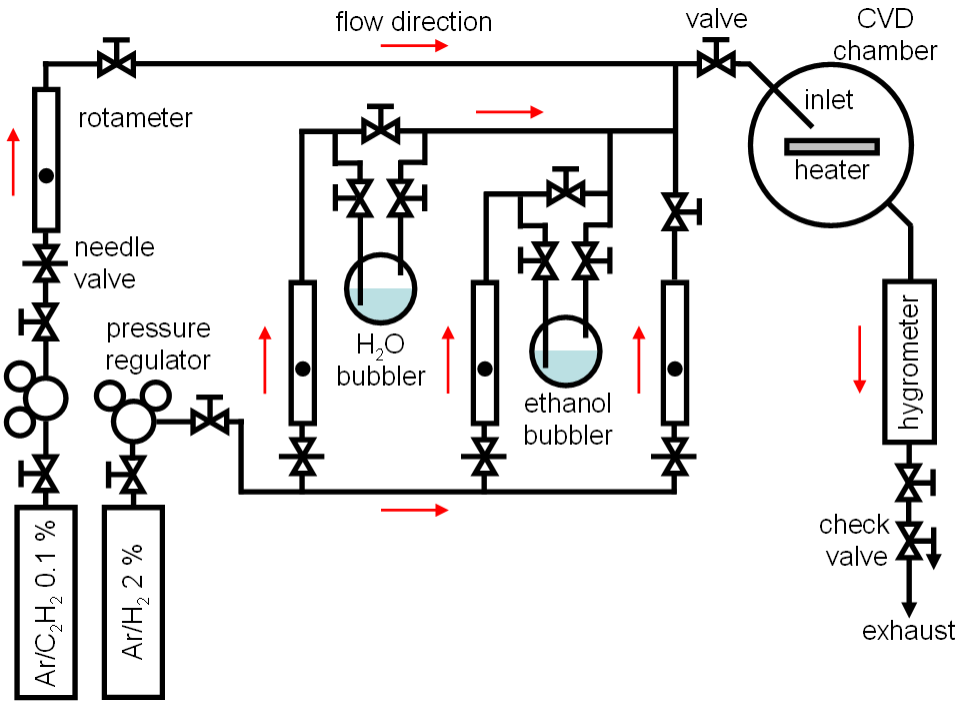


Figure 15: CVD gas flow diagram. See text for details.

height. This window is used for the *in situ* optical microscopy using a large working distance optical microscope and digital camera (Edmunds Optics EO1312C), providing a resolution of 2 μm for forests that can grow up to 3 mm in height. The *in situ* optical imaging system is discussed further in Section 1.5.

The fact that the gas enters the reaction chamber from one side of the substrate was not observed to have an effect on the uniformity of the growth. When asymmetric patterns were rotated (see for example Fig. 1a of Chapter 7), the same growth was observed regardless of orientation. When large unpatterned substrates were used, growth was uniform across the entire sample. The edges near to and away from the gas inlet grew at the same rate and reached the same final height. All of this suggests that by the time the gas has traveled from the inlet to the substrate, it is quite evenly distributed.

The exact growth procedure (type of gas, amount of gas, flow rate, timing) used in this thesis varies from one chapter to another and is described in those chapters.

1.4.4 Chemistry of CVD growth

This section contains a brief review of some important aspects of chemistry used in this thesis as well as some discussion of the chemical reactions that take place during CVD growth of carbon nanotubes. A general chemical reaction can be written as follows

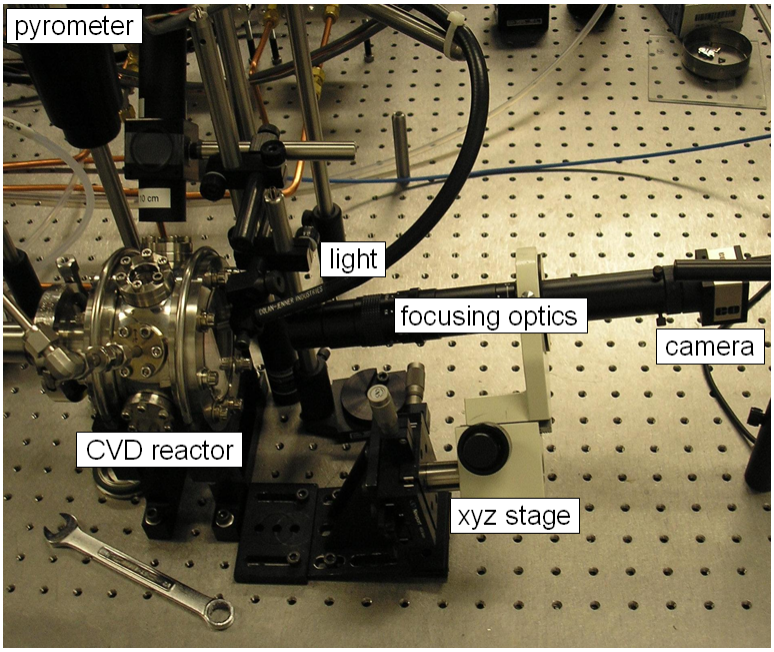


Figure 16: Photograph (with labels) of the *in situ* optical setup and CVD reactor.

[39]:

$$m_j\text{Reactants}_j \rightleftharpoons n_i\text{Products}_i \tag{1.4}$$

where n_i and m_j are the stoichiometric coefficients of the products and reactants respectively.

A chemical reaction is said to be "spontaneous" if it is allowed to proceed in the forward direction by the laws of thermodynamics [39]. The spontaneity of a chemical reaction is determined from change in free energy of the reaction $\Delta G_{\text{reaction}}$: if $\Delta G_{\text{reaction}} < 0$, the reaction is spontaneous [39]. The free energy of the reaction $\Delta G_{\text{reaction}}$ is defined as:

$$\Delta G_{\text{reaction}} = \sum_i n_i \Delta G_{f,\text{products},i} - \sum_j m_j \Delta G_{f,\text{reactants},j} \tag{1.5}$$

where the subscript f denotes the free energy of formation of the relevant products and reactants.

The free energy is a thermodynamic quantity that is related to the enthalpy H and entropy S: $\Delta G = \Delta H - T\Delta S$ where T is the reaction temperature [39]. Knowing ΔH and ΔS, one can calculate the temperature for which a reaction becomes spontaneous.

The change in free energy of a reaction $\Delta G_{\text{reaction}}$ can be calculated for almost any reaction from tabulated values of ΔG_f° or ΔH_f° and S°, such as those in *The Handbook of Chemistry and Physics* [103]. Tabulated values are generally given for chemicals in their standard state (atmospheric pressure and 0°C [39], designated by °), thus, for gaseous

chemicals it is necessary to account for the actual pressures of the products and reactants relative to standard atmospheric pressure [39]:

$$\Delta G_{\text{reaction}} = \Delta G^{\circ}_{\text{reaction}} + \sum_i n_i k_B T \ln\left(P_i/P^{\circ}\right) - \sum_j m_j k_B T \ln\left(P_j/P^{\circ}\right) \tag{1.6}$$

where k_B is the Boltzmann constant, P_i and P_j are the partial pressures of the reactants and products respectively, and P° is atmospheric pressure.

Just because a reaction is thermodynamically favourable (as determined by $\Delta G < 0$) does not mean that the reaction will necessarily be observed to occur [39]. A reaction must also occur at an appreciable rate. For example, for the reaction $\text{C}_{\text{diamond}} \rightarrow \text{C}_{\text{graphite}}$ is thermodynamically favourable, but is not observed because it is too slow [39]. In general, the rate of a reaction is proportional to some power of the concentration of reactants (or intermediates) and a rate constant τ^{-1} [39]:

$$\text{Rate} = \tau^{-1} \prod_j [\text{Reactant}_j]^{q_j} \tag{1.7}$$

where τ has units of [s]. The q_j are the order of the reaction with respect to the reactant, and may or may not be related to the stoichiometric coefficients of the balanced chemical reaction [39]. Furthermore, complex reactions can be broken down into elementary steps, and intermediate products may appear in the rate equation while other reactants may not appear at all [39]. The overall order of the reaction is the sum of the individual q_j in Equation (1.7) [39].

The rate constant τ^{-1} generally has an activated dependence with activation energy E that is given by the Arrhenius equation [39]:

$$\tau^{-1} = \tau_o^{-1} \exp\left(-E/k_B T\right) \tag{1.8}$$

where T is the temperature and τ_o^{-1} represents the attempt frequency. By plotting the logarithm of τ^{-1} as a function of $1/k_B T$ (called an Arrhenius plot), the activation energy E can be determined from the slope of the straight line, and the constant τ_o^{-1} can be determined from the intercept [39]:

$$\ln\left(\tau^{-1}\right) = \frac{-E}{k_B T} + \ln\left(\tau_o^{-1}\right) \tag{1.9}$$

This activated behaviour is expected to be seen in a situation with three distinct energy levels that correspond to an initial state, a final state, and an intermediate state

with an energy that is higher than the other two [39]. The activation energy is a result of climbing over the barrier (imposed by the intermediate state) from the initial state to the final state [39]. The CVD growth of carbon nanotubes is observed to have a growth rate that follows this type of activated dependence (see Chapter 2 and Chapter 3).

During the CVD growth of carbon nanotubes, the carbon source gas is converted into nanotubes in a chemical reaction. The following discussion is about the reactions that occur for acetylene as that source gas; however, the behaviour of ethanol is analogous. The complete decomposition of acetylene into carbon nanotubes (represented by carbon in the form of nanotubes, C(CNT)) can be written as:

$$\mathrm{C_2H_2(gas)} \rightleftharpoons \mathrm{2C(CNT) + H_2(gas)} \tag{1.10}$$

This is the overall reaction and can be broken down into elementary step steps. One proposed scheme is [104]:

$$\begin{aligned} \mathrm{C_2H_2(gas)} &\rightleftharpoons \mathrm{C_2H_2(ads)} \\ \mathrm{C_2H_2(ads)} &\rightleftharpoons \mathrm{2CH(ads)} \\ \mathrm{CH(ads)} &\rightleftharpoons \mathrm{C(ads) + H(ads)} \\ \mathrm{2H(ads)} &\rightarrow \mathrm{H_2(gas)} \\ \mathrm{C(ads)} &\rightarrow \mathrm{C(CNT)} \end{aligned} \tag{1.11}$$

where (ads) indicates a species that is adsorbed on the catalyst nanoparticle. In this scheme, the reaction rate is Rate $= \tau^{-1} \left[\mathrm{C_2H_2}\right]^{1/2}$ (in agreement with the experimental results of Reference 104) and τ^{-1} has an activation energy of $E \sim 1$ eV [104].

1.4.5 Growth process at the atomic level

Having discussed what nanotubes are and the macroscopic chemical reactions that lead to their synthesis, it is important to look down to the atomic level and discuss what happens at this scale in the self-assembly process that occurs during CVD growth. The exact details of these atomic scale processes are not entirely known, nor agreed upon [2, 6], though there are many common aspects to most theories. Here, the general growth process is discussed while trying to take into account all of the various ideas presented in the literature. Although the following discussion concerns only acetylene, the behaviour of ethanol is analogous.

In CVD growth, the gas is delivered to the sample directly by a nozzle in the reaction

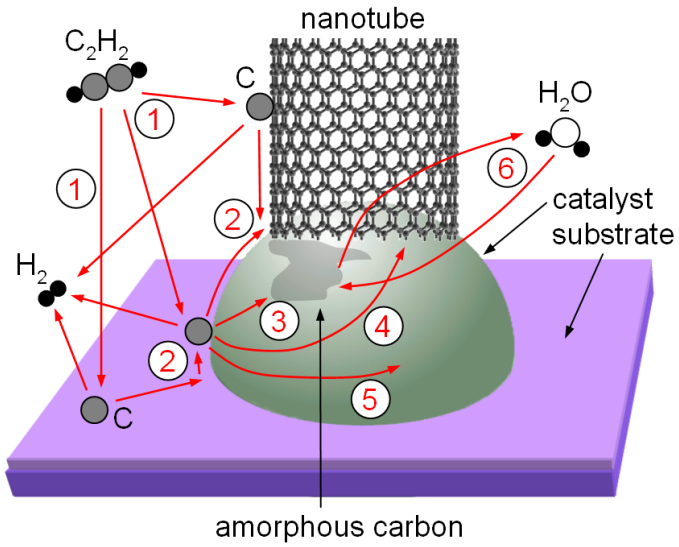


Figure 17: Schematic diagram of growth processes occurring at the atomic level. Important steps are: (1) adsorption onto the substrate, catalyst nanoparticle, or nanotube; (2) surface diffusion across the catalyst nanoparticle, substrate, or nanotube itself to the growth site; (3) formation of parasitic byproducts including amorphous carbon coating; (4) bulk diffusion through the catalyst nanoparticle to the growth site; and (5) chemical reactions with the catalyst nanoparticle to form carbides. Also pictured is the effect of water (6), which etches amorphous carbon from the nanoparticle. Adapted from Reference 58.

chamber. In the gas phase there is much diffusion, and in the case of hot-walled CVD systems, there can be significant gas phase reactions [87]. In a cold-walled CVD reactor, the gas phase reactions are significantly reduced. In the CVD reactor used in this thesis, the carbon source gas is delivered into the reactor through a 3 mm (inner) diameter pipe that is aimed at the sample at a distance of approximately 7 mm. Because the 7 mm distance is more than the mean free path of the gas in these conditions [103], there is thus plenty of opportunity for the gas to diffuse or undergo gas phase reactions before hitting the sample. When the carbon source gas hits the sample, there is further opportunity for gas phase diffusion, as discussed in Chapter 7.

When the gas does impinge upon the catalyst nanoparticles there are several things that can occur that are analogous to crystal growth (see Fig. 17): the gas can simply bounce off the surface, it can adsorb physically, or chemically, with or without dissociating [58]. Adsorption can also occur on the nanotube itself or the substrate. Once adsorbed, desorption back into the gas phase can occur. Gas that adsorbs onto the substrate or nanotube must diffuse to the catalyst nanoparticle in order to contribute to growth. These steps are indicated by pathway 1 in Fig. 17. There is no general consensus regarding the chemical nature (metal or oxide) and physical state (solid or liquid) of the catalyst nanoparticle [2, 6].

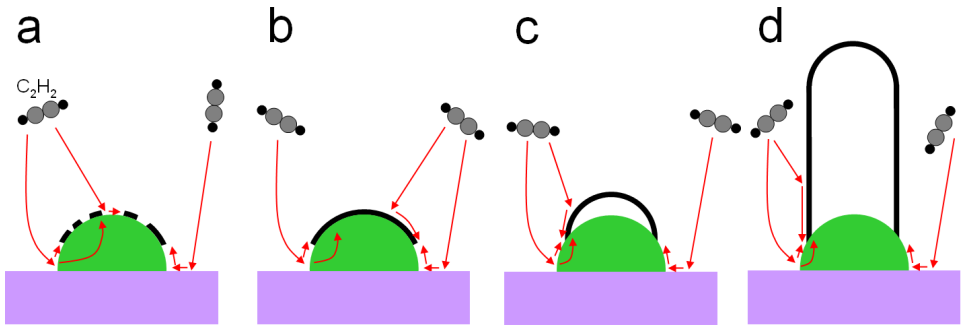


Figure 18: Schematic (cross section) diagram of CNT growth. (a) Carbon atoms begin to cluster together and interact on the surface of the catalyst nanoparticle (green). (b) A graphitic network is formed. This is the carbon nanotube cap. (c) As more more carbon is added, the cap lifts off from the nanoparticle surface. (d) The nanotube begin to grow. Purple represents the substrate material and red arrows show possible pathways for the carbon source, as illustrated in more detail in Fig. 17.

When the carbon source reaches the catalyst nanoparticle, either by direct impingement or diffusion, several processes can occur. If the gas is still in a molecular form, it can dissociate into carbon atoms and hydrogen [2, 58]. The carbon can diffuse along the surface to the growth site (pathway 2 Fig. 17) [36, 58, 104, 105] or it can create an amorphous carbon coating on the nanoparticle (and thus encapsulating it); this is detrimental to growth (pathway 3 Fig. 17) [36, 58, 106, 107]. It is also possible that bulk phase reactions occur and the carbon dissolves into the catalyst nanoparticle [2, 30, 33, 36]. Once dissolved, the carbon can then diffuse through the bulk of the catalyst nanoparticle to the growth site as indicated by pathway 4 in Fig. 17 [33, 36, 104]. The adsorbed carbon can also react with the catalyst nanoparticle and lead to the formation of carbides (pathway 5 Fig. 17) [106]. Some of the amorphous carbon buildup (created via pathway 3 Fig. 17) can be removed by water (pathway 6 Fig. 17).

When a sufficient carbon density is reached, the carbon atoms begin to interact with one another (Fig. 18a). Eventually a network is formed, and it is commonly believed that this network takes the form of a carbon nanotube cap [2, 6] (which can be though of as a hemispherical half of a fullerene, see Fig. 18b). The size and shape (and thus curvature) of the cap is affected by the size and shape of the catalyst nanoparticle [77]. New carbon atoms can only be added to the nanotube at the edges of this network, which is at the interface between the nanotube and the catalyst nanoparticle. However, carbon atoms can adsorb onto the surface of the nanotube as well (thus contributing to defects), but this kind of addition does not contribute to the lengthening of the nanotube.

As time passes, more and more carbon reaches the edges of the newly formed nanotube cap and is added to its edges. Eventually, a critical amount of carbon is achieved and the nanotube cap is lifted off from the catalyst nanoparticle [2, 6] (Fig. 18c). For carbon

nanotube forest growth as seen in this thesis, the catalyst nanoparticle remains attached to the growth substrate. New carbon is added to the edges of this cap and thus forms the nanotube, between the cap and the nanoparticle (Fig. 18d). The nanotube is continuously precipitated from the nanoparticle due to saturation with carbon [2, 30, 36, 106]. The constant supply of carbon thus feeds the growth of the nanotube, which is continuously extruded from the nanoparticle at a rate determined by the nanotube's diameter and number of walls, and the rate at which new carbon is added to the lattice (which is a function of the source gas flow rate or pressure).

It should be noted that in other CVD growth systems that do not produce forests, there is a growth mode where the extruding nanotube remains attached to the substrate, and the nanoparticle is lifted off from the surface as the nanotube grows [2, 30, 36]. This is the "tip-growth" mode, as opposed to the "base growth" mode (described and illustrated in Fig. 17) where the nanoparticles remain attached to the substrate.

1.4.6 The growing forest

The van der Waals forces from neighbouring nanotubes will cause nearby nanotubes to bundle together [1, 54] when they come near one another. Because not all nanotubes and nanoparticles will be completely identical, the nanotubes in a forest will also have slightly different growth rates (see following Chapters). This has the effect of inducing additional wandering and meandering, taking the nanotubes further away from a straight configuration. Furthermore, any barriers encountered will divert the growth of nanotubes [25].

As a carbon nanotube forest is growing, neighbouring nanotubes will interact with one another, the substrate, the catalyst, and the support. These interactions and some of their consequences will now be introduced, though detailed discussion will be present in later chapters. These interactions (or rather the energies they create) are: adhesion to the substrate (and catalyst and support), cohesion to neighbouring nanotubes, and strain due to deformations. They are illustrated in Fig. 19, from left to right: adhesion, cohesion, and strain.

Strain is the general energy that results from the nanotube being bent out of its perfectly straight orientation, which is the lowest energy configuration. All nanotubes in forests are bent and are thus strained.

In general, when the adhesion energy outweighs the cohesion energy, nanotubes stick to the substrate better than they stick to one another. If the difference in adhesion and cohesion is large enough, it is possible that cracks will develop in the forest where

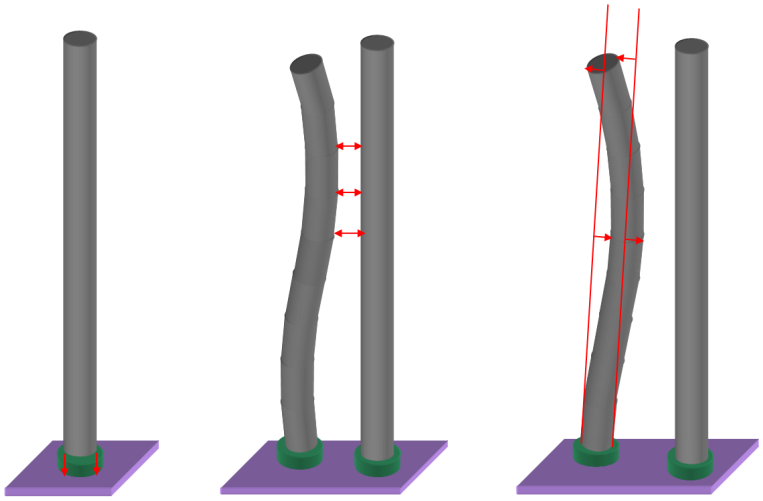


Figure 19: Energies within forests, from left to right: adhesion, cohesion, and strain.

large sections of the forest will separate from one another and neighbouring nanotubes are separated. This is analogous to an epitaxial layer (in the growth of crystals) that is subject to tensile strain [45]: the layer will eventually crack apart to relieve the strain once a critical thickness is surpassed. The strain is relieved by creating new surfaces. Cracking in a carbon nanotube forest is illustrated in Fig. 20.

In contrast, when the cohesion energy outweighs the adhesion energy, nanotubes stick to one another better than they stick to the substrate. With a large enough difference, the nanotubes will separate and lift off from from the substrate surface (this process is described as delamination). Again, an analogy with epitaxial growth can be made. In an epitaxial layer that is subject to compressive strain, it is often favourable to relieve this strain by detaching from the substrate, thus creating a new surface on the bottom of the layer [45]. This also occurs after a certain thickness is surpassed, and this thickness is often greater than that for cracking [45]. The delamination process is depicted in Fig. 20.

1.4.7 Termination

Nanotube growth does not continue indefinitely, though there are growth processes that can produce nanotubes sufficiently long (10 cm) that the length is limited by the size of the reactor [3]. Growth eventually stops due to a process called termination [6]. Nanotube forest growth, when described by the height of the forest as a function of time $H(t)$ (called a growth curve), can be written as an exponentially decaying function (in which growth occurs at an increasingly slower rate) with a form [57]:

$$H(t) = \beta\tau\left(1 - e^{-t/\tau}\right) \tag{1.12}$$

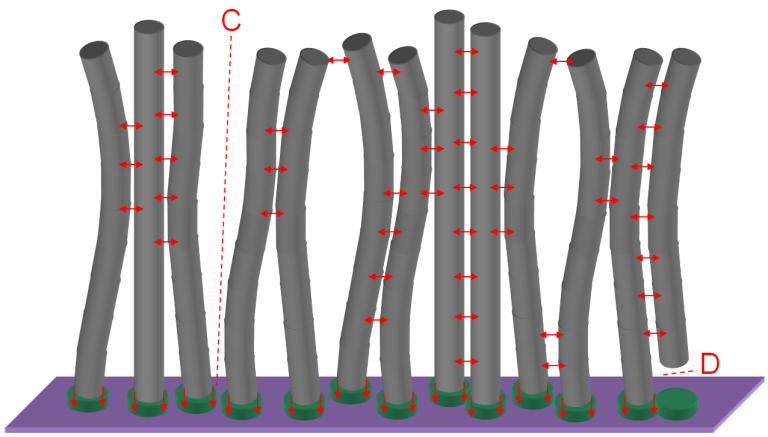


Figure 20: Interactions between individual nanotubes within a forest. Arrows indicate cohesive and adhesive forces, as depicted in Fig. 19. "C" marks a crack where the cohesion energy is overcome, and "D" marks a delamination event where the adhesion energy is overcome.

where β is the initial growth rate at time $t = 0$, and τ is the characteristic time of the exponential decay of the growth rate. Equation (1.12) can be deduced from very simple models of growth [57], or can be derived from a more complex model as a special case [108]. As $t \longrightarrow \infty$, the height of the forest reaches an asymptote (its final height) $H_{t\longrightarrow\infty} = H_F = \beta\tau$. Oftentimes, however, it is observed that growth terminates abruptly [61, 109, 110] (see also Chapter 3) at a time called the termination time τ_T (and an equivalent termination height H_T).

The yield of a synthesis process is the amount of material that is produced. For CNT forests, the yield is a function of the area that the forest covers, the density of the forest, and the final height that it reaches upon termination. Generally when discussing the yield in this thesis, it refers primarily to the final height of the forests.

In the initial phases of CNT growth, the growth rate is typically decaying exponentially, but this decay rate is very slow, especially when compared to the time scale of the sudden termination. Because the growth rate appears almost linear, this growth phase is sometimes referred to as the "steady growth phase". Strictly speaking, the growth rate may be slowly varying. Several mechanisms for the observed sudden termination have been proposed. These mechanisms and other more general termination mechanisms will now be briefly introduced and discussed.

Termination mechanisms can be placed into two groups: (1) those that can be understood on the basis of a single nanotube (but still apply to all growth scenarios such as forest growth) and (2) those that can be understood only by considering the collective effects of many nanotubes interacting with each other (and thus relevant only for forest growth). Some mechanisms explain the slowly decaying termination while others explain

the observed abrupt termination. Depending on the exact CVD conditions, different mechanisms may dominate over others.

One prominent single nanotube termination mechanism is a poisoning or coating of the catalyst by parasitic carbon reactions [58, 107]. In these mechanisms the adsorbed or dissolved carbon can either change the chemical or physical state of the catalyst nanoparticle, rendering it inert, or it can overcoat the catalyst nanoparticle with an amorphous carbon layer (as shown in Fig. 17), stopping the diffusion of new carbon atoms the the growth front of the nanotube. It is thought that the H_2 used in the CVD growth helps keep the nanoparticle in the appropriate reduced chemical state [81], while the H_2O scavenges the amorphous carbon and removes it [82].

Another potential single nanotube termination mechanism is Ostwald ripening [85] whereby the larger catalyst nanoparticles grow even larger at the expense of the smaller nanoparticles as materials diffuse across the surface between them. As the nanoparticles grow and shrink (and even disappear) they are no longer the right size to support nanotube growth, leading to termination. It has been proposed that water plays a role in reducing Ostwald ripening by adsorbing onto the surface between the nanoparticles and preventing the migration of material between adjacent nanoparticles [85]. A mechanism related to Ostwald ripening (related in the sense that it too is a time-dependent change of the catalyst nanoparticle size) is the diffusion of the catalyst into the supporting layer [111–113], here Al_2O_3. This mechanism proposes that the nanoparticles shrink due to this diffusion and eventually leading to the termination of growth and the disappearance of the nanoparticles from the surface.

An early proposal for collective termination in nanotube forests is the blocking of gas phase diffusion through the forest by the nanotubes in the forest itself [98, 114]. In this mechanism the growing nanotubes in the forest impede the delivery of new gas to the catalyst nanoparticles at the base of the forest, leading to a gradual slowing and eventual termination of growth.

Other collective termination mechanisms for nanotube forests are avalanche effects of the single termination mechanisms. Increasing numbers of single nanotubes terminating cause a cascading effect through their interactions with neighbouring nanotubes (for example Reference 110). One such proposed mechanism is called termination by density decay [115]. It is proposed to occur when the density of CNTs in the forest drops (due to the growth of individual nanotubes terminating) below the critical level necessary to allow for vertical alignment (which occurs because the nanotubes are so dense there is nowhere to grow but up). The density of the forest decreases because some individual nanotubes terminate and, through their interactions with their neighbours, can be lifted

off the substrate at their base, leaving a "hole" in the new forest that grows beneath them. When this critical density is crossed, the forest ceases to grow, although individual nanotubes may continue to grow, thus causing the characteristic loss of alignment that is observed at the base of some forests [115].

A final collective termination mechanism does not necessarily require that individual nanotubes stop growing, but instead involves the interactions between nanotubes and the resulting strain. These mechanisms are discussed in more detail throughout this thesis, but are summarized here. When a nanotube in a forest stops growing, it is still interacting with the growing nanotubes around it. This terminated nanotube can either be ripped off the substrate by the growing nanotubes around it (delamination), or it can anchor the growing nanotubes to the substrate and suppress further forest growth. The same situation can arise when the difference in the growth rates of neighbouring nanotubes is sufficiently large. One form of this mechanism has been proposed in Reference 110 and another is proposed in Chapter 3 of this thesis. This strain driven termination mechanism is, in many ways, analogous to strain in crystal growth.

1.5 Optical microscopy

One of the primary techniques used in this thesis is *in situ* optical microscopy. The system used is pictured in Fig. 16. Because the forests are macroscopic objects, they are easily resolved by an optical microscope. The basic physical principles of optical microscopy will not be discussed here, but several factors relevant to the present application will be discussed.

Here, the nanotube forests grow vertically, as shown in Fig. 14 and they are imaged in profile such that their height can be easily tracked using the camera. To build a growth curve (a plot of forest height H versus growth time t), the height of the forest was extracted from the images taken by the camera, frame by frame, because automation would have been difficult given the sometimes very limited contrast available. The scale of the images was determined for each forest by measuring the width of the patterned catalyst island in the image and calibrating using the known diameter of the island. Many forest heights were also measured by SEM to corroborate the optical calibration.

The very limited contrast is one of the main problems that had to be addressed. Carbon nanotube forests are very black [28], which is a result of their excellent absorption. This excellent absorption leads to difficulty in illuminating the sample and achieving sufficient contrast. As shown in Fig. 16, the light was mounted almost parallel to the camera (almost perpendicular to the side walls of the forest) in order to maximize the

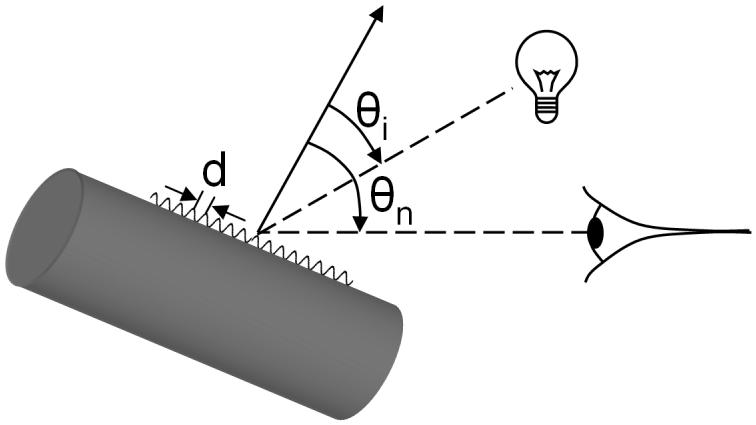


Figure 21: Optical diffraction setup diagram showing optical path, angles θ_i and θ_n, grating spacing d, light source location, observation point, and nanotube (gray cylinder).

amount of reflection from this surface.

Another important problem in imaging carbon nanotubes with optical microscopy is the limited focal depth that is characteristic to the method [116]. This was a problem that was particularly relevant for small diameter forests, which often tipped to the side and out of the focal plane of the camera. Furthermore, when the camera was mounted perfectly in the plane of the substrate (at an inclination of 0°), it was difficult to find anything to focus on until the nanotubes started to grow. To solve this second problem, the optical camera was mounted 5° to the plane of the substrate, as shown in Fig. 16. This had the added benefit of being able to observe the initial moments of growth and the evolution of the shape of the top surface of the forest as it grew (though, for the larger forests, there were issues due to the aforementioned lack of focal depth). Both of these observations play important roles in the data analysis performed in the course of this thesis research.

In Chapters 5 and 6 a novel diffraction effect is studied. Here, light of bright colours is, remarkably, reflected from the nanotube forest sidewalls when the sidewalls are illuminated with white light. This suggests that there is a microscale feature on the forest sidewalls that acts as a diffraction grating. This phenomenon is visible *in situ*, but is also studied *ex situ* using the same camera and microscope, but in a configuration more suitable for maximizing the diffraction effect, as shown in Fig. 21. In this setup, the light source is either a white light or a 1 mW HeNe laser (633 nm). The "observer" is either the camera or a simple power meter for the purpose of measuring the grating's efficiency.

Finally, the angles and other quantities depicted in Fig. 21 correspond to the grating equation [117]:

$$n\lambda_n = d\,(\sin\theta_n + \sin\theta_i) \tag{1.13}$$

where n is the order of intensity maximum (generally $n = 1$ in this thesis), λ_n is the wavelength of light observed at the intensity maximum (633 nm HeNe for laser illumination), d is the grating spacing, θ_n is the angle of the intensity maximum (observation angle) with respect to the normal of the grating, and θ_i is the angle of incidence with respect to the normal of the grating.

1.6 Raman spectroscopy

Throughout this thesis, and carbon nanotube research in general, Raman spectroscopy is used extensively. It is a versatile optical technique that can be easily performed in a lab using a table-top setup consisting of a laser, a spectrometer, and focusing optics. From a solid state physics point of view, the basic physical mechanism of Raman spectroscopy is the inelastic scattering of light from optical phonons in the material (Raman scattering) [42, 50]. In a general context, the scattered light can help identify materials based on the characteristic spectra that each substance has as a result of its characteristic phonons (that are in turn a result of the crystal structure). For carbon nanotubes, Raman spectroscopy can provide information beyond just the crystal structure (nanotube chirality and hence diameter), including the defect density and band gap [118, 119]. Furthermore, Raman spectroscopy is generally non-destructive [120].

In this thesis Raman spectroscopy is used to analyze the carbon nanotube forests *ex situ*. It should be emphasized that in this thesis, Raman spectroscopy itself is not studied, but is rather used as a tool to study the carbon nanotubes. The following discussion is, as a result, presented to convey a general understanding of the underlying physics, how to interpret the spectra for carbon nanotubes, and what information can be determined from these spectra.

1.6.1 Theory

Compared to the elastic Rayleigh scattering (elastic scattering), Raman scattering is inelastic and thus involves a change in energy (or wavelength) of the scattered light when compared to the incident light. Raman scattering is about 6 orders of magnitude weaker than Rayleigh scattering [42]. This change in energy is exactly equal to the energy of the phonon that the photon interacts with [42, 50]. Energy can be lost by the creation of a phonon in the material (a Stokes process) or gained through the absorption of a phonon that is already in the material (an anti-Stokes process). These processes are illustrated (in their most basic form) in Fig. 22 with Feynman diagrams [50, 74] and energy level

diagrams.

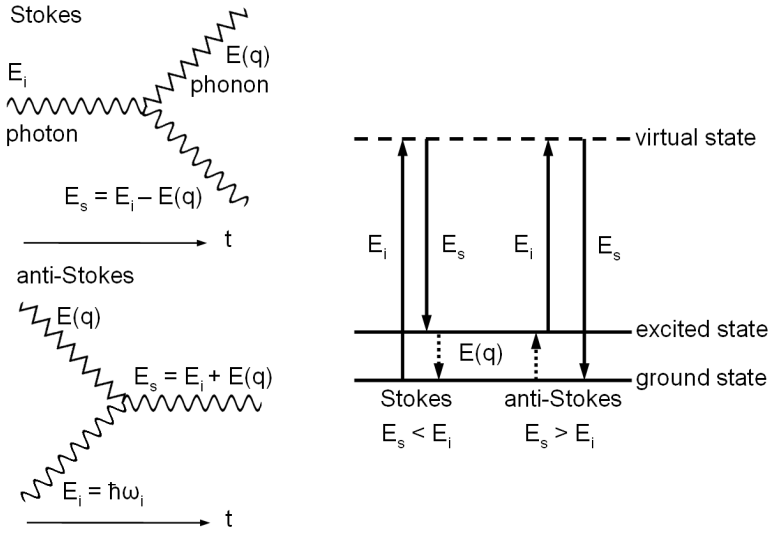


Figure 22: Diagrams of Raman scattering. Left: Feynman diagrams. Right: energy level diagrams.

Raman scattering can be understood through the conservation of momentum and energy of the interactions illustrated in Fig. 22 [42]. The incident photon has a momentum $\hbar\vec{k_i}$, the scattered photon has a momentum $\hbar\vec{k_s}$, and the phonon has a momentum $\hbar\vec{q}$, where $\vec{q}$ is the wave vector of the phonon. Similarly, the incident photon has an energy $\hbar\nu_i$, the scattered photon has an energy $\hbar\nu_s$, and the phonon has an energy $\hbar\nu\,(\vec{q})$. Conservation of momentum and energy can be written as [42, 50]:

$$\hbar\vec{k_i} = \hbar\vec{k_s} \pm \hbar\vec{q} \pm \hbar\vec{G} \tag{1.14}$$

$$\hbar\nu_i = \hbar\nu_s \pm \hbar\nu(\vec{q}) \tag{1.15}$$

For the conservation of momentum (Equation (1.14)) the term $\hbar\vec{G}$ (where $\vec{G}$ is a reciprocal lattice vector) is a result of the periodic nature of crystal structures and the fact that we can only know the crystal momentum to within a reciprocal lattice vector [42]. The energy of the incident photon is shifted by the phonon energy.

From the conservation of momentum and the fact that $\vec{q} << \vec{k_i}, \vec{k_s}$, Raman spectroscopy cannot determine complete phonon dispersion curves since it can only see phonons near $\vec{q} = 0$ (the center of the Brillouin zone) [1, 42]. Furthermore, not all phonon modes in a crystal will generate peaks in a Raman spectrum [1]. The phonon modes that do give rise to Raman scattering and the characteristic peaks in the Raman spectra are called "Raman-active" modes [74].

The phonon dispersion curves of carbon nanotubes can be calculated in a similar

way to the electronic band structure [1]. Using a zone-folding method, the graphene phonon dispersion curves can be sliced up into the appropriate curves for nanotubes. The main effect of this is to introduce new non-zero low energy modes near $\vec{q} = 0$ into the graphene dispersion curves [1]. The Raman spectra and the phonons that give rise to the characteristic features will be discussed in Section 1.6.4.

All Raman spectra referred to in this thesis are Stokes shifted. In order to acquire an anti-Stokes Raman spectrum, the relevant Raman-active phonons in the material must already exist when the laser interacts with the material [42]. For this reason, and especially at low temperatures, Stokes spectra are generally more intense than anti-Stokes spectra. However, an anti-Stokes Raman spectrum does have the advantage of not overlapping with a material's fluorescence spectrum, which, like the Stokes spectrum, is down shifted in energy with respect to the incident light.

The Raman shift ω of a particular scattered photon is generally given using the wavenumber (in units of [cm^{-1}]) difference between the incident light (wavelength λ_i) and scattered light (wavelength λ_s) according to the formula:

$$\omega = \left(\frac{1}{\lambda_i} - \frac{1}{\lambda_s}\right) \tag{1.16}$$

where λ must be written in units of [cm].

A final point about Raman spectroscopy is resonance. Resonance occurs when the incoming photon energy ($\hbar\nu_o$) or outgoing photon energy ($\hbar\nu$) are equal to an electronic transition E_{ii} in the material that one is analyzing [42]. When a photon of resonant energy is absorbed by a nanotube, the nanotube is excited into a real state, instead of into a "virtual state" as shown in Fig. 22. This makes the resonant scattering process significantly more probable and can increase the intensity of a Raman peak [42] by up to several orders of magnitude [121].

When a resonance is detected, it gives information about the electronic structure of the material [42]. For carbon nanotubes, the resonance energies are the E_{ii} and M_{ii} energy gaps between the van Hove singularities in the density of states (see Fig. 8). Therefore, the resonance conditions of nanotubes depend on the diameter and chirality of the nanotubes [122]. Furthermore, because of these resonance conditions, Raman spectra depend on the laser excitation energy ($\hbar\nu_o$) [42]. Different peaks will appear, disappear, or shift at different excitation energies. Because the electronic structure of a nanotube is sensitive to its surroundings, the electronic transition energies, and hence the resonance conditions, will change depending on their surroundings.

1.6.2 Raman imaging

It is possible to use Raman scattered light to generate an image in the same way that one would use Rayleigh scattered light in a typical optical microscope [59, 123]. This is called Global Raman Imaging (GRI) and requires that the collected light pass through a filter to remove the overpowering Rayleigh scattered light, and to further select a Raman band (a region of the spectrum) of interest to image. Furthermore, with the appropriate choice of the excitation energy, the Raman shifted-light is still in the visible wavelengths and does not need a special detector. GRI is able to detect individual nanotubes [59, 123]. This is due to the high contrast between a nanotube and the surface that it rests upon, and not due to high resolution, which is limited by the wavelength of the photons. Real-time images are acquired by illuminating the sample with a defocused laser and collecting all of the scattered light within a desired wavelength range and sending it to a CCD camera [59, 123]. At 20× magnification (the typical value used to acquire Raman spectra), this camera viewed an area of approximately 200 μm × 200 μm, though the area illuminated by the laser was much smaller. At 20× magnification, the laser illuminated an approximately 100 μm diameter spot or ∼30 μm × 3 μm rectangle produced by a cylindrical lens. In this thesis, the Raman images are only used to focus the 532 nm Raman system.

1.6.3 Experimental setup

Throughout this thesis, two different Raman spectrometers are used to acquire data: a commercial system with a 785 nm laser (Horiba Jobin Yvon LabRAM HR) and a 532 nm Nd:YAG laser system that was built in house.

The experimental setup for the 532 nm Raman system used in this thesis is shown in Fig. 23. It is essentially an optical microscope mounted on its side that uses laser illumination, a series of filters, and a grating spectrometer for detection. The system is focused optically with a CCD camera that creates an image from the Raman scattered light.

The path of the light (as depicted in Fig. 23) is as follows: the light is emitted by a frequency doubled 2 W continuous wave Nd:YAG laser (thus operating at 532 nm). The light then passes through a 532 nm band-pass filter (BP) to ensure that the beam is monochromatic by removing any other wavelengths. Next, the light passes through a defocusing lens (L1) to spread out the beam. This lens is changeable and often a cylindrical lens is used to produce a slit shaped beam profile covering an area of approximately 100 μm^2 (this includes thousands of CNTs when analyzing a forest). The light then passes

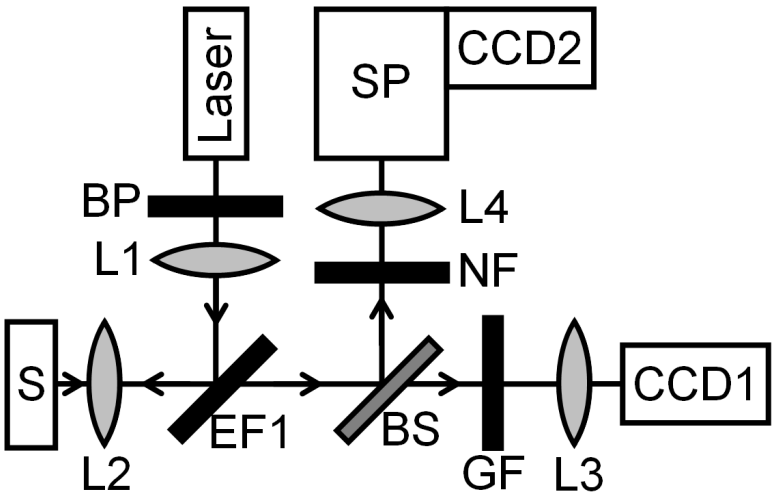


Figure 23: Schematic of the 532 nm Raman spectrometer. See text for details.

through a dichroic mirror (EF1), which reflects 532 nm and passes all light of higher wavelength. The beam reflected by this mirror is redirected to the microscope objective (L2), which is also changeable to allow different magnifications (from 5× to 50×). The light is then scattered by the sample (S) and collected by the same objective (L2), and again passes through the dichroic mirror (EF1), which lets only the Raman-shifted light pass straight through.

At this point, the beam passes through a beam splitter (BS), with half of the light directed toward a CCD camera (CCD1, Andor iXon X-1630) for Raman imaging and half of the light directed toward a grating spectrometer (SP) for spectroscopy. The portion directed toward the CCD camera goes through a changeable filter (GF) to select a Raman band for imaging (here it is the G band, as described in the next section), and finally a focusing lens (L3), to focus the light onto the CCD camera.

From the beam splitter (BS), the portion of the beam for spectroscopy passes through a notch filter (NF) to remove any Rayleigh scattered light and then through a lens (L4) that focuses the light onto the (changeable) slit of the grating spectrometer (SP, Oriel Instruments 260i). The slit is typically 25 μm wide, though slits 10 μm wide, 100 μm wide, and 500 μm wide are also available. The defocusing lens (L1) is cylindrical in part because it optimally defocuses the light into the same shape as the slit. Care must be taken to align the slit shaped beam with the center of the spectrometer slit. When using the cylindrical lens, most of the illuminated area contributes to the recorded spectra. The spectrometer itself has an 1800 line/mm grating that is centered to analyze Raman shifts from approximately 100 cm^{-1} to 1700 cm^{-1} (though below 150 cm^{-1}, the spectra are affected by the cut off edge from the filters). The spectrum is captured by a CCD camera attached to the spectrometer (CCD2, Andor Newton). This camera is 1024 pixels

wide, thus with the 1800 line/mm grating, the resolution is approximately 1.6 cm^{-1} per pixel.

Two methods were used to calibrate the Raman system prior to each use. The first method involved calibrating the spectrometer using a mercury/argon lamp (which has a well defined spectrum) that was parallel to the optical path of the scattered light entering the spectrometer. The second method involved performing Raman spectroscopy on a piece of Teflon (which has a well defined Raman spectrum) and calibrating the spectrometer to this standard. The latter procedure was adopted part way through the research in this thesis and superseded the mercury/argon lamp.

The 785 nm Raman system has a similar setup, except that it is more like an upright microscope and the sample is mounted horizontally. This system is focused by looking at a Rayleigh scattered optical image. This system has the ability to raster the sample and create a Raman map and allows the acquisition of many data points automatically. In terms of the optical setup, it is essentially the same as the 532 nm system and will not be described further.

Here, the samples were analyzed in plan view from the tops of the forests (90° to the silicon substrate), and the laser was linearly polarized parallel to the silicon substrate surface. In other words, the laser was polarized perpendicular to the average nanotube axis, which was orthogonal to the substrate surface.

Aside from the precautions necessary to safely operate a laser (the 532 nm system is completely enclosed), there is one main precaution necessary when using the Raman spectrometer. If the focused laser spot has a power density that is too high, it can deposit enough energy into the nanotube sample that it begins to burn. It has been reported that the threshold for burning is on the order of 0.1 $mW/\mu m^2$ [124]. Signs of burning can be seen in the Raman spectrum, and, moreover, visible damage can be seen when the sample is removed from the spectrometer. To prevent this, the laser power density was reduced and often tested near the edge of the sample to ensure that it did not burn. With the correct power settings, spectra were then acquired from the desired region of the forest.

The exact acquisition parameters (number of acquisitions, acquisition time, laser energy, spot size, power, magnification) vary from one chapter to another, and are described as required.

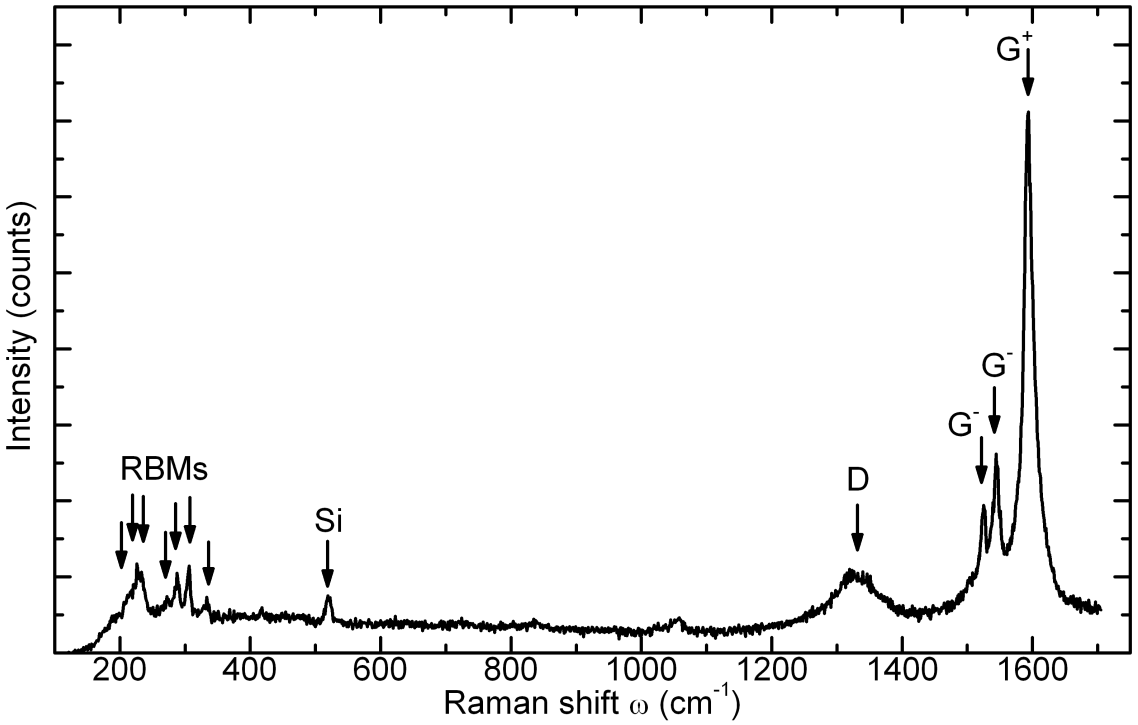


Figure 24: Typical Raman spectrum for a carbon nanotube forest. Main features are indicated and labeled with arrows. See text for details.

1.6.4 Spectral features

A typical Raman spectrum of carbon nanotubes is shown in Fig. 24. This spectrum was acquired from a forest sample that was prepared for this research using the 532 nm Raman spectrometer. It should be noted that the spectrum is the result of many nanotubes of different chiralities and thus shows the features of all of these nanotubes at once. The main features are indicated with arrows and are discussed in the following sections.

All spectra in this thesis are presented on a linear scale (vertical and horizontal), though the horizontal scale often has a break in it in order to focus on the most relevant regions of the spectra. Spectra are often normalized to 1 at the maximum of the G band (or the G^+ peak in the case of a structured G band) where 0 is taken to be the baseline of the flat background. Spectra are also often presented in the form of a waterfall plot where a series of spectra are presented on the same set of axes with the same vertical scale, but offset vertically for clarity (alternating colours are also often used to improve readability).

G band

The most prominent feature in Fig. 24 is the G band [120, 121], which consists of a single G^+ peak at $\sim$1594 cm^{-1} and several smaller G^- peaks slightly to the left at 1545 cm^{-1} and 1525 cm^{-1}. These modes correspond to in-plane vibrations of the graphene lattice from which the nanotube is constructed, as shown in Fig. 25. When superimposed over a cylindrical coordinate system (with the nanotube axis centered on the z-axis) the G^+ mode is thought to be the component of in-plane vibrations parallel to $\hat{z}$ and the G^- mode is thought to be the component of in-plane vibrations parallel to $\hat{\theta}$ [121]. The diameter dependence of the G^- mode is a result of the curvature of the nanotube along the direction of the vibration [121].

The G band itself is the result of a simple first order scattering process from a Raman-active phonon mode in a carbon nanotube [120, 121]. An individual nanotube will produce a single G^+ peak at approximately 1594 cm^{-1} (with shifts depending on the environment [125] and slightly on chirality [126]) and a single G^- peak with a position (in units of [cm^{-1}]) that depends on diameter d (in units of [nm]) as [120]:

$$\omega\left(G^-\right) = \omega\left(G^+\right) + \frac{B}{d^2} \tag{1.17}$$

where B is a constant that depends on whether the nanotube is a semiconductor or a metal, and slightly on the environment in which the nanotube was measured. B has a value of approximately -45 $cm^{-1}nm^2$ for semiconducting nanotubes and -80 $cm^{-1}nm^2$ for metallic nanotubes.

Because the G^- peaks shift according to diameter and the resonance energies are also diameter-dependent, different G^- peaks will show up at different excitation energies in a forest sample, which generally contains a large variety of different chiralities (and diameters). Because of the broad distribution of nanotubes in a forest, resonance does not have a large effect on the G^+ peak because its position is diameter independent and because there will always be some nanotubes in resonance and contributing to its intensity.

The G^+ peak and semiconducting G^- peaks have a narrow Lorentzian line shape [120, 121]. The metallic G^- peaks have a broader asymmetric non-Lorentzian line shape that is generally considered to be a Breit–Wigner–Fano line shape (BWF) [120, 121].

Although the presence of G^- modes is often used as an indication of the presence of SWNTs, recent evidence [127] shows that thin MWNTs can also produce G^- peaks. For large diameter nanotubes, the difference in the Raman shift between the G^- peaks and G^+ peaks is small [120, 121]. The two peaks can be close enough together that they

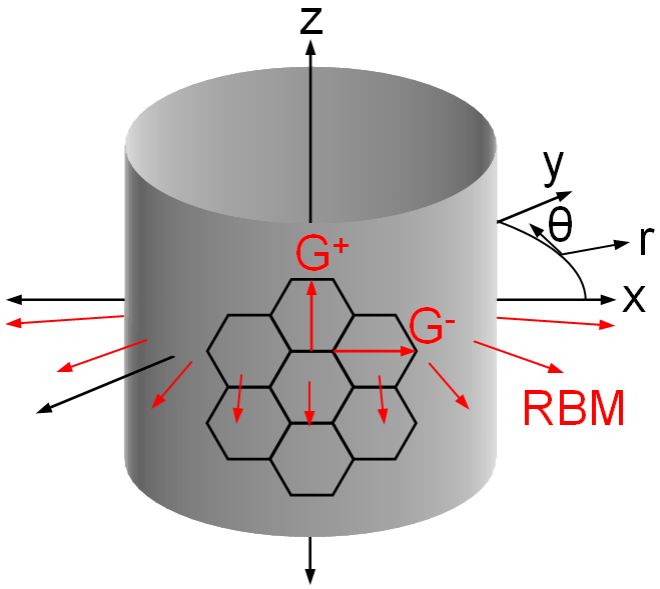


Figure 25: Schematic diagram of the main Raman modes in a carbon nanotube (indicated and labeled with arrows). See text for details.

overlap and merge into a single asymmetric peak [120, 121].

D band

The D band is generally a broad Lorentzian peak that occurs between 1300 cm^{-1} and 1350 cm^{-1}, though its position depends on the excitation energy and diameter [120, 122]. The Raman shift of the D band (in units of [cm^{-1}]), for a single SWNT, is a function of the nanotube diameter d (in units of [nm]) given by [128]:

$$\omega\,(\mathrm{D}) = A + \frac{B}{d} \tag{1.18}$$

where both A and B are constants that depend on the laser excitation energy. For 2.41 eV laser excitation, $A = 1354.8$ cm^{-1} and $B = -16.5$ cm^{-1}nm [128]. For an ensemble of nanotubes, such as the forests analyzed throughout this thesis, the observed Raman shift and peak width of the D band depend on the diameter distribution of the nanotubes in the forest.

The D band is not a simple first order process like the G band [121, 122]. Its origin is a non-Raman-active phonon mode that becomes activated in the presence of defects in the nanotube lattice due to increased phonon scattering events [122]. The D band is therefore a second order process and can be taken as an indication of the number of defects in the nanotube lattice [125]. Potential defects were discussed in Section 1.3.

Experimentally, the most important Raman parameter considered in this thesis (and

many other works on carbon nanotubes) is the ratio of the intensity of the D band to the intensity of the G band (the D/G ratio) [125]. This parameter gives a relative measure of the number of defects in the sample being studied because the D band intensity is representative of the number of defects and the G band intensity is proportional to the amount of material (perfect sp^2 bonded carbon atoms). This ratio is only meaningful if the defect density is not too high [118]. The larger the D/G ratio, the more defects in the sample. Because defects would ideally be minimized, an improvement in the D/G ratio is understood to mean a decrease in the D/G ratio.

In this thesis, the D/G ratio is calculated using the integrated intensity underneath Lorentzian curves fitted to the D band and G band. If G^- modes are present, the ratio is taken with respect to the G^+ mode. Multiple Lorentzian curves are fitted simultaneously to all of the peaks D band and G band region.

The exact relationship between defect density and the D/G ratio for graphene has recently been studied [118], and these results can be used in the study of carbon nanotubes. For graphene, the D/G ratio (I_D/I_G) is found to be proportional to the defect density n_D [118]:

$$n_D = \frac{(1.8 \pm 0.5) \times 10^8}{\lambda_i^4} \, (I_D/I_G) \, \text{defects/nm}^2 \tag{1.19}$$

where λ_i is the wavelength (in units of [nm]) of the excitation laser. In this equation, the D/G ratio is calculated by taking the ratio of the peak intensities of the D band and G band. The relationship between the integrated intensity and peak intensity of a Lorentzian curve is straightforward and is discussed in Appendix E (Section *D/G Ratio From Peak vs Integrated Intensities*).

Radial breathing modes

The other main feature on the Raman spectrum shown in Fig. 24 is the radial breathing mode (RBM) region of the spectrum from approximately 150 cm^{-1} to 400 cm^{-1} [120, 121]. An individual SWNT will produce a single peak in this region with the peak position (in units of [cm^{-1}]) determined by the nanotube diameter d (in units of [nm]) [120, 121]. The most widely used mathematical description of this dependence is [120, 121]:

$$\omega \, (\text{RBM}) = A + \frac{B}{d} \tag{1.20}$$

where the exact values of A and B depend on the environment that surrounds the nanotubes [122]. In general, A is a constant between 0 cm^{-1} and 10 cm^{-1} and B is a constant between 230 cm^{-1}nm and 250 cm^{-1}nm [122]. Theoretically, this mathematical

form can be rationalized as follows: larger diameter SWNTs are softer, and thus their RBM phonons are less energetic [1]. A sheet of graphene does not have an RBM at all.

Like the G band, the RBM has a Lorentzian line shape and is the result of a simple first order scattering process from a Raman-active phonon mode in a carbon nanotube [120, 121]. The relevant vibration is shown in Fig. 25. The RBM corresponds to out of plane vibrations in the $\hat{r}$ direction of the cylindrical coordinate system. As the name suggests, it can be viewed as the radial expansion and contraction of the nanotube.

Like the G^- peaks, the RBMs are very sensitive to excitation energy and resonance effects [125]. Because the RBM peaks shift according to diameter and the resonance energies are also diameter-dependent, different RBM peaks will show up at different excitation energies in a forest sample, because of the large variety of different chiralities (and diameters) present in the forest.

Generally, the presence of RBMs is attributed to the presence of SWNTs. However, thin MWNTs (such as DWNTs and TWNTs) can also have detectable RBMs [127, 129] that are broadened due to the interaction of neighbouring walls [129]. Factors such as the overall Raman spectrum (with strong RBMs and G^- peaks) and the thickness of the catalyst layer can aid in determining the likelihood of SWNTs being present in the sample (thinner layers are likely to produce more SWNTs) [93]. Other observations are needed to confirm the presence of SWNTs.

Resonance can be a particularly important factor in the analysis of the RBMs in a Raman spectrum. As an example, consider an ensemble of CNTs (such as a CNT forest) for which abundant SWNTs are expected. A Raman spectrum without any RBMs only indicates that there are no *resonant* SWNTs in the sample; the lack of RBMs does not prove that there are no SWNTs in the sample at all. Similarly, the presence of RBMs indicates that there are likely SWNTs in the sample being analyzed [121] but does not prove that all of the nanotubes in the sample are single-walled.

Nanotubes with a sufficiently large diameter would produce an RBM with a Raman shift that is below the cut-off of the filter that blocks the Rayleigh scattered light. For example, if $A = 0$ cm^{-1} and $B = 248$ cm^{-1}nm [120] in Equation (1.20) and the lower detection limit is 150 cm^{-1}, then the largest diameter CNT that can be detected is 1.65 nm.

A final point regarding the RBMs is that one can extract the diameter, chirality, and resonance energy (which also depends on the diameter) of a nanotube with an observable RBM [125]. All of this information can be brought together in a Kataura plot [119], as shown in Fig. 26, which plots the energy separation of the E_{ii} and M_{ii} transitions for each chirality (n, m) (each represented as a single point for each energy transition data

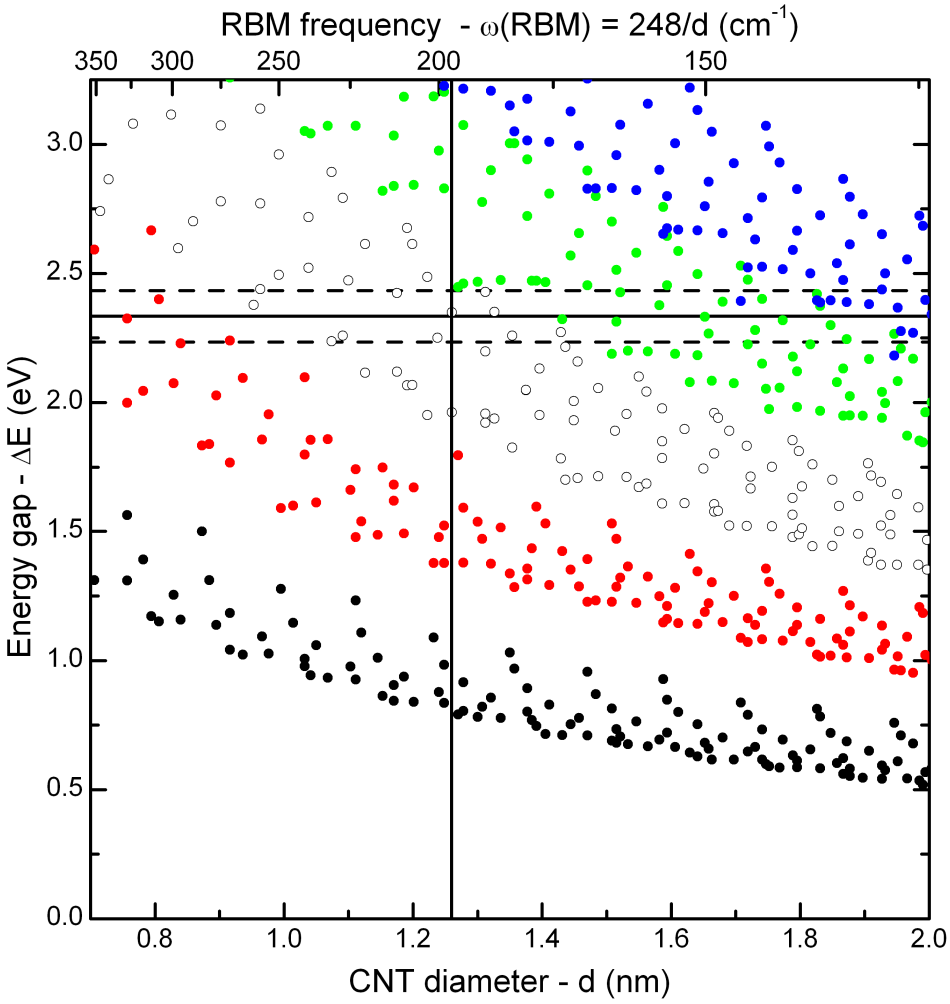


Figure 26: Kataura plot for specific energy and diameter ranges. Energy gaps ΔE (E_{ii} or M_{ii} in CNT density of states) as functions of SWNT diameter d and equivalent RBM frequency $\omega\,(\mathrm{RBM}) = 248/d$. Solid circles correspond to semiconducting SWNT energy transitions: E_{11} (black), E_{22} (red), E_{33} (green), and E_{44} (blue). Open circles correspond to the metallic SWNT energy transition M_{11}. Data from Nugraha et al. [66].

set in Fig. 26) as a function of nanotube diameter or Raman shift. From this plot it is possible to identify not only the diameter of a nanotube but also the chirality. The energy separations do not perfectly follow a single line; this is due to small effects of the chirality.

To demonstrate the utility of the Kataura plot, consider a Raman spectrum of a carbon nanotube with an RBM at a Raman shift of 197 ± 2 cm^{-1} (chosen as a hypothetical example). Using Equation (1.20) (with $A = 0$ cm^{-1} and $B = 248$ cm^{-1}nm), this means the diameter corresponding to this RBM is $d = 1.26 \pm 0.01$ nm, as indicated in Fig. 26. There are 4 possible SWNTs with this diameter (within the uncertainty), with chiralities: $(11, 7)$, $(14, 3)$, $(12, 6)$, and $(16, 0)$; and diameters: 1.25 nm, 1.25 nm, 1.26 nm, and

1.27 nm respectively. With the Kataura plot, it is possible to determine which one of these nanotubes is responsible for the RBM.

In practice, to determine the nanotube chirality from the Kataura plot (Fig. 26) one would draw a vertical line on the Kataura plot at the position of the RBM (for multiple RBMs, multiple vertical lines would need to be drawn, each corresponding to an observed RBM Raman shift). The vertical solid line in Fig. 26 marks the position of an RBM with a Raman shift of 197 ± 2 cm^{-1}. The points that this line intersects correspond to the above 4 nanotubes. Next, a horizontal line (corresponding to the laser excitation energy, and hence the resonance energy) is drawn on the Kataura plot. The horizontal solid line on Fig. 26 shows the laser energy 532 nm and the dashed lines show a narrow resonance window ($\pm$0.1 eV [130]). Anywhere that this horizontal line intersects (or passes near) a point there will be a resonant nanotube that can generate a peak in the corresponding RBM region of the Raman spectrum (at the Raman shift that corresponds to the point) if that nanotube is present in the sample.

Where the horizontal line and vertical line intersect will be the nanotube responsible for the observed RBM, which in this case is a metallic $(12, 6)$ SWNT with diameter 1.26 nm and a Raman shift of 197 cm^{-1}. This metallic nanotube is in resonance with the laser and produces the RBM. The other 3 carbon nanotubes listed above are not in resonance with the laser and thus do not produce (observable) RBMs.

In practice there are a number of difficulties that arise when trying to assign chiralities from a Raman spectrum. Significant uncertainty is a result of the fact that both the transition energies E_{ii} and the RBM frequency $\omega\,(\mathrm{RBM})$ of a carbon nanotube depend on the environment surrounding the nanotube [125]. This leads to uncertainty in converting RBM frequency to nanotube diameter. Additionally, the resonance energy has a certain width [125]. As the carbon nanotube diameter increases (right side of Fig. 26), neighbouring diameters become closer together and harder to distinguish on a Kataura plot (relative to the uncertainty in determining the diameter from the RBM). Finally, as the order of the transition i (as in E_{ii} or M_{ii}) increases, the spacing between neighbouring orders becomes increasingly small to the point of overlap [66] (see Fig. 26). Some of these problems can be partially mitigated by using multiple laser lines or a tunable laser and generating a map of the Raman spectra as a function of excitation energy [125].

A plot (and method) similar to the Kataura plot for RBMs has recently been demonstrated for semiconducting G^- peaks [126], which behave similarly to the RBMs.

Other features and background noise

There are other Raman modes in the spectra of carbon nanotubes, but these are generally less intense than the above described features [122]. Some of these features, the intermediate frequency modes (IFM), occur between the RBM region of the spectrum and the D band (between ∼400 cm^{-1} and ∼1000 cm^{-1}) [122]. These features are noticeably very weak in Fig. 24 and mostly absent in many of the other spectra in this thesis. There are also other modes with Raman shifts above the G band [121, 122], but these were not recorded in this thesis. Here, the spectrometer grating was chosen to maximize the resolution in the 100 cm^{-1} to 1700 cm^{-1} range because it contained the peaks of interest: the G band, D band, and RBMs.

There is a peak present in Fig. 24 (at ∼500 cm^{-1}) that is a result of the silicon substrate [131] upon which the nanotube forest is attached. In this case, the forest was short enough that the laser light was able to penetrate deep enough to see the silicon. In most forests, this peak was not visible. For even thinner forests, this peak greatly increases in size, and another much broader peak (also related to the Si substrate) near 1000 cm^{-1} can be seen [131]. The presence of these peaks is therefore indicative that the forest being analyzed is not very tall.

The background of the acquired spectra is generally quite flat throughout the entire range and is mostly due to out of focus light reaching the CCD camera of the grating spectrometer. Most of the noise in the spectrum can be attributed to the same cause. Indeed it is noticeable that forests with very rough top surfaces or smoothly varying top surfaces always have a much noisier spectrum (or one without a flat background) than those with flat smooth top surfaces.

The intensity does drop somewhat near the edges of the spectrum, but is particularly noticeable at low Raman shifts below the RBM region of the spectrum. This drop off at low Raman shifts is due to the filter used to remove the intense Rayleigh scattered component from the collected light.

1.7 Electron microscopy

Electron microscopy is generally analogous to optical microscopy. Similar to how an optical microscope illuminates a sample with a beam of light, an electron microscope illuminates the sample with a beam of energetic electrons (on the order of keV) [50, 132]. Unlike optical microscopes that use glass lenses to focus light, the electron beam in an SEM is focused and raster scanned with a series of electromagnetic lenses [116, 132].

In optical microscopy, the resolution of an image is limited by the wavelength of the light. In electron microscopy, the resolution can be much higher due to the much smaller wavelength of the electrons. The extreme resolution and magnification available with electron microscopy make it very well suited to studying nanostructures [50] like carbon nanotubes. An example of a scanning electron microscope image is shown in Fig. 6b.

1.7.1 Scanning electron microscopy

In a scanning electron microscope (SEM), a highly focused electron beam is raster scanned across the sample at a rapid rate [116, 132] (quick enough to create a real time image of $\sim 10^6$ pixels). The primary electrons in the beam then interact with the material. The volume of the material in which this interaction takes place is called the scattering volume [116]. When interacting with the material in the scattering volume, the primary beam electrons can undergo either elastic or inelastic scattering [116]. The elastically scattered primary electrons that can be detected are called backscattered electrons [116] (elastic scattering in the forward direction puts the electrons deeper into the sample). Inelastically scattered primary electrons can produce more electrons through collisions with loosely bound electrons in the material. These are called secondary electrons and they can be ejected from the material and detected [116]. The secondary electrons have much lower energies than the backscattered electrons [116].

The primary beam of electrons in an SEM is focused and raster scanned with a series of electromagnetic lenses [116, 132]. A schematic of an SEM is shown in Fig. 27 and a general description of an SEM is given in the following section.

At each point in the raster scanning process, the backscattered and secondary electrons are collected to create one pixel of the larger image of the sample [50, 116, 132]. By scanning from one point to another, an image can be built up from these pixels. The intensity of the detected electrons is a result of the properties of the material being analyzed [50, 116]. In an SEM, the image resolution is limited by the size of the electron beam (which is larger than the wavelength of the electrons) and the scattering volume of the electrons in the material [116].

Compared to optical microscopy, SEM has a very large focal depth, allowing it to create detailed images of 3D samples [116, 132]. This large focal depth is a result of the very narrow and focused electron beam [116]. For the study of carbon nanotube forests, another advantage of SEM over optical microscopy is that SEM provides significantly better contrast than optical methods. For carbon nanotube forests, even features with dimensions well above the resolution limit of optical microscopy can be difficult to see

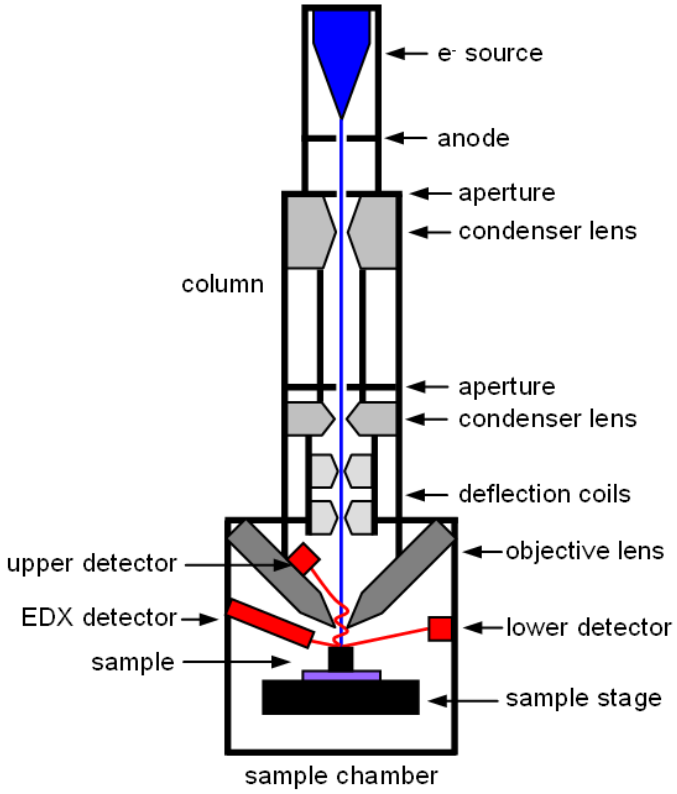


Figure 27: Diagram of an SEM. The electron beam follows the blue path from the electron source (blue) to the sample (black and purple) through a series of apertures and lenses (gray) to focus and scan the beam. Electrons are scattered by the sample; secondary electrons and characteristic x-rays are emitted (all red). The signals are detected by the detectors (upper and lower detectors for electrons and EDX detector for characteristic x-rays). Figure adapted from Hitachi S-4700 user manual.

due to very low contrast (see for example Fig. 7). A comparison of an optical image and an SEM image of a carbon nanotube forest is shown in Fig. 3 of Chapter 5.

In addition to the backscattered electrons and secondary electrons, there is another kind of electron that is created in the bombardment of a material with an electron beam: Auger electrons that are produced by the Auger effect [133]. These are analyzed in Auger electron spectroscopy (AES), which can be performed in an SEM with an appropriate Auger electron detector. AES can help identify which elements are present in a sample [133]. Similar to Auger electrons, characteristic x-rays can also be emitted by the sample, and can be detected by an energy dispersive x-ray (EDX) detector in an SEM [74, 116, 132]. The spectra generated by these techniques will be discussed in the following sections.

Auger electrons and characteristic x-rays are both the result of the same process [116, 133], which is illustrated in Fig. 28. A high energy electron strikes an electron in an inner orbital of an atom in the material (1 in Fig. 28) and scatters. The inner orbital

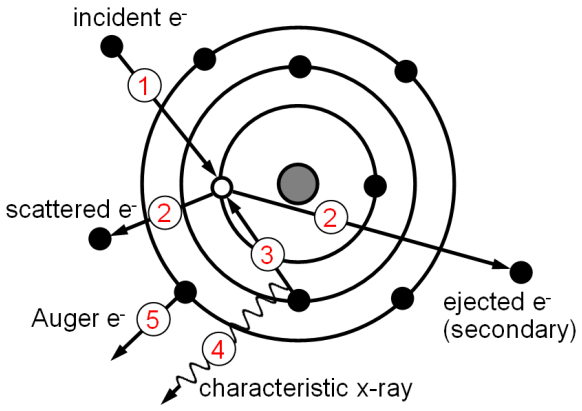


Figure 28: Processes leading to the emission of a characteristic x-ray (1-2-3-4) or an Auger electron (1-2-3-5). See text for full description. Pictured is an atom, with nucleus, energy levels, electrons, incident electron, and emitted x-ray.

electron is ejected from the atom, thus ionizing the atom (2 in Fig. 28). This ion is not in its ground state [116], so an electron from an outer orbital will drop down and fill the place of the ejected electron (3 in Fig. 28). The electron that drops down must release its excess energy (due to the difference in energy of the orbitals). It can emit a characteristic x-ray with an energy equal to the difference in energy between the outer orbital and inner orbital (4 in Fig. 28) that is detected by EDX [116]. Alternatively, this excess energy may not be emitted as an x-ray, but could instead be absorbed by another outer orbital electron, which gains this energy as kinetic energy and is ejected from the atom as an Auger electron (5 in Fig. 28). These Auger electrons carry away an energy equal to this characteristic energy minus the binding energy and can then be detected in AES [133].

Because of electron scattering processes in the material, only Auger electrons within ∼10 nm of the surface will retain enough energy to escape the material and reach the detector [74, 133]. AES is therefore exclusively a surface technique. Characteristic x-rays, on the other hand, can originate from much deeper in the material (∼1 μm) due to the greater penetrating power of x-ray versus electrons [74, 133]. The trade-off is that EDX cannot see very thin layers on the surface, whereas these thin layers will be readily visible in AES. Because the Co catalyst layer was very thin, AES was used to characterize this thickness instead of EDX. Furthermore, for lighter elements (atomic number less than ∼30), the Auger electron yield is greater than the characteristic x-ray yield [133].

One of the main disadvantages of electron microscopy is a result of the fact that, unlike the photons in optical microscopy, electrons are charged particles. The main problem that this causes is that the sample may become charged if it is not sufficiently conductive and not properly grounded to remove the impinging electrons [116]. Once

charged, the sample will affect the incoming electrons by diverting the beam and causing artefacts in the image [116]. Another downside to electron microscopy is that it can damage the sample by creating defects or doping [125]. These have profound effects on the optical properties of semiconducting carbon nanotubes. For the research carried out in this thesis, these effects are of little consequence.

1.7.2 SEM instrumentation

Two different SEMs were used in this thesis. The primary instrument (Hitachi S-4700 field emission SEM) was used for imaging and EDX. The other instrument (PHI 700 Scanning Auger Nanoprobe) was used for AES. Both instruments are very similar and only a general overview of the instrumentation will be given. A general schematic (of the Hitachi S-4700) is shown in Fig. 27.

In both instruments, the electron beam is created by a field emission source [116], which, in the S-4700 is a sharp single crystal of tungsten subjected to an electric field. The beam then passes through the electron beam column and is focused by a series of condenser lenses [116]. The deflection coils raster the beam across the sample to create the final image.

The imaging detectors are scintillators attached to photomultiplier tubes (PMT); this type of detector is known as an Everhart-Thornley detector [116]. When an electron strikes the scintillator, photons are emitted, which are collected by the PMT, which then converts them back into electrons in increasing numbers on the successive electrodes. The final electrons are then collected as the signal. In the S-4700, there are two electron detectors: one in the sample chamber and another behind the objective lens, called a "through the lens" detector. The "through the lens" detector captures low energy electrons ejected from the material (secondary electrons) in a magnetic field that channels them back though the objective lens to the detector [116].

The EDX detector (Oxford Instruments AZtec, a silicon drift detector) in the S-4700 is also in the sample chamber. The AES detector in the PHI 700 is a cylindrical mirror analyzer that is located behind the objective lens. The emitted Auger electron are collected from the chamber around the outside of the objective lens, unlike the "through the lens" detector in the S-4700.

The entire electron beam column (see Fig. 27) is kept under a high vacuum (by differential pumping) ranging from 10^{-7} Pa near the electron gun to 10^{-5} Pa near the sample chamber, which is also under vacuum [116]. This high vacuum is necessary to prevent the electrons from scattering before reaching the sample. In both SEM instruments, the

sample stage has 5 degrees of movement, 3 lateral (x, y, and z), one rotational and one tilt. This allows for most parts of the sample to be imaged. Furthermore, different sample holders are available that hold the sample at an angle to allow for further imaging access.

1.7.3 Auger electron spectra and characteristic x-ray spectra

Each element has its own characteristic Auger/EDX spectrum based on the spacing of its energy levels [116, 132]. Because AES is used more prominently in this thesis, only the Auger spectra will be described here. The analysis of EDX spectra is analogous to the analysis of AES data in almost every way, because the two techniques differ primarily in how the energy is transported away from the atom and not in how the energy is created [116].

The different energies of the Auger electrons for the same element have several origins. The first is the energy level of inner shell from which the original electron was ejected [116, 132, 133]. The second is the energy level of the outer shell from which the electron that drops down to replace it comes from [116, 132, 133]. The third is the energy level of the outer shell from which the ejected electron originates [116, 132, 133] (for AES only). The difference in energy between these shells gives rise to the characteristic Auger spectra of each element [116, 133]. Elements of lower atomic number have fewer shells and therefore fewer transitions and peaks in their spectra when compared to heavy elements with many electron shells [133].

A typical AES spectrum is shown in Fig. 29. This spectrum is of a silicon substrate (with deposited layers of silica, alumina, and cobalt, as described in Section 1.4.2) used in this thesis. AES spectra are typically presented in a form in which the raw spectrum has been differentiated [133] to make the peaks easier to identify over the sloping background. By comparing a spectrum to standard spectra for each element, every peak in the Auger spectrum can be assigned to a particular element. In Fig. 29, the features corresponding to each element are identified (C, O, Co, Al, Si). The feature marked with a * contains several peaks of higher order transitions in Co, Al, and Si.

With the SEM, it is possible to perform a line scan across the surface of the sample, taking a spectrum at each point [116]. From these individual spectra it is possible to assemble a line profile of the relative abundance of each element detected. These line profiles are used in Chapter 7. It is also possible to create 2D chemical maps using a raster scanning process, but this kind of scan is not used in this thesis.

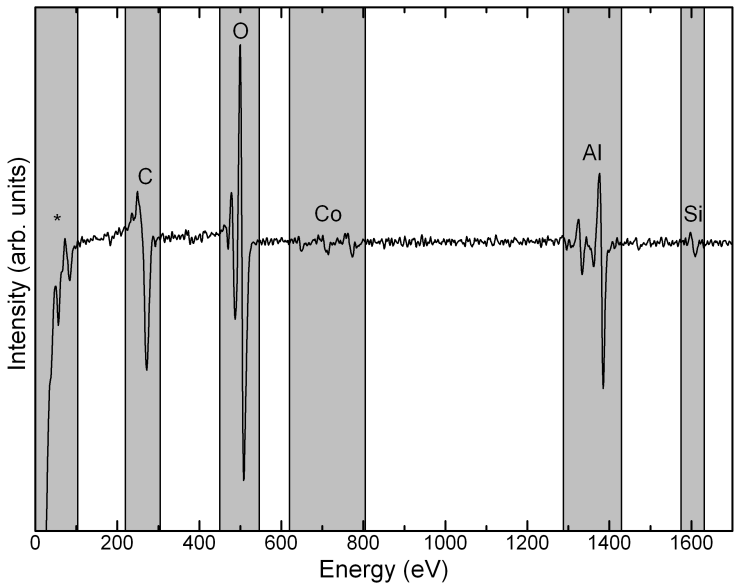


Figure 29: Auger electron spectrum for a silicon substrate (with deposited layers) used in this thesis. Peaks are identified. Visible peaks are silicon, oxygen, aluminum and cobalt, along with carbon, which is a contaminant and is not indicative of carbon nanotubes because this particular substrate was not used for growth.

1.8 Summary

This first chapter presented all the important background information necessary to understand the results that will be presented in the subsequent chapters of this thesis. Carbon nanotubes were discussed, and the important points regarding their physical structure from this discussion are the crystal structure, number of walls, chirality, defect density, and the forest structure. Further to this, the phonon modes and electronic structure of carbon nanotubes play an important role in resonance Raman spectroscopy. Next, crystals, defects, growth and chemical vapour deposition were discussed. The discussion of CVD included both the general overview of the process and apparatus and an atomic level picture of how nanotubes self-assemble from the carbon source gas.

Several analytic techniques were discussed, including scanning electron microscopy, optical microscopy and, most importantly, Raman spectroscopy. Within Raman spectroscopy, the important Raman modes were introduced. The radial breathing modes (RBMs) indicate the presence of single walled carbon nanotubes and allow the determination of the nanotubes' diameters [120, 125]. The D band and the G band represent, respectively, the amount of defects and graphitic sp^2 bonded carbon in the sample. The ratio of the intensity of these two bands (the D/G ratio) is commonly used as a metric for comparing the number of defects from one sample to another [125]. Furthermore, the

G band can be split into separate G^+ modes and G^- modes, the former of which is fixed in position, and the latter of which is indicative of single walled carbon nanotubes and depends on their diameter, much like the RBMs [120].

With these most important points in mind, one should be able to fully understand and appreciate the material presented in the main body of this thesis, which includes seven chapters, each devoted to a single peer-reviewed publication.

Chapter 2 details the correlations between the characteristic energy scales of growth, termination of growth, and number of defects present (as determined by the D/G ratio) in CNTs grown by ethanol CVD. This chapter also demonstrates some of the primary methods used to gather data in this thesis, such as *in situ* optical microscopy and Raman spectroscopy.

Chapter 3 analyzes CNT forests grown by acetylene CVD. The acetylene grown forests are much taller than the ethanol grown forests of Chapter 2. These taller forests manifest several distinct morphologies that are analyzed using SEM. A link between the morphology and the termination of growth is analyzed in terms of the balance of forces within the forests. The dependence of the D/G ratio on growth temperature in this chapter is found to be the same as was observed in Chapter 2. This correlation between the D/G ratio for two different carbon sources is revisited in Chapter 8. Chapter 4 provides some further details about the interactions between the individual nanotubes in the forests and discusses the overall morphology of the forests.

Chapter 5 and Chapter 6 analyze a microscale rippling morphology on the sidewalls of the forests. This rippling morphology is seen to be sufficiently regular that the forests can act as diffraction gratings when illuminated with white light, which is surprising considering that CNT forests are well known for being very black [28]. It is proposed that the ripples are a means of strain relief to counteract a non-uniform growth rate. Chapter 7 contains a thorough study of this non-uniform growth rate and the effect of the catalyst island size. This analysis is accomplished by developing a gas phase diffusion model in which all parameters are based on real physical quantities and are measured or estimated from known values. These parameters include the efficiency at which the acetylene source gas is converted into CNTs and the density of the CNT forests.

Chapter 8 looks at the composition of the actual forests produced in these synthesis processes using Raman spectroscopy. The temperature dependence of the D/G ratio is found to be the same for a large variety of growth parameters, including ethanol (from Chapter 2) and acetylene carbon sources (from Chapter 3), catalyst thickness, and the species of carbon nanotubes produced. This suggests that the number of defects as a function of temperature is intrinsic to the growth process of not just carbon nanotubes,

but the graphene lattice in general. The Raman spectra also provide information about the diameters of the SWCNTs in the forests. The diameter is observed to be temperature-dependent. A thermodynamic model is proposed to link the CNT diameter to the CVD conditions during growth.

Overall, from the analysis of the data collected in all the chapters, physical mechanisms and models are proposed to explain the observations and serve as a basis for future CVD growth optimization procedures. The mechanisms that are identified and the models that are developed allow for a rational approach to synthesis by knowing how each growth parameter affects each aspect of the outcome. The overall goal of carbon nanotube synthesis is to be able to grow application-specific carbon nanotubes with a specific chirality (and hence diameter and electronic type: metal or semiconductor), number of walls, length, crystallinity, and quantity. The results of the research in this thesis make steps towards many of these requirements: in particular, determining why nanotubes stop growing (thus understanding how to make longer nanotubes), how to control the yield, and how to exercise some control over what kind of nanotubes are produced in terms of their diameter and crystallinity.

References

[1] R Saito, G Dresselhaus, and M S Dresselhaus. *Physical Properties of Carbon Nanotubes*. Imperial College Press, London, UK, 1998.

[2] M Kumar and Y Ando. *J. Nanosci. Nanotech.*, 10:3739–58, 2010.

[3] X Wang, Q Li, J Xie, Z Jin, J Wang, Y Li, K Jiang, and S Fan. *Nano Lett.*, 9:3137–41, 2009.

[4] P M Ajayan and O Z Zhou. In M S Dresselhaus, G Dresselhaus, and P Avouris, editors, *Carbon Nanotubes: Synthesis, Structure, Properties, and Applications*, pages 391–425. Springer, Germany, 2001.

[5] D Tománek, A Jorio, M S Dresselhaus, and G Dresselhaus. In A Jorio, G Dresselhaus, and M S Dresselhaus, editors, *Carbon Nanotubes: Advanced Topics in the Synthesis, Structure, Properties and Applications*, pages 1–12. Springer, Germany, 2008.

[6] C Journet, M Picher, and V Jourdain. *Nanotechnology*, 23:142001, 2012.

[7] M Endo, M S Strano, and P M Ajayan. In A Jorio, G Dresselhaus, and M S Dresselhaus, editors, *Carbon Nanotubes: Advanced Topics in the Synthesis, Structure, Properties and Applications*, pages 13–61. Springer, Germany, 2008.

[8] J I Sohn, S Lee, Y-H Song, S-Y Choi, K-I Cho, and K-S Nam. *Appl. Phys. Lett.*, 78:901–3, 2001.

[9] Y J Jung, S Kar, S Talapatra, C Soldano, G Viswanathan, X Li, Z Yao, F S Ou, A Avadhanula, R Vajtai, S Curran, O Nalamasu, and P M Ajayan. *Nano Lett.*, 6:413–8, 2006.

[10] E Kymakis and G A J Amaratunga. *Appl. Phys. Lett.*, 80:112–4, 2002.

[11] C Rutherglen and P Burke. *Nano Lett.*, 7:3296–9, 2007.

[12] K Jensen, J Weldon, H Garcia, and A Zettl. *Nano Lett.*, 7:3508–1, 2007.

[13] C Kocabas, H Kim, T Banks, J A Rogers, A A Pesetski, J E Baumgardner, S V Krishnaswamy, and H Zhang. *Proc. Nat. Acad. Sci.*, 105:1405–9, 2008.

[14] K Bradley, J C P Gabriel, and G Grüner. *Nano Lett.*, 3:1353–5, 2003.

[15] T Yamada, Y Hayamizu, Y Yamamoto, Y Yomogida, A Izadi-Najafabadi, D N Futaba, and K Hata. *Nat. Nano.*, 6:296–301, 2011.

[16] K Balasubramanian and M Burghard. *Small*, 1:180–92, 2005.

[17] D R Kauffman and A Star. *Angew. Chem. Int. Ed.*, 47:6550–70, 2008.

[18] Z Liu, X Li, S M Tabakman, K Jiang, S Fan, and H Dai. *J. Am. Chem. Soc.*, 130:13540–1, 2008.

[19] Z Liu, S Tabakman, K Welsher, and H Dai. *Nano Res.*, 2:85–120, 2009.

[20] A Bianco, K Kostarelos, and M Prato. *Curr. Opin. Chem. Biol.*, 9:674–9, 2005.

[21] A A Bhirde, V Patel, J Gavard, G Zhang, A A Sousa, A Masedunskas, R D Leapman, R Weigert, J S Gutkind, and J F Rusling. *ACS Nano*, 3:307–16, 2009.

[22] N W S Kam, M O'Connell, J A Wisdom, and H Dai. *Proc. Nat. Acad. Sci.*, 102:11600–5, 2005.

[23] C J Gannon, P Cherukuri, , B I Yakobson, L Cognet, J S Kanzius, C Kittrell, R B Weisman, M Pasquali, H K Schmidt, R E Smalley, and S A Curley. *Cancer*, 110:2654–65, 2007.

[24] M Zhang and K R Atkinson andR H Baughman. *Science*, 306:1358–61, 2004.

[25] E Joselevich, H Dai, J Liu, K Hata, and A H Windle. In A Jorio, G Dresselhaus, and M S Dresselhaus, editors, *Carbon Nanotubes: Advanced Topics in the Synthesis, Structure, Properties and Applications*, pages 101–64. Springer, Germany, 2008.

[26] L Ge, S Sethi, L Ci, P M Ajayan, and A Dhinojwala. *Proc. Nat. Acad. Sci.*, 104:10792–5, 2007.

[27] A Hamdan, J Cho, R Johnson, J Jiao, D Bahr, R Richards, and C Richards. *Nanotechnology*, 21:015702, 2010.

[28] Z-P Yang, L Ci, J A Bur, S-Y Lin, and P M Ajayan. *Nano Lett.*, 8:446–51, 2008.

[29] N R Wilson and J V Macpherson. *Nat. Nano.*, 4:483–91, 2009.

[30] H Dai. In M S Dresselhaus, G Dresselhaus, and P Avouris, editors, *Carbon Nanotubes: Synthesis, Structure, Properties, and Applications*, pages 29–53. Springer, Germany, 2001.

[31] J-C Charlier and S Iijima. In M S Dresselhaus, G Dresselhaus, and P Avouris, editors, *Carbon Nanotubes: Synthesis, Structure, Properties, and Applications*, pages 55–81. Springer, Germany, 2001.

[32] S Iijima. *Nature*, 354:56–58, 1991.

[33] R T K Baker, P S Harris, R B Thomas, and R J Waite. *J. Catal.*, 30:86, 1973.

[34] A Oberlin, M Endo, and T Koyama. *J. Cryst. Growth*, 32:335–49, 1976.

[35] G G Tibbetts. *J. Cryst. Growth*, 66:632–8, 1984.

[36] R T K Baker. *Carbon*, 27:315–23, 1989.

[37] H W Kroto, J R Heath, S C O'Brien, R F Curl, and R E Smalley. *Nature*, 318:162–3, 1985.

[38] P R Wallace. *Phys. Rev.*, 71:622–34, 1947.

[39] R Chang. *Chemistry, 7^{th} Edition*. McGraw-Hill, New York, USA, 2002.

[40] K P C Vollhardt and N E Schore. *Organic Chemistry: Structure and Function, 4^{th} Edition*. Freeman, New York, USA, 2003.

[41] M S Dresselhaus and M Endo. In M S Dresselhaus, G Dresselhaus, and P Avouris, editors, *Carbon Nanotubes: Synthesis, Structure, Properties, and Applications*, pages 11–28. Springer, Germany, 2001.

[42] H Ibach and H Luth. *Solid State Physics: An Introduction to the Principles of Materials Science, 3^{rd} Edition*. Springer, Germany, 2003.

[43] C A Hunter and J K M Sanders. *J. Am. Chem. Soc.*, 112:5525–34, 1990.

[44] H Dai. *Acc. Chem. Res.*, 35:1035–44, 2002.

[45] J E Ayers. *Heteroepitaxy of Semiconductors*. CRC Press, USA, 2007.

[46] M Remškar. *Adv. Mat.*, 16:1497–504, 2004.

[47] R Tenne, M Remškar, A Enyashin, and G Seifert. In A Jorio, G Dresselhaus, and M S Dresselhaus, editors, *Carbon Nanotubes: Advanced Topics in the Synthesis, Structure, Properties and Applications*, pages 631–71. Springer, Germany, 2008.

[48] D Golberg, Y Bando, Y Huang, T Terao, M Mitome, C Tang, and C Zhi. *ACS Nano*, 4:2979–93, 2010.

[49] D T Bong, T D Clark, J R Granja, and M R Ghadiri. *Angew. Chem. Int. Ed.*, 40:988–1011, 2001.

[50] C Kittel. *Introduction to Solid State Physics, 8^{th} Edition*. Wiley, USA, 2005.

[51] X Zhao, Y Liu, S Inoue, T Suzuki, R O Jones, and Y Ando. *Phys. Rev. Lett.*, 92:125502, 2004.

[52] N G Chopra, L X Benedict, V H Crespi, M L Cohen, S G Louie, and A Zettl. *Nature*, 377:135–8, 1995.

[53] Q Zhang, W Zhou, W Qian, R Xiang, J Huang, D Wang, and F Wei. *J. Phys. Chem. C*, 111:14638–43, 2007.

[54] E Einarsson, H Shiozawa, C Kramberger, M H Rümmeli, A Grüneis, T Pichler, and S Maruyama. *J. Phys. Chem. C*, 111:17861–4, 2007.

[55] F Márquez, V López, C Morant, R Roque-Malherbe, C Domingo, E Elizalde, and F Zamora. *J. Nanomater.*, 2010:189214, 2010.

[56] G Eres, A A Puretzky, D B Geohegan, and H Cui. *Appl. Phys. Lett.*, 84:1759–61, 2004.

[57] D N Futaba, K Hata, T Yamada, K Mizuno, M Yumura, and S Iijima. *Phys. Rev. Lett.*, 95:056104, 2005.

[58] A A Puretzky, D B Geohegan, S Jesse, I N Ivanov, and G Eres. *Appl. Phys. A*, 81:223–40, 2005.

[59] K Kaminska, J Lefebvre, D G Austing, and P Finnie. *Nanotechnology*, 18:165707, 2007.

[60] I Gunjishima, T Inoue, and A Okamoto. *Appl. Phys. Lett.*, 91:193102, 2007.

[61] A A Puretzky, G Eres, C M Rouleau, I N Ivanov, and D B Geohegan. *Nanotechnology*, 19:055605, 2008.

[62] C Mattevi, C T Wirth, S Hofmann, R Blume, M Cantoro, C Ducati, C Cepek, A Knop-Gericke, S Milne, C Castellarin-Cudia, S Dolafi, A Goldoni, R Schloegl, and J Robertson. *J. Phys. Chem. C*, 112:12207–13, 2008.

[63] S Yasuda, D N Futaba, M Yumura, S Iijima, and K Hata. *Appl. Phys. Lett.*, 93:143115, 2008.

[64] J Lefebvre, S Maruyama, and P Finnie. In A Jorio, G Dresselhaus, and M S Dresselhaus, editors, *Carbon Nanotubes: Advanced Topics in the Synthesis, Structure, Properties and Applications*, pages 287–319. Springer, Germany, 2008.

[65] M S Strano. *J. Am. Chem. Soc.*, 125:16148–53, 2003.

[66] A R T Nugraha, R Saito, K Sato, P T Araujo, A Jorio, and M S Dresselhaus. *Appl. Phys. Lett.*, 97:091905, 2010.

[67] A A Shvedova, A Pietroiusti, B Fadeel, and V E Kagan. *Toxicol. Appl. Pharm.*, 261:121–33, 2012.

[68] Y Liu, Y Zhao, B Sun, and C Chen. *Acc. Chem. Res.*, 46:702–13, 2013.

[69] K Donaldson, R Aitken, L Tran, V Stone, R Duffin, G Forrest, and A Alexander. *Toxicol. Sci.*, 92:5–22, 2006.

[70] C-W Lam, J T James, R McCluskey, S Arepalli, and R L Hunter. *Crit. Rev. Toxicol.*, 36:189–217, 2006.

[71] K Kostarelos. *Nat. Biotechnol.*, 26:774–6, 2008.

[72] J B Hudson. *Surface Science: An Introduction*. Wiley, Toronto, Canada, 1998.

[73] A J Stone and D J Wales. *Chem. Phys. Lett.*, 128:501–3, 1986.

[74] P Y Yu and M Cardona. *Fundamentals of Semiconductors: Physics and Materials Propeties, 4^{th} Edition*. Springer, Germany, 2010.

[75] F Ding, A R Harutyunyan, and B I Yakobson. *Proc. Nat. Acad. Sci.*, 106:2506–9, 2009.

[76] R Rao, D Liptak, T Cherukuri, B I Yakobson, and B Maruyama. *Nat. Mater.*, 11:213–6, 2012.

[77] C L Cheung, A Kurtz, H Park, and C M Lieber. *J. Phys. Chem. B*, 106:2429–33, 2002.

[78] G Eres, A A Kinkhabwala, H Cui, D B Geohegan, A A Puretzky, and D H Lowndes. *J. Phys. Chem. B*, 109:16684–94, 2005.

[79] P Nikolaev, M J Bronikowski, R K Bradley, F Rohmund, D T Colbert, K A Smith, and R E Smalley. *Chem. Phys. Lett.*, 313:91–7, 1999.

[80] S Maruyama, R Kojima, Y Miyauchi, S Chiashi, and M Kohno. *Chem. Phys. Lett.*, 360:229–34, 2002.

[81] P Finnie, A Li-Pook-Than, J Lefebvre, and D G Austing. *Carbon*, 44:3199–206, 2006.

[82] K Hata, D N Futaba, K Mizuno, T Namai, M Yumura, and S Iijima. *Science*, 306:1362–4, 2004.

[83] T Yamada, A Maigne, M Yudasaka, K Mizuno, D N Futaba, M Yumura, S Iijima, and K Hata. *Nano Lett.*, 8:4288–92, 2008.

[84] D N Futaba, J Goto, S Yasuda, T Yamada, M Yumura, and K Hata. *Adv. Mat.*, 21:1–5, 2009.

[85] P B Amama, C L Pint, L McJilton, S M Kim, E A Stach, P T Murray, R H Hauge, and B Maruyama. *Nano Lett.*, 9:44–9, 2009.

[86] P Finnie, J Bardwell, I Tsandev, M Tomlinson, M Beaulieu, J Fraser, and J Lefebvre. *J. Vac. Sci. Technol. A*, 22:747–51, 2004.

[87] G Zhong, S Hofmann, F Yan, H Telg, J H Warner, D Eder, C Thomsen, W I Milne, and J Robertson. *J. Phys. Chem. C*, 113:17321–5, 2009.

[88] E R Meshot, D L Plata, S Tawfick, Y Zhang, E A Verploegen, and A J Hart. *ACS Nano*, 3:2477–86, 2009.

[89] M Cantoro, S Hofmann, S Pisana, V Scardaci, A Parvez, C Ducati, A C Ferrari, A M Blackburn, K-Y Wang, and J Robertson. *Nano Lett.*, 6:1107–12, 2006.

[90] J Bond, J Lefebvre, D G Austing, L Tay, and P Finnie. *Nanotechnology*, 18:135603, 2007.

[91] M Chhowalla, K B K Teo, C Ducati, N L Rupesinghe, G A J Amaratunga, A C Ferrari, D Roy, J Robertson, and W I Milne. *J. Appl. Phys.*, 90:5308–17, 2001.

[92] D Takagi, Y Homma, and Y Kobayashi. *Physica E*, 24:1–5, 2004.

[93] B Zhao, D N Futaba, S Yasuda, M Akoshima, T Yamada, and K Hata. *ACS Nano*, 3:108–14, 2008.

[94] R J Hill, editor. *Physical Vapor Deposition*. Temescal, USA, 1986.

[95] D M Mattox. *Handbook of Physical Vapor Deposition (PVD) Processing*. Elsevier, USA, 2010.

[96] A J Hart and A H Slocum. *J. Phys. Chem. B*, 110:8250–7, 2006.

[97] M J Bronikowski. *Carbon*, 44:2822–32, 2006.

[98] G Zhong, T Iwasaki, J Robertson, and H Kawarada. *J. Phys. Chem. B*, 111:1907–10, 2007.

[99] G-H Jeong, N Olofsson, L K L Falk, and E E B Campbell. *Carbon*, 47:696–704, 2009.

[100] M F L De Volder, D O Vidaud, E R Meshot, S Tawfick, and A J Hart. *Microelectron. Eng.*, 87:1233–38, 2010.

[101] S Dittmer, J Ek-Weis, O A Nerushev, and E E B Campbell. *J. Nanosci. Nanotech.*, 10:4015–22, 2010.

[102] G Cao. *Nanostructures and Nanomaterials: Synthesis, Properties & Applications*. Imperial College Press, London, UK, 2004.

[103] W M Haynes, editor. *CRC Handbook of Chemistry and Physics, 91st Edition (Internet Version 2011)*. CRC Press/Taylor and Francis, USA, 2011.

[104] C T Wirth, C Zhang, G Zhong, S Hofmann, and J Robertson. *ACS Nano*, 3:3560–6, 2009.

[105] S Hofmann, G Csányi, A C Ferrari, M C Payne, and J Robertson. *Phys. Rev. Lett.*, 95:036101, 2005.

[106] H Kanzow and A Ding. *Phys. Rev. B*, 60:11180–6, 1999.

[107] S Helveg, C López-Cartes, J Sehested, P L Hansen, B S Clausen, J R Rostrup-Nielsen, F Abild-Pedersen, and J K Nørskov. *Nature*, 427:426–9, 2004.

[108] N Latorre, E Romeo, F Cazaña, T Ubieto, C Royo, J I Villacampa, and A Monzoń. *J. Phys. Chem. C*, 114:4773–82, 2010.

[109] E R Meshot and A J Hart. *Appl. Phys. Lett.*, 92:113107, 2008.

[110] J-H Han, R A Graff, B Welch, C P Marsh, R Franks, and M S Strano. *ACS Nano*, 2:53–60, 2008.

[111] P B Amama, C L Pint, S M Kim, L McJilton, K G Eyink, E A Stach, R H Hauge, and B Maruyama. *ACS Nano*, 4:895–904, 2010.

[112] S M Kim, C L Pint, P B Amama, D N Zakharov, R H Hauge, B Maruyama, and E A Stach. *J. Phys. Chem. Lett.*, 1:918–22, 2010.

[113] S M Kim, C L Pint, P B Amama, R H Hauge, B Maruyama, and E A Stach. *J. Mater. Res.*, 25:1875–85, 2010.

[114] C Singh, M S P Shaffer, and A H Windle. *Carbon*, 41:359–68, 2003.

[115] M Bedewy, E R Meshot, H Guo, E A Verploegen, W Lu, and A J Hart. *J. Phys. Chem. C*, 113:20576–82, 2009.

[116] J Goldstein, D Newbury, D Joy, C Lyman, P Echlin, E Lifshin, L Sawyer, and J Michael. *Scanning Electron Microscopy and X-Ray Microanalysis, 3^{rd} Edition*. Springer, USA, 2003.

[117] F L Pedrotti and L S Pedrotti. *Introduction to Optics, 2^{nd} Edition*. Prentice-Hall, USA, 1993.

[118] L G Cançado, A Jorio, E H Martins Ferreira, F Stavale, C A Achete, R B Capaz, M V O Moutinho, A Lombardo, T S Kulmala, and A C Ferrari. *Nano Lett.*, 11:3190–6, 2011.

[119] H Kataura, Y Kumazawa, Y Maniwa, I Umezu, S Suzuki, Y Ohtsuka, and Y Achiba. *Synthetic Met.*, 103:2555–8, 1999.

[120] M S Dresselhaus, G Dresselhaus, R Saito, and A Jorio. *New J. Phys.*, 5:139.1–.17, 2003.

[121] M S Dresselhaus, G Dresselhaus, R Saito, and A Jorio. *Phys. Rep.*, 409:47–99, 2005.

[122] R Saito, C Fantini, and J Jiang. In A Jorio, G Dresselhaus, and M S Dresselhaus, editors, *Carbon Nanotubes: Advanced Topics in the Synthesis, Structure, Properties and Applications*, pages 251–86. Springer, Germany, 2008.

[123] K Kaminska, J Lefebvre, D G Austing, and P Finnie. *Phys. Rev. B*, 73:235410, 2006.

[124] W H Hung, R Kumar, A Bushmaker, S B Cronin, and M J Bronikowski. *Appl. Phys. Lett.*, 91:093121, 2007.

[125] A Jorio, E Kauppinen, and A Hassanien. In A Jorio, G Dresselhaus, and M S Dresselhaus, editors, *Carbon Nanotubes: Advanced Topics in the Synthesis, Structure, Properties and Applications*, pages 63–100. Springer, Germany, 2008.

[126] H Telg, J G Duque, M Staiger, X Tu, F Hennrich, M M Kappes, M Zheng, J Maultzsch, C Thomsen, and S K Doorn. *ACS Nano*, 6:904–11, 2012.

[127] T C Hirschmann, P T Araujo, H Muramatsu, X Zhang, K Nielsch, Y A Kim, and M S Dresselhaus. *ACS Nano*, 7:2381–7, 2013.

[128] A G Souza Filho, A Jorio, G G Samsonidze, G Dresselhaus, M A Pimenta, M S Dresselhaus, A K Swan, M S Ünlü, B B Goldberg, and R Saito. *Phys. Rev. B*, 67:035427, 2003.

[129] R Pfeiffer, F Simon, H Kuzmany, and V N Popov. *Phys. Rev. B*, 72:161404(R), 2005.

[130] C Fantini, A Jorio, M Souza, M S Strano, M S Dresselhaus, and M A Pimenta. *Phys. Rev. Lett.*, 93:147406, 2004.

[131] J H Parker, Jr., D W Feldman, and M Ashkin. *Phys. Rev.*, 155:712–5, 1967.

[132] R A Serway, C J Moses, and C A Moyer. *Modern Physics, 3^{rd} Edition.* Thomson-Brooks/Cole, USA, 2005.

[133] K D Childs, B A Carlson, L A LaVanier, J F Moulder, D F Paul, W F Stickle, D G Watson, and C L Hedburg. *Handbook of Auger Electron Spectroscopy, 3^{rd} Edition.* Physical Electronics, Inc., USA, 1995.

Chapter 2

Kinetic critical temperature and optimized chemical vapor deposition growth of carbon nanotubes

as published* in *Chemical Physics Letters*, Volume 469, Pages 293–297, 2009.
http://dx.doi.org/10.1016/j.cplett.2008.12.095

This article includes supplementary material. The printable portion of that material is reproduced here in Appendix A. The multimedia portion of that material is available from the University of Ottawa's thesis repository (uO Research) as indicated in the List of videos, as well as the article's publisher's website, which can be accessed using the above hyperlink.

*In accordance with University of Ottawa regulations, the contact email address has been removed from this article.

Foreword

This chapter looks at the chemical vapour deposition growth of vertically aligned carbon nanotube forests using ethanol (CH_3CH_2OH) as the carbon source. In this CVD process, the only active species are ethanol and hydrogen gas (H_2); the only other gas is the carrier gas, argon. The ethanol is obtained by passing the pure Ar/H_2 gas (2% H_2, 98% Ar) through a bubbler. There is also a pathway that allows some of the Ar/H_2 gas to bypass the bubbler, thus allowing the concentration of ethanol to be varied systematically in a straightforward way.

Many other processes capable of producing tall forests use water vapour [1], which adds additional chemical reactions and complexities to modeling and understanding the growth of carbon nanotubes. By examining one of the more simple processes, these factors can be eliminated and the underlying science can be more directly analyzed.

Knowing that ethanol CVD can produce forests [2], though not as tall as forests produced by more complex processes, one asks whether or not the ethanol CVD process can be optimized to provide a similar yield. Here, it was concluded that this is not possible, but in doing so a thorough study of both the growth kinetics and defect density of the forests was undertaken to better understand what is occurring. In particular, a link between the growth kinetics and the defect density (as determined by Raman spectroscopy) in the produced carbon nanotubes is found. This link suggests that a common process affects both of these important parameters. Furthermore, a change in the temperature dependence of the analyzed parameters suggests that more than one growth mechanism exists, with each dominating in a different temperature regime.

Experimentally, this chapter is very important: it is the first use of the *in situ* optical microscope, which required considerable manipulation in order to get the lighting right while attempting to image the extremely black carbon nanotube forests. This optical microscope was used in all subsequent research, usually as the primary means of data acquisition.

Many of the results from this chapter motivated further research and provided direction to subsequent chapters. One particularly interesting and important result is that not only did the kinetic parameters follow an activated temperature dependence, but so did many of the Raman parameters such as the D/G ratio and the number of resonant RBMs, which represent the defect density and density of SWNTs respectively. The fact that these processes are activated also suggests that many of them may also have an origin in a chemical reaction at some stage of CVD growth process. These activated parameters are revisited in Chapter 8 and studied in more detail with acetylene as the

source gas.

---

[1] K Hata, D N Futaba, K Mizuno, T Namai, M Yumura, and S Iijima. *Science*, 306:1362–4, 2004.

[2] S Maruyama, E Einarsson, Y Murakami, and T Edamura. *Chem. Phys. Lett.*, 403:320–3, 2005.

Chemical Physics Letters 469 (2009) 293–297

Contents lists available at ScienceDirect

Chemical Physics Letters

journal homepage: www.elsevier.com/locate/cplett

Kinetic critical temperature and optimized chemical vapor deposition growth of carbon nanotubes

P. Vinten [a,b], J. Lefebvre [a], P. Finnie [a,b,*]

[a] Institute for Microstructural Sciences, National Research Council Canada, Building M-50, 1200 Montreal Road, Ottawa, ON, Canada K1A 0R6
[b] Department of Physics, University of Ottawa, 150 Louis Pasteur, Ottawa, ON, Canada K1N 6N5

ARTICLE INFO

Article history:
Received 18 September 2008
In final form 23 December 2008
Available online 3 January 2009

ABSTRACT

The existence of a critical temperature T_c in the chemical vapor deposition growth of carbon nanotubes, including single-walled nanotubes, is shown by *in situ* optical imaging of growing nanotube forests. At T_c, the temperature dependence of the chemical processes and characteristics of the grown nanotubes change. The lifetime and initial growth rate show this critical temperature and are linked by a characteristic energy through the initial growth rate decay. *Ex situ* Raman spectroscopy shows that the number of radial breathing modes, G band, and D band show the same characteristic energies and T_c.

Crown Copyright © 2009 Published by Elsevier B.V. All rights reserved.

1. Introduction

Chemical vapor deposition (CVD) is a leading approach for the synthesis of carbon nanotubes, with single-walled nanotubes (SWNTs) being routinely synthesized in high yield using many source gases and types of catalyst [1]. Still, the CVD microscopic growth process is only understood in broad terms. The underlying critical physical and chemical steps have yet to be clearly identified. This is a barrier toward rational synthesis of SWNTs. *In situ* studies are promising for improving our understanding of the growth process. Nanotube forests (close packed vertically aligned arrays) are particularly useful for *in situ* studies of growth dynamics [2–8] due to their macroscopic size. Forests have been grown by CVD for over a decade [9,10] and have more recently been grown with large fractions of SWNTs [4,11–13]. Here, we use *in situ* optical imaging of growing forests [5,14,15] to show the existence of a critical point for thermal CVD that is kinetic in origin. The critical point appears in the temperature dependence, at a critical temperature T_c, of the initial growth rate β and the lifetime τ. The initial growth rate and the lifetime are linked by a characteristic energy through the initial growth rate decay β/τ. This suggests that the origin of their scaling is a single molecular process. *Ex situ* Raman spectral properties and the abundance of SWNTs also show this critical point, which provides a link to the kinetic parameters. We attribute the critical point to the optimum feeding of the system with carbon source gas, which has direct consequences on the growth dynamics and properties of the grown nanotubes.

2. Experiment

Nanotubes were grown in a cold wall CVD reactor similar to those described in previous reports [16,17]. Cold wall CVD reactors are well suited to optical monitoring because they allow excellent optical access to the sample [14,17,18]. Samples were $\sim 0.4\ cm^2$ square pieces of 0.5 mm thick Si with 1 μm SiO_2. Catalyst layers, nominally of 250 nm Al_2O_3 and 0.8 nm Co [19], were deposited by e-beam evaporation through a shadow mask to produce a regularly spaced pattern of 0.7 mm diameter circles. Samples were heated to the growth temperature T in pure carrier gas (98% Ar, 2% H_2) flowing at 260 sccm at atmospheric pressure. T was measured with a two color infrared pyrometer. Ethanol vapor was used as the carbon source [20] by diverting the carrier gas through a bubbler and delivering it to the sample through a narrow tube directed down at an angle of $\sim 45°$. When no noticeable growth occurred for an ~5 min interval, the reactor was purged with pure carrier gas for several minutes before allowing it to cool. Forests were grown vertically and imaged *in situ* nearly edge on (~5°) using a long working distance optical microscope and digital camera. Videos were recorded for each growth run (see Supplementary material). Final height H_f was calibrated *ex situ* via scanning electron microscopy (SEM, Hitachi S-4700). SEM observation indicates that most nanotubes in the forest are aligned and reasonably straight, implying that the height of the forests is approximately the length of the individual nanotubes.

Raman spectra were obtained *ex situ* using a commercial confocal Raman system (Jobin Yvon Labram) with a 300 line/mm grating and 50X extra-long working distance microscope objective. We used 785 nm and 1 mW excitation on a spot of ~1 μm in diameter and a confocal hole of 100 μm. At this power density, there was no damage to the forests, however if the power was increased by even less than an order of magnitude, irreversible damage was done to

* Corresponding author. Address: Institute for Microstructural Sciences, National Research Council Canada, Building M-50, 1200 Montreal Road, Ottawa, ON, Canada K1A 0R6.
E-mail address: [REDACTED].

0009-2614/$ - see front matter Crown Copyright © 2009 Published by Elsevier B.V. All rights reserved.
doi:10.1016/j.cplett.2008.12.095

the forests. The total laser exposure was identical for all points with a total of 9 s acquisition composed of three 3 s acquisitions at each data point. We scanned each sample across a 5×5 grid covering a 120 μm × 120 μm area. This was done twice for a total of 50 spectra per sample. The samples were analyzed from the tops of the forests (90° to the substrate), and the laser was linearly polarized parallel to the substrate surface (perpendicular to the average nanotube axis, which was vertical).

3. Results

Several video frames of a growth at 725 °C are shown in Fig. 1a. Fig. 1b shows the height of the forest H as a function of growth time t, extracted from the video with ~2 μm resolution. The line is a fit to the exponential decay model of [3]: $H(t) = \beta\tau(1 - e^{-t/\tau})$. Here, $H_f = H|_{t\to\infty} = \beta\tau$. The second time derivative (the time derivative of the growth rate) has β/τ as the exponential prefactor. In [3], this functional form of $H(t)$ was used for water assisted ethylene CVD. The same functional form has also been used to explain optical absorption data for ethanol CVD [7]. A low magnification SEM image, similar to those used to calibrate H_f, is shown in Fig. 1c. This model provided a good fit at all T. As verification, all of the height data was collapsed onto a single curve of normalized height vs normalized time (Fig. 1d) by dividing H by H_f and t by τ. For a perfect fit, all data would collapse on the red curve. All of our data is close to this single curve and we therefore conclude that the fit is indeed universal to a good approximation.

Fig. 2a shows a plot of H_f vs $1/k_BT$ where k_B is Boltzmann's constant. Forest heights of ~125 μm were typical for 675 °C < T < 870 °C. Below 675 °C, H_f dropped off rapidly. Above 870 °C, H_f decreases with increasing T, with a characteristic energy of -2.3 ± 0.3 eV. Note that the characteristic energy has a sign opposite to that of the slope. If a dataset Y fits a straight line on a ln Y vs $1/k_BT$ plot, we define the characteristic energy as the negative of the slope. Then, if the dataset Y is a reaction rate, the characteristic energy is positive and has the meaning of activation energy.

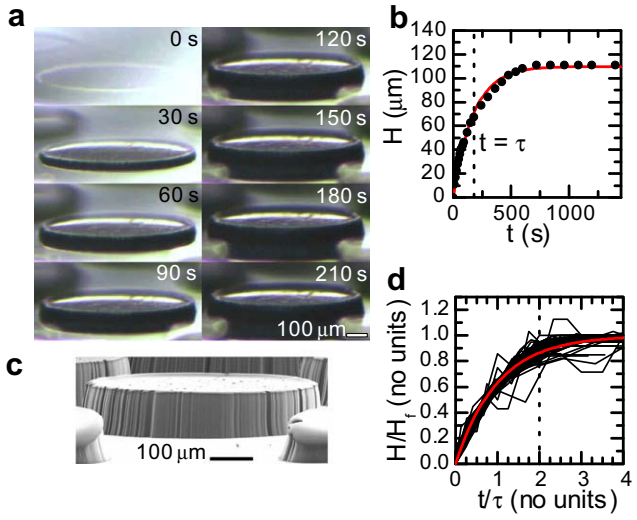


Fig. 1. (a) Video frames from a growth at 725 °C (see Supplementary material). Angle of inclination is ~ 5°. (b) Height H as a function of growth time t (points) and exponential decay fit (line). (c) Low magnification *ex situ* SEM image of the same forest at a similar angle. (d) In a plot of normalized height H/H_f vs normalized time t/τ, all data collapsed onto a single curve (red). The red line is the ideal situation, where $H_f = \tau = 1$. (For interpretation of the references to colour in this figure legend, the reader is referred to the web version of this article.)

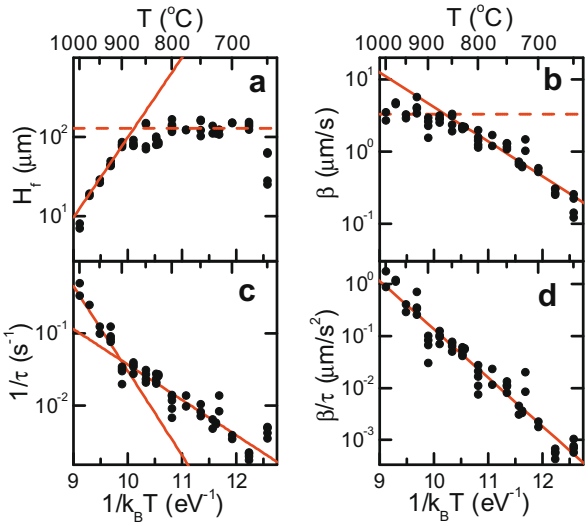


Fig. 2. Plots of kinetic parameters vs $1/k_BT$. (a) Final height H_f; (b) initial growth rate β; (c) inverse lifetime $1/\tau$; and (d) initial growth rate decay β/τ. All show the same functional form with characteristic energies. (a–c) show critical point. Solid lines are linear fits, dashed lines are to guide the eye.

Plots of β vs $1/k_BT$ and $1/\tau$ vs $1/k_BT$ (Fig. 2b and c, respectively) reveal simple linear scaling of both parameters, but with a change in slope at $T_c \approx 870$ °C. These two parameters are rates: the nanotube growth rate and the catalyst decay rate, respectively. It is reasonable to assume that these rates correspond to the rates of specific chemical steps. These plots are then Arrhenius plots and the characteristic energy has the meaning of activation energy. Above T_c, β is approximately constant at 3.3 ± 1.0 μm/s, and is therefore not limited by T. Below T_c, β is activated at 1.1 ± 0.1 eV, similar to previous reports for thermal CVD with other catalysts and source gases [6,7,21–24]. The lifetime τ also shows a change in temperature dependence at $T_c \approx 870$ °C. Above T_c, $1/\tau$ shows an activation energy of 2.4 ± 0.2 eV, a similar order of magnitude for iron catalyst and ethylene source gas [25]. Below T_c, $1/\tau$ shows an activation energy of 1.2 ± 0.1 eV, the same value within error as β (as expected the activation energies of β are simply the sums of the energies in H_f and $1/\tau$). Ref. [7] reported an activated β at the optimum pressure (we use a constant pressure), but observed a constant τ. This activated β is likely another manifestation of the critical point. The fact that β and τ have the same activation energy below T_c suggests that they are directly and causally linked by the same molecular process. This is the rate limiting step of the growth process, which may be, for example, the chemical decomposition of ethanol.

Further evidence for a single molecular process comes from a plot of the ratio β/τ vs $1/k_BT$ (Fig. 2d). This parameter β/τ represents the rate of the process that causes the growth to slow down exponentially. β/τ shows a characteristic energy of 2.4 ± 0.2 eV over the entire temperature range, with no evidence of a critical temperature. As expected, this energy is the sum of the activation energies of β and $1/\tau$, but importantly β/τ shows only one characteristic energy across the entire temperature range, which suggests it originates in a single molecular process. At high T, both τ and β/τ show, within error, the same high characteristic energy. This energy then represents a process that competes with growth and only occurs alongside growth. It acts at all T but only dominates above T_c. Interestingly, this energy is the same, within error, to the activation energy for defect diffusion, which has recently been determined to be ~2.2 eV [26]. We speculate that defect diffusion to the growth front is a possible explanation for the growth termination and the observed values of τ. Alternatively, others have

attributed the activation energy of τ to catalyst deactivation via interaction with the catalyst support [25].

Elementary considerations provide some insight into these characteristic energies. Kinetic limits can arise from processes at the single nanotube level or from the collective effects of many nanotubes. A collective process of interest is the degree to which diffusion through the forest limits growth [5,27–30]. Here, τ decreases even as H_f decreases (at high T), contrary to expectations if diffusion through the forest is important. Also, our forests have edges, so extreme edge effects would be expected if diffusion through the forest was important. However, these forests are relatively uniform in height. Therefore, growth limitations due to diffusion through the forest are neglected and we turn our attention to effects at the single nanotube level.

For a single nanotube, β can be estimated if we assume ethanol molecules behave like an ideal gas and are carried at equilibrium (partial pressure $P \approx 6$ kPa at room temperature) with the carrier gas to the reaction site. The molecular impingement rate on a nanoparticle of ~1–2 nm diameter is ~ 4–20×10^8 s^{-1} (using flux $F = P(2\pi m k_B T)^{-1/2}$ where m is the mass). For a ~1–2 nm diameter SWNT, with carbon surface density $\sim 4 \times 10^{19}$ m^{-2}, this corresponds to $\beta \sim 1$–16 mm/s, much higher than observed. If there is an energy barrier to growth $E = 1.1$ eV that scales the impingement rate by a factor e^{-E/k_BT}, then (using $T = T_c$) $\beta \sim 0.015$–0.22 μm/s, a similar order of magnitude to the observed value. Conversely, considering the observed value of 3.3 μm/s at T_c, this impingement rate would correspond to an energy barrier of ~0.6–0.8 eV which is close to the observed value.

Raman spectroscopy provides further insight into the growth kinetics. Raw spectra in the SWNT radial breathing mode (RBM) region ($\omega \leqslant 300$ cm^{-1}) and D and G band regions are shown in Fig. 3a for several T. For all spectra (except 600 °C, which was not a vertically aligned forest but rather had only surface tubes) the focal depth of the laser was entirely within the forest because the Si peak around 500 cm^{-1} was completely absent from the spectra. The focal depth is therefore less than ~10 μm, the shortest forest analyzed (1000 °C).

Fig. 3b shows the D/G integrated intensity ratio I_D/I_G vs $1/k_BT$. This is a common measure of the quality of the sample. I_D/I_G as a function of T reaches a minimum, consistent with previous reports [6,27,31–33]. We identify this minimum at T_c and the characteristic energy gives it new meaning. I_D/I_G decreases with T with a characteristic energy of -1.1 ± 0.1 eV below T_c. Above T_c it increases with a characteristic energy of 1.1 ± 0.1 eV, the same value. The temperature dependence of I_D/I_G therefore contains information beyond sample quality. Very recently, *in situ* Raman spectral data with the $\ln(I_D/I_G) \propto 1/k_BT$ functional form and characteristic energy has been presented and from it, an activated and critical β and τ were inferred [24]. The energy of 1.1 eV characterizes the limiting step in this chemical process as an activation energy in the Arrhenius plot of β, but also manifests itself in I_D/I_G. This suggests that the generation of non-sp^2 bonds, such as the build-up of amorphous carbon, vacancies, or other defects, is linked to the growth process. At T_c, we speculate that there is optimum feeding of carbon source gas and that any deviation from T_c will produce more defects, thus increase I_D/I_G.

The average number of RBMs per spot N (here we used 50 Raman spectra) is statistically meaningful and we find that it is a good metric for comparing samples [34]. Since the spot size is ~1 μm, N is effectively the surface density of resonant SWNTs (i.e.: SWNTs/μm^2). Forests of nanotubes are not especially dense, typically consisting of small bundles of several tubes spaced by, on the order of, 100 nm. A 1 μm diameter spot would then see on the order of 1000 nanotubes. Our samples have wide chirality and diameter distributions, and are not intentionally enriched in any particular species of nanotube. As a result, only a small fraction of SWNTs are resonant with any given excitation wavelength. Typically, we observe small numbers (usually 5 or less) of RBMs in the spectra and the number varies from spot to spot. While this is not a rigorous measurement of the fraction, density, or number of SWNTs, it is a measure of the number of SWNTs that are resonant with the excitation wavelength. (Histograms of the observed peaks are available in the Supplementary material.) We find that this resonant RBM density is an excellent metric for comparing samples.

The RBM results (plotted vs $1/k_BT$ Fig. 4a) are consistent with [33] in that more RBMs are observed around 850 °C than at lower T. For all $T > 700$ °C RBMs were detected, with N peaking at ~5 near T_c. At all T, RBMs were widely distributed in the range 180–230 cm^{-1} (corresponding to diameters 1.1–1.4 nm where ω [cm^{-1}] = 248/d [nm] [35]). However, above T_c one narrow diameter (~1 nm) mode at 260 cm^{-1} was regularly detected. Surprisingly, N showed characteristic energies (-0.55 ± 0.1 eV and 2.2 ± 0.4 eV above and below T_c, respectively) peaking near T_c. This implies that N is directly connected to the chemical kinetics of nanotube growth. The physical origin of this connection is still unclear.

The G band intensity I_G, which represents the amount of carbon in graphitic form, (plotted vs $1/k_BT$ in Fig. 4b) increased significantly with T with a characteristic energy of 1.5 ± 0.3 eV below

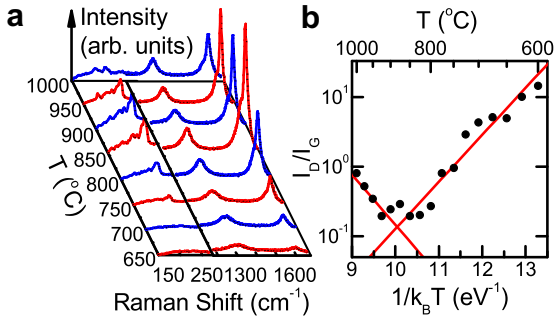


Fig. 3. (a) Raman spectra in RBM and D/G regions for various growth temperatures T. (b) Plot of D/G ratio I_D/I_G vs $1/k_BT$. Solid lines are linear fits.

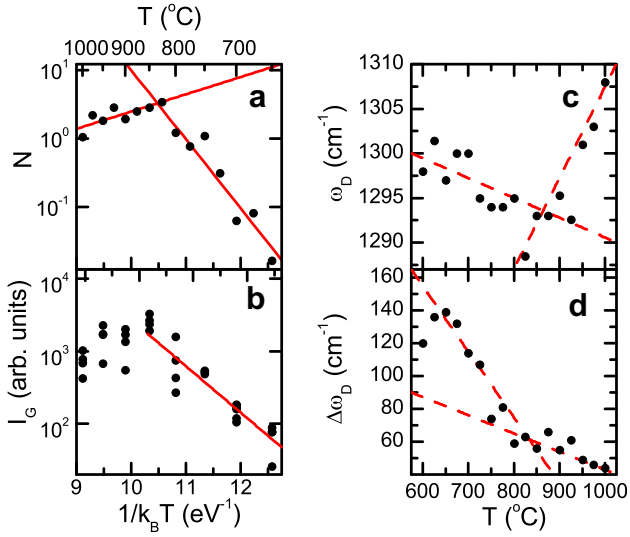


Fig. 4. Plots (vs $1/k_BT$) of (a) average number of RBMs per spot N and (b) G band integrated intensity I_G. (c) Center of D band ω_D and (d) width (FWHM) of D band $\Delta\omega_D$ determined by Lorentzian fits as a function of T. (a) and (b) show characteristic energies. All show critical temperature. Solid lines are linear fits, dashed lines are to guide the eye.

T_c, peaking near T_c before decreasing again. There is too much scatter in the data to determine if there is a characteristic energy above T_c. The D band intensity remained relatively uniform, but it showed more subtle variations in other features.

Fig. 4c shows that the position of the D band ω_D (as a function of T), as determined by Lorentzian fits [36], first decreases and then increases rapidly above T_c. Shifts in ω_D have been attributed to a change in the nanotube diameter [36,37]. For a collection of nanotubes, ω_D is related to the average nanotube diameter [36]. Changes in nanotube diameter have in turn been linked to changes in T [38] and source gas concentration [39].

Fig. 4d shows that the full width at half maximum (FWHM) of the D band $\Delta\omega_D$ (as a function of T) decreases rapidly until T_c, above which it decreases more slowly. We note that while the $\Delta\omega_D$ decreases, I_D/I_G and ω_D increase. This is a more complicated evolution than the overly simple view that more defects leads to a broader, higher D band peak. It is possible that above T_c, a narrower, higher D band corresponds to more of one specific kind of defect.

Below T_c, nanotube growth is slow and the supply of carbon is likely more than sufficient. We speculate that defects may be generated due to overfeeding at low T. Our data (specifically the 1.1 eV activation energy barrier to growth) appears consistent with poor transport of carbon, a commonly proposed limiting mechanism [6,22,23,28,40–42]. As T rises to T_c, β increases more than tenfold and we speculate that the supply of carbon may become insufficient to sustain such high growth rates [43] and defects are increasingly produced as T rises. At T_c, defects are minimized and, in this sense, the growth is optimized. We suppose that the system is then also optimally fed.

We made a preliminary investigation of the effect of feeding by diluting the ethanol/carrier gas mixture and performing *ex situ* Raman spectroscopy of the D and G bands on the resultant forests using a custom built Raman imaging system (described in detail in Ref. [44]) and 532 nm excitation. Below T_c, diluting the ethanol reduced I_D/I_G, consistent with [33]. When diluted to 10% of the initial concentration at 750 °C, I_D/I_G fell from ~1.1 to ~0.4. We conclude that below T_c the system is strongly overfed, consistent with the kinetic data. Above T_c, diluting the ethanol still reduced I_D/I_G, but only marginally (from ~0.3 to ~0.2 at 950 °C). This is contrary to the underfeeding suggested by the slight increase in I_D/I_G with T and decrease in N with T. The slight increase in I_D/I_G with concentration allows us to conclude only that the system is less sensitive to feeding at high T.

4. Conclusion

In summary, there are several important findings: (1) β plateaus above a critical temperature T_c. (2) τ shows the same critical temperature and is connected to β. (3) The D/G ratio also shows the same critical temperature and is also connected to β. (4) Other Raman features show the same critical temperature. (5) β, τ, β/τ, I_D/I_G and N all have the same functional form ($\ln Y \propto 1/k_B T$) where the constant of proportionality is some characteristic energy that was measured for each quantity. For β and τ, these energies may be interpreted as activation energies for some chemical process. (6) Here, we rule out diffusion through the forest as a limiting factor of the growth rate. Future models should provide a detailed explanation of the growth kinetics, the critical point, the Raman spectral features, and the connections between them.

The value of *in situ* measurements of carbon nanotube growth kinetics is clear. Furthermore, a wealth of data about the growth kinetics is imprinted on *ex situ* Raman spectral features. We expect similar experiments in the near future to yield even greater insights and play an important role in developing more complete models of nanotube synthesis.

Acknowledgements

We are grateful for preliminary work by J. Bond, assistance with the Raman system by L. Tay, the continuing support of P. Marshall, and the assistance of H. Tran, P. Chow-Chong, M. Denhoff, K. Kaminska, J. Fraser, and D.G. Austing. P.V. was supported by OGS, NSERC, and NRC-GSSSP. P.V. and P.F. were supported by an NSERC Discovery Grant. P.F. is grateful for the support of JST-CREST.

Appendix A. Supplementary material

Supplementary data associated with this article can be found, in the online version, at doi:10.1016/j.cplett.2008.12.095.

References

[1] E. Joselevich, H. Dai, J. Liu, K. Hata, A.H. Windle, in: A. Jorio, G. Dresselhaus, M.S. Dresselhaus (Eds.), Ch. Carbon Nanotube Synthesis and Organization, Topics in Applied Physics, vol. 111, Springer-Verlag, 2008, p. 101.
[2] G. Eres, A.A. Puretzky, D.B. Geohegan, H. Cui, Appl. Phys. Lett. 84 (2004) 1759.
[3] D.N. Futaba, K. Hata, T. Yamada, K. Mizuno, M. Yumura, S. Iijima, Phys. Rev. Lett. 95 (2005) 056104.
[4] A.A. Puretzky, D.B. Geohegan, S. Jesse, I.N. Ivanov, G. Eres, Appl. Phys. A 81 (2005) 223.
[5] A.A. Puretzky, G. Eres, C.M. Rouleau, I.N. Ivanov, D.B. Geohegan, Nanotechnology 19 (2008) 055605.
[6] S.K. Pal et al., Nanotechnology 19 (2008) 045610.
[7] E. Einarsson, Y. Murakami, M. Kadowaki, S. Maruyama, Carbon 46 (2008) 923.
[8] E. Einarsson et al., J. Nanosci. Nanotech. 8 (2008) 6093.
[9] Z.F. Ren, Z.P. Huang, J.W. Xu, J.H. Wang, P. Bush, M.P. Siegal, P.N. Provencio, Science 282 (1998) 1105.
[10] S. Fan, M.G. Chapline, N.R. Franklin, T.W. Tombler, A.M. Cassell, H. Dai, Science 283 (1999) 512.
[11] Y. Murakami, S. Chiashi, Y. Miyauchi, M. Hu, M. Ogura, T. Okubo, S. Maruyama, Chem. Phys. Lett. 385 (2004) 298.
[12] K. Hata, D.N. Futaba, K. Mizuno, T. Namai, M. Yumura, S. Iijima, Science 306 (2004) 1362.
[13] G.F. Zhong, T. Iwasaki, K. Honda, Y. Furukawa, I. Ohdomari, H. Kawarada, Chem. Vap. Dep. 11 (2005) 127.
[14] K. Kaminska, J. Lefebvre, D.G. Austing, P. Finnie, Nanotechnology 18 (2007) 65707.
[15] I. Gunjishima, T. Inoue, A. Okamoto, Appl. Phys. Lett. 91 (2007) 193102.
[16] P. Finnie, J. Bardwell, I. Tsandev, M. Tomlinson, M. Beaulieu, J. Fraser, J. Lefebvre, J. Vac. Sci. Technol. 22 (2004) 747.
[17] P. Finnie, A. Li-Pook-Than, J. Lefebvre, D.G. Austing, Carbon 44 (2006) 3199.
[18] S. Chiashi, Y. Murakami, Y. Miyauchi, S. Maruyama, Chem. Phys. Lett. 386 (2004) 89.
[19] J. Kong, A.M. Cassell, H. Dai, Chem. Phys. Lett. 292 (1998) 567.
[20] S. Maruyama, R. Kojima, Y. Miyauchi, S. Chiashi, M. Kohno, Chem. Phys. Lett. 360 (2002) 229.
[21] C. Ducati, I. Alexandrou, M. Chhowalla, G.A.J. Amaratunga, J. Robertson, J. Appl. Phys. 92 (2002) 3299.
[22] Y.T. Lee, N.S. Kim, J. Park, J.B. Han, Y.S. Choi, H. Ryu, H.J. Lee, Chem. Phys. Lett. 372 (2003) 853.
[23] K.-E. Kim, K.-J. Kim, W.S. Jung, S.Y. Bae, J. Park, J. Choi, J. Choo, Chem. Phys. Lett. 401 (2005) 459.
[24] M. Picher, V. Jourdain, E. Anglaret, Growth regimes of CCVD-grown SWCNTs determined by in situ Raman spectroscopy, poster B 85, Ninth International Conference on the Science and Applications of Nanotubes, NT08 (2008).
[25] M.J. Bronikowski, J. Phys. Chem. C 111 (2007) 17705.
[26] S. Iijima, private communication (May 2008).
[27] C. Singh, M.S.P. Shaffer, A.H. Windle, Carbon 41 (2003) 359.
[28] O.A. Louchev, T. Laude, Y. Sato, H. Kanda, J. Chem. Phys. 118 (2003) 7622.
[29] G. Zhong, T. Iwasaki, J. Robertson, H. Kawarada, J. Phys. Chem. B 111 (2007) 1907.
[30] R. Xiang et al., J. Phys. Chem. C 112 (2008) 4892.
[31] H. Cui, G. Eres, J.Y. Howe, A. Puretzky, M. Varela, D.B. Geohegan, D.H. Lowndes, Chem. Phys. Lett. 374 (2003) 222.
[32] G. Eres, A.A. Kinkhabwala, H. Cui, D.B. Geohegan, A.A. Puretzky, D.H. Lowndes, J. Phys. Chem. B 109 (2005) 16684.
[33] H.E. Unalan, M. Chhowalla, Nanotechnology 16 (2005) 2153.
[34] J. Bond, J. Lefebvre, D.G. Austing, L. Tay, P. Finnie, Nanotechnology 18 (2007) 135603.
[35] A. Jorio et al., Phys. Rev. Lett. 86 (2001) 1118.
[36] A. Jorio, M.A. Pimenta, A.G. Souza Filho, R. Saito, G. Dresselhaus, M.S. Dresselhaus, New J. Phys. 5 (2003) 139.
[37] A.G. Souza Filho et al., Phys. Rev. B 67 (2003) 035427.

[38] Y. Yao, Q. Li, J. Zhang, R. Liu, L. Jiao, Y.T. Zhu, Z. Liu, Nat. Mater. 6 (2007) 283.
[39] C. Lu, J. Liu, J. Phys. Chem. B 110 (2006) 20254.
[40] S. Helveg et al., Nature 427 (2004) 426.
[41] S. Hofmann, G. Csányi, A.C. Ferrari, M.C. Payne, J. Robertson, Phys. Rev. Lett. 95 (2005) 036101.
[42] H. Kanzow, A. Schmalz, A. Ding, Chem. Phys. Lett. 295 (1998) 525.
[43] L. Ci et al., Chem. Phys. Lett. 349 (2001) 191.
[44] K. Kaminska, J. Lefebvre, D.G. Austing, P. Finnie, Phys. Rev. B 73 (2006) 235410.

Chapter 3

Distinct termination morphologies for vertically aligned carbon nanotube forests

as published* in *Nanotechnology*, Volume 21, Article 035603 (7 Pages), 2010.
http://dx.doi.org/10.1088/0957-4484/21/3/035603

Copyright notice: ©2010 IOP Publishing Ltd.

This article includes supplementary material. The printable portion of that material is reprinted here in Appendix B. The multimedia portion of that material is available from the University of Ottawa's thesis repository (uO Research) as indicated in the List of videos, as well as the article's publisher's website, which can be accessed using the above hyperlink.

*In accordance with University of Ottawa regulations, the contact email address has been removed from this article.

Foreword

Having concluded in Chapter 2 that ethanol was not able to produce forests with heights beyond the 100 μm scale, it was necessary to determine if this was due to using ethanol as a source gas or the general growth process that was being implemented. This chapter is a study of acetylene (C_2H_2) CVD, which has been shown to be one of the most efficient carbon sources for nanotube growth [1]. Furthermore, using water vapour during growth was shown to dramatically increase the heights attainable by the forests for CVD growth with ethylene, a hydrocarbon very similar to acetylene [2]. The general idea is that the water vapour fulfills the same etching function as the hydroxyl (OH) group in ethanol, while the acetylene fulfills the function of growth. This decouples the two parameters, but simultaneously introduces another control parameter, thus potentially increasing the complexity.

This chapter explores acetylene as a carbon source. Not only does acetylene produce much taller forests, but several interesting morphological features, that were not seen in the short ethanol grown forests, presented themselves and warranted further study. Additionally, the simple smooth kinetics observed in Chapter 2 were replaced by a two stage growth curve that has an exponential curve as well as an abrupt termination that cuts short the smooth exponentially decaying curve [3]. By thoroughly studying the various morphologies of the forests, it is possible to correlate them to interactions between individual nanotubes in the forest and the resulting energies (adhesion, cohesion, and strain, as discussed in Chapter 1), which is a recurring theme for much of the rest of the research in this thesis.

This chapter proposes that the interactions between nanotubes in a forest may contribute to how a forest grows and, importantly, may help explain why a forest stops growing. A forest is not simply a set of independently growing nanotubes, but is instead a complex structure where the constituent nanotubes do affect one another. The two stage growth curve shows that more than one termination mechanism is involved; this is discussed in this chapter and becomes a recurring theme in subsequent chapters.

As in the previous chapter, this chapter also shows that the kinetic parameters and D/G ratio follow an activated temperature dependence, despite the change in carbon source. This observation suggests that the temperature dependence of these parameters is independent of the carbon source and in fact fundamental to the growth of carbon nanotubes. These observations are discussed in more detail in Chapter 8.

Experimentally, this chapter is the basis for the acetylene CVD that is used throughout the remainder of this thesis, though many further improvements and refinements are

made along the way.

---

[1] G Eres, A A Kinkhabwala, H Cui, D B Geohegan, A A Puretzky, and D H Lowndes. *J. Phys. Chem. B*, 109:16684–94, 2005.

[2] K Hata, D N Futaba, K Mizuno, T Namai, M Yumura, and S Iijima. *Science*, 306:1362–4, 2004.

[3] E R Meshot and A J Hart. *Appl. Phys. Lett.*, 92:113107, 2008.

Nanotechnology **21** (2010) 035603 (7pp) doi:10.1088/0957-4484/21/3/035603

Distinct termination morphologies for vertically aligned carbon nanotube forests

P Vinten[1,2], P Marshall[1], J Lefebvre[1] and P Finnie[1,2]

[1] Institute for Microstructural Sciences, National Research Council Canada, Building M-50, 1200 Montreal Road, Ottawa, ON, K1A 0R6, Canada
[2] Department of Physics, University of Ottawa, 150 Louis Pasteur, Ottawa, ON, K1N 6N5, Canada

E-mail: [REDACTED]

Received 12 August 2009, in final form 13 November 2009
Published 7 December 2009
Online at stacks.iop.org/Nano/21/035603

Abstract
Vertically aligned carbon nanotube forests, including single-walled nanotubes, are imaged optically as they grow *in situ* from cobalt/alumina catalyst using water-assisted acetylene chemical vapor deposition. Three distinct termination morphologies are identified and investigated optically and via scanning electron microscopy. Quantitative growth dynamics are extracted and show gradual deceleration and sudden termination of growth. The termination morphology is discussed in terms of the balance of forces within the forest. We speculate that sudden termination is a collective effect arising from an imbalance in these forces.

S Supplementary data are available from stacks.iop.org/Nano/21/035603/mmedia

(Some figures in this article are in colour only in the electronic version)

1. Introduction

Initially, single-walled carbon nanotube (SWNT) yields were low, but in recent years growth via chemical vapor deposition (CVD) has advanced in terms of choice of catalyst and support, the use of more reactive carbon sources such as acetylene [1–4] and the use of an enhancer such as water vapor [5]. Millimeter tall forests of SWNTs and/or MWNTs (multi-walled carbon nanotubes) are now regularly synthesized [1, 3, 5–17] and research has shifted focus from how nanotube growth is initiated to the increasingly important question of how nanotube growth terminates [15, 18, 19]. Several reports demonstrate that nanotube forests grow at an initially rapid rate which drops off either gradually [7, 20, 21] or suddenly [15, 22, 23]. Because nanotube forests are attached to a substrate and grown in such abundance, process monitoring can be as simple as making *in situ* videos of forest growth [4, 21, 22, 24, 25]. Due to the large number of nanotubes in close proximity within forests, mechanical stresses induced by interactions between nanotubes are very important factors contributing to their growth [10, 18, 24, 26].

Here, we report the temperature dependence of the growth dynamics of nanotube forests obtained from *in situ* video monitoring of forests growing from ∼mm diameter thin film catalyst islands. We find that forest termination is strongly temperature-dependent and that there are three morphologically distinct modes of forest termination. Rather than sudden termination just being a consequence of catalyst poisoning, we speculate that, for tall forests, termination is a collective effect caused by the buildup of strain on individual nanotubes and the balance between this strain and the forces present in the forest that keep the nanotubes attached to the substrate and to one another.

2. Experimental procedures

Forests were grown in a cold-walled CVD reactor (which provides excellent optical access to the sample [27–30]) operated at atmospheric pressure as described previously [21], with additional details given in other references [27, 28]. Forests were imaged *in situ* through a large glass window using a long focal length optical microscope and camera at an ∼5° glancing angle to the substrate.

The substrates were ∼0.4 cm^2 square pieces of 0.5 mm thick Si with 1 μm thermal SiO_2. Layers of nominally 250 nm Al_2O_3 and 0.8 nm Co were deposited by e-beam evaporation through a shadow mask to produce catalyst islands. For dynamics studies, masks with 700 μm diameter circles in a tightly packed hexagonal configuration were used. For

 © 2010 IOP Publishing Ltd Printed in the UK

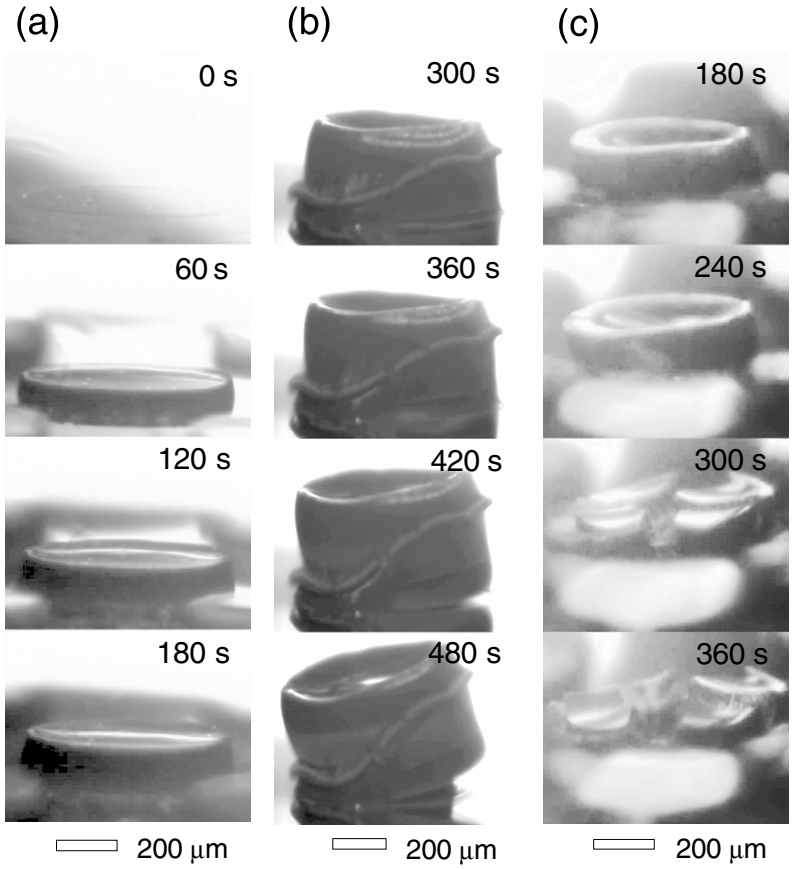


Figure 1. Frames from *in situ* videos (changed to black and white and contrast-enhanced) showing forests growing and terminating by: (a) stopping uniformly at 900 °C, (b) delaminating at 730 °C and (c) cracking at 720 °C. Original videos provided as supplementary material (available at stacks.iop.org/Nano/21/035603/mmedia).

follow-up qualitative studies, we used a lower density pattern consisting of 800 μm diameter circles and a tightly packed pattern consisting of 100 μm diameter circles. Here, the carbon source was acetylene (C_2H_2) [2] and the growth was assisted by water vapor [5], supplied by passing pure Ar through a bubbler.

Prior to growth the reactor was purged with pure Ar flowing at 2 l min^{-1} for 10 min. Samples were heated to the growth temperature T (measured with a two-color infrared pyrometer) in Ar/H_2 (98%/2%, 260 sccm). Water was then introduced at 60 sccm for 5 min, keeping the total gas flow rate at 260 sccm. Dilute acetylene (Ar/C_2H_2, 99.9%/0.1%) was then introduced at 180 sccm to initiate growth, while turning the Ar/H_2 and Ar/H_2O down to 60 and 20 sccm, respectively. After the growth was determined to have halted, the chamber was purged with pure Ar and the sample was cooled for 5 min. Because the process and its end state are highly temperature-dependent, a series of otherwise identical samples were grown over a large range of temperatures; more than one sample was grown at some temperatures. After growth, forest morphologies were examined in detail by scanning electron microscopy (SEM). Raman spectra were acquired: acquisition parameters, spectra and derived quantities are provided as supplementary material (figure S1, available at stacks.iop.org/Nano/21/035603/mmedia). D to G ratios decreased with T and the average number of radial breathing modes (RBMs) [21, 31] increased with T from none at ~700 °C to abundant at ~850 °C. Intense RBMs provide strong evidence for the presence of SWNTs, but do not exclude the possibility that MWNTs are also present in our forests. These Raman results are consistent with our previous report using ethanol as a carbon source [21].

3. Results and discussion

Frames from three different *in situ* videos are shown in figure 1. For clarity, the contrast has been enhanced and the images have been converted from color to black and white. The original color videos are provided as supplementary material (videos S1, S2, and S3 respectively available at stacks.iop.org/Nano/21/035603/mmedia). Figure 1(a) shows a high temperature growth (900 °C) from an initial circular catalyst island at time $t = 0$ s to a final forest at $t = 180$ s. Generally, at these higher temperatures, the terminal forest height H_t was relatively small. Forests simply grew at a gradually decreasing rate until stopping rather abruptly

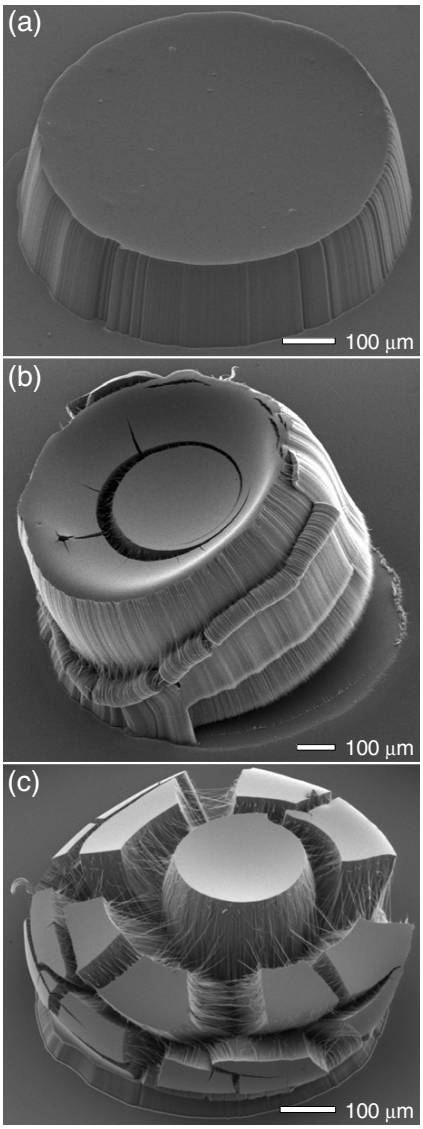


Figure 2. Post-growth SEM images taken at a ∼45° angle: (a) uniformly terminated forest, (b) delaminated forest and (c) cracked forest. (a) and (b) are the same forests as in figure 1.

at H_t. There was no abrupt change in the appearance of the forest, and we classify this appearance as the first termination morphology: uniform. Upon termination, these forests have a relatively flat top surface and smooth sidewalls. At slightly lower temperatures, forests grew taller, but still grew relatively uneventfully. The uniform termination morphology was observed for all temperatures above ∼760 °C, which reached heights up to 500 μm. An SEM image of this forest is shown in figure 2(a).

At lower temperatures (730 °C $<$ T $<$ 760 °C) the termination was very different. Figure 1(b) shows the second major termination morphology: delamination. As the forest (T = 730 °C) neared termination, the bottom of the forest peeled off the substrate. Up until t = 300 s the forest looks similar to the uniform forest of figure 1(a). Post-growth delamination of forests has been reported to occur readily with simple processing [32, 33], including the use of water [32]. Excessive water vapor exposure during growth has also been observed to cause delamination [14]. It has also been noted that forests tend to fall off the substrate easily [14], which is often the case here. Delamination of continuous films during growth has been previously reported [10]. We have occasionally seen forests completely delaminate. However, as shown here, the forest has only partially delaminated and terminates with some nanotubes still connected to the substrate. This is clearly visible at t = 480 s, for example. An SEM image of this forest is shown in figure 2(b). The local delamination process appears to happen at or close to the time at which the entire forest stops growing. Other than delaminating, the forests are generally intact and have hardly changed otherwise.

Many samples show re-growth on the catalyst layer beneath the delaminated forest, but we have only ever observed a re-growth of a very short forest after delamination. More often, the remaining catalyst appears to be inactive or nearly so. Occasionally, only the outer nanotubes delaminate (partial delamination), which causes the base of the growing forest to narrow. On crowded samples, where it is difficult to see the base of the forest, we can sometimes infer that a delamination event has occurred because the top of the forest will appear to suddenly tilt just before termination, as seen in the delamination event presented here (see supplementary material video S2 available at stacks.iop.org/Nano/21/035603/mmedia). Follow-up SEM observation of tilted forests confirms that many of the tilting forests had indeed delaminated. Unpatterned (uniform catalyst) substrates sometimes show even more dramatic delamination effects, such as a forest grown on an unpatterned sample completely curling up onto itself (see supplementary material video S4 available at stacks.iop.org/Nano/21/035603/mmedia).

Figure 1(c) shows the third termination morphology: cracking. Cracking of continuous nanotube forests has been previously observed by *in situ* optical imaging [24]. Here, up until t = 180 s the forest, grown at T = 720 °C, looks similar to the uniform forest of figure 1(a). This forest then suddenly splits into five wedge-shaped pieces which gradually bend outwards. Cracking occurs close to or at growth termination. These circular forests show remarkably symmetrical cracking patterns which can be threefold, fourfold, fivefold, and higher N-fold; even circular cracking sometimes occurs. Cracking occurs at the lowest temperatures T $<$ 730 °C, although some samples show cracking and delamination simultaneously. There appears to be no abrupt transition between the two. It is notable that the cracked forests remain attached to the substrate.

Scanning electron microscope images (figure 2) show greater detail. Uniform forests, such as the example in figure 2(a), have relatively flat top surfaces and smooth sidewalls. Delaminated forests, such as the example in figure 2(b), often show small cracks on the top surface, in addition to delamination. Overall, the top surface appears smooth, but concave. In figure 2(b), a small fraction of the nanotubes remain attached to the substrate on the left-hand side. The outer edge of the forest has also peeled away from

the bulk of the forest. This peeling started quite early, as can be seen from video S2 in the supplementary material (available at stacks.iop.org/Nano/21/035603/mmedia). We often observe such peeling effects. Figure 2(c) shows an SEM image of a cracked forest, grown at $T = 720\,^{\circ}\mathrm{C}$. This forest remains attached to the substrate. Many nanotubes can be seen bridging the cracks between the intact portions of the forest.

More insight into the morphological data can be obtained from the dynamical evolution of the forest height, which was extracted from the *in situ* videos. Figure 3(a) shows the height of the forest H versus growth time t (circles), as sampled at 10 s intervals from the video in figure 1(a). From the start of forest growth to the sudden termination point, an excellent fit is obtained for an exponentially decaying initial growth rate that is consistent with a proposed growth equation [7]: $H(t) = \beta\tau(1 - \mathrm{e}^{-t/\tau})$, where β is the initial growth rate and τ is the characteristic time. However, the growth suddenly stops at a terminal height H_t (indicated by a horizontal line) as previously reported from *in situ* observations [15, 22] and inferred from *ex situ* data [11, 19].

This general form is valid over the entire range of temperatures analyzed (figure 3(b)). Several growth temperatures are indicated by arrows pointing at the terminal height. Complete terminal height H_t versus temperature T information can be found in figure 4(a). Cracked forests (red dashed lines) do not show sudden termination in figure 3(b) because, once cracking began, it was too difficult to track the height of the forest quantitatively. Sudden termination was observed at a terminal time τ_t soon after cracking began. The difference between linear and exponential growth prior to sudden termination is rather small [15] and can easily be missed if sampling rates are too low. The slow growth rate decay, which, at least in the absence of water vapor, is thought to arise from carbon coatings that render seed nanoparticles inactive [34]. The sudden termination suggests that the terminal height H_t likely originates from a different mechanism.

The temperature dependence of the extracted kinetic parameters is shown in figure 4. The solid black circles in figure 4(a) show the observed terminal height of the forest H_t versus inverse temperature $1/k_\mathrm{B}T$, where k_B is Boltzmann's constant. The terminal height H_t for the cracked forests (red squares in figure 4(a)) could not be directly measured because these forests generally self-destructed. In these cases, H_t was calculated from the terminal time τ_t and the initial growth rate β using the relation $H_\mathrm{t} = \beta\tau_\mathrm{t}$. The open circles represent the projected final height $\mathcal{H}_\mathrm{f}$, which is the height the forest would have reached had the exponential decay dynamics continued and is given by $\mathcal{H}_\mathrm{f} = \beta\tau$. All lines are linear fits that show a characteristic energy [21], defined as the negative of the slope of a straight line on a plot of $\ln Y$ versus $1/k_\mathrm{B}T$, where Y is an arbitrary dataset. The actual forest height rapidly dropped to zero both below 720 °C and above 900 °C. Outside of this temperature range, a straight line approximation is not valid.

H_t decreases from ~700 to ~200 μm with increasing T, with a characteristic energy of -1.0 ± 0.5 eV, which can be viewed as an effective 'activation' energy for sudden termination. The projected final heights $\mathcal{H}_\mathrm{f}$ drop more rapidly

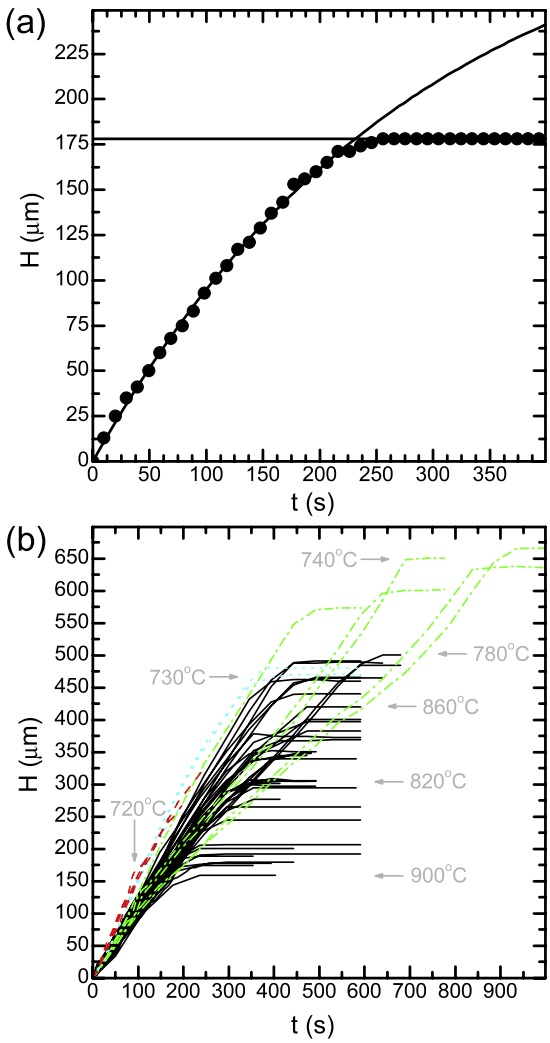


Figure 3. (a) Height H versus growth time t (circles) for a forest growing at 900 °C. Lines are an exponential fit ($t < 220$ s) and a horizontal line ($t > 220$ s). Data extracted from video S1 (see supplementary material available at stacks.iop.org/Nano/21/035603/mmedia), shown in figure 1(a). (b) Experimental data for H versus t for all temperatures (~50 growths, 720–900 °C). Termination morphology indicated by color: uniform (black solid line), delamination (cyan dotted line), partial delamination (green dot-dash line) and cracking (red dashed line). Several growth temperatures indicated by arrows pointing at terminal height.

with temperature at a characteristic energy of -2.0 ± 0.5 eV, which is comparable to the scale found for ethanol CVD of nanotube forests at high temperature [21]. In this sense, the dynamics of forest growth from acetylene and ethanol are similar. The difference in the temperature dependence of the terminal height H_t and the projected final height $\mathcal{H}_\mathrm{f}$ strongly suggests that the sudden termination arises from a different mechanism than the gradual slowing of growth represented in the exponential decay dynamics. In other words, it is likely that sudden termination is not just a runaway process of gradual termination, but is rather more likely to be a process originating from a different mechanism entirely.

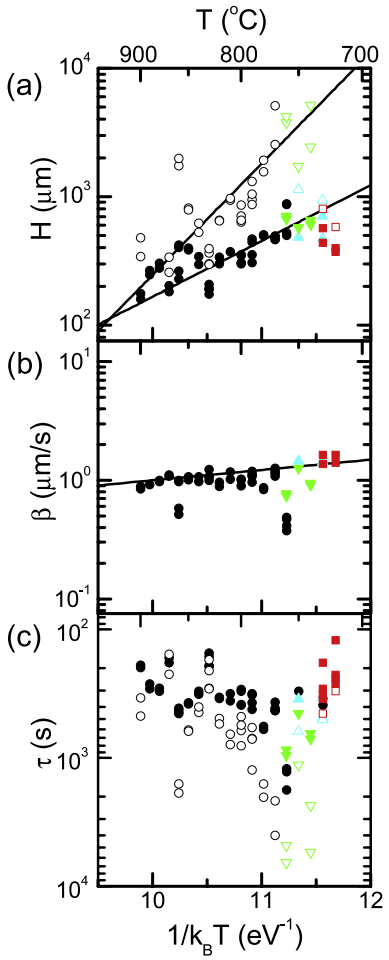


Figure 4. Inverse temperature ($1/k_{\mathrm{B}}T$) dependence of the logarithms of kinetic parameters: (a) sudden termination height H_{t} (solid points) and projected final height $\mathcal{H}_{\mathrm{f}}$ (open points), (b) initial growth rate β and (c) sudden termination time τ_{t} (solid points) and characteristic time τ (open points). Linear fits have characteristic energies: -1.0 ± 0.5 eV for H_{t}, -2.0 ± 0.5 eV for $\mathcal{H}_{\mathrm{f}}$ and -200 ± 200 meV for β. Termination morphology indicated by color and shape: uniform (black circles), delamination (cyan upward triangles), partial delamination (green downward triangles) and cracking (red squares).

In addition to the height, other dynamical parameters were investigated. The initial growth rate β, as determined from the exponential fit (figure 4(b)), decreases with increasing T with a characteristic energy of approximately -200 ± 200 meV. The small magnitude of the characteristic energy and the decreasing rate with temperature suggest that this energy corresponds to desorption (see, for example, Hudson [35]) or detachment of weakly adsorbed carbon-containing molecules. Small activation energies (of the order of meV) are expected for the desorption of physisorbed molecules because their primary interaction is through the weak van der Waals force. Increased desorption of carbon-containing molecules at high growth temperatures would lead to the observed decrease in the growth rate. Furthermore, 200 meV is the approximate desorption energy for small hydrocarbons from graphite, some metals, and oxides [36, 37]. We therefore conclude that this slight temperature dependence likely originates from the molecular desorption of carbon that could have otherwise been incorporated into a nanotube. The sudden termination time τ_{t} (figure 4(c), closed circles) is similar to H_{t} and is largely determined by the height of the forest in the sense that a slightly lower growth rate takes slightly longer to reach a critical height. There were some forests for which the only reliable dynamics data that could be measured was a direct measurement of τ_{t} from the *in situ* videos due to extreme peeling of the outer layers. The characteristic time of the exponential growth rate decay τ, obtained by fitting, is also plotted (open circles).

We now turn to the possible physical mechanisms that may be responsible for the different termination morphologies as well as the sudden termination phenomenon. There is already one published model for sudden termination by Han *et al* [18] and we compare our data to this report first. Han *et al* proposed a model in which sudden termination is caused by the balance between the mechanical links between the tops of the nanotubes in the forest and the enthalpy of formation of the graphene lattice. In their model, the concave geometry often observed on the top surfaces of the forests originates from the halted growth of one nanotube which generates an outwardly propagating front of growth termination. However, our *in situ* observations show that the concave geometry of the top surface starts forming during the early stages of growth (see supplementary material video S2 available at stacks.iop.org/Nano/21/035603/mmedia). Han *et al* also predict that the center of curvature may lie anywhere across the top surface of the forest. However, we observe the center of curvature is essentially always the center of the top surface of the forest (see supplementary material figure S2 available at stacks.iop.org/Nano/21/035603/mmedia). Collective effects, such as those discussed by Han *et al*, may well be responsible for sudden termination: however, their specific model does not reproduce the data we observe.

The 'normal' configuration for a forest is to be bound to the substrate, with a top surface, side surfaces and a bottom interface. Nanotubes in a forest are far from the long and straight configuration that would minimize the internal strain energies for perfect nanotubes. Instead, they are bent, twisted, stretched and compressed through interactions with neighboring nanotubes, possibly due to slight differences in growth rate. Nanotubes in a forest are also far from the tightly packed configuration that would maximize their cohesion energies. Rather, strong adhesion energies bind the nanotubes to the substrate with boundary conditions set by the size of the catalyst island and the density of catalyst nanoparticles. The nanotubes are then arranged into small bundles that wander back and forth. The competition between strain, cohesion and adhesion leads to macroscopic morphological changes, and it is reasonable to conclude that this competition also leads to sudden growth termination. By observation of figure 2, it is clear that these forests are indeed subjected to forces within that deform them.

Nanotube forests are never in an absolute minimum energy configuration and are thus instead in some metastable state in which changes are likely driven by the continuous buildup of strain. We suppose that the internal strain energy of the

nanotubes in the forest is balanced against the strong cohesion energies between nanotubes and adhesion energies between the nanotubes and the nanoparticles on the substrate. For the purpose of this discussion, we provide rough estimates for the magnitudes of these energies.

The adhesion energy can be roughly estimated by considering how the nanotube interacts with the substrate. In the base growth mode, a nanotube is first linked to itself along its length, then to the catalyst nanoparticle (Co), support (Al_2O_3) and substrate (Si:SiO_2). Failure occurs at the weakest point, which is at least as weak as the chemical bonds holding the tube together longitudinally. The bond dissociation energy of a C–C bond in a diatomic molecule is given in the *Handbook of Chemistry and Physics* [38] as 6.409 ± 0.160 eV. We use this value (6.4 eV) as an order-of-magnitude estimate for the energy of a C–C bond in a nanotube. For a 2 nm diameter zigzag SWNT (25, 0), there are 25 bonds through any slice perpendicular to the nanotube axis. Thus, we estimate an approximately 160 eV upper limit for the adhesion energy. Other points may be weaker, for example the nanotube–catalyst interface or the catalyst–substrate interface. Importantly, this energy is independent of nanotube length.

The cohesion energy is much weaker on a per carbon atom basis, but builds up quickly with increasing contact area. Using the binding energy between graphene sheets (∼80 meV/carbon atom [39]), it only takes ∼2000 carbon atoms for the van der Waals cohesion energy to equal the ∼160 eV adhesion energy. For graphene, this value corresponds to a ∼108 nm^2 contact area (using 0.054 nm^2/carbon atom as the surface density of graphene). Longer nanotubes have more contacts with neighbors, so this energy is an increasing function of length. In contrast with graphene, nanotubes within a forest typically come into contact only once every μm and the contact lengths are short, thus the actual cohesion energies are weaker than calculated. Furthermore, the lattices of neighboring nanotubes in a bundle will not be in perfect registry. It may require several μm of forest height for the cohesion energy to match the adhesion energy.

Finally, the magnitude of the strain energy is estimated from the bending energy. Using the thin rod approximation (see, for example, Landau and Lifshitz [40]), the bending energy per unit length is given by $E_{\mathrm{bend}}/L = \frac{\pi}{8} Y r^4/R^2$, where $Y = 1$ TPa is Young's modulus, $r = 1$ nm is the nanotube radius and $R = 350$ nm is the bending radius. The bending radius corresponds to a nanotube constrained laterally to 100 nm and wandering with a 1 μm period. These length scales are estimated from typical high magnification SEM images (see supplementary material figure S3 available at stacks.iop.org/Nano/21/035603/mmedia), which show that the nanotubes are organized into small bundles that wander back and forth. As a crude estimate, we suppose that the nanotubes typically come into contact with each other on the order of once every μm, with a spacing of approximately 100 nm between bundles. The estimated bending energy is 20 eV μm^{-1}, which means that 8 μm of forest height is sufficient to accumulate the equivalent of the ∼160 eV adhesion energy in bending strain energy.

For very short forests ($H < 8$ μm) the adhesion energy dominates over the cohesion and strain energies, but this is not the case for tall forests ($H \gg 8$ μm). We expect there will be some height threshold above which adhesion becomes compromised by strain and cohesion. More detailed data concerning the nanotube wandering length scales and inter-nanotube contact areas would be required to accurately predict this height. Experimentally, the only morphology changes we observed occurred on forests taller than ∼100 μm.

Based on these competing processes, all with similar energies, we conclude that the delaminated forest in figure 2(b) reduces its total energy by creating a new surface at its base. The loss of adhesion energy is compensated by relieving strain energy and possibly gaining cohesion energy. In a cracked forest, such as the forest shown in figure 2(c), the total energy is reduced by creating new side surfaces and space for local deformations to occur. The loss of cohesion energy is compensated by relieving strain energy, while there may be little or no change in the adhesion energy.

It is important to note that cracking provides good evidence for strain in nanotube forests. Indeed, among all three forces at play here, only strain is a force field with long range action. The macroscopic extent of the cracks in figure 2(c) and their high degree of symmetry are both signatures of long range effects. This is in contrast with adhesion and cohesion forces which act more locally.

In materials science, sudden termination of continuous growth due to collective effects has long been recognized and is commonly observed for the growth of bulk crystals. A layer that is not exactly matched to the substrate's elastic constants will grow continuously up to a critical thickness, above which dislocations will appear. In the Stranski–Krastanov growth mode (see, for example, Ayers [41]), strain and/or surface energies drive a transition from smooth continuous growth to rough island growth. It is plausible then that the sudden termination of nanotube forests could be an analogous effect.

Continuous growth of nanotube forests requires a balance between the internal nanotube strain energies, the adhesion energy attaching the nanotubes to the nanoparticles and substrate, and the cohesion energies between the nanotubes and bundles. The fact that sudden termination occurs very near to or at the same time as delamination and cracking suggests that termination may originate from the same root cause: the need for the forest to collectively accommodate the imbalance of the forces within. Sudden termination is then likely the result of the buildup of strain such that continued steady growth is no longer energetically favorable.

4. Conclusion

In summary, three main termination morphologies for CVD-grown nanotube forests have been observed and identified: uniform, delamination and cracking. Uniform termination is characterized by the sudden termination of the forest while maintaining its shape. Delamination is characterized by part or all of the forest detaching itself from the substrate as growth terminates, while remaining intact and retaining its shape. Cracking is characterized by a forest breaking apart as it terminates by splitting into several pieces. We speculate

that what determines the termination morphology is energy minimization, and that this is a collective effect of the many nanotubes in the forest. The buildup of strain in the forest is relaxed by the detachment of the forest from the substrate (delaminating) or the splitting apart of the forest (cracking). Likewise, the buildup of strain may make it energetically more favorable for the forest to stop growing, without going to the extreme of completely delaminating or cracking. The termination morphologies appear to be closely related to the phenomenon of sudden growth termination and give insights into the reasons for termination.

The goal of 'infinitely' tall SWNT forests should involve optimizing not just individual SWNT growth, but also optimizing collective effects. *In situ* methods provide valuable insights into the mechanisms responsible for nanotube forest growth and termination. Efforts to balance the energies present during growth, particularly through the use of *in situ* methods, appear to be a promising route to improving forest growth.

Acknowledgments

The authors thank the following IMS staff for their support: L Tay, H Tran, M Denhoff and J Fraser. PV was supported by OGS, NSERC, NRC-GSSSP and PF's NSERC Discovery Grant.

References

[1] Eres G, Puretzky A A, Geohegan D B and Cui H 2004 *Appl. Phys. Lett.* **84** 1759
[2] Eres G, Kinkhabwala A A, Cui H, Geohegan D B, Puretzky A A and Lowndes D H 2005 *J. Phys. Chem.* B **109** 16684
[3] Zhang C, Pisana S, Wirth C T, Parvez A, Ducati C, Hofmann S and Robertson J 2008 *J. Diamond Relat. Mater.* **17** 1447
[4] Mattevi C *et al* 2008 *J. Phys. Chem.* C **112** 12207
[5] Hata K, Futaba D N, Mizuno K, Namai T, Yumura M and Iijima S 2004 *Science* **306** 1362
[6] Geohegan D B, Puretzky A A, Ivanov I N, Jesse S, Eres G and Howe J Y 2003 *Appl. Phys. Lett.* **83** 1851
[7] Futaba D N, Hata K, Yamada T, Mizuno K, Yumura M and Iijima S 2005 *Phys. Rev. Lett.* **95** 056104
[8] Puretzky A A, Geohegan D B, Jesse S, Ivanov I N and Eres G 2005 *Appl. Phys.* A **81** 223
[9] Li Q, Zhang X, DePaula R F, Zheng L, Zhao Y, Stan L, Holesinger T G, Arendt P N, Peterson D E and Zhu Y T 2006 *Adv. Mater.* **18** 3160
[10] Hart A J and Slocum A H 2006 *J. Phys. Chem.* B **110** 8250
[11] Bronikowski M J 2007 *J. Phys. Chem.* C **111** 17705
[12] Noda S, Hasegawa K, Sugime H, Kakehi K, Zhang Z, Maruyama S and Yamaguchi Y 2007 *Japan. J. Appl. Phys.* **46** L399
[13] Yasuda S, Futaba D N, Yumura M, Iijima S and Hata K 2008 *Appl. Phys. Lett.* **93** 143115
[14] Patole S P, Park J H, Lee T Y, Lee J H, Patole A S and Yoo J B 2008 *Appl. Phys. Lett.* **93** 114101
[15] Meshot E R and Hart A J 2008 *Appl. Phys. Lett.* **92** 113107
[16] Hasegawa K, Noda S, Sugime H, Kakehi K, Maruyama S and Yamaguchi Y 2008 *J. Nanosci. Nanotechnol.* **8** 6123
[17] Pint C L, Pheasant S T, Parra-Vasquez A N G, Horton C, Xu Y and Hauge R H 2009 *J. Phys. Chem.* C **113** 4125
[18] Han J-H, Graff R A, Welch B, Marsh C P, Franks R and Strano M S 2008 *ACS Nano* **2** 53
[19] Stadermann M *et al* 2009 *Nano Lett.* **9** 738
[20] Einarsson E, Murakami Y, Kadowaki M and Maruyama S 2008 *Carbon* **46** 923
[21] Vinten P, Lefebvre J and Finnie P 2009 *Chem. Phys. Lett.* **469** 293
[22] Puretzky A A, Eres G, Rouleau C M, Ivanov I N and Geohegan D B 2008 *Nanotechnology* **19** 055605
[23] Hasegawa K, Noda S and Yamaguchi Y 2008 Sudden-termination of millimeter-thick vertically aligned single-walled carbon nanotube growth evidenced by real-time monitoring *NT08: 9th Int. Conf. on the Science and Applications of Nanotubes* talk T 23
[24] Hart A J, van Laake L and Slocum A H 2007 *Small* **3** 772
[25] Gunjishima I, Inoue T and Okamoto A 2007 *Appl. Phys. Lett.* **91** 193102
[26] Hart A J and Slocum A H 2006 *Nano Lett.* **6** 1254
[27] Finnie P, Bardwell J, Tsandev I, Tomlinson M, Beaulieu M, Fraser J and Lefebvre J 2004 *J. Vac. Sci. Technol.* A **22** 747
[28] Finnie P, Li-Pook-Than A, Lefebvre J and Austing D G 2006 *Carbon* **44** 3199
[29] Chiashi S, Murakami Y, Miyauchi Y and Maruyama S 2004 *Chem. Phys. Lett.* **386** 89
[30] Kaminska K, Lefebvre J, Austing D G and Finnie P 2007 *Nanotechnology* **18** 165707
[31] Bond J, Lefebvre J, Austing D G, Tay L and Finnie P 2007 *Nanotechnology* **18** 135603
[32] Murakami Y and Maruyama S 2006 *Chem. Phys. Lett.* **422** 575
[33] Pint C L, Xu Y-Q, Pasquali M and Hauge R H 2008 *ACS Nano* **2** 1871
[34] Yamada T, Maigne A, Yudasaka M, Mizuno K, Futaba D N, Yumura M, Iijima S and Hata K 2008 *Nano Lett.* **8** 4288
[35] Hudson J B 1992 *Surface Science: An Introduction* (New York: Wiley)
[36] Bruch L W, Diehl R D and Venables J A 2007 *Rev. Mod. Phys.* **79** 1381
[37] Yang S, Ouyang L, Phillips J M and Ching W Y 2006 *Phys. Rev.* B **73** 165407
[38] Luo Y-R 2009 Bond dissociation energies *CRC Handbook of Chemistry and Physics* (*Internet Version 2009*) 89th edn, ed D R Lide (Boca Raton, FL: CRC Press/Taylor and Francis)
[39] Charlier J-C, Gonze X and Michenaud J-P 1994 *Europhys. Lett.* **28** 403
[40] Landau L D and Lifshitz E M 1986 *Theory of Elasticity* 3rd edn (Oxford: Reed)
[41] Ayers J E 2007 *Heteroepitaxy of Semiconductors* (Boca Raton, FL: CRC Press)

Chapter 4

Morphological Instabilities and the Dynamics of Carbon Nanotube Forest Growth

as published in *ECS Transactions*, Volume 35, Issue 25, Pages 3–12, 2011.
http://dx.doi.org/10.1149/1.3655505

Copyright notice: ©The Electrochemical Society, Inc. 2011. All rights reserved. Except as provided under U.S. copyright law, this work may not be reproduced, resold, distributed, or modified without the express permission of The Electrochemical Society (ECS). The archival version of this work was published in *ECS Transactions*, Volume 35, Issue 25, Pages 3–12, 2011.

Foreword

This chapter is a follow-up to Chapter 3 in the sense that it elaborates on the ideas presented in Chapter 3, while adding many new ideas, many of which will be further addressed in subsequent chapters. Most importantly, this chapter first introduces the idea of (and presents evidence for) the growth rate of the nanotubes not being uniform across the entire forest, but following a very specific pattern. This concept is a key component of Chapter 5, Chapter 6, and Chapter 7, and plays a critical role in how the forests form and is the source of the strain in the forests. This chapter first mentions the rippling pattern that is the main subject of Chapter 5 and Chapter 6. Finally, this chapter shows evidence that the areal density of carbon nanotubes in the forests decreases as growth proceeds [1], which is discussed further in Chapter 7.

All of the observations in this chapter lead to the conclusion that the morphology of the forest has many important clues about the interactions between the individual nanotubes in the forest and the origin of strain in the forest. Having already described these interactions in Chapter 3, this chapter provides additional details about how these interactions may be involved in the termination of carbon nanotube forest growth. This chapter also provides a further comparison of the magnitude of these interactions and their effects on carbon nanotubes.

---

[1] M Bedewy, E R Meshot, H Guo, E A Verploegen, W Lu, and A J Hart. *J. Phys. Chem. C*, 113:20576–82, 2009.

ECS Transactions, 35 (25) 3-12 (2011)
10.1149/1.3655505 ©The Electrochemical Society

Morphological Instabilities and the Dynamics of Carbon Nanotube Forest Growth

P. Finnie[a,b], P. Vinten[b,a], P. Marshall[a], and J. Lefebvre[a]

[a] Institute for Microstructural Sciences, National Research Council Canada, Building M-50, 1200 Montreal Road, Ottawa, Ontario, K1A 0R6, Canada
[b] Department of Physics, University of Ottawa, 150 Louis Pasteur, Ottawa, Ontario, K1N 6N5, Canada

Vertically aligned carbon nanotube forests show various morphologies on both macro- and micro-scales. These morphologies are a result of growth mechanisms and interactions between nanotubes. By investigating these morphologies, we study both the growth mechanisms and the interactions. We examine forest morphologies *in situ*, dynamically during chemical vapor deposition growth and *ex situ*, post growth. *In situ* observations allow the separate characterization of nucleation, growth and termination phases, and the exploration of connections between morphology and growth. Forests systematically show different morphologies, ranging from uniform to cracked, delaminated, and periodically rippled. These are discussed in terms of the balance of forces within the forests including cohesion, adhesion, and stiffness. We propose a simplified model that predicts termination as a result of an imbalance in the forces present. We show that growth rate differences drive many morphological effects, and these differences originate in the nucleation phase due to gas diffusion.

Introduction

One of the most successful approaches for the synthesis of carbon nanotubes has been chemical vapor deposition (CVD) using a carbon containing source gas and a substrate upon which a thin film or nanoparticle catalyst has been deposited (1,2). If the yield is high, growth can result in forests of nanotubes growing up out of the substrate. In recent years, vertically aligned carbon nanotube forests have been grown to increasing heights (3-6). For practical and purely scientific reasons, effects limiting the height are a subject of great interest. At the same time, there is immense variety in forests: they may consist of multiwalled carbon nanotubes (MWNT) or significant fractions of single walled nanotubes (SWNT), they can range in density, and they can show a variety of macro- and micro-scale morphologies which can change with time and film thickness. It is becoming apparent that additional effects govern the growth of ensembles of nanotubes beyond those governing individual nanotubes.

In situ studies are helpful to help clarify issues in the synthesis process, and vertically aligned carbon nanotube forests are especially suited to such studies (7), which can be as simple as observing the forest as it grows with a camera (8-12), for example in a cold wall CVD reactor. The earliest data from MWNT forests typically showed a constant rate

that would ultimately terminate, however at that time forest heights were limited, and the data was not well resolved. Since then, forest heights have been extended into the multi-millimeter and even centimeter regime, and the shape of the growth curves have been modeled and measured with higher fidelity.

In most cases, forests do not show a linear growth curve (constant growth rate). Usually, they tend to show an exponential deceleration in the height as a function of time (7,13). Ideally, nanotubes would grow indefinitely, to arbitrary lengths, but this exponential deceleration puts limits on the ultimate height for many processes. More recently it has become clear that forest heights often stop increasing abruptly (8,14-16). In a recent report nanotubes were grown to centimeter lengths without any apparent termination, though gradual termination was evident (6). Thus, for most synthesis processes the forest height is limited by either gradual or sudden termination. Gradual termination appears to have a plausible explanation in catalyst poisoning. There has been recent progress in understanding sudden termination, and several models have been proposed (15,17,18). One picture is that sudden termination comes simply from the cumulative effect of gradual termination, and the forest terminates once it falls below a threshold to be self-supporting (17). Another picture is that cross-linking of the top of the forest causes a force feedback which increases the free energy required to add carbon (18). We have proposed that strain building up in the layer may cause it to become favorable to delaminate or otherwise significantly alter the relationship between the catalyst and the substrate (15).

Distinct from termination, but likely related, is the morphology of the forest. Recently, investigating growth on finite sub-mm diameter catalyst islands we found that a variety of forest morphologies were routinely obtained (15). At low temperatures, much of the morphological evolution took place late in the growth, at least raising the possibility that it is connected with termination. We suppose that these morphological changes could be explained in terms of the driving force of growth rate differences and the physical/chemical nature of interactions between nanotubes and the substrate, nanotubes and themselves, and the inherent strength of nanotubes. Here we summarize some of these morphological changes, and discuss their origins and their magnitudes.

In this paper we show how non-uniform growth rates originate at the very earliest, nucleation stages of growth. We provide additional evidence to the growing body of data showing that the internal structure of a forest changes with time. We review several of the forces that must be considered when evaluating the interactions between nanotubes within a forest and explicitly explain how these forces could give rise to transitions in the (meta-)stable configuration of the forest morphology. It is predicted that the energetically favored state of the forest morphology depends on the lengths of the nanotubes present in the forest. We show that it is possible for a length dependent termination to originate from such a transition.

We have seen that morphology of these micro-patterned carbon nanotube forests is diverse, and at the same time the termination dynamics are surprisingly complicated. We consider the origins of these effects, and consider whether, and how, they may be related.

Experimental

Carbon nanotube forests were grown by chemical vapor deposition using acetylene as the carbon source. The reactor is cold-walled with a resistive heater, and was operated at atmospheric pressure. The seed catalyst material was e-beam evaporated cobalt (0.8 nm) and alumina (250 nm) deposited on thermally oxidized silicon wafers which were patterned by shadow masking (100 μm to 800 μm diameter circles). The gas ratios during growth were acetylene (0.1%), with the assistance of water vapor (~0.1%), and hydrogen (0.5%), balance argon, supplied by a nozzle at an angle and arriving at a total flow of 0.25 L/min. The growth was tracked *in situ* with a camera and long working distance microscope optics directed at the growth sample at a glancing angle of ~5° to the plane of the sample (see figure 1). See our previous reports for a more detailed account (15).

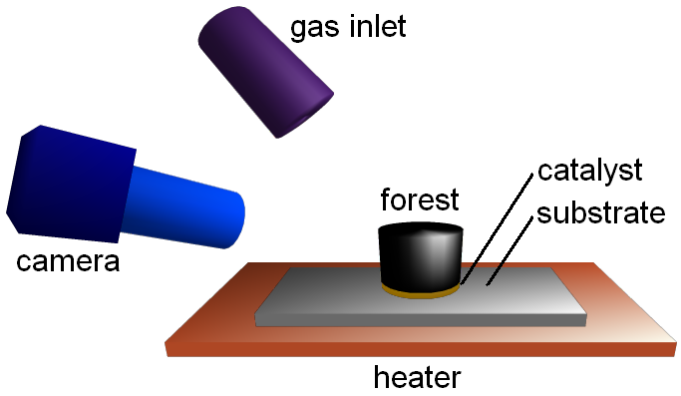


Figure 1. (Color online) Chemical vapor deposition reactor arrangement. Forests are grown by chemical vapor deposition and tracked optically *in situ* with a camera. A resistive heater is used. A thin film cobalt catalyst on alumina is prepared in circular islands on thermally oxidized silicon wafers. Source gases are supplied through a nozzle directed toward the substrate.

Results

Previously, with this setup we observed the growth dynamics and extracted kinetic growth parameters for nanotube forests and how they changes with temperature. Briefly, over a large range in temperatures (~700°C - 900°C) the growth rate in terms of height vs. time shows an initial growth rate of about 1 μm/s, slowing very gradually with an exponential deceleration, until a critical point where the growth halts abruptly. The initial growth rate was found to decrease very slightly with increasing temperatures, with an associated (de-)activation energy of 200 meV. The magnitude of this energy suggests that hydrocarbon desorption from the surface is a possible explanation. Parasitic gas phase reactions which limit the supply of the active precursor could be another explanation for the gradual decrease with temperature.

The exponential decay can be extrapolated to a projected final height. This projected final height decreases rapidly with temperature, with centimeter scale projected heights for 700°C, and 100 μm scale heights at 900°C. The projected final height decreases with a (de-)activation energy of ~2 eV. The actual final height is much shorter at low

temperatures due to sudden termination, with millimeter scale heights realized for 700°C and 100 μm scale heights at 900°C with a projected cross-over between projected and actual final heights. The actual final height decreases with a (de-)activation energy of ~1 eV. The extremely different values of final height and projected final height, and their different scaling is a first hint that the mechanisms underlying the two could be different. In terms of the duration of growth, the projected lifetime ranges from hours at 700°C to minutes at 900°C, with an activation energy of ~2 eV, whereas the actual lifetime does not vary as much, is always on the order of 10 minutes, and shows no clear scaling with temperature. This is another way of looking at the data and also suggests a different mechanism for the two processes.

We also reported that the gross morphology of the forest islands varies. In figure 2 we take a new view at this type of data. Figure 2a shows the result of self-terminated growth at a relatively high temperature (860°C). A slightly concave top surface can be seen and the sidewalls curve inward somewhat. At lower temperatures, this concavity becomes more pronounced, as can be seen in figure 2b, which was terminated early by stopping the carbon supply. At lower temperatures, morphologies become even more complicated, with self-delamination common in the range 730°C and 760°C (figure 2c) and even cracking and "exploding" at lower temperatures (figure 2d). In the intermediate range of temperatures (~730°C to ~830°C), the forests reproducibly show periodic ripples on their outer surface of wavelength ~1 μm, extending over a large range (19,20). The ripples are so regular, over much of the forest height, that one can even obtain optical diffraction patterns from them.

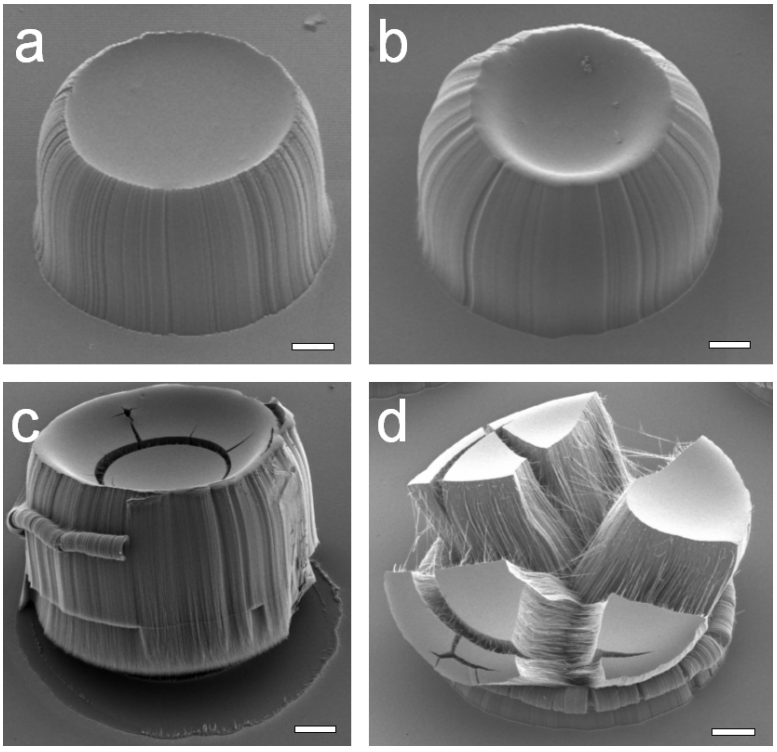


Figure 2. Morphologies of carbon nanotube forests. (a) Slightly concave, 860°C, self-terminated. (b) Pronounced concavity, 760°C, intentionally stopped. (c) Delaminated, 730°C, self-terminated. (d) Exploded, 720°C, self-terminated. All scale bars are 100 μm.

The concavity, rippling, and several other morphological changes are driven by variations in the growth rate across the catalyst island. *In situ* observations reveal that the growth rate difference is present at nucleation. Figure 3 shows a series of frames at 1 second intervals from a growth movie taken at 760°C on a 700 μm seed catalyst circle. Carbon growth on the catalyst island is black. It is clear that the growth is not uniform across the sample. Rather, in a cylindrically symmetric process, the growth is fastest at the outside, and fills in the interior later. The supply of reactive carbon is limited by diffusion of the gas to the growth sites. The outside part of the catalyst island receives extra supply due to the fact that carbon is not consumed by the surrounding exposed silicon oxide. The growth rate differences are driven by the supply of carbon, and by the consumption of carbon by other catalyst particles.

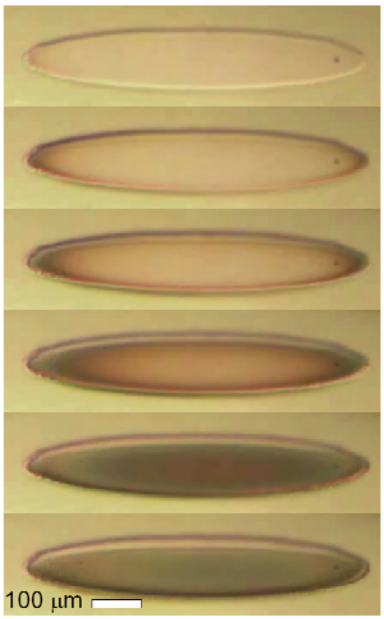


Figure 3. (Color online) Nucleation dynamics. A series of optical images from the camera looking into the reactor, taken at 1 second intervals, of a circular seed catalyst island at the onset of growth at 760°C.

In addition to the gross morphological changes of the forest, the internal arrangement of nanotubes, that is the internal morphology, is changed dramatically. Others have seen significant changes by other means. Nanotube diameters are reported to increase dramatically with forest height (21). Scanning electron microscopy and small angle X-ray scattering reveal that many forests become disordered before termination (14), and mass evolution experiments show that deceleration in the mass growth rate can precede sudden termination (17).

An interesting view of the evolution of the internal forest morphology is obtained simply by removing a forest island with sticky tape attached to the top. The forests stick more strongly to the tape than the substrate and are removed, intact, with virtually no

obvious change in overall shape after removal from the substrate. In figure 4a, the base of a forest in the steady growth phase at 760°C is shown as seen in a scanning electron microscope. In figure 4b an identically grown forest is shown immediately after sudden termination. It is clear that the base of the forest is much less dense at the termination stage, consistent with prior measurements.

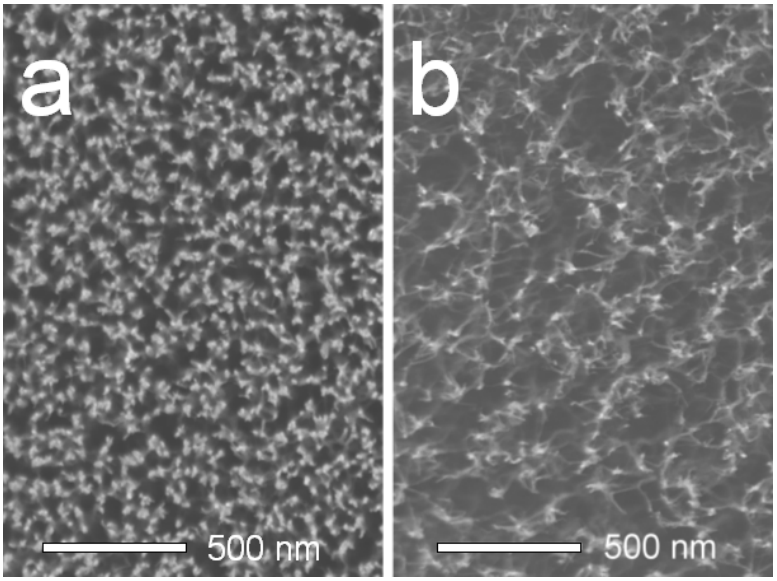


Figure 4. Root morphology. SEM images for an intentionally terminated forest (a) and for a self-terminated forest (b).

Discussion

To try to understand the above morphological transitions, and the mechanisms of sudden termination, it is worth considering the physical/chemical interactions between nanotubes and their relative magnitudes. There are three obvious effects to consider, outlined in reference (15). Here we elaborate on that discussion. First there is the energy scale involved in keeping the nanotube in place. One can consider several effects. The seed particle should adhere to the substrate, the nanotube should adhere to the seed particle, and the nanotube must not break along its length. The lowest of all these energies is what limits the attachment of the nanotube to the substrate. The breakage of the nanotube along its length is then an upper limit to this energy. According to CRC tables, the energy to break a C-C bond is 6.4 eV (22). For a (25,0) SWNT as illustrated in figure 5a, it takes 160 eV at most to break the nanotube. This is an upper bound to the adherence/internal coherence of a SWNT.

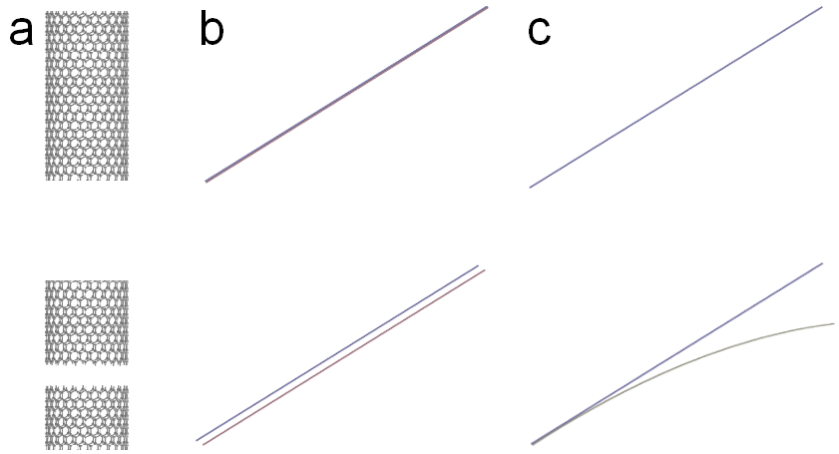


Figure 5. (Color online) Transformations requiring similar energies. (a) Breaking of the nanotube, or its adhesion to the substrate. (b) Debundling of a pair of nanotubes. (c) Deforming a nanotube.

Another interaction is the van der Waals interaction between the neighboring nanotubes. Graphene sheets adhere with an energy of ~20 meV/Carbon atom (23). A rigorous value for this cohesion energy is complicated by the fact that carbon atoms may or may not be registry, and the contact area between nanotubes depends on their diameters. If we consider (25,0) nanotubes, which are 2 nm in diameter, and suppose that they are effectively in contact with each other over a 1 nm width, we find that a 430 nm length is sufficient to build up a cohesion energy of 160 eV if we use the graphene surface density of 0.054 nm^2/C. Figure 5b is drawn to scale, showing the same amount of energy to debundle the pair as to break a nanotube.

Finally there is the mechanical stiffness of the nanotube. At a crude level of approximation this can be estimated from a rigid rod according to $E = \pi Y r^4 L / 8 R^2$, where, Y is Young's modulus (~1 TPa for a SWNT), r is the nanotube radius, R is the radius of curvature, and L is the length over which the nanotube is curved. If we consider the same 430 nm length (25,0) nanotube, 160 eV corresponds to a bend of radius of curvature of 2.5 μm. This is illustrated to scale in figure 5c.

These interactions can be used to explain the different morphologies, and the various morphological transitions. For these finite sized islands at the pressures used here, gas diffusion and catalyst activity give rise to the driving force of a non-uniform growth rate. The rippling instability can be understood by the buckling of the nanotube in response to the non-uniform growth rate. The wavelength of rippling can be roughly predicted if it is determined by the need to balance cohesion and bending (20). A 0.1 μm scale bending radius is predicted if the cohesion energy and bending energies are equivalent, with the great uncertainty regarding choice of contact area. Nonetheless, this very crude approximation predicts the observed rippling scale.

The cracking and exploding morphology is understandable if the strain energy can be reduced by debundling nanotubes. The delaminated morphology can be understood if strain energy can be reduced by severing the nanotube from the substrate. At low temperatures, both these processes often occur in late phases of the growth of finite

forests. It is worth pointing out that a forest of nanotubes is only ever in some metastable state. The minimum energy configuration would be graphite under ordinary conditions. It is also worth pointing out that in order to make a transformation between states, an activation energy would ordinarily be involved and so there is a kinetic element to making the transition. That is, even though the transition may be energetically favored, it must also be reached in a short enough time scale.

Finally we explicitly consider two simplified scenarios in which transitions between growth modes may be expected as nanotube lengths increase. These are scenarios which could terminate nanotube growth. Whether or not they are responsible for sudden termination, such transitions should be possible to observe under the right conditions.

The first scenario is likely not the origin of the transition, however, it illustrates very clearly how such a transition could take place by balancing two effects. It involves the balance of adhesion with cohesion and is illustrated schematically in figure 6. Considering two nanotubes, one possible configuration is for both nanotubes to adhere to their catalyst particles, and to be otherwise separate (figure 6a). The adherence to the catalyst particle saves some energy, but there is no energy saving from bundling. This configuration is more favorable for short nanotubes. Another possible configuration is for the nanotubes to bundle together, which decreases the total energy, but to do so, they may need to detach from the catalyst (figure 6b). This is more energetically favorable for longer nanotubes. Formally if an energy A is saved by attachment, and an energy B per unit length L is saved by bundling, then the total energy is $E = -2A$ for the initial configuration, and $E = -A - BL$ for the final configuration. There is then a cross-over length of $L = A / B$. This length holds for a generalization to many nanotubes. As an example, if *A* is 160 eV and B is 20 meV/nm, the transition occurs after 8 μm of contact length. If nanotubes are in contact over a smaller area, as would be the case for meandering nanotubes, this transition would occur at a proportionally larger length.

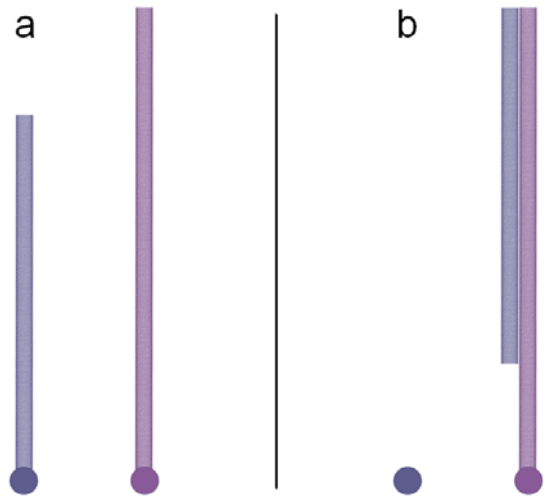


Figure 6. (Color online) Balancing adhesion with cohesion. (a) Nanotubes adhering to catalyst particle. (b) One nanotube detached and bundled.

The second scenario is more realistic, would appear to explain morphological changes, and may help explain sudden termination. However, it is harder to parameterize mathematically because it is more dependent on the precise geometrical configuration of the forest. Consider two nanotubes growing from two seed particles which are bound together at the top by van der Waals forces (figure 7). If the nanotubes grow at different rates, strain can build up as the nanotubes lengthen and try to satisfy the constraints of cohesion between nanotubes and adhesion to the catalyst particle (figure 7a). Strain energies can be relieved by breaking the adhesion to the nanoparticle (figure 7b). The latter scenario becomes more favorable as more strain builds up. This may explain delaminated morphologies and is also a potential explanation for sudden termination. Another way to relieve the strain is to maintain the adhesion to the substrate, but to break the van der Waals cohesion, and this would explain the cracking morphology.

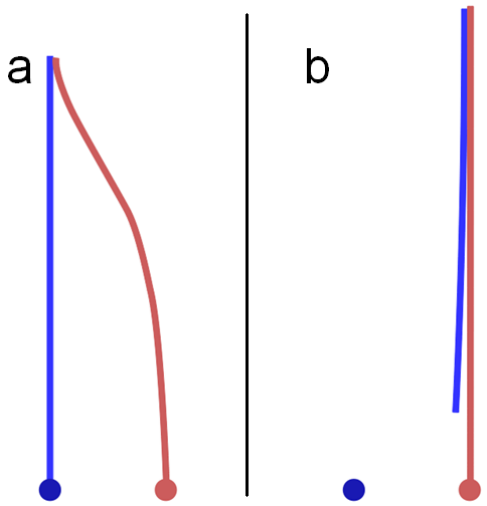


Figure 7. (Color online) Balancing adhesion with strain. (a) Both nanotubes adhering to seed particles, with one strained. (b) One nanotube detached and strain relieved.

Conclusions

In situ observations show that gradual and sudden termination show different scaling. On sub-millimeter scale catalyst patterns, drastic gross morphological changes occur which may also be related to termination. The morphological changes are driven by non-uniform nanotube growth rates, which begin in the nucleation stage. At the same time, the microscopic morphology of the forest at the base is very different for a self-terminated forest as compared to an intentionally terminated forest. Forest morphologies can be interpreted in terms of the effects of adhesion, cohesion, and strain. Simplified models balancing adhesion with cohesion or adhesion with strain predict a cross-over from adherence to detachment. Thus, morphology and termination might be connected in such a fashion. Regardless, to understand forests it has become necessary to move beyond considering them as simply collections of non-interacting nanotubes growing independently. Collective effects must be considered.

Acknowledgments

We are grateful to Hue Tran, Mike Denhoff, and Jeff Fraser for technical assistance at various stages of this work. We are grateful for funding from an NSERC Discovery Grant, an NSERC CGS, and an NRC GSSSP.

References

1. Z. F. Ren, Z. P. Huang, J. W. Xu, J. H. Wang, P. Bush, M. P. Siegal, and P. N. Provencio, *Science*, 282, 1105 (1998).
2. J. Kong, H. T. Soh, A. M. Cassell, C. F. Quate, and H. Dai, *Nature*, 395, 878 (1998).
3. Y. Murakami, S. Chiashi, Y. Miyauchi, M. Hu, M. Ogura, T. Okubo, and S. Maruyama, *Chem. Phys. Lett.*, 385, 298 (2004).
4. K. Hata, D. N. Futaba, K. Mizuno, T. Namai, M. Yumura, and S. Iijima, *Science*, 306, 1362 (2004).
5. G. Zhong, T. Iwasaki, J. Robertson, and H. Kawarada. *J. Phys. Chem. B*, 111, 1907 (2007).
6. S. Yasuda, D. N. Futaba, T. Yamada, J. Satou, A. Shibuya, H. Takai, K. Arakawa, M. Yumura, and K. Hata, *ACS Nano*, 3, 4164 (2009).
7. A. A. Puretzky, D. B. Geohegan, S. Jesse, I. N. Ivanov, and G. Eres, *Appl. Phys. A*, 81, 223 (2005).
8. A. A. Puretzky, G. Eres, C. M. Rouleau, I. N. Ivanov, and D. B. Geohegan, *Nanotechnology*, 19, 055605 (2008).
9. I. Gunjishima, T. Inoue, and A. Okamoto, *Appl. Phys. Lett.*, 91, 193102 (2007).
10. A. J. Hart, L. van Laake, and A. H. Slocum, *Small*, 3, 772 (2007).
11. S. Yasuda, D. N. Futaba, M. Yumura, S. Iijima, and K. Hata, *Appl. Phys. Lett.*, 93, 143115 (2008).
12. P. Vinten, J. Lefebvre, and P. Finnie, *Chem. Phys. Lett.*, 469, 293 (2009).
13. D. N. Futaba, K. Hata, T. Yamada, K. Mizuno, M. Yumura, and S. Iijima, *Phys. Rev. Lett.*, 95, 056104 (2005).
14. E. R. Meshot and A. J. Hart, *Appl. Phys. Lett.*, 92, 113107 (2008).
15. P. Vinten, P. Marshall, J. Lefebvre, and P. Finnie, *Nanotechnology*, 21, 035603 (2010).
16. S. Noda and H. Sugime, *Carbon*, 48, 2203 (2010).
17. M. Bedewy, E. R. Meshot, H. Guo, E. A. Verploegen, W. Lu, and A. J. Hart, *J. Phys. Chem. C*, 113, 20576 (2009).
18. J.-H. Han, R. A. Graff, B. Welch, C. P. Marsh, R. Franks, and M. S. Strano, *ACS Nano*, 2, 53 (2008).
19. P. Vinten, J. Lefebvre, and P. Finnie, *Appl. Phys. Lett.*, 97, 101901 (2010).
20. P. Vinten, J. Bond, P. Marshall, J. Lefebvre, and P. Finnie, *Carbon*, in press (2011).
21. K. Hasegawa and S. Noda, *Appl. Phys. Express*, 3, 045103 (2010).
22. Y.-R. Luo, *Bond Dissociation Energies* in *CRC Handbook of Chemistry and Physics, 89th Edition*, D. R. Lide, Editor, CRC Press/Taylor and Francis, USA (2009).
23. M. C. Schabel and J. L. Martins, Phys. Rev. B, 46, 7185 (1992).

Chapter 5

Visible iridescence from self-assembled periodic rippling in vertically aligned carbon nanotube forests

as published* in *Applied Physics Letters*, Volume 97, Article 101901 (3 Pages), 2010.
http://dx.doi.org/10.1063/1.3485084

Copyright notice: Reprinted with permission from: Phillip Vinten, Jacques Lefebvre, Paul Finnie, *Applied Physics Letters*, Vol. 97, Article 101901, 2010. Copyright 2010, American Institute of Physics.

*In accordance with University of Ottawa regulations, the contact email address has been removed from this article.

Foreword

In Chapter 4, a rippling pattern was first mentioned but was not elaborated on in much detail other than stating several properties and a possible origin. In this chapter, the rippling pattern and its properties are elaborated on significantly, while the possible origin is expanded upon, though the full treatment of the origin of the ripples is left to Chapter 6.

The rippling pattern itself is a self-organized phenomenon that naturally occurs during growth. All the nanotubes on the side walls for the forest have a regular undulating pattern that is like ripples on a pond. The ripples have a consistent wavelength over a significant length relative to their wavelength and are coherent: all nanotubes are observed to participate and the crests and troughs of the ripples are in registry with one another. No external influences are responsible for their formation, such as the presence of an external force [1]. Such naturally occurring spontaneous rippling has been previously observed in CVD growth of carbon nanotube forests [2–8]. Here, the rippling pattern is sufficiently coherent that the diffraction of visible light is observed.

The fact that this rippling pattern can reflect light at all is surprising because carbon nanotube forests are known to be among the blackest objects available [9]. In this research, the rippling pattern was first observed on smaller catalyst islands (100 μm diameter circles) that were being used to see what effect catalyst patterning had on the growth kinetics and final height of the forests. A thorough study of this island size dependence is presented in Chapter 7.

Once the rippling pattern was observed, it was quickly determined that the long range order observed in this pattern was indicative of significant interaction between the individual nanotubes in the forests, in particular the strain energy and cohesion energy. It is proposed that the interactions between neighbouring nanotubes creates the conditions necessary for this self-organized collective morphological effect (see Chapter 6 for more details). The size of the ripples (their wavelength) is physically measured using SEM and correlates well with the observed diffraction, suggesting that the long-range order and consistency of the ripples allow them to act as a diffraction grating and thus reflect light.

---

[1] A J Hart and A H Slocum. *Nano Lett.*, 6:1254–60, 2006.

[2] H Wang, Z Xu, and G Eres. *Appl. Phys. Lett.*, 88:213111, 2006.

[3] Q Zhang, W Zhou, W Qian, R Xiang, J Huang, D Wang, and F Wei. *J. Phys. Chem. C*, 111:14638–43, 2007.

[4] Y Zhang, G Zou, S K Doorn, H Htoon, L Stan, M E Hawley, C J Sheehan, Y Zhu, and Q Jia. *ACS Nano*, 3:2157–62, 2009.

[5] X Cui, W Wei, C Harrower, and W Chen. *Carbon*, 47:3441–51, 2009.

[6] M Bedewy, E R Meshot, H Guo, E A Verploegen, W Lu, and A J Hart. *J. Phys. Chem. C*, 113:20576–82, 2009.

[7] Y Zhang, J M Gregoire, R B van Dover, and A J Hart. *J. Phys. Chem. C*, 114:6389–95, 2010.

[8] S Dittmer, J Ek-Weis, O A Nerushev, and E E B Campbell. *J. Nanosci. Nanotech.*, 10:4015–22, 2010.

[9] Z-P Yang, L Ci, J A Bur, S-Y Lin, and P M Ajayan. *Nano Lett.*, 8:446–51, 2008.

Visible iridescence from self-assembled periodic rippling in vertically aligned carbon nanotube forests

Phillip Vinten,[1,2] Jacques Lefebvre,[1] and Paul Finnie[1,2,a)]
[1]*Institute for Microstructural Sciences, National Research Council Canada, Building M-50, 1200 Montreal Road, Ottawa, Ontario K1A 0R6, Canada*
[2]*Department of Physics, University of Ottawa, 150 Louis Pasteur, Ottawa, Ontario K1N 6N5, Canada*

(Received 20 May 2010; accepted 28 June 2010; published online 7 September 2010)

We observe iridescence in the form of spectrally dispersed white light reflected from the structured sidewalls of vertically aligned carbon nanotube forests. The iridescence is a result of diffraction from a self-assembled periodic rippling pattern on the forest sidewalls that acts as a reflection grating. We measure the grating spacing via white light and laser diffraction experiments and see good agreement with the spacing of the rippling pattern as measured via scanning electron microscopy. The periodic rippling pattern self-assembles during chemical vapor deposition growth of the forests. © *2010 American Institute of Physics*. [doi:10.1063/1.3485084]

Optical properties of ensembles of carbon nanotubes, such as forests of vertically aligned nanotubes, are increasingly of interest. For example, Yang *et al.*[1] report that nanotube forests are among the blackest known materials when observed along the axes of the nanotubes. However, at other angles of incidence, nanotube forests are noticeably reflective, particularly from their sidewalls. If the sidewall surface has a periodic modulation, then one would expect it to act as a diffraction grating and spectrally disperse white light. Such a periodic rippling pattern can form spontaneously during growth.[2–6] Ripples can also be obtained by compressing a forest along the axis of the nanotubes, either during growth,[7] or postgrowth.[8–10] Iridescence from periodic arrangements of individual vertically aligned multiwalled nanotubes on a substrate[11–13] and periodic arrangements forests on a substrate[14] has previously been observed. Here, it is the rippled structure of the forest itself that causes the iridescence, not their arrangement on the substrate. The periodicity of the ripples is extremely consistent and they generally have a spacing similar to the wavelength of visible light. When a large enough area of ripples is present on the sidewalls of a forest, we easily observe brilliant colors reflected from the forests as a result of optical diffraction via a reflection grating effect. Using simple optics and scanning electron microscopy (SEM), we show that the iridescence is indeed a result of the rippling pattern.

Forests were grown at 760 °C using a cold-walled chemical vapor deposition reactor operated at atmospheric pressure using C_2H_2 as the carbon source and H_2 and H_2O vapor as enhancers. Samples were approximately 5 $\times 5$ mm^2 pieces of Si/SiO_2 patterned with circular Al_2O_3/Co catalyst islands (100–800 μm in diameter). Details can be found in a previous report.[15] Optical images were acquired through a long focal length microscope with a digital camera, with the color balance adjusted so the image on the monitor appeared as it does to the naked eye. A 1 mW HeNe (632.8 nm) laser, focused with a lens and passed through a variable intensity filter was used for laser illumination. The laser and white light source were parallel. All optical components, including the sample, rotated about a common axis through the sample.

Figure 1(a) shows an optical image of white light diffraction from numerous 100 μm diameter forest pillars. Forests are organized on a hexagonal grid with ~100 μm spacing at the base. The forests usually become bent and tipped over during growth. Colors are more brilliant slightly out of focus, likely because they dominate over the blackness around them. Figure 1(b) shows an SEM image of the ripples on a forest from Fig. 1(a), which appear similar to previous reports.[2–10] Here, ripples form spontaneously during growth, likely due to a growth rate difference between different nanotubes in the forest,[3,4] which in turn causes a compressive strain that bends the nanotubes. It is known that growing nanotubes exert a mechanical force,[7] which likely causes the compressive strain. The presence of strain is also suggested by the ripples generated by intentional compression of forests.[7–10] The periodic nature of the ripples is likely due to the balance between the stiffness of the nanotubes that resists bending and the van der Waals interaction between nanotubes. The van der Waals interaction is also responsible for the long range synchronization of the amplitude and the wavelength. The observed ripple spacing is similar to the average length over which nanotubes come into contact with one another in a forest.[15,16]

The angular positions of the intensity maxima of a grating are given by the grating equation: $n\lambda = d(\sin\theta_n + \sin\theta_i)$ where n is the order of the maximum (here $n=1$), λ is the wavelength observed at the maximum, d is the grating spac-

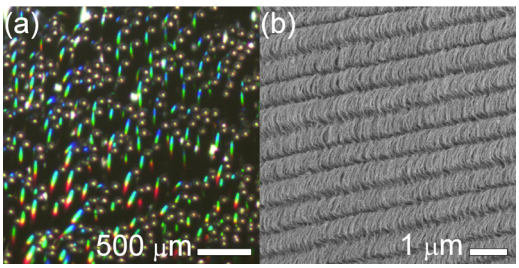


FIG. 1. (Color online) (a) Optical image of white light diffraction from numerous 100 μm diameter forest pillars. (b) SEM image of periodic rippling pattern from a forest on the same sample.

a)Electronic mail: [REDACTED].

0003-6951/2010/97(10)/101901/3/$30.00 © 2010 American Institute of Physics

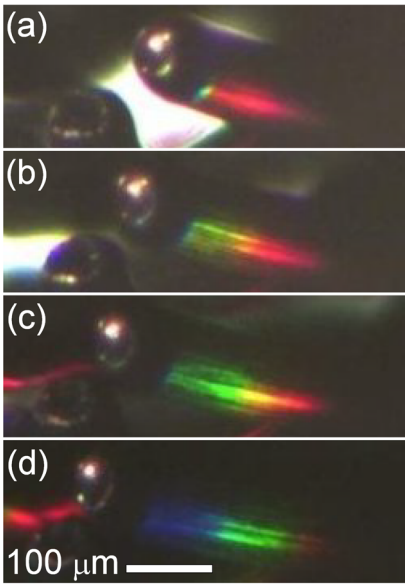


FIG. 2. (Color online) Optical images of forest (100 μm diameter) being rotated by ~5° intervals (angle of incidence and observation change simultaneously) showing a change in color from red (a) to green-red (b) and (c) to blue-green (d).

ing, θ_n is the angle of the maximum (angle of observation), and θ_i is the angle of incidence. The grating constant is $N=1/d$.

Optical images of white light diffraction from a single 100 μm forest (Fig. 2) show that tilting the forest by ~5° toward normal incidence (θ_n and θ_i decrease simultaneously) causes a change in color from red (a) to green-red (b) and (c) to blue-green (d). This change in color can be used to estimate d. For these measurements, θ_n is fixed, θ_i is scanned across the sample, and λ is estimated from the observed color. Using the grating equation, d was calculated for several (λ, θ_i) pairs for the same area of a forest and averaged. Results for three different 700 μm diameter forests (forests W1–W3) are given in Table I. To confirm that the diffraction is indeed a result of the ripples, d was measured by SEM at the same location that the diffraction was observed. These values are presented in Table I, along with corresponding values of N. We used 700 μm diameter forests because these larger forests are usually perpendicular to the substrate, which makes angular measurements easier. Larger forests are also easier to manipulate, have a smaller curvature, and larger surface area than the smaller forests.

We also measured d with HeNe laser illumination using 400 μm diameter forests (forests L1–L3). Here, $\lambda = 632.8$ nm and θ_n and θ_i are varied simultaneously by rotating the sample. Angular measurements include slight corrections, obtained by SEM observation, to account for the fact that the 400 μm forests are not exactly perpendicular to the substrate. Figure 3(a) shows an optical image of forest L1 illuminated by both white light and the HeNe laser and reflecting colors. An SEM image of forest L1 from approximately the same view point is shown in Fig. 3(b). Figure 3(c) is a close up SEM image of the area indicated (approximately) in Figs. 3(a) and 3(b), where measurements were taken, showing the periodic rippling pattern that acts as the reflection grating. Compared to Fig. 1(b), these ripples have a very small amplitude, but even these small ripples are sufficient to produce a pronounced grating effect. Quantitative results for forest L1 and specific regions of two other forests measured with laser diffraction are given in Table II.

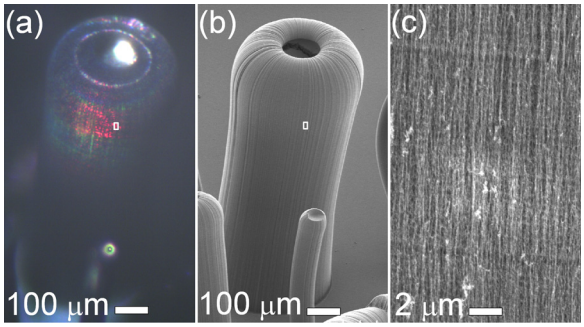


FIG. 3. (Color online) Forest L1 (400 μm diameter). (a) Optical image (black-white contrast enhanced) with white light and HeNe laser illumination showing reflected colors. (b) SEM image of the same forest. (c) Close up of area indicated (approximately) in (a) and (b) showing grating. Grating parameters given in Table II.

Grating efficiency was measured by diffracting the 1 mW HeNe laser (632.8 nm), of which 10% was incident on the grating area, and collecting 0.1 μW from the first order maximum, giving a grating efficiency of 0.1%. This is impressive because the forest is very sparse, and also because nanotubes are known for their strong absorption.

For all forests, both those measured by white light (Table I) and laser illumination (Table II), d is similar whether measured optically or by SEM. The discrepancy between the optical and SEM value of d is larger for the white light measurements than for the laser measurements. This is primarily a result of the uncertainty in the wavelength of the light which was simply estimated by eye from the color of the digital image, and is uncertain by as much as ±25 nm. Any further discrepancy is most likely caused by the fact that these gratings are not ideal because they are not, in general, flat. Not only are the forests round, but their sidewalls curve inward near the top, as seen in Fig. 3(b). Furthermore, there is only ever a small flat area of ripples to act as a single unified grating, making it difficult to align, particularly in

TABLE I. Grating spacing d for three forests (700 μm diameter), measured by white light diffraction and SEM, and grating constant $N=1/d$, determined by SEM.

Forest	d_{WL} (nm)	d_{SEM} (nm)	N_{SEM} (mm^{-1})
W1	310 ± 40	500 ± 20	2020 ± 60
W2	440 ± 100	490 ± 5	2040 ± 20
W3	330 ± 140	470 ± 10	2130 ± 50

TABLE II. Grating spacing d for three forests (400 μm diameter), measured by HeNe (632.8 nm) laser diffraction and SEM, and grating constant $N=1/d$, determined by SEM.

Forest	d_{HeNe} (nm)	d_{SEM} (nm)	N_{SEM} (mm^{-1})
L1[a]	440 ± 10	466 ± 5	2150 ± 20
L2	740 ± 30	620 ± 10	1610 ± 40
L3	1500 ± 100	1540 ± 40	650 ± 20

[a]See Fig. 3.

defining the normal direction. Even small errors in angular measurements can cause large uncertainties in d.

The grating spacing d is generally the same order of magnitude from one forest to another, but variations exist. In particular, the large d of forest L3 is the result of a stacking fault in the rippling pattern that effectively doubles the spacing of the pattern. It is somewhat remarkable that the ripples are regular enough over a large enough area to give rise to the diffraction of visible light. With proper control over the formation of the ripples it should be possible to create a variety of gratings, particularly highly dispersive gratings with narrow spacing (high grating constants). In the present report, gratings with ~2000 lines/mm are routinely obtained.

In summary, we observe brilliant iridescence of light reflected by carbon nanotubes forests. These colors are a result of a reflection grating effect generated by a periodic rippling pattern on the sidewalls of the forests. The diffracted colors were correlated with the rippling pattern by measuring the grating spacing via white light and laser diffraction, and then comparing this value to SEM measurements of the same area, with reasonably good agreement. We obtain predominantly highly dispersive gratings but also gratings of low dispersion. The periodic rippling pattern forms spontaneously during growth, providing a self-assembled method to fabricate high dispersion gratings.

The authors thank J. Bond for preliminary work and the following IMS staff for their support: P. Marshall, J. Fraser, H. Tran, and M. Denhoff. P.V. was supported by NSERC, NRC-GSSSP, and P.F.'s NSERC Discovery Grant.

[1]Z.-P. Yang, L. Ci, J. A. Bur, S.-Y. Lin, and P. M. Ajayan, Nano Lett. **8**, 446 (2008).
[2]H. Wang, Z. Xu, and G. Eres, Appl. Phys. Lett. **88**, 213111 (2006).
[3]Q. Zhang, W. Zhou, W. Qian, R. Xiang, J. Huang, D. Wang, and F. Wei, J. Phys. Chem. C **111**, 14638 (2007).
[4]Y. Zhang, G. Zou, S. K. Doorn, H. Htoon, L. Stan, M. E. Hawley, C. J. Sheehan, Y. Zhu, and Q. Jia, ACS Nano **3**, 2157 (2009).
[5]X. Cui, W. Wei, C. Harrower, and W. Chen, Carbon **47**, 3441 (2009).
[6]M. Bedewy, E. R. Meshot, H. Guo, E. A. Verploegen, W. Lu, and A. J. Hart, J. Phys. Chem. C **113**, 20576 (2009).
[7]A. J. Hart and A. H. Slocum, Nano Lett. **6**, 1254 (2006).
[8]A. Cao, P. L. Dickrell, W. G. Sawyer, M. N. Ghasemi-Nejhad, and P. M. Ajayan, Science **310**, 1307 (2005).
[9]V. L. Pushparaj, L. Ci, S. Sreekala, A. Kumar, S. Kesapragada, D. Gall, O. Nalamasu, A. M. Pulickel, and J. Suhr, Appl. Phys. Lett. **91**, 153116 (2007).
[10]B. N. Wang, R. D. Bennett, E. Verploegen, A. J. Hart, and R. E. Cohen, J. Phys. Chem. C **111**, 17933 (2007).
[11]K. Kempa, B. Kimball, J. Rybczynski, Z. P. Huang, P. F. Wu, D. Steeves, M. Sennett, M. Giersig, D. V. G. L. N. Rao, D. L. Carnahan, D. Z. Wang, J. Y. Lao, W. Z. Li, and Z. F. Ren, Nano Lett. **3**, 13 (2003).
[12]Y. Wang, K. Kempa, B. Kimball, J. B. Carlson, G. Benham, W. Z. Li, T. Kempa, J. Rybczynski, A. Herczynski, and Z. F. Ren, Appl. Phys. Lett. **85**, 2607 (2004).
[13]J. Rybczynski, K. Kempa, Y. Wang, Z. F. Ren, J. B. Carlson, B. R. Kimball, and G. Benham, Appl. Phys. Lett. **88**, 203122 (2006).
[14]K.-C. Hsieh, T.-Y. Tsai, D. Wan, H.-L. Chen, and N.-H. Tai, ACS Nano **4**, 1327 (2010).
[15]P. Vinten, P. Marshall, J. Lefebvre, and P. Finnie, Nanotechnology **21**, 035603 (2010).
[16]A. A. Zbib, S. Dj Mesarovic, E. T. Lilleodden, D. McClain, J. Jiao, and D. F. Bahr, Nanotechnology **19**, 175704 (2008).

Chapter 6

Origin of periodic rippling during chemical vapor deposition growth of carbon nanotube forests

as published* in *Carbon*, Volume 49, Pages 4972–4981, 2011.
http://dx.doi.org/10.1016/j.carbon.2011.02.017

This article includes supplementary material. The printable portion of that material is reprinted here in Appendix C. The multimedia portion of that material is available from the University of Ottawa's thesis repository (uO Research) as indicated in the List of videos, as well as the article's publisher's website, which can be accessed using the above hyperlink.

*In accordance with University of Ottawa regulations, the contact email address has been removed from this article.

Foreword

This chapter is a follow up to Chapter 5 and provides a thorough examination of the self-organized spontaneous rippling pattern and the mechanism by which they form. In particular, this chapter makes use of observations in Chapter 4 of a non-uniform growth rate across the catalyst island. Further observations presented in this chapter include analyzing the interior of the forest structure with SEM (by breaking the forests open) to examine how the ripples behave as a function of position. The result of this analysis agrees with previous observations (Chapter 4) of a non-uniform growth rate. In addition, the diffraction of white light is observed to occur *in situ* while the nanotubes forests are growing, which confirms that they do form as a result of and during the growth process. Finally, the diffraction is observed and followed as the growth terminates and the reactor is purged of the carbon source and cooled down to room temperature, thus showing that thermal relaxation does not play a role in the formation of the ripples either.

Several previous reports have proposed growth rate differences between the nanotubes and interactions between these nanotubes as the source of the observed rippling [1–5]. This chapter provides *in situ* observations of the rippling morphology (via the diffraction grating effect), thus demonstrating that the ripples do indeed form during growth and not afterward.

Using the non-uniform growth rate as the primary source of strain, it is possible to describe the rippling pattern quite well and create a clear picture of how the nanotubes in the forest grow. This result validates the understanding of strain that was developed in Chapter 3 and Chapter 4. It also reinforces the picture that interactions between individual nanotubes in the forests play a significant role in the evolution and morphology of forests, and even affect the growth kinetics of carbon nanotube forests.

---

[1] H Wang, Z Xu, and G Eres. *Appl. Phys. Lett.*, 88:213111, 2006.

[2] Q Zhang, W Zhou, W Qian, R Xiang, J Huang, D Wang, and F Wei. *J. Phys. Chem. C*, 111:14638–43, 2007.

[3] Y Zhang, G Zou, S K Doorn, H Htoon, L Stan, M E Hawley, C J Sheehan, Y Zhu, and Q Jia. *ACS Nano*, 3:2157–62, 2009.

[4] Y Zhang, J M Gregoire, R B van Dover, and A J Hart. *J. Phys. Chem. C*, 114:6389–95, 2010.

[5] S Dittmer, J Ek-Weis, O A Nerushev, and E E B Campbell. *J. Nanosci. Nanotech.*, 10:4015–22, 2010.

CARBON 49 (2011) 4972–4981

available at www.sciencedirect.com

ScienceDirect

journal homepage: www.elsevier.com/locate/carbon

Origin of periodic rippling during chemical vapor deposition growth of carbon nanotube forests

P. Vinten [a,b], J. Bond [a,b], P. Marshall [a], J. Lefebvre [a], P. Finnie [a,b,*]

[a] Institute for Microstructural Sciences, National Research Council Canada, Building M-50, 1200 Montreal Road, Ottawa, ON, Canada K1A 0R6

[b] Department of Physics, University of Ottawa, 150 Louis Pasteur, Ottawa, ON, Canada K1N 6N5

ARTICLE INFO

Article history:
Received 25 November 2010
Accepted 8 February 2011
Available online 13 February 2011

ABSTRACT

Carbon nanotube forests are arrays of roughly vertically aligned nanotubes. Under certain growth conditions, these forests can show a growth instability that gives rise to periodic ripples that are coherent over a forest-sized scale. Previously, we showed that the uniformity and synchronization of the ripples is sufficient for them to behave as diffraction gratings for visible light. Here, we identify the conditions that reproducibly promote the formation of these ripples. We investigate the formation mechanism via *ex situ* scanning electron microscopy and *in situ* optical imaging. While the rippling amplitude varies appreciably, the rippling wavelength varies very little and can be estimated from simple mechanical considerations. We provide evidence that the rippling is a consequence of cohesive interactions between nanotubes and the build up of strain, driven by a non-uniform growth rate. The origin of the non-uniform growth rate is explained.

Crown Copyright © 2011 Published by Elsevier Ltd. All rights reserved.

1. Introduction

The growth of vertically aligned carbon nanotube forests is studied extensively because it represents one of the highest yield methods of nanotube growth. Originally observed in multi-walled carbon nanotube (MWCNT) samples, vertically aligned single-walled carbon nanotube (SWCNT) forests are now the focus of much attention. Over large length scales, the nanotubes in forests appear densely packed and, on average, very straight and well aligned. However, closer analysis via scanning electron microscopy (SEM) reveals that, on the micrometer scale, forests are mostly empty space filled with individual nanotubes and bundles of nanotubes that are far from straight, and instead meander back and forth in a seemingly random and disordered manner. Under certain growth conditions, the meandering becomes highly ordered, coherent, and synchronized over lengths of hundreds of μm such that the sidewalls of the forest have a rippling pattern on them. Previous reports of ripples on as-grown forests, such as in the present report, include ripples on forests grown with externally applied forces *in situ* [1], wandering nanotubes in forests due to specific catalyst pretreatment and preparation methods [2–5], ripples near the base of tall forests [6,7], and ripples due to a temperature non-uniformity in micrometer scale local heating [8]. A similar rippling pattern can also occur on forests (composed of initially straight nanotubes) that are intentionally subjected to externally applied mechanical compression *ex situ* [9–11]. The interactions between nanotubes have previously been shown to be important for forest morphology [6–8,12–19], and will be considered here.

In the present report, the forests are not compressed by external forces. The rippled nanotubes self-assemble during chemical vapour deposition (CVD) growth of the forests without any intentional special catalyst preparation or pretreatment, and are, most importantly, entirely reproducible. Remarkably, the ripples we obtain are sufficiently regular over

* *Corresponding author:* Address: Institute for Microstructural Sciences, National Research Council Canada, Building M-50, 1200 Montreal Road, Ottawa, ON, Canada K1A 0R6.
E-mail address: [REDACTED].

0008-6223/$ - see front matter Crown Copyright © 2011 Published by Elsevier Ltd. All rights reserved.
doi:10.1016/j.carbon.2011.02.017

a large enough area that they produce an easily observed optical effect: iridescence caused by the diffraction of visible light via a surface grating effect [20]. This iridescence provides a means to observe the ripples optically since they are too small for direct observation with visible light. In particular, it allows us to observe the ripples *in situ* and thus provides valuable clues to the nature of the formation mechanism responsible for these ripples. We identify the reactor conditions that promote the formation of ripples. Using *in situ* observations as well as *ex situ* SEM observations, we support a formation mechanism: the ripples are a growth instability caused by the build-up of strain within the forest as it grows due to a difference in growth rate between different nanotubes in the forest.

2. Experimental procedures

Samples were grown by water-assisted [21] CVD using acetylene as the carbon source [22–25], and alumina/cobalt thin films as the catalyst. We used a cold-walled CVD reactor, operated at atmospheric pressure, as described in our previous reports [12,26], with additional details given in [27,28]. The carbon source was supplied as dilute acetylene gas (0.1% C_2H_2, 99.9% Ar), assisted by hydrogen (2% H_2, 98% Ar) and water vapour obtained by passing pure Ar through a bubbler. Samples were ~ 0.3 cm^2 square pieces of 0.5 mm thick Si with 1 μm thermal SiO_2, and catalyst layers of nominally 250 nm Al_2O_3 and 0.8 nm Co deposited by e-beam evaporation through a shadow mask to produce 100 μm to 800 μm diameter circles in evenly spaced patterns. Some samples were also prepared using photolithography, but they are not presented in detail here. Forests grown under this range of conditions are expected to consist of a mixture of MWCNTs and SWCNTs [12].

In the present report, we vary the temperature and the source gas flow rate (see Appendix for procedural details). Unless otherwise stated, all forest growth self-terminated without external intervention such as stopping the flow of the carbon source. No external forces are applied to the forests during growth or after growth. *In situ* optical images and videos were acquired through the large glass window in the reactor using a long focal length optical microscope and digital camera at a glancing angle of ~5° to the substrate. *Ex situ* optical images and videos were acquired using the same microscope and camera in a different configuration. SEM images were obtained *ex situ* using a Hitachi S-4700 field emission SEM.

3. Results

Terminal forest heights H_t for the rippled forests varied from ~200 μm to ~500 μm for the 100 μm diameter forests and were ~1 mm for the 700 and 800 μm diameter forests. Maximum forest height, top surface concavity, and curvature of the sidewalls all occurred around 760 °C and 180 sccm source gas flow rate. Ripples form reproducibly on forests grown in the temperature range 730 °C $< T <$ 800 °C at a source gas (C_2H_2) flow rate of 180 sccm, with the most prominent ripples (largest amplitudes) appearing around 760 °C. For forests grown at temperatures progressively further from 760 °C, the height, concavity, and curvature of the sidewalls all decreased, while the ripples simultaneously disappeared (their amplitude vanished). Outside of the above temperature range no rippling occurred; the top surfaces of the forests are flat and the sidewalls are smooth and vertical.

A similar trend was observed for the C_2H_2 flow rate dependence. Rippling occurred reproducibly for source gas flow rates (other gas flow rates fixed) between 100 sccm and 220 sccm at a growth temperature of 760 °C. The most prominent ripples occurred around 180 sccm: the same flow rate as the maximum forest height, concavity, and curvature of the sidewalls. At gas flow rates progressively further from 180 sccm, the height, concavity, and curvature of the sidewalls all decreased, while at the same time the ripples disappeared by diminishing amplitudes. Outside of the above flow rate range there are no ripples, the top surfaces of the forests are flat, and the sidewalls are smooth and vertical. Unlike the amplitude, the wavelength of the ripples did not vary much or show a clear trend with any change in the growth parameters.

The smaller diameter forests (100 μm) had ripples over most of the temperature and flow rate ranges analyzed, while the larger diameter forests (700 μm) had ripples only over a narrow temperature and flow rate range centered on 760 °C and 180 sccm. This suggests that there is a dependence on catalyst island size.

The rippling on the forests' sidewalls is synchronized over length scales similar to the size of the forest (see Fig. 1a). The rippling is characterized by smooth consistent curves without any sharp kinks or bends. For any given nanotube, the rippling occurs in a plane, thus they are not helixes such as those observed in other systems [29]. The ripples generally encircle the entire forest (Fig. 1a) from near the top on the curved portion of the sidewalls (Fig. 1b) and down the vertical sidewalls (Fig. 1c–d) where the amplitude slowly fades to zero (Fig. 1e–f) before reaching the base of the forest, where the nanotubes appear straight. In some previous reports, the ripples were observed to form only at the base of the forest [6,7]. Here, the ripples extend for a significant portion of the forest height, as seen in an earlier report [8]. Furthermore, all nanotubes on the forests' sidewalls participate in the rippling; no straight nanotubes are visible, in contrast to several other previous studies [2,3].

The ripples have a clearly defined and measurable wavelength and amplitude (see Fig. 2a for an example). The rippling amplitude was measured using SEM by looking tangentially to the circular cross section of the cylindrical forests. This shows the wave-like profile of the ripples, as shown in the example in Fig. 2a. The amplitude can then be simply measured as the height of the wave-like profile. From analyzing many forests, the amplitude is observed to vary from one forest to another, ranging from as large as ~1 μm to as small as zero. Although the rippling amplitude decreases gradually from the top of any given forest to the bottom, the variation is slow enough that it appears approximately constant (extremely slowly varying) over short distances of several tens of μm (see Fig. 2a).

The wavelength can be measured in the same way as the amplitude, though most wavelength measurements were taken using SEM looking normally toward the rippled

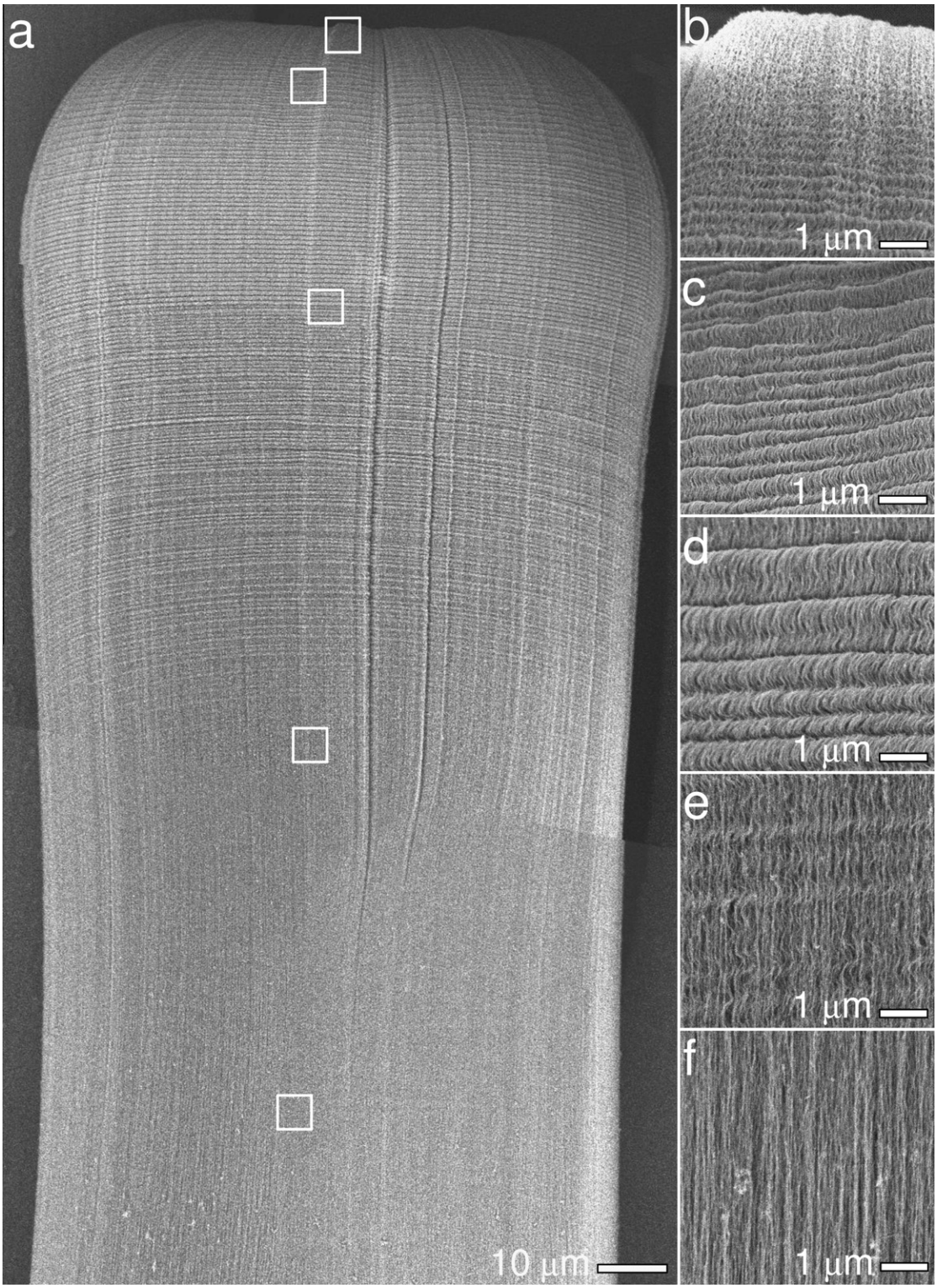


Fig. 1 – SEM images of rippled forest. (a) Top part of forest (~350 μm tall) grown on a 100 μm diameter catalyst island. This image was constructed from several individual SEM images. (b–f) Close-ups of indicated areas in (a). The ripples in (b) appear to have a short wavelength because the forest is curving away from the plane of view. This forest was grown at 730 °C using 180 sccm C_2H_2 flow rate.

sidewalls, similar to Fig. 3c. For such wavelength measurements, a high contrast between the peaks and valleys of the rippling pattern is more important than a high resolution that can distinguish the individual nanotubes. From analyzing many forests, the wavelength is observed to vary between ~300 nm and ~1 μm. This length is similar to the length scale

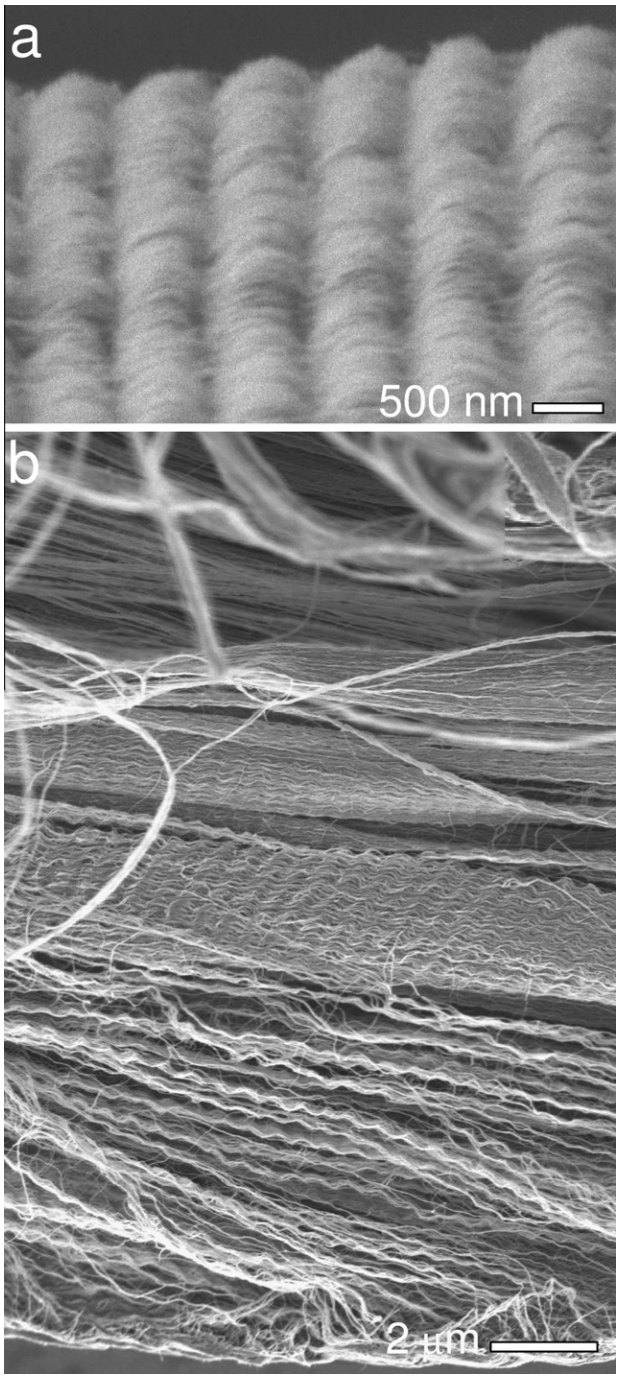


Fig. 2 – SEM images of ripples on 100 μm diameter forests. (a) Wavelength and amplitude seen looking tangential to the forest circumference (at a glancing angle to the outer wall of the forest). (b) Forest (horizontal orientation) split open along its length, showing the amplitude decreasing to zero toward the center of the forest. The view is along the forest radius, looking into the split, toward the center of the forest. This image was constructed from several individual SEM images. These forests were grown at 730 °C and 760 °C respectively, using 180 sccm C_2H_2 flow rate.

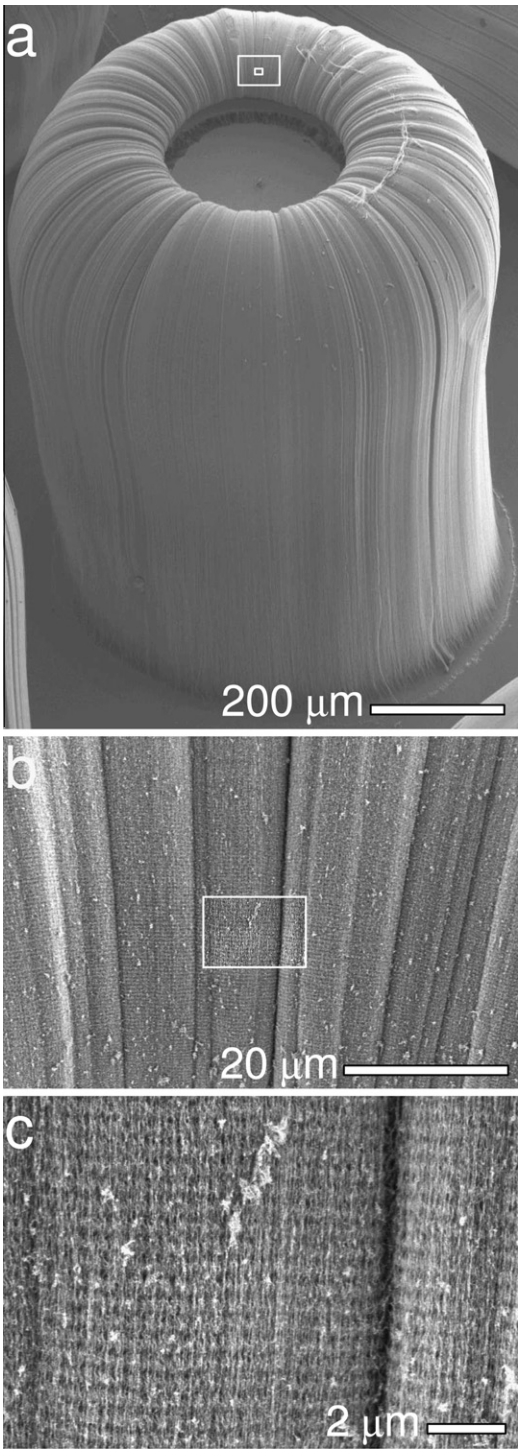


Fig. 3 – SEM images of rippled forest (700 μm diameter, ~1 mm tall). (a) Entire forest viewed at 45°. (b) Close-up image of larger box in (a) showing ripples over a wide area. (c) Close-up of box in (b). The ripple spacing is 470 ± 10 nm. This forest was grown at 760 °C using 220 sccm C_2H_2 flow rate.

that wandering nanotubes in a forest typically come into contact with one another [12,13]. While the wavelength did not vary significantly over short distances of several dozen μm on any given forest, it did vary significantly from one forest to another, even forests grown under the same conditions

or on the same growth substrate. The wavelength showed no clear trend with location on the forest.

While there are areas of several μm² of approximately constant wavelength and amplitude on many forests, there are occasionally abrupt changes from one wavelength and/or amplitude to another (see Fig. 1d). Such changes in wavelength are "faults" or "dislocations" in which ripples of similar wavelength become locally mismatched, as is apparent in Fig. 1c.

In situ optical monitoring during growth reveals that all the nanotubes in a forest start growing at the same time from the flat substrate (see our previous reports [12,26]). It also reveals that the top surface of the forest becomes concave as soon as the forests begin to grow, and it quickly evolves to its final form (see Fig. 1a and Fig. 3a) within a few minutes after growth is initiated (under the present growth conditions). The concave top surface must then be caused by the outer nanotubes of the forest growing faster than the inner nanotubes, clearly demonstrating the existence of a growth rate difference. This growth rate difference is well defined by the shape of the concave top surface. All rippled nanotube forests observed in the present report have concave top surfaces, which leads us to believe that, in the present case, concavity and rippling are intimately related.

Because of their small size, ripples are not directly observable using optical imaging. Previously, we showed that rippled forests, such as those in the present report, can be observed optically via diffraction because they behave as gratings [20]. This effect allows their periodicity to be directly calculated from the simple grating equation, and shows that the ripples are very consistent over significant areas, for if they were not, clear diffraction patterns, such as those observed here, would not be seen. By comparing the optically determined grating spacing with the rippling wavelength determined from SEM images of the same location on the forest as the diffraction, we correlate the diffraction to the rippled nanotubes. The fact that diffraction occurs in the visible region of the spectrum is itself an indicator that the wavelength and amplitude of the ripples are the order of magnitude as the wavelength of visible light.

In situ diffraction of white light is visible in Fig. 4a, which is a frame from video S1 (see supplementary material); a red patch of reflected light is visible on the far side of the growing forest's curved sidewalls. An SEM image of this forest is shown in Fig. 3, with the approximate location of the rippled nanotube forest grating responsible for the diffraction indicated. *Ex situ* optical examination of this forest allows the full range of angles of incidence and observation to be analyzed. Long working distance optical microscope observations of diffraction in Fig. 5 show the results from this forest in approximately the same location as seen in Fig. 4a and Fig. 3. The observed colour changes from red to blue (a–j) as the angle of incidence is swept across the sample in 4° intervals. Based on the diffraction data the grating spacing is 330 ± 140 nm, which agrees with the 470 ± 10 nm measured by SEM [20].

Iridescence was also observed *in situ* from many smaller 100 μm diameter forests growing simultaneously (see Fig. 4b and supplementary material video S2), showing that this is not an isolated phenomenon.

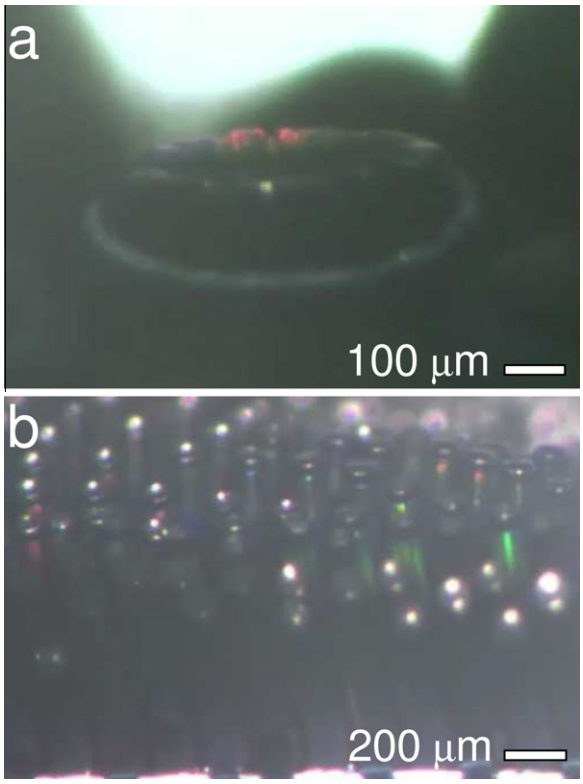


Fig. 4 – *In situ* optical images. (a) Growing 700 μm diameter forest showing iridescence (red patch) from the far side of its curved sidewalls. An SEM image of this forest is shown in Fig. 3. Iridescence occurs near the area indicated in Fig. 3. Here, the forest is observed at an ~5° glancing angle, but in the same direction as in Fig. 3. See supplementary material video S1. (b) Iridescence from multiple 100 μm diameter forests. See supplementary material video S2. Both forests were grown at 760°C using 220 sccm and 180 sccm C_2 H_2 flow rates respectively. (For interpretation of the references to colour in this figure legend, the reader is referred to the web version of this article.)

By observing the iridescence from forests as they are cooled post-growth in the reactor, we see that the diffracted colours do not change, hence the wavelength of the ripples does not change (see supplementary material video S3, which shows a sample of 100 μm diameter forests). The post-growth cooling process is therefore not involved in ripple formation. Furthermore, this shows that the ripples are remarkably stable over a wide range of temperatures. Even as the temperature is reduced from ~800 °C to room temperature (over a factor of 3 in absolute temperature) the diffracted colours, and hence the ripple wavelength, do not change at all, meaning that any thermal expansion and other relaxation effects are negligible. From *in situ* observations of iridescence, it is clear that the ripples form during the growth of the forests, and that they are minimally affected afterward.

To gain more insight into ripple formation, and because the ripples are not directly observable via optical imaging, a series of forests was grown under identical reactor conditions and intentionally halted (prior to ordinary self-termination) by stopping the flow of process gases after various growth

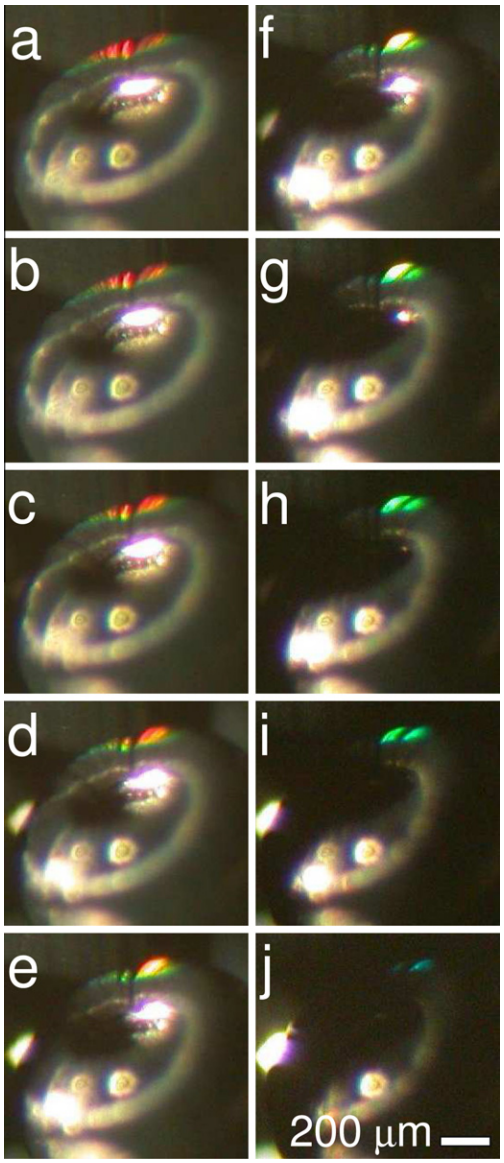


Fig. 5 – Long working distance *ex situ* optical images showing the diffraction grating effect from the forest in Fig. 3 and Fig. 4a. Colours progress from red to blue (a–j) as the angle of incidence is swept across the sample in 4° intervals. (For interpretation of the references to colour in this figure legend, the reader is referred to the web version of this article.)

times and purging the reactor with pure Ar. Subsequent *ex situ* SEM imaging of these forests reveals that ripples begin forming within the first minute, before the top surface of the forest has reached its final concave shape. On forests intentionally terminated early enough (less than 10–20 min of growth time, depending on reactor conditions), ripples are observed to extend all the way to the base of the forest. However, after longer growth times (more than 10–20 min), the rippling amplitude near the base of the forest becomes so small that ripples are not observable and the nanotubes appear straight as they near the bottom of the forest, as seen in self-terminated forests, such as Fig. 1a.

More insight into the nature and origin of these ripples comes from destructively examining a forest. By breaking open a forest with tweezers, it can be seen, using SEM, that the inner most nanotubes in the forest (those nearest the center of the circular cross section) are straight. Moving inward from the sidewalls, where the outer nanotubes are rippled with large amplitudes, toward the center, the amplitude of the ripples decreases to zero (see Fig. 2b). Thus, the rippling is not evenly distributed across the forest, unlike the random distributions in several previous reports [2,3]. The distribution observed here is different than a previously observed non-random distribution [8].

4. Discussion

Several previously published reports observe rippling as a result of *ex situ* compression [9–11]. Cao et al. [9] and Pushparaj et al. [10] see the nanotubes near the bottom of their forests buckle when an external force is applied *ex situ*. The buckling slowly disappears toward the top of the forest. They propose that this buckling is due to the compression and the spatial restrictions from neighbouring nanotubes. It is important to note that the ripples observed in these reports are not formed during the growth of the forest, but are instead formed afterward by applying an external force. Nevertheless, the visual similarities can give insight into the present data.

Hart and Slocum [1] applied external mechanical compression to forests as they grew and showed that growing nanotubes exert a force. The authors propose that the mechanical force exerted by growing nanotubes and the lateral constraint of neighbouring nanotubes forces them into their “serpentine” structure. They noted that higher applied forces produced ripples with smaller wavelengths and that the wavelength decreased toward the base of the forest. While these ripples did form during the growth of the forest, it was a result of the externally applied force.

Some reports of ripples, such as those presented here, do not involve the application of external forces, but instead have ripples that naturally form during the growth process. Rippling in specially prepared catalyst samples is observed in several reports [2–5]. Qiang Zhang et al. [2] propose that the ripples are caused by the close proximity of the nanotubes to each other and a difference in the growth rate between different nanotubes in the forest that is caused by a non-uniform catalyst nanoparticle size. They see a mixture of straight nanotubes (slow growing) and rippled nanotubes (fast growing) and note a random distribution of the rippling phenomenon. They also mention that the woven structure of nanotubes at the top of the forest causes the faster growing nanotubes to bend. Yingying Zhang et al. [3] similarly propose a difference in growth rate caused by a non-uniform catalyst nanoparticle size as the cause of the rippling. They see a random distribution of the rippled nanotubes throughout the forest, but note that it is the smaller diameter nanotubes growing from smaller catalyst nanoparticles that grow faster and are thus forced to ripple. Yongyi Zhang et al. [5] propose that their ripples are due to mechanical stresses in the forest caused by a spatial growth rate difference from an intentionally non-uniform catalyst layer.

Wang et al. [6] propose that different growth rates between nanotubes cause the faster growing tubes to adopt curved structures, both helical and zig zag. Their ripples become more prominent later in the forest growth and seem randomly distributed throughout the forest, mixed with straight nanotubes. Bedewy et al. [7] see ripples only several μm from the base of the forest, and propose that their ripples are caused by the collapse of the forest structure due to growth cessation of individual nanotubes.

Dittmer et al. [8] see a non-random distribution of ripples in their forests, though their distribution is essentially the opposite of the present report (straight nanotubes on the edges). They explain their ripples as a result of mechanical interaction between nanotubes and a non-uniform growth rate across their small forests that is in turn a result of a non-uniform temperature across their sample due to their local heating process.

The fact that ripples form during many different CVD processes, indicates that ripples are not specific to any one choice of source gas or reactor geometry.

As described above, several previous reports [2,3,5,6,8] propose that a growth rate difference was the cause of the ripples. A key difference between the present report and most of those reports [2,3,5,6] is in the distribution of the fast and slow growing nanotubes within the forest. In those reports, the distribution was random, but here the distribution is spatially non-uniform. Another report [8] saw a non-uniform growth rate distribution, but it is unlike the concentric growth rate distribution observed here.

Morphological similarities between our rippled forests and those which are generated by externally applied forces [1,9–11] suggest that strain within the forest plays a role in ripple formation.

Strain and a growth rate difference are linked together: a growth rate difference will cause the faster growing outer nanotubes to be strained by the mechanical force they exert during growth [1] against the forest above the growth front, which is held together by van der Waals interactions between nanotubes. Relative to the faster growing outer nanotubes, the forest is anchored to the substrate by the slower growing inner nanotubes. The forest and substrate then behave as top and bottom boundary conditions respectively and thus enforce a uniform vertical growth rate (equal to the slower growth rate of the inner nanotubes) upon all of the nanotubes in the forest. This top boundary condition is similar to the woven structure described by Qiang Zhang et al. [2], but is more than just a layer – it is the entire forest.

Rippling, then, is a growth instability that occurs to relieve strain. Rippling allows the faster growing outer nanotubes to grow to a longer length than the slower growing inner nanotubes in a given time interval, while still growing to the same height above the substrate in that time interval. Spatial constraints due to neighbouring nanotubes then cause the rippling [1–3,9,10] because all nanotubes are constrained to wander within a narrow region of the forest. The long range synchronization of the rippling pattern is due to the cohesive van der Waals interactions between nanotubes.

The overall forest growth would proceed as follows. When the forest begins growing, we suppose that the faster growth rate of the outer nanotubes is at first accommodated by the forest adopting the concave top surface, and later by the sidewalls curving in toward the center. This relieves strain in the process by allowing the faster growing outer nanotubes to reach their full length. As the forest gets taller it becomes increasingly rigid, and these two mechanisms cannot relieve all of the strain so the outer nanotubes begin to ripple. When the forest is sufficiently tall (when the top surface has reached its final shape) it can no longer relieve strain through increased concavity of its top surface or curving in of the sidewalls because it is too rigid. It then enforces the rigid top boundary condition over the growth front and the forest as a whole grows at a uniform rate with rippling as the sole means of strain relief. The concave top surface is therefore linked to the rippling of the sidewalls of the forests, however, it does not guarantee the presence of ripples if the growth rate difference is not sufficiently large, as described below.

As more time elapses after growth initiation, the ripples formed have progressively smaller amplitudes until the amplitude eventually reaches zero, thus terminating the rippling (see Fig. 1). We speculate that the rippling terminates because the outer nanotubes' faster growth rate decreases faster and they stop growing sooner than the inner nanotubes. This results in a decreasing growth rate difference as growth progresses, and therefore decreased mechanical strain and rippling. It has previously been shown [26,30–33] that the faster a nanotube grows (such as the outer nanotubes relative to the inner nanotubes in the present case), the sooner it stops growing. We have previously reported [12] that, under growth conditions similar to those used here, the outer nanotubes of forests have a tendency to terminate before the inner nanotubes and detach themselves from the substrate. Similarly, Bedewy et al. [7] showed (via mass density measurements of forests) that some nanotubes stop growing before the forest reaches its terminal height.

It has been shown that a non-uniform catalyst thickness can cause a growth rate difference and even cause rippling [5]. Here, we can rule this out as the cause of the growth rate difference and rippling. Edge effects are expected in the shadow mask catalyst preparation technique, and these could result in a non-uniform catalyst thickness, and therefore affect the growth rate. However, we also prepared some samples by photolithography, for which much smaller scale edge effects are expected. Both techniques resulted in the same growth rate differences and the same rippling, so we can rule out catalyst thickness variations as the cause.

For tall forests, it is sometimes speculated that the nanotubes impede the gas phase diffusion of the source gas through the forest. We can rule this out as a cause of the growth rate difference because, here, the growth rate difference exists even during the initial moments of growth when the forests are still very short. This is demonstrated by the increasing concavity of the top surface of the forest within the first minute of growth. We thus conclude that diffusion of the source gas through the forest is not the cause of the growth rate difference. This conclusion is consistent with previous reports [1,19,26,34].

A non-uniform temperature is known to cause a growth rate difference, and it has even been shown to be the cause of rippling when a sufficiently large difference is present [8]. Here, this is not the case as the heater is much larger than

the catalyst islands and non-uniformities are generally small (around ±10 °C at the most).

The most likely origin of the growth rate difference is a non-uniform local gas distribution across the catalyst island. The inner catalyst nanoparticles are surrounded by other nanoparticles consuming reactive carbon whereas the outer catalyst nanoparticles are only partially surrounded by other nanoparticles, and otherwise by non-carbon-consuming silicon dioxide. The source gas molecules impinging upon the silicon dioxide are not used for nanotube growth and thus create a larger local concentration of source gas near the edge of the forest [34]. Because the outer nanoparticles therefore receive more carbon than the inner nanoparticles, they grow faster (under the present conditions, the growth rate is limited by the carbon supply because increasing the flow rate increases the growth rate). Unlike the above diffusion through the forest being impeded by the nanotubes, this is strict gas-phase diffusion without impediment.

Given that C_2H_2 will move by gas-phase diffusion, we would expect that any variation in concentration across the catalyst/substrate boundary would have a characteristic length scale ℓ, which is expected to be on the order of the gas diffusion length (~1 μm). We expect ℓ to be independent of the size of the catalyst island. This then yields a differently shaped gas distribution across the diameter of the catalyst island for different sized islands, and hence produces the observed nanotube growth rate profile. Different growth profiles for different sized islands is possibly the reason why we see the ripples form on the 100 μm diameter forests over a wider range of conditions than the larger forests.

To estimate the magnitude of the growth rate difference involved in rippling, the rippled nanotubes on the sidewalls of the forest are assumed to be sinusoidal with amplitude 100 nm and wavelength 700 nm, as seen in Fig. 2a. Therefore, the rippled outer nanotubes are ~20% longer than the straight inner nanotubes over one period. This length difference therefore requires an ~20% faster growth rate for the outer nanotubes when compared to the inner nanotubes. This estimate is very sensitive to the amplitude/wavelength ratio. As the amplitude decreases toward the base of the forest, the growth rate difference will decrease as well. The growth conditions that lead to ripple formation are those for which a sufficiently large growth rate difference is present between different nanotubes in the forest.

The amplitude of the rippling pattern depends strongly on the growth conditions. We suppose then that variations in amplitude from one forest to another on the same growth sample are likely due to slight variations in local CVD conditions across the sample. Conversely, we see no such dependence for the wavelength, which does not generally vary much for any given forest on the several μm scale, as evidenced by the presence of clear diffraction patterns. The wavelength of the ripples likely depends primarily on the physical properties and density of the nanotubes in the forest. Variations in wavelength from one forest to another on the same sample are likely due to variations in the composition of the forests, specifically the relative numbers of different nanotubes [13] as defined by their diameter, number of walls, and crystallinity. Variations within a forest, other than abrupt changes due to "faults", are likely caused by variations in the local density of nanotubes, which is a result of nanotube wandering and the growth cessation of some individual nanotubes.

Finally, we can estimate the rippling wavelength by considering a pair of straight nanotubes interacting with each other along their length L via a van der Waals interaction. The cohesion energy of this interaction for one nanotube is $E_{co} = \epsilon_{co}\Omega^{-1}bL$, where $\epsilon_{co} \sim 25$ meV per carbon atom is the binding energy between graphene sheets [35], $\Omega \sim 0.026$ nm^2 per carbon atom is the surface density of graphene, and bL is the area of interaction (contact area) with $b \sim a = 0.14$ nm (the C–C bond length).

Using the thin rod approximation (see for example Landau and Lifshitz [36]), the bending energy is given by $E_{bend} = \frac{\pi}{8} Y r^4 L/R^2$, where $Y = 1$ TPa is Young's modulus, r is the nanotube radius, and R is the bending radius. Setting $E_{co} = E_{bend}$ and assuming the ripple wavelength λ is on the same order of magnitude as R yields the relation:

$$\lambda \sim R = \sqrt{\frac{\pi}{8}\frac{Y\Omega}{\epsilon_{co}}\frac{r^4}{b}}$$

Importantly, this relation depends only on the properties of the nanotube itself through the radius r. If we take $r = 1$ nm, then the predicted wavelength is $\lambda \sim 140$ nm, which is on the same order of magnitude as the observations. The largest uncertainty in this estimate is the effect of the cohesion interaction (given by the contact area bL), which is manifested in the estimate for λ as $b \sim a = 0.14$ nm (the C–C bond length). Furthermore, the estimate is limited by the approximating the nanotube to be solid rod.

Because the rippling wavelength is fixed for a given type of nanotube (defined here exclusively by its radius r) according to this simple model, the rippling amplitude is a monotonic increasing function of the growth rate difference, which is in turn controlled by the reactor conditions. This agrees well with our observations that the wavelength has no clear dependence on the growth conditions, while the growth rate difference (as seen in the forest concavity) and amplitude have a maximum at the same growth conditions.

5. Conclusion

In summary, we grew vertically aligned carbon nanotube forests that had periodic ripples on their sidewalls. These ripples behave as surface diffraction gratings and allowed us to observe the ripples *in situ*. We showed that the ripples self-assemble during CVD growth of the forests under the appropriate reactor conditions, which were identified. We use this *in situ* data to support a formation mechanism: rippling occurs to relieve strain within the forest that is a result of a difference in growth rate between different nanotubes in the forest. This growth rate difference was observed using simple *in situ* optical microscopy. The order of magnitude of the rippling wavelength was predicted using a simple solid rod model for nanotubes.

Carbon nanotube forest growth is not simply the growth of many individual nanotubes: collective effects alter the way that the individual nanotubes grow within the forest. The rippling phenomenon shows that the interactions between

nanotubes in forests are indeed very important factors to consider in formulating a model for the growth of vertically aligned carbon nanotube forests. Studying and understanding the rippling is thus another step toward understanding the overall growth of nanotube forests, and eventually tailoring them to specific applications.

Acknowledgments

The authors thank the following IMS staff for their assistance and support: J. Fraser, H. Tran, M. Denhoff, and B. Lamontagne. P.V. was supported by NSERC, NRC-GSSSP and P.F.'s NSERC Discovery Grant.

Appendix A. Experimental methods

Before each growth run, the reactor was purged for 10 min with pure Ar flowing at 2 l min^{-1}. Samples were heated to the growth temperature *T* (measured with a two-colour infrared pyrometer) in an Ar/H_2 (2% H_2, 98% Ar) gas environment, with a flow rate of 170 sccm to 300 sccm, corresponding to the eventual source gas flow rate. Water vapour was then introduced by passing Ar through the bubbler to account for 25% of the total gas flow rate for 5 min while reducing the Ar/H_2 flow rate to 75% of the total gas flow rate, keeping the total gas flow rate constant. Dilute acetylene (0.1% C_2H_2, 99.9% Ar) was then introduced (90 sccm to 220 sccm) to initiate growth, while turning the Ar/H_2 and Ar/H_2O flow rates down to 60 sccm and 20 sccm, respectively, for a total gas flow rate of 170 sccm to 300 sccm. After the growth was determined to have halted via self-termination (by visual inspection with the camera), the chamber was purged for 5 min with pure Ar flowing at 2 l min^{-1}. The heater was then shut off and the Ar was allowed to flow for another 5 min before it was shut off. For forests that were intentionally terminated prior to self-termination, the process gases were stopped and the reactor was immediately purged with pure Ar. All samples remained in the Ar environment inside the reactor for at least another 30 min prior to removal to atmosphere.

Appendix B. Supplementary data

Supplementary data associated with this article can be found, in the online version, at doi:10.1016/j.carbon.2011.02.017.

REFERENCES

[1] Hart AJ, Slocum AH. Force output, control of film structure, and microscale shape transfer by carbon nanotube growth under mechanical pressure. Nano Lett 2006;6:1254–60.
[2] Zhang Q, Zhou W, Qian W, Xiang R, Huang J, Wang D, et al. Synchronous growth of vertically aligned carbon nanotubes with pristine stress in the heterogeneous catalysis process. J Phys Chem C 2007;111:14638–43.
[3] Zhang Y, Zou G, Doorn SK, Htoon H, Stan L, Hawley ME, et al. Tailoring the morphology of carbon nanotube arrays: from spinnable forests to undulating foams. ACS Nano 2009;3:2157–62.
[4] Cui X, Wei W, Harrower C, Chen W. Effect of catalyst particle interspacing on the growth of millimeter-scale carbon nanotube arrays by catalytic chemical vapor deposition. Carbon 2009;47:3441–51.
[5] Zhang Y, Gregoire JM, van Dover RB, Hart AJ. Ethanol-promoted high-yield growth of few-walled carbon nanotubes. J Phys Chem C 2010;114:6389–95.
[6] Wang H, Xu Z, Eres G. Order in vertically aligned carbon nanotube arrays. Appl Phys Lett 2006;88:213111.
[7] Bedewy M, Meshot ER, Guo H, Verploegen EA, Lu W, Hart AJ. Collective mechanism for the evolution and self-termination of vertically aligned carbon nanotube growth. J Phys Chem C 2009;113:20576–82.
[8] Dittmer S, Ek-Weis J, Nerushev OA, Campbell EEB. Growth of aligned mwnt arrays using a micrometer scale local-heater at low ambient temperature. J Nanosci Nanotech 2010;10:4015–22.
[9] Cao A, Dickrell PL, Sawyer WG, Ghasemi-Nejhad MN, Ajayan PM. Super-compressible foamlike carbon nanotube films. Science 2005;310:1307–10.
[10] Pushparaj VL, Ci L, Sreekala S, Kumar A, Kesapragada S, Gall D, et al. Effects of compressive strains on electrical conductivities of a macroscale carbon nanotube block. Appl Phys Lett 2007;91:153116.
[11] Wang BN, Bennett RD, Verploegen E, Hart AJ, Cohen RE. Characterizing the morphologies of mechanically manipulated multiwall carbon nanotube films by small-angle x-ray scattering. J Phys Chem C 2007;111:17933–40.
[12] Vinten P, Marshall P, Lefebvre J, Finnie P. Distinct termination morphologies for vertically aligned carbon nanotube forests. Nanotech 2010;21:035603.
[13] Zbib AA, Mesarovic SD, Lilleodden ET, McClain D, Jiao J, Bahr DF. The coordinated buckling of carbon nanotube turfs under uniform compression. Nanotech 2008;19:175704.
[14] Hart AJ, Slocum AH. Rapid growth and flow-mediated nucleation of millimeter-scale aligned carbon nanotube structures from a thin-film catalyst. J Phys Chem B 2006;110:8250–7.
[15] Zhang L, Li Z, Tan Y, Lolli G, Sakulchaicharoen N, Requejo FG, et al. Influence of a top crust of entangled nanotubes on the structure of vertically aligned forests of single-walled carbon nanotubes. Chem Mater 2006;18:5624–9.
[16] Hart AJ, van Laake L, Slocum AH. Desktop growth of carbon-nanotube monoliths with in situ optical imaging. Small 2007;3:772–7.
[17] Meshot ER, Hart AJ. Abrupt self-termination of vertically aligned carbon nanotube growth. Appl Phys Lett 2008;92:113107.
[18] Puretzky AA, Eres G, Rouleau CM, Ivanov IN, Geohegan DB. Real-time imaging of vertically aligned carbon nanotube array growth kinetics. Nanotech 2008;19:055605.
[19] Han JH, Graff RA, Welch B, Marsh CP, Franks R, Strano MS. A mechanochemical model of growth termination in vertical carbon nanotube forests. ACS Nano 2008;2:53–60.
[20] Vinten P, Lefebvre J, Finnie P. Visible iridescence from self-assembled periodic rippling in vertically aligned carbon nanotube forests. Appl Phys Lett 2010;97:101901.
[21] Hata K, Futaba DN, Mizuno K, Namai T, Yumura M, Iijima S. Water-assisted highly efficient synthesis of impurity-free single-walled carbon nanotubes. Science 2004;306:1362–4.
[22] Eres G, Puretzky AA, Geohegan DB, Cui H. In situ control of the catalyst efficiency in chemical vapor deposition of vertically aligned carbon nanotubes on predeposited metal catalyst films. Appl Phys Lett 2004;84:1759–61.
[23] Eres G, Kinkhabwala AA, Cui H, Geohegan DB, Puretzky AA, Lowndes DH. Molecular beam-controlled nucleation and growth of vertically aligned single-wall carbon nanotube arrays. J Phys Chem B 2005;109:16684–94.

[24] Zhang C, Pisana S, Wirth CT, Parvez A, Ducati C, Hofmann S, et al. Growth of aligned millimeter-long carbon nanotube by chemical vapor deposition. Diamond Relat Mater 2008;17:1447–51.
[25] Mattevi C, Wirth CT, Hofmann S, Blume R, Cantoro M, Ducati C, et al. In-situ x-ray photoelectron spectroscopy study of catalyst-support interactions and growth of carbon nanotube forests. J Phys Chem C 2008;112:12207–13.
[26] Vinten P, Lefebvre J, Finnie P. Kinetic critical temperature and optimized chemical vapor deposition growth of carbon nanotubes. Chem Phys Lett 2009;469:293–7.
[27] Finnie P, Bardwell J, Tsandev I, Tomlinson M, Beaulieu M, Fraser J, et al. Cold wall chemical vapor deposition of single walled carbon nanotubes. J Vac Sci Technol 2004;22:747–51.
[28] Finnie P, Li-Pook-Than A, Lefebvre J, Austing DG. Optimization of methane cold wall chemical vapor deposition for the production of single walled carbon nanotubes and devices. Carbon 2006;44:3199–206.
[29] Bajpai V, Dai L, Ohashi T. Large-scale synthesis of perpendicularly aligned helical carbon nanotubes. J Am Chem Soc 2004;126:5070–1.
[30] Picher M, Anglaret E, Arenal R, Jourdain V. Self-deactivation of single-walled carbon nanotube growth studied by in situ raman measurements. Nano Lett 2009;9:542–7.
[31] Meshot ER, Plata DL, Tawfick S, Zhang Y, Verploegen EA, Hart AJ. Engineering vertically aligned carbon nanotube growth by decoupled thermal treatment of precursor and catalyst. ACS Nano 2009;3:2477–86.
[32] Bosnick K, Dai L. Growth kinetics in a large-bore vertically aligned carbon nanotube film deposition process. J Phys Chem C 2010;114:7226–30.
[33] Picher M, Anglaret E, Jourdain V. High temperature activation and deactivation of single-walled carbon nanotube growth investigated by in situ raman measurements. Diamond Relat Mater 2010;19:581–5.
[34] Jeong GH, Olofsson N, Falk LKL, Campbell EEB. Effect of catalyst pattern geometry on the growth of vertically aligned carbon nanotube arrays. Carbon 2009;47:696–704.
[35] Schabel MC, Martins JL. Energetics of interplanar binding in graphite. Phys Rev B 1992;46:7185–8.
[36] Landau LD, Lifshitz EM. Theory of elasticity. 3rd ed. Oxford: Uk; 1986. Reed.

Chapter 7

Critical role of gas phase diffusion and high efficiency in vertically aligned carbon nanotube forest growth

This chapter is based on an article that is accepted for publication (4 April 2013) in the journal *Carbon*. That article can be accessed via the following hyperlink:
`http://dx.doi.org/10.1016/j.carbon.2013.04.007`

This article includes supplementary material. The printable portion of that material is reprinted here in Appendix D. The multimedia portion of that material is available from the University of Ottawa's thesis repository (uO Research) as indicated in the List of videos, as well as the article's publisher's website, which can be accessed using the above hyperlink.

Foreword

This chapter serves to unite many of the observations of previous chapters. A comprehensive gas phase diffusion model is developed that predicts a non-uniform distribution of acetylene across the patterned catalyst area. The non-uniform distribution of gas leads to a non-uniform growth rate, which may be the origin of much of the strain in the carbon nanotube forests. The non-uniform gas distribution also leads to a non-uniform termination rate across the patterned catalyst island. Together, the non-uniform growth rate and the non-uniform termination rate can explain the observed concavity of the top surface of the forests from all previous chapters, the delamination seen in Chapter 3 and Chapter 4, the non-uniform initial growth rate seen in Chapter 4, and the rippling seen in Chapter 5 and Chapter 6, and in particular the fact that the rippling amplitude decreases closer to the center of the forest such that the nanotubes in the center of the forest are straight.

By uniting all of these observations, a comprehensive picture of forest growth can be developed. The sequence of events that occur during forest growth is illustrated in Fig. F1, with each stage described below:

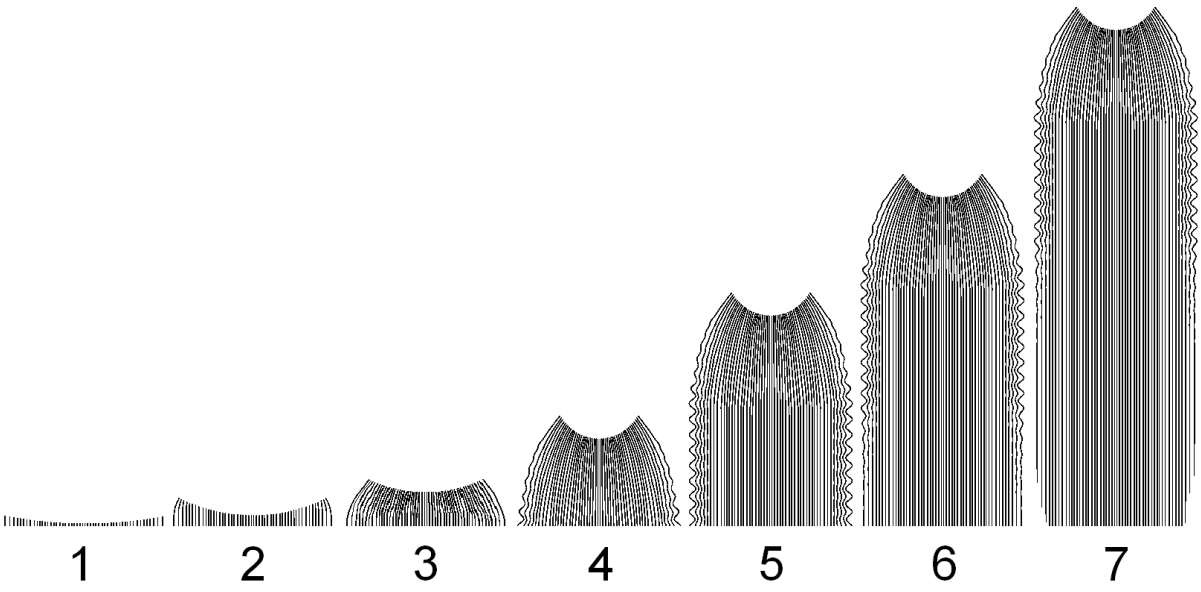


Figure F1: Illustration of rippling mechanism. See text for details.

1. The forest begins growing, with the nanotubes near the edge of the catalyst island growing slightly faster due to a non-uniform gas distribution that is analyzed in detail in this chapter.

2. The edges of the forest are slightly taller than the center, thus giving it a concave top surface due to faster growth rate of the nanotubes near the edge. The shape of this surface is determined by the growth rate gradient, which is in turn determined by the non-uniform distribution of gas.
3. As the nanotubes grow taller, there is significant interaction along their length which "freezes in" the shape of the forest that has already been grown. Further concavity increases are a result of this "frozen" part of the forest being bent inwards by the faster growing nanotubes near the edge of the forest. This causes the observation of the outer nanotubes bending inward, toward the center of the forest.
4. As growth continues, the "frozen in" upper portion of the forest becomes thicker and more difficult to deform further by bending. At this stage, the outer nanotubes begin to buckle and rippling begins as a way for the outer nanotubes to reach a greater length (but still the same overall vertical distance from the substrate) in the same time as the slower growing nanotubes toward the center of the forest.
5. Eventually, the "frozen in" part of the forest is so thick that it cannot be bent anymore and its shape is fixed. At this point, rippling becomes the only means for the outer nanotubes to reach their greater length and continue growing. This is accompanied by the observed increase in rippling amplitude.
6. From Chapter 6, we know that, in general, nanotubes that grow faster slow down and terminate more rapidly than slower growing nanotubes. In this case, the growth rate of the edge nanotubes slows down and the rippling amplitude subsides gradually (as the growth rate becomes more equalized across the forest), and the nanotubes eventually become straight.
7. At this point, all nanotubes now grow straight until termination, though the nanotubes near the edges may terminate and be lifted off the substrate (thus breaking their adhesion to the substrate) by the force exerted by the nanotubes in the forest that are still growing. At all stages, the inner nanotubes remain straight.

The missing piece in this picture of carbon nanotube forest growth is a thorough analysis of what causes the non-uniform growth rate across the sample. Until now it has been inferred from many observations of the forest morphology and growth kinetics that the non-uniform growth rate is caused by a non-uniform gas distribution. This chapter presents a model of gas phase diffusion that can explain the supposed non-uniform gas distribution.

The analysis of gas phase diffusion is accomplished by growing forest from various sized catalyst islands. The different sizes of catalyst island will produce different con-

ditions for the gas phase diffusion of the source gas and will result in different forest morphologies. This chapter thus studies the dependence of the kinetic parameters on the size of the patterned catalyst island and develops a mathematical model of gas phase diffusion to explain the results. This chapter also provides an estimate of the density of carbon nanotube in the forests, which was alluded to in Chapter 4, as well as a measurement of the efficiency at which acetylene is converted into carbon nanotubes, which turns out to be significant and likely has a large impact on the growth of carbon nanotubes. The efficiency is an important parameter when one considers an atomic scale model of carbon nanotube growth.

By using these measured quantities and others in the gas phase diffusion model, the model does not rely on arbitrary fitting parameters. Each parameter in the model has a physical meaning and at least some way of being directly measured or estimated with reasonable accuracy. By avoiding arbitrary fitting parameters, the understanding that this model provides is greatly increased.

Critical role of gas phase diffusion and high efficiency in vertically aligned carbon nanotube forest growth

P. Vinten[a,b], P. Marshall[b], T. Quance[b], J. Lefebvre[b], P. Finnie[a,b]

[a] *Department of Physics, University of Ottawa, 150 Louis Pasteur, Ottawa, ON, K1N 6N5, Canada*

[b] *National Research Council Canada, Building M-50, 1200 Montreal Road, Ottawa, ON, K1A 0R6, Canada*

Abstract

In this paper, the growth kinetics of vertically aligned carbon nanotube forests depend on the size of the patterned catalyst films from which they grow. Forests are grown using chemical vapour deposition on thin film catalyst islands patterned at the 100 μm scale on silicon wafers. The smaller the pattern, the faster the forest grows and the earlier it stops growing. Furthermore, the shape and structure of the forests, in particular the concavity of their top surface, also depend on the size of the catalyst islands. This result can be understood as a consequence of the high efficiency by which the acetylene source gas is converted into carbon nanotubes (here $\sim$30%) and a varying local amount of acetylene source gas available for growth. A diffusion model can explain the observed shape and structure of the forests and their growth kinetics by using experimentally measured parameters. The model also gives insight into the density and growth rate of carbon nanotube forests and suggests a mechanism that coordinates growth rates across the sample and, under certain conditions, can limit the fraction of catalyst nanoparticles that produce nanotubes.

1 Introduction

Chemical vapour deposition (CVD) growth of carbon nanotubes (CNTs) is often used to grow vertically aligned CNT forests on a substrate with a thin film catalyst layer deposited onto it prior to growth [1]. This thin film can be patterned into different shapes and sizes [2–8]. The size of these patterned catalyst islands can have an effect on the growth kinetics of the CNT forests that grow from them, as well as the shape and structure of these forests. Here, we analyze the effect of the catalyst island size by simultaneously growing forests from several different sizes of circular catalyst islands (100 μm to 800 μm diameter). We gather detailed *in situ* kinetics data using optical microscopy [9–14]. Smaller catalyst islands

produce forests that grow faster and stop growing (terminate) earlier than forests grown from larger islands.

We describe the shape and structure of a forest as the "forest morphology". The morphology of a forest includes macroscopic observations such as the concavity of the top surface of the forest, the curvature of the forest's sidewalls [15, 16], and the delamination from the substrate near the forest's edges [17], as well as microscopic observations such as the CNT density within the forest, the CNT bundling within the forest, and the geometry of the CNTs within a forest, including the rippling effect on the forest sidewalls [15, 18]. Here we observe and analyze several of these aspects of the forest morphology and link them to the growth kinetics of the forests.

The forest morphology and growth kinetics can both potentially be explained by supposing that gas diffuses from areas with a high concentration to the growth areas with a low concentration. A diffusion model is developed with experimentally measurable parameters, including the mass density of the forest and the efficiency of growth. The model is then related to our observations. The high efficiency by which acetylene is converted into CNTs (here $\sim$30%) affects both the forest morphology and growth kinetics, in particular the concavity of the top surface of the forests. Our diffusion model offers a potential explanation for the observed forest morphology and can approximate the experimentally observed growth kinetics. It also suggests a mechanism which coordinates growth rates and, under certain conditions, may limit the areal density of CNTs within the forest and the fraction of catalyst nanoparticles that actively grow CNTs.

2 Experimental procedures

Carbon nanotube forests were grown using water-assisted CVD [2] with dilute C_2H_2 as the carbon source [19, 20] and Co/Al_2O_3 thin films as the catalyst in a cold-walled CVD reactor operated at atmospheric pressure. Both the growth temperature T and the C_2H_2 flow rate F were varied (see Appendix D, Section 2.1 for details). Unless otherwise stated, all forest growth stopped on its own.

Samples were $\sim$30 mm^2 square pieces of 0.5 mm thick Si with 1 μm thermal SiO_2 and catalyst layers of nominally 250 nm Al_2O_3 and 0.8 nm Co deposited by e-beam evaporation through a shadow mask to produce regular patterns (see Fig. 1a) of circular catalyst islands with diameters of 100 μm, 200 μm, 400 μm, and 800 μm. This pattern allows the simultaneous growth of multiple forests with different sizes. Other samples were prepared using the same catalyst but different shadow masks (close-packed 700 μm diameter circles and widely spaced 800 μm diameter circles) or no shadow mask (cleaved to $\sim$60 mm^2). Figure 1b shows a scanning electron microscope (SEM) image of forests grown at 820°C using this catalyst pattern.

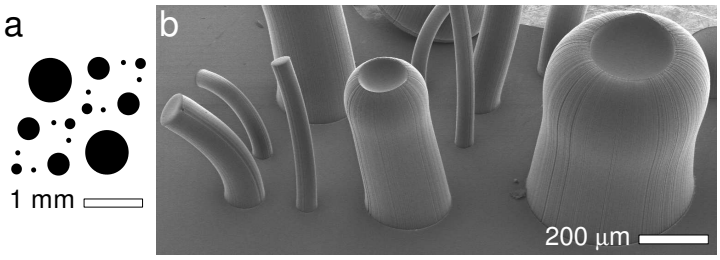


Figure 1: Catalyst pattern. (a) The pattern of the shadow mask used in the catalyst preparation (diameters: 100 μm, 200 μm, 400 μm, and 800 μm). (b) A scanning electron microscope image of forests grown at 820°C using this catalyst pattern, viewed at ∼45° to the substrate. The four forests at the front of the image correspond to the bottom of (a). Optical images and an *in situ* video of this forest growing are available in Appendix D, Fig. S1 and Video S1.

3 Results and discussion

3.1 Kinetic observations

Figure 2a shows growth curves (plots of forest height H as a function of growth time t) for the four different sizes of forests (100 μm, 200 μm, 400 μm, and 800 μm diameter circles) grown simultaneously at 760°C (see Appendix D, Fig. S2 for additional growth curves). The four forests do not grow at the same rate, terminate at the same time, or height, despite being exposed to identical conditions. This dependence on the size of the catalyst island is typical for all temperatures, and the differences are systematic. The smaller the catalyst island, the faster the forest grows and the earlier the growth terminates. Larger catalyst islands produce forests that grow for a longer period of time at a slower rate, but reach a greater final height.

Another prominent feature seen in Fig. 2a is that the two larger forests have accelerating growth curves, especially later in the growth process. These accelerating growth curves are the exception rather than the rule and occurred at lower growth temperatures T (<780°C) for larger diameter catalyst islands. Except for these low temperatures, the vast majority of forests grew at an exponentially decaying rate (appearing almost linear in many cases) with a sudden termination (see Fig. 2b and Appendix D, Fig. S2 for examples). The forests with an accelerating growth curve were observed to gradually delaminate around the edge during this accelerating stage of their growth (observed by *in situ* optical microscopy and *ex situ* scanning electron microscopy, see Appendix D, Fig. S3 and Fig. S4), suggesting that the growth kinetics of a forest are linked to its structure.

As a function of the growth temperature T, the termination height H_T is peaked at 760 °C, in the millimeter range, with the larger diameter island forests generally reaching greater termination heights. A dependence of forest height on island size [4] and total patterned catalyst area [6] have been reported previously. In Ref. 6, it was the total area of catalyst that was varied (with that area consisting of a varying number of closely spaced but equally sized islands). Here, the total area and number of islands is constant but the size of the

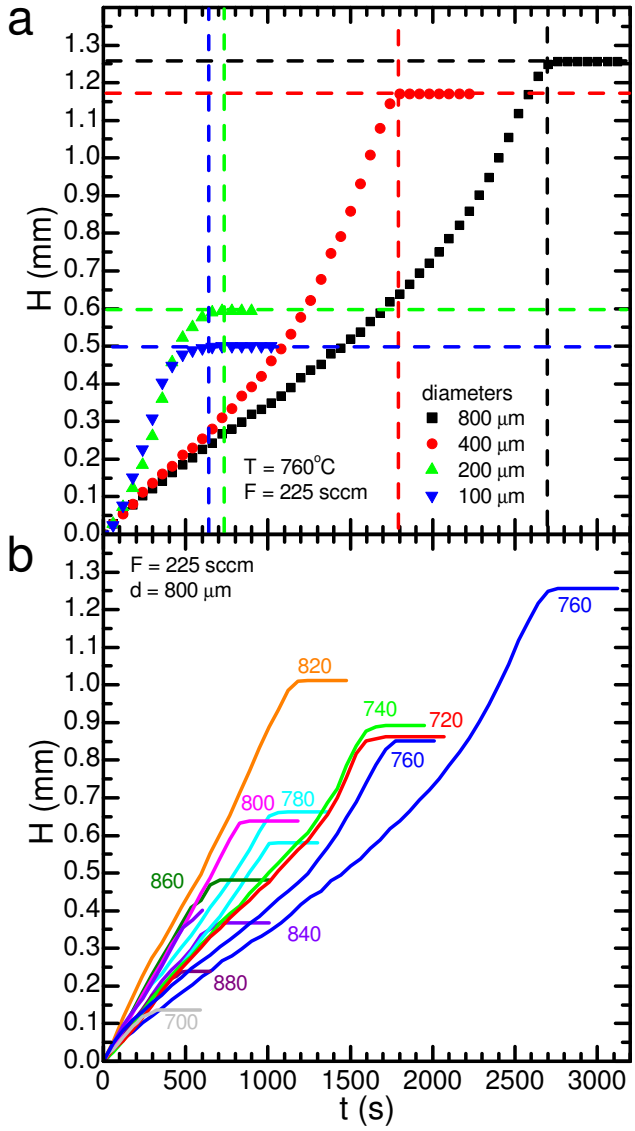


Figure 2: Growth curves. (a) Height H vs growth time t for four forests grown simultaneously at 760°C from catalyst islands of different sizes. Termination height H_T and termination time τ_T are indicated by dashed lines (horizontal and vertical respectively). (b) H vs t for 800 μm diameter forests for all growth temperatures (indicated in °C). Two curves were obtained for growth temperatures 760°C, 780°C, and 840°C.

individual components does vary.

The growth kinetics as a function of catalyst island diameter d for various T are shown in Fig. 3. For the temperatures with two growth curves (760°C, 780°C, and 840°C), the average is shown here. Except at the lowest growth temperature (T = 700°C), the initial growth rate β (Fig. 3a) is faster for smaller d. The termination time τ_T is the time when macroscopic forest growth has stopped. Some mechanisms that can cause termination are discussed at the end of this paper. As seen in Fig. 3b, τ_T is larger for larger d.

In Fig. 1b, the smaller diameter forests are slightly bent. Only the forests with the

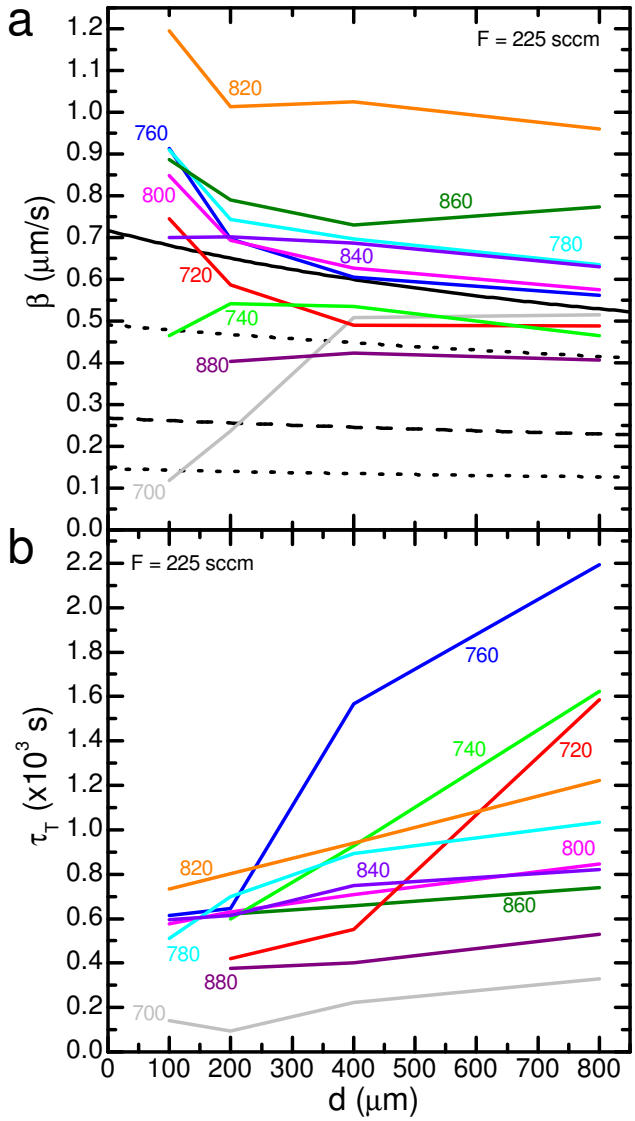


Figure 3: Kinetic parameters. (a) Initial growth rate β and (b) termination time τ_T vs catalyst island diameter d, with growth temperatures indicated (°C). Dashed line in (a) is the theoretical prediction for 760°C, with the dotted lines giving the error (see text). Solid black line in (a) is a prediction for 760°C using parameters from the linear best fit in Fig. 4a (see Table 1).

largest aspect ratios (the tallest of the narrow diameter forests, see Fig. 2b and Appendix D, Fig. S3) are observed to bend, and even then, not all of them are bent. Some forests bend toward the neighbouring forests while some bend away from the others. The shorter forests (grown at higher temperatures) do not bend at all. This bending is undoubtedly driven by strain in the forest; however, the growth rate and termination time do not seem to be affected by this bending. The measured heights and growth rates take this into account by tracking the position of the top of the forest even if it has shifted sideways (thus measuring the true height of the forest). Forests that bend out of the focal plane cannot be tracked meaningfully (this is confirmed by post growth *ex situ* SEM). We observe the same trends

(see Fig. 3) with respect to catalyst island diameter (height, growth rate, and termination time) regardless of the magnitude of the final height and whether or not the forests are bent.

As a function of increasing C_2H_2 flow rate F, the initial growth rate β (see Fig. 4a) increases, as noted previously [21], whereas the termination time τ_T decreases (plotted as $1/\tau_T$, a rate, in Fig. 4b). The anti-correlation of these kinetic parameters is consistent with previous work [14, 22–26]. These observations suggest that both processes (growth and termination) are controlled by the amount of carbon available for growth and that our CVD reactor operates in a supply limited regime. An increase in the amount of C_2H_2 available for growth (through an increase in F) increases the initial growth rate β and termination rate $1/\tau_T$.

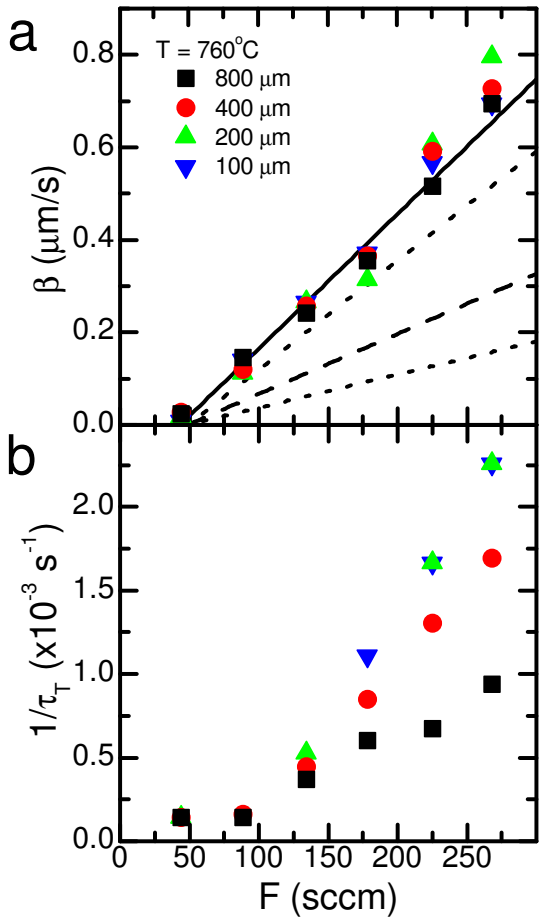


Figure 4: Flow rate dependence. (a) Initial growth rate β and (b) inverse termination time (a rate) $1/\tau_T$ vs C_2H_2 flow rate F for four different island sizes. Solid line in (a) is a linear best fit to the 800 μm catalyst island, dashed line is the theoretical prediction, and the dotted lines give the error (see text).

The C_2H_2 entering the reaction chamber (at a volumetric flow rate F) is delivered directly to the sample by a narrow tube (~3 mm inner diameter) from a distance of several mm at an angle of ~45°. The flow rate F can be related to an impingement rate I of C_2H_2 onto the catalyst nanoparticle by the relationship $I = n_o F/A_o$ where n_o is the concentration of an

ideal gas at standard temperature and pressure (STP conditions), F is the volumetric flow rate in units of $[m^3/s]$, and A_o ∼130 mm^2 is the area over which the gas spreads after it has traveled (and diverged) from the nozzle to the plane of the substrate. A_o must be at least as large as the largest sample on which we observe uniform growth; therefore, $A_o \geq 130$ mm^2. In our calculations we use the minimum value $A_o = 130$ mm^2. The product $n_o F$ has the meaning of the number of C_2H_2 molecules flowing into the reactor per second.

In Fig. 4a, the initial growth rate β remains at zero even with a small C_2H_2 flow rate, such that $\beta \propto F - F_{min}$. Here F_{min} is a minimum flow rate and the intercept along the horizontal axis in Fig. 4a, with a value of $F_{min} \sim 43$ sccm (of 0.1% C_2H_2 in Ar). This is equivalent to a minimum impingement rate of $I_{min} \sim 1.7 \times 10^{20}$ C_2H_2/m^2/s. There are several possible explanations. At a very low total flow rate, gas will likely not reach the substrate at all. We minimize this effect by maintaining a significant flow of the Ar carrier gas even when the C_2H_2 flow rate is low. Another possibility that may explain the existence of F_{min} is nucleation effects related to a minimum concentration of gas required to nucleate a CNT. Similarly, a minimum concentration of C_2H_2 is likely necessary to overcome the etching effects of the H_2O.

It has previously been reported that a minimum impingement rate (3×10^{22} C_2H_2/m^2/s) is required for the growth of vertically aligned CNT forests [21]. Here, forests grow at much lower impingement rates. This difference might have several origins, such as our use of water as a growth enhancer, our use of Co as a catalyst, or our use of atmospheric pressure. Even if we assume that all of the C_2H_2 entering our reactor at the maximum flow rate (270 sccm of 0.1% C_2H_2 in Ar) hits the substrate (by setting A_o equal to the size of the substrate, 30 mm^2), we find $I = 4.6 \times 10^{21}$ C_2H_2/m^2/s, which is still an order of magnitude less than the previously reported value.

3.2 Gas diffusion observations

The growth kinetics of CNT forests clearly depend on the size of the patterned catalyst islands from which they grow. The shape of the forests (concave top surface and inward curving sidewalls [15, 16]), their structure (rippled sidewalls [15, 18] and delamination from the outside inward [17]), and their non-uniform initial growth from the outer edge inward [15, 16] (see Fig. 5 and Video S2) suggest a non-uniform growth rate across the catalyst island that depends on the catalyst island diameter: CNTs on the outer edge grow faster than those toward the center of the catalyst island. We suppose that these features in the forest morphology and the size-dependent growth kinetics are related.

Two possible explanations for these observations are (1) variations in the thickness of the catalyst as a function of radial position (such edge effects due to the deposition process) and (2) gas phase diffusion of the C_2H_2 into the region above the Co catalyst island from the region above surrounding SiO_2. In both cases, strain is certainly present and most definitely

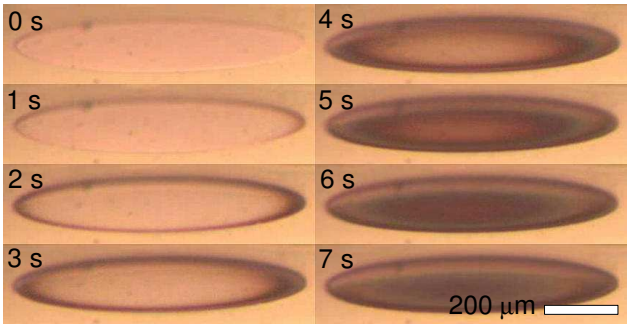


Figure 5: Frames from an *in situ* video (Video S2) of the non-uniform initial growth rate of a CNT forest growing on a 800 μm diameter catalyst island at 760°C (viewed at $\sim$5° angle to the substrate). Growth times are indicated.

contributes to the smoothness of the concave top surfaces and the delamination. In an ideal forest of perfectly parallel identical CNTs growing in unison, there would be no strain. Even if these CNTs were touching one another, but still growing at the same rate, strain would likely be minimal. In a real forest, the CNTs are not all growing at exactly the same rate and will push and pull on one another through interactions. This will introduce significant strain into the forests. Both of these mechanisms cause a non-uniform growth rate and, hence, strain.

Gas phase diffusion would imply that more gas reaches the outer regions of the catalyst island than the inner region, thus leading to a variation in growth rate. In the supply limited regime seen here, a greater supply of gas would lead to a faster growth rate. The non-uniform initial growth from the outer edge inward [15, 16] (Fig. 5) in particular suggests that there is more than simply strain causing all of our morphological observations.

A variation in catalyst layer thickness (and thus nanoparticle size [27, 28]) could cause a variation in growth rate. However, we analyzed the catalyst uniformity and edge effects using a scanning Auger microscope (SAM) to perform detailed and highly localized Auger electron spectroscopy (AES). AES is an extremely sensitive surface technique than can detect monolayers of material and give a very accurate indication of the relative thickness of the layer from one location to another [29] (laterally, the resolution is on the order of 1 μm). Therefore, AES is ideally suited to search for edge effects in the thickness of the thin (0.8 nm) Co layer (see Appendix D, Section 2.3 for further details). AES does not reveal any edge effects on the length scale necessary to explain our observations (see Appendix D, Fig. S5). The edge effects that are seen are only several μm for the mechanical mask and less than 200 nm for the photolithographic mask. For both samples, the top surface of the forests grown from them is concave over much larger length scales (that are similar for both samples), which suggests that the short range edge effects seen in the deposited catalyst layer are not responsible for our observations, consistent with our previous conclusion [15]. Additionally, AES reveals that heating the sample for growth does not change the shape of these edge effects and that the deposited Co does not diffuse onto the surrounding SiO_2 (see Appendix D, Fig. S5).

On the other hand, there is further evidence for a gas phase diffusion model that is seen when examining the effect of the spacing of the catalyst islands. A widely spaced pattern 800 μm diameter islands (arranged in a square lattice with 1.8 mm spacing between the edges of the circular catalyst islands) grew *faster* and terminated *earlier* than the close-packed 700 μm diameter islands (arranged in a hexagonal lattice with 450 μm spacing between the edges of the circular catalyst islands), despite having larger island sizes (see Fig. 6). The more rapid growth and earlier termination of the widely spaced pattern (despite its larger island size) suggest that it received more gas. This extra gas would have come from the larger area of unreactive SiO_2 surrounding the islands.

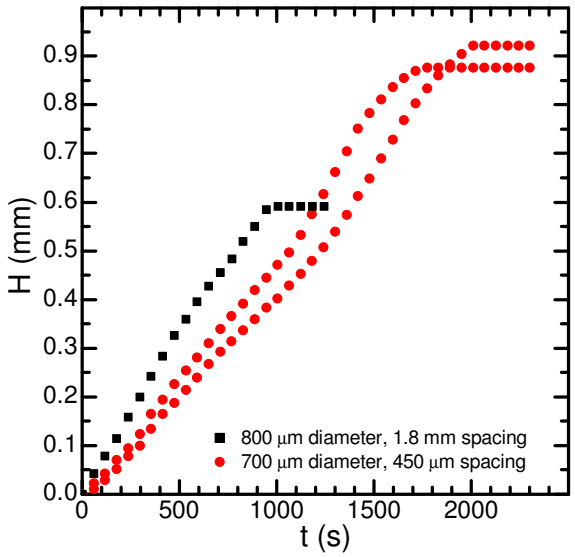


Figure 6: Island spacing growth curves: height H vs growth time t for forests grown from different sized islands with different spacings (indicated) at 760°C. The two red curves simply represent two identical forests growing simultaneously from the same substrate.

Therefore, we suppose that the above observations are a result of gas phase diffusion. More gas is available around the outer edge of the catalyst islands. It has previously been suggested that less gas reaches the center of the catalyst islands as a result of the forest itself hindering the diffusion of the gas [5]. Here, it is not the forest that hinders diffusion because the non-uniformity in growth is seen from the instant the gas is introduced: CNT growth begins around the outer edge of the catalyst island first [14, 16], as seen in Fig. 5.

Ex situ Raman spectroscopy does not reveal any significant variations in the composition of the forests as a function of catalyst island size (see Appendix D, Fig. S6). Smaller diameter forests had a smaller signal to noise ratio, which is a result of the smaller forests having a smaller flat area over which to gather the spectra, thus creating more out of focus light. The D/G ratio (which is a measure of the defect density of the CNTs) did not vary significantly. Similarly, there was not much variation in the radial breathing mode (RBM) region of the spectrum, in terms of the peaks present and their intensities. The RBMs indicate the pres-

ence of single-walled carbon nanotubes (SWCNTs), but do not rule out the possibility that there are also multi-walled carbon nanotubes (MWCNTs) in the forests. These observations suggest that the type of CNTs grown is largely independent of the catalyst island size.

3.3 Gas diffusion model

The distribution of gas in the reactor on the scale of the patterned catalyst islands can be estimated in a simplified model of gas phase diffusion. In this model, each catalyst island acts as a sink for carbon source gas, while the non-patterned areas will simply reflect the impinging carbon source gas (and thus effectively not interact with the carbon source gas). This excess gas will diffuse toward and into the area above the catalyst islands. This scenario will lead to a non-uniform distribution of carbon source gas [6] on the scale of the patterned catalyst islands, with the patterned areas receiving more gas than that which directly impinges upon them, particularly around the edges. This gas phase diffusion model is shown schematically in Fig. 7.

To quantify this gas phase diffusion model, we consider a thin boundary layer of gas above the substrate, with a thickness equal to the diffusion length L. All gas molecules within the layer are thus capable of interacting with the substrate. The gas in this layer is considered to move only in two dimensions. Vertical movements will be either impingement onto the catalyst and subsequent growth with a time constant τ_g, or escape from the layer with time constant τ_d. This layer is stagnant near the surface and is replenished from the gas impinging from above at a rate $I = 8.6 \times 10^{20}$ $C_2H_2/m^2/s$ (from $F = 225$ sccm). We assume that all gas impinging upon the catalyst island (of radius $R = d/2$) is used immediately for growth and that any gas impinging upon the surrounding SiO_2 is not used for growth. Gas above the SiO_2 diffuses (with diffusion coefficient D, determined below) into the area above the catalyst, thus contributing to replenishing gas lost to the growth process. This is shown schematically in Fig. 7a-b. The result is that each catalyst island is exposed to 100% of the gas that directly impinges upon it, and then some more gas that diffuses inward to the catalyst island from the surrounding SiO_2.

The illustrated situation is governed by a 2D gas phase diffusion equation describing the concentration $n(\vec{r}, t)$ of the gas (per unit area of catalyst surface):

$$\frac{\partial n}{\partial t} = D\nabla^2 n + I - \frac{n}{\tau_d} - \frac{n}{\tau_g} \tag{1}$$

where the first term $D\nabla^2 n$ is the diffusion term, the second term I represents the amount of gas added to the system per unit time, the third term n/τ_d represents desorption and non-interaction, and the fourth term n/τ_g represents growth. Outside of the growth area, the last term $n/\tau_g = 0$ because $\tau_g \longrightarrow \infty$ when no growth occurs. Equation (1) is solved in the steady state ($\partial n/\partial t = 0$) using an infinite strip of catalyst of width $2R$, centered on the y-axis as

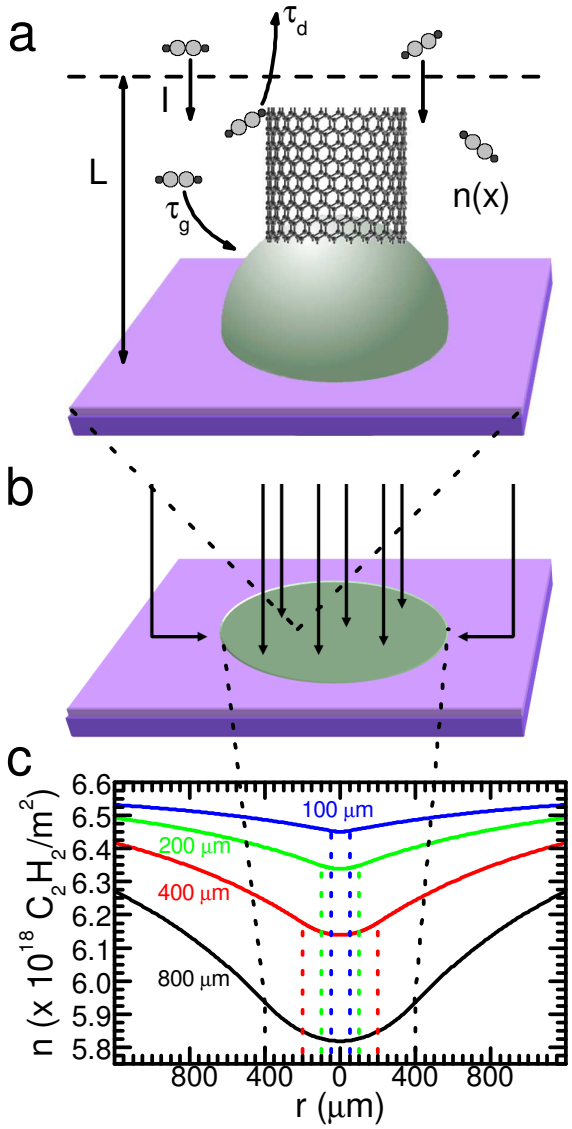


Figure 7: (a) Diagram of the microscopic processes occurring during CVD growth of CNTs. C_2H_2 molecules with a concentration $n(x)$ exist in a thin layer of thickness equal to the diffusion length L. Molecules are added to this layer at a rate I. Molecules in the layer can contribute to growth with a time constant τ_g or escape the layer (either directly or by adsorption then subsequent desorption) with a time constant τ_d. Nanoparticle (green), support (purple), and CNT (black) are pictured. (b) Diagram of the origin of the non-uniform local gas distribution. Gas impinging directly upon catalyst island (circle) is used for growth. Gas impinging upon the substrate (rectangle) is not used and diffuses into the region above the catalyst, yielding a non-uniform local gas distribution and a relative increase in the amount of gas available for growth. (c) Gas concentration over the catalyst island for the four island sizes studied here: n vs position r from the center of the catalyst island (Equation (2)). Dotted lines indicate edge of catalyst island.

the boundary conditions (see Appendix D, Fig. S7). Thus, for $x > R$ (or $x < -R$), the term n/τ_g vanishes from Equation (1). For our circular catalyst islands, the solution would be in the form of Bessel functions. This would be a more exact treatment, but a linear geometry is simpler and illustrates the most important aspects (see Appendix D, Section 2.5.1 for

further discussion of the Bessel function solution). Here, only the linear solution for $x > 0$ is presented because the solution is symmetric. The solution to Equation (1) is:

$$n(x) = AI\epsilon\tau_d \frac{\cosh\left(x/\sqrt{D(1-\epsilon)\tau_d}\right)}{\cosh\left(R/\sqrt{D(1-\epsilon)\tau_d}\right)} + I(1-\epsilon)\tau_d\,; \qquad x < R$$
$$n(x) = -BI\epsilon\tau_d \frac{\exp\left(-x/\sqrt{D\tau_d}\right)}{\exp\left(-R/\sqrt{D\tau_d}\right)} + I\tau_d\,; \qquad x > R \tag{2}$$

where the parameter $\epsilon = \tau_d/(\tau_g + \tau_d)$ is the efficiency by which the C_2H_2 source gas is converted into CNTs (see Appendix D, Section 2.5 for further details). The coefficients A and B depend on ϵ, τ_d, D, and R; A and B are shown in Appendix D, Equation (S1). For fixed values of R, they are essentially independent of the other parameters (for reasonable values of those parameters). The value of the diffusion coefficient D can be estimated using data from the Handbook of Chemistry and Physics [30]. Several systems similar to C_2H_2 in Ar were considered and data were extrapolated to 760°C, giving an estimated value of $D \sim (1.5 \pm 0.5) \times 10^{-4}$ m^2/s. Both ϵ and τ_d can be determined, as described below.

The efficiency ϵ is defined as the ratio of the amount gas used for growth (per unit time) to the amount of gas flowed into the reactor (per unit time). Experimentally, the amount of gas used for growth is determined by measuring the mass of carbon used for growth by weighing the resultant forest. The amount of gas flowed into the reactor (and hence its mass) can be determined from the C_2H_2 flow rate F and the growth time Δt, which is equivalent to the termination time τ_T. The efficiency ϵ can be thus be written as:

$$\epsilon = \frac{\text{mass of CNTs}}{\text{mass of C flowed into reactor}} = \frac{M}{2m_C\gamma n_o F\Delta t} \tag{3}$$

where M is the mass of the forest, m_C is the mass of a carbon atom, the 2 assumes both carbon atoms in C_2H_2 contribute to CNT growth, n_o is the concentration of an ideal gas at STP conditions, F is in units of $[m^3/s]$, and $\Delta t = \tau_T$, the termination time. We include a correction factor $\gamma = A_s/A_o$ for the flow rate that takes into account the CVD reactor's efficiency at delivering C_2H_2 to the sample. $A_s \sim 30$ mm^2 is the area of the substrate and $A_o \sim 130$ mm^2 as before, thus $\gamma \sim 0.23$. If A_o was larger than our conservative estimate, the calculated efficiency ϵ would be higher. Equation (3) is only valid for unpatterned substrates where the effects of diffusion do not need to be taken into account, and all gas that hits the substrate can contribute to growth.

To measure ϵ, forests were grown on larger ($\sim$60 mm^2) unpatterned substrates at 760°C. These much larger uniform forests grew for a much longer period of time ($\sim$1 hour on average) compared to the patterned catalyst islands, which is consistent with the observed trends for the patterned catalyst islands. Measured masses were between 1 mg and 4 mg and measured to 0.1 mg accuracy. Five uniform forests were grown under identical conditions

and weighed, giving $\epsilon = (29 \pm 7)\%$. Here, the error is determined by the standard deviation of the averaged values, although the largest source of error is the uncertainty over how much of the gas strikes the substrate. For ethylene, this figure has previously been reported as 32% [31]. This high observed growth efficiency is an important factor in the observed forest morphology and growth kinetics. If the efficiency was not so high, diffusion effects would be significantly less pronounced.

The time constant τ_d can be determined by letting $x \to \infty$ (Equation (2)), such that $n \to n_{\infty,2D} = I\tau_d$ where $I = 8.6 \times 10^{20}$ $C_2H_2/m^2/s$. The parameter $n_{\infty,2D}$ can be related to the density of a three dimensional ideal gas $n_{\infty,3D} = P/kT$, where k is Boltzmann's constant. Because we have considered a thin layer of gas with a thickness equal to the diffusion length $L = \sqrt{D\tau_d}$, all molecules within the thin layer can be considered as being able to interact with the substrate during the time scale τ_d. In solving Equation (1), we approximated the true 3D problem with a 2D problem. The 2D density of C_2H_2 molecules is the number of molecules within the thin boundary layer of height L above the substrate per unit area. Thus, a projection of the three dimensional density onto the two dimensional surface will yield the two dimensional density: $n_{\infty,2D} = Ln_{\infty,3D} = \sqrt{D\tau_d}P/kT$. Here $P = 90$ Pa is the partial pressure of C_2H_2 and $T = 760°C$ is the growth temperature. Substituting $n_{\infty,2D} = I\tau_d$ into this last equation and solving for τ_d, we find $\tau_d \sim 7.6 \times 10^{-3}$ s.

The solution $n(x)$ to Equation (1) is plotted in Fig. 7c for the four island sizes used. In Fig. 7c, it is the centers of the forests that have the lowest concentration of source gas n, and therefore the lowest growth rates. The observed features in the forest morphology (concavity, sidewall curvature, rippling), along with the non-uniform growth from outside inward, are natural consequences of the solution because the edges will receive more gas and grow faster. As seen in Fig. 7c, the smaller islands have a more uniform gas distribution across their areas, which leads to reduced concavity compared to the larger islands, a trend that is observed here (see Fig. 1b).

We suppose that the growth rate of a forest as a whole is limited by the slowest growing CNTs in the forest. In this paper, the concave top surfaces suggest that, on average, the slowest growing CNTs in the forest are those at the center of the forest. In Fig. 7c, the smallest diameter catalyst island has a noticeably higher gas concentration at its center $n(0)$ than the larger islands. Thus, gas phase diffusion will lead to the smaller forests growing faster (and terminating earlier) because more gas is available to them at their centers.

The late stage growth rate increase can also be explained using Equation (2) and Fig. 7c and the observation that the outer CNTs delaminate. Because they receive more gas, the outer CNTs grow faster and terminate before the rest of the CNTs in the forest. When these outer CNTs terminate, the forest as a whole is still growing and the outer CNTs are lifted off from the substrate. This delamination causes the base of the forest to become relatively narrower. As seen in Fig. 7c, a narrower forest will subsequently receive more gas and thus grow faster. As more and more outer CNTs delaminate, the forest becomes increasingly

narrow and grows at an increasing rate.

Termination is observed to occur earlier for larger C_2H_2 flow rates F (see Fig. 4b), and hence larger C_2H_2 concentrations n. Therefore, it will also occur earlier for smaller forests because they receive more gas (as seen in Fig. 7c), in agreement with our observations (see Fig. 3b). In this way, the experimentally observed carbon consuming termination mechanism can explain the observed catalyst island size dependence of the termination time τ_T.

3.4 Growth rate

We now quantitatively compare the predictions of our model to our observations by relating the concentration of the C_2H_2 source gas $n(x)$ to the growth rate β as a function of catalyst island diameter d and C_2H_2 flow rate F. Assuming that it is the slower growing CNTs at the center of the forest that determine the overall growth rate of the forest, we need to relate $n(0)$ to β. Experimentally, we find that $\beta \propto F - F_{min}$ and our calculations show that $n \propto I \propto F$. To include the effect of F_{min}, we suppose that $\beta \propto n - n_{min}$ where n_{min} is a minimum concentration related to F_{min}. An earlier paper [32] found a growth rate dependence of $n^{0.6}$ by considering a very large range of concentrations, albeit under otherwise varying growth conditions. Although $\beta \propto n - n_{min}$ fits our data better than a power law dependence, we have not varied the pressure over a wide range like Ref. 32 and our data cannot completely rule out a power law dependence on a wider scale.

In Equation (1), the growth rate β is determined by the term n/τ_g, which gives the amount of C_2H_2 striking the catalyst per unit area per unit time. The areal density of CNTs on the catalyst σ [CNTs/m^2] determines the number of C_2H_2 molecules contributing to the growth of a single CNT. We observe that σ is constant over the range of catalyst island sizes used in this paper. The linear density of carbon atoms within a CNT λ [Carbon atoms/m] (which is a function of the CNT diameter and number of walls) determines the linear growth rate. Thus, the growth rate of a CNT forest is given by:

$$\beta = \frac{2\left(n\left(0\right) - n_{min}\right)}{\sigma\lambda\tau_g} = \frac{2\left(n\left(0\right) - n_{min}\right)}{\rho\tau_g} \tag{4}$$

where the 2 assumes both carbon atoms in C_2H_2 contribute to growth and $\rho = \sigma\lambda$ is the number density of carbon atoms in the forest. The time constant τ_g is related to τ_d by the expression $\tau_g = \tau_d\left(1-\epsilon\right)/\epsilon$ (see Appendix D) and has a value $\tau_g \sim 1.9\times10^{-2}$ s. We estimate $n_{min} = I_{min}\tau_d = 1.3\times10^{18}$ C_2H_2/m^2. As a function of growth time t, we can approximate the growth rate as constant (see Fig. 2) because it is only very slowly varying.

The final parameter in Equation (4) that must be determined is the number density of carbon atoms in the forest ρ. To determine ρ, we measured the volumes of the forests used to determine ϵ and found an average mass density of $\rho_m = 40 \pm 10$ mg/cm^3. Additionally, we measured the masses and volumes of another 3 forests grown under slightly different

conditions and found that the density did not vary significantly. Our value agrees with previous reports that vary from 24-72 mg/cm^3 [33–39]. Dividing ρ_m by the mass of a carbon atom m_C, we find the carbon number density to be $\rho = (2.2 \pm 0.5) \times 10^{27}$ Carbon atoms/m^3.

Knowing all of the parameters, we now plot (see Fig. 4a) the growth rate β (Equation (4)) as a function of C_2H_2 flow rate F for 800 μm diameter catalyst islands grown at $T = 760$°C (dashed line). The dotted lines show the error bounds, which were calculated by propagating the errors on the parameters in Equation (4). We also plot (see Fig. 3a) β as a function of catalyst island diameter d ($d = 2R$) for $T = 760$°C (dashed line, with errors given by dotted lines). In both plots, Equation (4) underestimates the measured growth rates, which fall just outside the error bounds. Qualitatively, it also underestimates the amount of curvature in Fig. 3a.

These underestimations are most likely a result of the values of ϵ, ρ, n_{min}, and D (and therefore τ_d) that we have used. The efficiency ϵ has likely been underestimated because we assumed that all of the C_2H_2 entering the reactor hits the area A_o. In reality, much of the gas will not hit the area A_o due to gas phase diffusion, divergence of the stream of gas, and parasitic reactions, resulting in a larger value for ϵ. While cold-walled CVD is probably ideal for minimizing parasitic reactions because of the small heated region, these reactions are still expected to occur. Furthermore, we have assumed that both carbon atoms in C_2H_2 are used in the growth of CNTs. The efficiency ϵ and forest density ρ were measured using forests grown on unpatterned substrates. The kinetics vary as a function of forest size, so it is possible that ϵ and ρ may also vary. The density ρ would also likely be overestimated because we assumed that all the measured mass was due to CNTs, when there is likely amorphous material and adsorbed gases in the forest.

If we slightly adjust the values of the measured parameters in our model (ϵ, ρ, n_{min}, D, and τ_d), while still keeping them reasonable (see Table 1), it is possible to generate good fits to the data for 760°C (solid black lines in Fig. 3a and Fig. 4a), which shows that the model can be a good explanation for the results. The slight adjustment was done by eye, and was done for the purpose of showing that the model *can* fit the data, not for the purpose of determining the values of the parameters in the model. However, it should be possible to determine the values of the parameters by fitting the model to the data.

Table 1: Values of parameters used to generate the curves in Fig. 3a and Fig. 4a. Predicted values are for the dashed lines (with error given by dotted lines), while fitted values are for the solid lines. Note that τ_d is determined by D and is not a free parameter. The errors quoted for n_{min} and τ_d are determined from D.

Parameter [units]	Predicted	Fitted
ϵ	0.29 ± 0.07	0.39
ρ [Carbon atoms/m^3]	$(2.2 \pm 0.5) \times 10^{27}$	1.3×10^{27}
n_{min} [C_2H_2/m^2]	$(1.3 \pm 0.5) \times 10^{18}$	6.5×10^{17}
D [m^2/s]	$(1.5 \pm 0.5) \times 10^{-4}$	1.0×10^{-4}
τ_d [s]	$(7.6 \pm 2.5) \times 10^{-3}$	5.1×10^{-3}

Now that we have a model of gas phase diffusion that can be directly related to our experimental results, we can discuss some specific features seen in Fig. 3a. First, there is an exception to the trend of the smaller islands growing faster, which occurs at 700°C. It is possible that at low T, C_2H_2 becomes oversupplied [14]. Thus, the additional gas received by diffusion would be further detrimental to growth, and have a larger effect on the smaller islands. The abrupt change between 720°C and 700°C could also be attributed to a sudden change in the physical structure or chemical state of the catalyst, such as a greater number of larger inactive catalyst nanoparticles at lower temperatures. Second, higher growth temperatures T generally show less dependence with catalyst island diameter d (and thus with the gas distribution). This is likely a result of the diffusion coefficient D increasing with temperature, and thus flattening out the curve.

The amount of curvature seen in Fig. 7c for the 800 μm forest means that the outer CNTs grow 3% faster (using the predicted values) than those at the center of the forest (because $\beta \propto n - n_{min}$). We previously estimated a growth rate difference of ∼20% as being necessary to cause the rippling phenomenon [15], based on the observed shape of the rippling pattern, which is also observed on some forests in the present paper. Using the fitted values, the growth rate difference becomes 8%, which is much closer to our previous estimate.

3.5 CNT density

Finally, we measure the CNT areal density σ and the linear density of carbon atoms within a CNT λ (an average for our forests). The latter can provide information about the type of CNT present in our forests while the former can give insight into gas diffusion and how it relates to nucleation.

To determine σ, we used scanning electron microscopy (SEM) to measure the areal density of CNT bundles σ_b in the forests (see Appendix D). Forests were grown at 760°C and intentionally terminated after 2 min of growth by halting the supply of C_2H_2. These forests were gently removed from the growth substrate, and their bottom surfaces were examined in cross section (see Appendix D, Fig. S8), making it possible to directly measure $\sigma_b = (2.0 \pm 0.4) \times 10^{10}$ bundles/cm^2, with no obvious variation as a function of catalyst island size (see Appendix D, Fig. S8 and Table S1). Near the edges of the forest, the bundle density σ_b was not measurably different than the bundle density at the center of the forest ($\sigma_b = (2.1 \pm 0.4) \times 10^{10}$ bundles/cm^2 at the edge and $\sigma_b = (2.2 \pm 0.4) \times 10^{10}$ bundles/cm^2 at the center, see Appendix D, Fig. S8).

To relate σ_b to σ the number of CNTs in each bundle must be known. Based on previous work [37, 40] each bundle is expected to contain a small number of CNTs, and this is consistent with the small diameter of the bundles seen in SEM images (see Appendix D, Fig. S8). For the sake of definiteness in the calculation we suppose there are 7 ± 3 CNTs in each bundle (or, in other words, 4 to 10 CNTs on average per bundle). Therefore, we

determine $\sigma = (1.4 \pm 0.8) \times 10^{11}$ CNTs/cm^2, which agrees with previously reported figures that range from 10^9-10^{13} cm^{-2} [33–37, 39, 41–45].

Knowing σ, we can calculate λ and determine the nature of the average CNT in our forests since λ is a function of diameter and number of walls: $\lambda = \pi N_{CNT} \left(d_{CNT} - \left(N_{CNT} - 1\right) \delta\right) / \Omega$. Here, d_{CNT} is the CNT diameter, N_{CNT} is the number of walls, $\delta = 0.34$ nm is the interlayer spacing in graphite, and $\Omega = 0.026$ nm^2/Carbon atom is the density of carbon in a graphene sheet. As defined above, $\lambda = \rho/\sigma$, thus $\lambda \sim 1600 \pm 1200$ Carbon atoms/nm for the average CNT in the forest.

This calculated linear density is large for SWCNTs, and so more likely represents few-walled narrow diameter MWCNTs. For example, a SWCNT with $\lambda = 1600$ Carbon atoms/nm, would have a diameter of ∼13 nm. On the other hand, a MWCNT with 3 walls and an outer diameter of 5 nm has $\lambda \sim 1600$ Carbon atoms/nm. We therefore suppose that the average CNT in our forests (at this growth temperature of 760°C) is a few-walled narrow diameter MWCNT, though the distribution of CNT species is likely quite broad and includes SWCNTs (the presence of which was suggested by the RBMs in the Raman spectra, Appendix D, Fig. S6).

The broad distribution of CNT diameters and wall numbers is consistent with the large uncertainty on λ and is consistent with Ref. 6, which reported an average wall number of 7 ± 3 for the equivalent island size. There are two main factors that could affect the accuracy of our measurement: (1) any meandering of the CNTs would cause λ to increase and (2) any non-CNT mass in the forest would also affect the value of λ.

In general, the density of catalyst nanoparticles (NPs) on the substrate surface is larger than the density of CNTs in the forest σ. In other words, the fraction of catalyst NPs that grow CNTs is small, which is especially true for growth in a supply limited process. Here, we can estimate the fraction of NPs that produce CNTs if we assume that the NPs are 5 nm hemispheres (the estimated diameter of the CNTs from above) and that the catalyst is deposited as a 0.8 nm thick disk. If the quantity of catalyst material remains constant, we find a NP density of $\sim 2.4 \times 10^{12}$ NPs/cm^2, meaning approximately 6% of NPs produce CNTs.

Although the length scales differ, our diffusion model can provide insight into this limited number of catalyst NPs that grow CNTs. This proposed mechanism is only one of many constraints (such as nucleation effects related to the catalyst NP size or composition [46, 47]) that limit the number of catalyst NPs that grow CNTs. The effect of diffusion on the limited number of catalyst NPs that grow CNTs is illustrated in Fig. 8. Once a CNT has nucleated and begins to grow, it requires a certain amount of source gas to obtain a sustainable growth rate. This gas is taken from nearby NPs, leaving them with less gas. In the simplest types of crystal growth nucleation models (see for example Hudson [48]), growth occurs when the adatom coverage exceeds a critical value as a result of a critical concentration of source gas n_{crit}. Thus, a growing CNT will locally deplete the carbon supply $n\left(x\right)$, keeping it below

the critical value n_{crit}, and preventing neighbouring NPs from nucleating or growing their own CNTs. So, although a NP may be present and capable of growing a CNT, it may fail to produce one because the supply of source gas has been reduced to a level below n_{crit} by CNTs growing nearby. There is thus a certain average distance between the nearest NPs growing CNTs. This then sets the fraction of NPs actively growing CNTs and the CNT density of the forest σ. This mechanism will also synchronize growth across the forest by ensuring that each growing CNT receives a similar amount of C_2H_2.

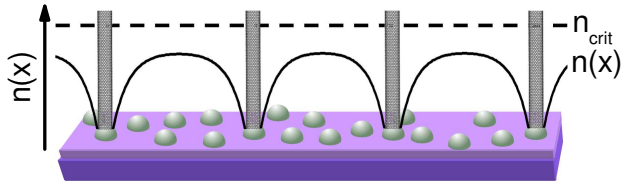


Figure 8: Diagram of catalyst nanoparticles and gas phase diffusion. In a supply limited process, catalyst nanoparticles compete for the source material: C_2H_2 is taken from neighbouring nanoparticles by growing CNTs, inhibiting the nearby nucleation and growth of CNTs. This sets the fraction of active catalyst nanoparticles and, therefore, the density of the CNT forest. C_2H_2 concentration n is plotted (solid line) as a function of position x. The dashed line is the critical concentration for nucleation n_{crit}. Nanoparticles (green), support (purple), and CNTs (black) are pictured.

3.6 Termination mechanisms

Finally, we briefly discuss some potential mechanisms that may lead to termination. Many mechanisms exist and likely occur simultaneously during growth. However, depending on their relative rates, it is probable that only one mechanism will induce termination (the most rapid mechanism). Here we speculate about which mechanisms are most likely to induce termination. We observe a gradual termination (exponential decay of growth) that is eventually overcome by a sudden termination. Termination is observed to be a function of both catalyst island diameter d (Fig. 3b) and C_2H_2 flow rate F (Fig. 4b), the latter of which supports the idea that termination may be caused (either directly or indirectly) by a carbon consuming reaction. This point was critical in the gas-phase diffusion model, regardless of the actual mechanism responsible for termination.

The observed gradual termination appears to be consistent with a mechanism of catalyst deactivation that is driven by a carbon consuming reaction that competes with growth, such as the poisoning of the catalyst nanoparticles or an amorphous carbon coating [49, 50]. This termination mechanism is affected by the amount of carbon available, as reported previously [6] and as seen in Fig. 4b. The dependence of termination on catalyst island diameter d can also be explained by this mechanism. The observed sudden termination might be explained by a build-up of strain [17, 51] as we have reported previously [17], which may be the result of some CNTs terminating before others due to catalyst deactivation (and thus dependent on d and F), or simply extreme differences in the growth rate.

Other termination mechanisms seem less likely. Termination due to source gas diffusion being blocked by the growing forest [5, 52] would predict that larger diameter forests would terminate earlier than the smaller forests, a trend opposite to our observations.

Termination by density decay [33] is a sudden termination mechanism in which forests stop growing when the CNT areal density σ drops below a critical value ($\sigma_c \sim 10^9$ CNTs/cm^2 for thin MWCNTs) [33] and vertical alignment is no longer favourable. This mechanism is also accompanied by a characteristic loss of alignment of the individual nanotubes (with respect to one another) at the base of the forest [33]. We see evidence that the density of our forests does decrease, implying that this mechanism is occurring. However, two observations suggest that although the density is decreasing in the present paper, it is not the cause of termination. One, although we do observe sudden termination, it is not accompanied by the characteristic loss of alignment of the individual CNTs (see Appendix D, Fig. S3a). And, two, the measured areal densities of our forests ($\sigma = (1.4 \pm 0.9) \times 10^{11}$ CNTs/cm^2 after 2 min of growth and $\sigma = (1.0 \pm 0.8) \times 10^{11}$ CNTs/cm^2 upon natural termination after 16 min of growth) are always, even at their natural termination, at least an order of magnitude greater than the critical density reported in Ref. 33. So, although density decay does appear to occur in our forests, it does not seem to be sufficient to cause termination.

Further possibilities for termination mechanisms include any form of time evolution in the catalyst NPs, examples of which include Ostwald ripening (the growth of large particles at the expense of smaller particles) [53, 54] and the diffusion of the catalyst into the support [54–56]. These effects are likely occurring on our samples. However, simple changes to the catalyst NPs with time do not explain the observed island size dependence. For any of these mechanisms to be the cause of termination, the time evolution of the catalyst NP size must depend on the catalyst island size. This might be possible, for example, if these mechanisms depend on the gas concentration. It has previously been reported [56] that these mechanisms have no clear dependence on the concentration of C_2H_2, though these observations were for much lower (100× lower) concentrations of C_2H_2. Thus, given that we observe a strong dependence for the termination time as a function C_2H_2 concentration, it seems unlikely that these mechanisms are the cause of termination on our samples.

4 Summary

We analyzed the effect of the size of patterned thin film catalyst regions on the growth of vertically aligned CNT forests. Forests grown on smaller catalyst islands grow faster and stop growing (terminate) earlier than forests grown on larger catalyst islands. We explained our observations with a gas diffusion model that shows that catalyst nanoparticles receive gas not only from direct impingement, but also from density gradients and the resulting gas phase diffusion between regions with differing growth activities. On substrates with patterned catalyst islands the smaller islands receive more gas than the larger ones. This causes both

the faster growth and earlier termination because both are controlled by the amount of source gas available. The gas phase diffusion also causes the characteristic concave shape of the top surface of the forests. Although our model is quite simple, experimental data can be fitted using parameters close to the experimentally measured values.

The observed size dependent effects occur in part because of the high efficiency by which C_2H_2 is converted into CNTs ($\sim$30%). This high efficiency and the critical role of gas phase diffusion in CNT growth provide a constraint that may limit the density of CNTs and synchronize their growth rates. The fact that the termination time τ_T depends on the concentration of the source gas supports the idea of termination being caused by a carbon consuming reaction. Based on this observation, one possible termination mechanism is catalytic deactivation (such as the poisoning of or amorphous carbon coating of the catalyst nanoparticle) with the observed sudden termination possibly caused by a build-up of strain in the forest.

Acknowledgments

The authors thank the following people: J. Fraser for assistance with SEM, B. Lamontagne for lithography, and H. Tran for e-beam deposition. P.V. was supported by NSERC, NRC-GSSSP, and P.F.'s NSERC Discovery Grant.

References

[1] Z F Ren, Z P Huang, J W Xu, J H Wang, P Bush, M P Siegal, and P N Provencio. Synthesis of large arrays of well-aligned carbon nanotubes on glass. *Science*, 282:1105–7, 1998.

[2] K Hata, D N Futaba, K Mizuno, T Namai, M Yumura, and S Iijima. Water-assisted highly efficient synthesis of impurity-free single-walled carbon nanotubes. *Science*, 306:1362–4, 2004.

[3] A J Hart and A H Slocum. Rapid growth and flow-mediated nucleation of millimeter-scale aligned carbon nanotube structures from a thin-film catalyst. *J. Phys. Chem. B*, 110:8250–7, 2006.

[4] M J Bronikowski. CVD growth of carbon nanotube bundle arrays. *Carbon*, 44:2822–32, 2006.

[5] G Zhong, T Iwasaki, J Robertson, and H Kawarada. Growth kinetics of 0.5 cm vertically aligned single-walled carbon nanotubes. *J. Phys. Chem. B*, 111:1907–10, 2007.

[6] G-H Jeong, N Olofsson, L K L Falk, and E E B Campbell. Effect of catalyst pattern geometry on the growth of vertically aligned carbon nanotube arrays. *Carbon*, 47:696–704, 2009.

[7] M F L De Volder, D O Vidaud, E R Meshot, S Tawfick, and A J Hart. Self-similar organization of arrays of individual carbon nanotubes and carbon nanotube micropillars. *Microelectron. Eng.*, 87:1233–38, 2010.

[8] S Dittmer, J Ek-Weis, O A Nerushev, and E E B Campbell. Growth of aligned mwnt arrays using a micrometer scale local-heater at low ambient temperature. *J. Nanosci. Nanotech.*, 10:4015–22, 2010.

[9] I Gunjishima, T Inoue, and A Okamoto. *In situ* growth rate control of carbon nanotubes by optical imaging method. *Appl. Phys. Lett.*, 91:193102, 2007.

[10] A J Hart, L van Laake, and A H Slocum. Desktop growth of carbon-nanotube monoliths with in situ optical imaging. *Small*, 3:772–7, 2007.

[11] A A Puretzky, G Eres, C M Rouleau, I N Ivanov, and D B Geohegan. Real-time imaging of vertically aligned carbon nanotube array growth kinetics. *Nanotechnology*, 19:055605, 2008.

[12] S Yasuda, D N Futaba, M Yumura, S Iijima, and K Hata. Diagnostics and growth control of single-walled carbon nanotube forests using a telecentric optical system for *in situ* height monitoring. *Appl. Phys. Lett.*, 93:143115, 2008.

[13] C Mattevi, C T Wirth, S Hofmann, R Blume, M Cantoro, C Ducati, C Cepek, A Knop-Gericke, S Milne, C Castellarin-Cudia, S Dolafi, A Goldoni, R Schloegl, and J Robertson. In-situ x-ray photoelectron spectroscopy study of catalyst-support interactions and growth of carbon nanotube forests. *J. Phys. Chem. C*, 112:12207–13, 2008.

[14] P Vinten, J Lefebvre, and P Finnie. Kinetic critical temperature and optimized chemical vapor deposition growth of carbon nanotubes. *Chem. Phys. Lett.*, 469:293–7, 2009.

[15] P Vinten, J Bond, P Marshall, J Lefebvre, and P Finnie. Origin of periodic rippling during chemical vapor deposition growth of carbon nanotube forests. *Carbon*, 49:4972–81, 2011.

[16] P Finnie, P Vinten, P Marshall, and J Lefebvre. Morphological instabilities and the dynamics of carbon nanotube forest growth. *ECS Trans.*, 35:3–12, 2011.

[17] P Vinten, P Marshall, J Lefebvre, and P Finnie. Distinct termination morphologies for vertically aligned carbon nanotube forests. *Nanotechnology*, 21:035603, 2010.

[18] P Vinten, J Lefebvre, and P Finnie. Visible iridescence from self-assembled periodic rippling in vertically aligned carbon nanotube forests. *Appl. Phys. Lett.*, 97:101901, 2010.

[19] G Eres, A A Puretzky, D B Geohegan, and H Cui. *In situ* control of the catalyst efficiency in chemical vapor deposition of vertically aligned carbon nanotubes on predeposited metal catalyst films. *Appl. Phys. Lett.*, 84:1759–61, 2004.

[20] G Eres, A A Kinkhabwala, H Cui, D B Geohegan, A A Puretzky, and D H Lowndes. Molecular beam-controlled nucleation and growth of vertically aligned single-wall carbon nanotube arrays. *J. Phys. Chem. B*, 109:16684–94, 2005.

[21] G Eres, C M Rouleau, M Yoon, A A Puretzky, J J Jackson, and D B Geohegan. Model for self-assembly of carbon nanotubes from acetylene based on real-time studies of vertically aligned growth kinetics. *J. Phys. Chem. C*, 113:15484–91, 2009.

[22] D N Futaba, K Hata, T Yamada, K Mizuno, M Yumura, and S Iijima. Kinetics of water-assisted single-walled carbon nanotube synthesis revealed by a time-evolution analysis. *Phys. Rev. Lett.*, 95:056104, 2005.

[23] M J Bronikowski. Longer nanotubes at lower temperatures: The influence of effective activation energies on carbon nanotube growth by thermal chemical vapor deposition. *J. Phys. Chem. C*, 111:17705–12, 2007.

[24] M Picher, E Anglaret, R Arenal, and V Jourdain. Self-deactivation of single-walled carbon nanotube growth studied by in situ raman measurements. *Nano Lett.*, 9:542–7, 2009.

[25] S Yasuda, D N Futaba, T Yamada, M Yumura, and K Hata. Gas dwell time control for rapid and long lifetime growth of single-walled carbon nanotube forests. *Nano Lett.*, 11:3617–23, 2011.

[26] K Hasegawa and S Noda. Moderating carbon supply and suppressing ostwald ripening of catalyst particles to produce 4.5-mm-tall single-walled carbon nanotube forests. *Carbon*, 49:4497–504, 2011.

[27] M Chhowalla, K B K Teo, C Ducati, N L Rupesinghe, G A J Amaratunga, A C Ferrari, D Roy, J Robertson, and W I Milne. Growth process conditions of vertically aligned carbon nanotubes using plasma enhanced chemical vapor deposition. *J. Appl. Phys.*, 90:5308–17, 2001.

[28] D Takagi, Y Homma, and Y Kobayashi. Selective growth of individual single-walled carbon nanotubes suspended between pillar structures. *Physica E*, 24:1–5, 2004.

[29] K D Childs, B A Carlson, L A LaVanier, J F Moulder, D F Paul, W F Stickle, D G Watson, and C L Hedburg. *Handbook of Auger Electron Spectroscopy, 3rd Edition*. Physical Electronics, Inc., USA, 1995.

[30] Diffusion in gases. In W M Haynes, editor, *CRC Handbook of Chemistry and Physics, 91st Edition (Internet Version 2011)*, pages 6.191–2. CRC Press/Taylor and Francis, USA, 2011.

[31] S Yasuda, D N Futaba, T Yamada, J Satou, A Shibuya, H Takai, K Arakawa, M Yumura, and K Hata. Improved and large area single-walled carbon nanotube forest growth by controlling the gas flow direction. *ACS Nano*, 3:4164–70, 2009.

[32] C T Wirth, C Zhang, G Zhong, S Hofmann, and J Robertson. Diffusion- and reaction-limited growth of carbon nanotube forests. *ACS Nano*, 3:3560–6, 2009.

[33] M Bedewy, E R Meshot, H Guo, E A Verploegen, W Lu, and A J Hart. Collective mechanism for the evolution and self-termination of vertically aligned carbon nanotube growth. *J. Phys. Chem. C*, 113:20576–82, 2009.

[34] D N Futaba, K Hata, T Namai, T Yamada, K Mizuno, Y Hayamizu, M Yumura, and S Iijima. 84% catalyst activity of water-assisted growth of single walled carbon nanotube forest characterization by a statistical and macroscopic approach. *J. Phys. Chem. B*, 110:8035–8, 2006.

[35] G F Zhong, T Iwasaki, and H Kawarada. Semi-quantitative study on the fabrication of densely packed and vertically aligned single-walled carbon nanotubes. *Carbon*, 44:2009–14, 2006.

[36] D N Futaba, K Hata, T Yamada, T Hiraoka, Y Hayamizu, Y Kakudate, O Tanaike, H Hatori, M Yumura, and S Iijima. Shape-engineerable and highly densely packed single-walled carbon nanotubes and their application as super-capacitor electrodes. *Nat. Mater.*, 5:987–94, 2006.

[37] E Einarsson, H Shiozawa, C Kramberger, M H Rümmeli, A Grüneis, T Pichler, and S Maruyama. Revealing the small-bundle internal structure of vertically aligned single-walled carbon nanotube films. *J. Phys. Chem. C*, 111:17861–4, 2007.

[38] S Yasuda, T Hiraoka, D N Futaba, T Yamada, M Yumura, and K Hata. Existence and kinetics of graphitic carbonaceous impurities in carbon nanotube forests to assess the absolute purity. *Nano Lett.*, 9:769–73, 2009.

[39] M Bedewy, E R Meshot, M J Reinker, and A J Hart. Population growth dynamics of carbon nanotubes. *ACS Nano*, 5:8974–89, 2011.

[40] F Márquez, V López, C Morant, R Roque-Malherbe, C Domingo, E Elizalde, and F Zamora. Structure and characterization of vertically aligned single-walled carbon nanotube bundles. *J. Nanomater.*, 2010:189214, 2010.

[41] R D Bennett, A J Hart, and R E Cohen. Controlling the morphology of carbon nanotube films by varying the areal density of catalyst nanoclusters using block-copolymer micellar thin films. *Adv. Mat.*, 18:2274–9, 2006.

[42] Y Murakami, S Chiashi, Y Miyauchi, M Hu, M Ogura, T Okubo, and S Maruyama. Growth of vertically aligned single-walled carbon nanotube films on quartz substrates and their optical anisotropy. *Chem. Phys. Lett.*, 385:298–303, 2004.

[43] D Yokoyama, T Iwasaki, T Yoshida, H Kawarada, S Sato, T Hyakushima, M Nihei, and Y Awano. Low temperature grown carbon nanotube interconnects using inner shells by chemical mechanical polishing. *Appl. Phys. Lett.*, 91:263101, 2007.

[44] Y Yamazaki, M Katagiri, N Sakuma, M Suzuki, S Sato, M Nihei, M Wada, N Matsunaga, T Sakai, and Y Awano. Synthesis of a closely packed carbon nanotube forest by a multi-step growth method using plasma-based chemical vapor deposition. *Appl. Phys. Exp.*, 3:055002, 2010.

[45] S Esconjauregui, M Fouquet, B C Bayer, C Ducati, and J Robertson. Catalyst design for the growth of highly packed nanotube forests. *Phys. Status Solidi B*, 248:2528–31, 2011.

[46] J C Burgos, H Reyna, B I Yakobson, and P B Balbuena. Interplay of catalyst size and metal-carbon interactions on the growth of single-walled carbon nanotubes. *J. Phys. Chem. C*, 114:6952–8, 2010.

[47] J C Burgos, E Jones, and P B Balbuena. Effect of the metal-substrate interaction strength on the growth of single-walled carbon nanotubes. *J. Phys. Chem. C*, 115:7668–75, 2011.

[48] J B Hudson. *Surface Science: An Introduction*. Wiley, Toronto, Canada, 1998.

[49] S Helveg, C López-Cartes, J Sehested, P L Hansen, B S Clausen, J R Rostrup-Nielsen, F Abild-Pedersen, and J K Nørskov. Atomic-scale imaging of carbon nanofibre growth. *Nature*, 427:426–9, 2004.

[50] A A Puretzky, D B Geohegan, S Jesse, I N Ivanov, and G Eres. In situ measurements and modeling of carbon nanotube array growth kinetics during chemical vapor deposition. *Appl. Phys. A*, 81:223–40, 2005.

[51] J-H Han, R A Graff, B Welch, C P Marsh, R Franks, and M S Strano. A mechanochemical model of growth termination in vertical carbon nanotube forests. *ACS Nano*, 2:53–60, 2008.

[52] C Singh, M S P Shaffer, and A H Windle. Production of controlled architectures of aligned carbon nanotubes by an injection chemical vapour deposition method. *Carbon*, 41:359–68, 2003.

[53] P B Amama, C L Pint, L McJilton, S M Kim, E A Stach, P T Murray, R H Hauge, and B Maruyama. Role of water in super growth of single-walled carbon nanotube carpets. *Nano Lett.*, 9:44–9, 2009.

[54] S M Kim, C L Pint, P B Amama, R H Hauge, B Maruyama, and E A Stach. Catalyst and catalyst support morphology evolution in single-walled carbon nanotube supergrowth: Growth deceleration and termination. *J. Mater. Res.*, 25:1875–85, 2010.

[55] P B Amama, C L Pint, S M Kim, L McJilton, K G Eyink, E A Stach, R H Hauge, and B Maruyama. Influence of alumina type on the evolution and activity of alumina-supported fe catalysts in single-walled carbon nanotube carpet growth. *ACS Nano*, 4:895–904, 2010.

[56] S M Kim, C L Pint, P B Amama, D N Zakharov, R H Hauge, B Maruyama, and E A Stach. Evolution in catalyst morphology leads to carbon nanotube growth termination. *J. Phys. Chem. Lett.*, 1:918–22, 2010.

Chapter 8

Thermodynamic and Energetic Effects on the Diameter and Defect Density in Single Walled Carbon Nanotube Synthesis

as published* in *The Journal of Physical Chemistry C*, Volume 117, Pages 3527–3536, 2013.
http://dx.doi.org/10.1021/jp308672a

Copyright notice: Reproduced with permission from [*J. Phys. Chem. C*, **2013**, *117* (7), pp 3527–3536.] Copyright 2013 American Chemical Society.

This article includes supplementary material, which is reprinted here in Appendix E.

*In accordance with University of Ottawa regulations, the contact email address has been removed from this article.

Foreword

This chapter differs from most of the previous chapters in the sense that it is not focused on maximizing the yield, studying the morphology, or analyzing what causes termination, but is instead focused on what species of nanotubes (as defined by the diameter) are produced in the CVD reaction. From Chapter 7, it was determined that to maximize the yield one must use large samples with a uniformly deposited catalyst (no patterning). It was also determined in previous chapters (Chapter 2 and Chapter 3) that an optimum temperature exists for maximizing the yield and for maximizing the D/G ratio and number of single walled carbon nanotubes (SWCNTs).

This chapter adds in the additional parameter of the thickness of the catalytic cobalt layer, which is reduced from 0.8 nm in the previous chapters to 0.35 nm here. This decrease is expected to increase the amount of SWCNTs that are produced [1]. The improvement in the D/G ratio is also immediately apparent (although there is a simultaneous drop in yield). Likewise, with this thinner catalyst layer, there are always multiple easily visible RBMs in the Raman spectra, implying a significant number of SWCNTs with varying chiralities. The RBMs are plentiful enough that the average, minimum, and maximum diameter of the SWCNTs can be analyzed as a function of growth temperature. A model based on the thermodynamics of the conversion of the acetylene source gas into carbon nanotubes reproduces the systematic minimum observed diameter. This thermodynamics model also provides general insight into the origin of the temperature dependence of the nanotube diameter and which parameters need to be adjusted in order to minimize the diameter. Further to that, the effect of other mechanisms is included to give an overview of how one can control the diameter distribution during synthesis.

The D/G ratio seen in this chapter is seen to have the same temperature dependence as in Chapter 2 and Chapter 3. Given the differing growth conditions of these chapters, this commonality strongly suggests that there is a process that is intrinsic to CNT growth that is responsible for determining the defect density. Many restrictions can be placed on the nature of this mechanism and a defect healing mechanism [2–4] is proposed to explain these observations. As a nanotube grows, defects that are initially formed in the lattice can be healed as growth proceeds. Those that are not healed are incorporated into the nanotube. Higher temperatures promote an increased amount of healing and lead to lower defect densities, which is the observed temperature dependence. Specifically, it is proposed that the observed temperature dependence of the D/G ratio is the result of the healing of one single type of simple defect that is abundant in the CNTs. This defect healing mechanism also satisfies the strict requirement of being independent of

most growth conditions and intrinsic to the growth of carbon nanotubes.

The results of this chapter will aid future research in two ways. First, the models discussed provide insight into the microscale growth process, both for the control of the SWCNT diameter and the control of the defect density. Second, many of the CVD growth parameters that control the D/G ratio and SWCNT diameter distribution are identified and their effects are discussed and quantified. These results will assist in both theoretical and experimental studies of the systematic and purposeful synthesis of a desired diameter distribution of SWCNTs with a minimized defect density. However, a trade-off between yield, defect density, and diameter is also observed, which means that it may not be possible to simultaneously optimize each parameter. Thus, optimizing the output of a CVD synthesis process for a specific application may entail making compromises. The proposed defect healing mechanism relates to the lattice of a carbon nanotube and not to any properties specific to carbon nanotubes. Thus it is possible that similar effects may also occur in the CVD growth of graphene and other related materials. If defects form in significant numbers initially, the defect healing mechanism may set a lower bound for the growth temperature that leads to high quality nanotubes and other related materials.

---

[1] B Zhao, D N Futaba, S Yasuda, M Akoshima, T Yamada, and K Hata. *ACS Nano*, 3:108–14, 2008.

[2] M Picher, E Anglaret, R Arenal, and V Jourdain. *Nano Lett.*, 9:542–7, 2009.

[3] A J Page, Y Ohta, Y Okamoto, S Irle, and K Morokuma. *J. Phys. Chem. C*, 113:20198–207, 2009.

[4] Q Yuan, Z Xu, B I Yakobson, and F Ding. *Phys. Rev. Lett.*, 108:245505, 2012.

THE JOURNAL OF PHYSICAL CHEMISTRY C

Article

pubs.acs.org/JPCC

Thermodynamic and Energetic Effects on the Diameter and Defect Density in Single-Walled Carbon Nanotube Synthesis

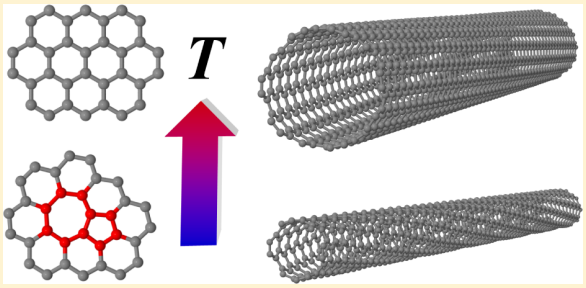
Phillip Vinten,[†,‡] Paul Marshall,[†] Jacques Lefebvre,[†] and Paul Finnie*[,†,‡]

[†]National Research Council Canada, Building M-50, 1200 Montreal Road, Ottawa, ON, K1A 0R6, Canada

[‡]Department of Physics, University of Ottawa, 150 Louis Pasteur, Ottawa, ON, K1N 6N5, Canada

Supporting Information

ABSTRACT: Single-walled carbon nanotube (SWCNT) ensembles are characterized by their defect density and diameter distribution. Here, SWCNTs are grown using chemical vapor deposition with acetylene as the carbon source and cobalt as the catalyst and analyzed ex situ, without any modification or processing, using Raman spectroscopy. The defect density shows an activated temperature dependence (activation energy ~0.8 eV or ~80 kJ/mol) with fewer defects at high growth temperatures for a wide range of experimental parameters. This is consistent with a single activated mechanism, such as the catalytic healing of defects, possibly a single simple defect. Consistent with previous reports, we see that low growth temperatures produce smaller diameter SWCNTs than high growth temperatures. Elementary thermodynamic considerations of the strain energy in the lattice constrain the SWCNT diameter distribution and its temperature dependence and appear consistent with our observations. A "phase diagram" for SWCNT growth is constructed and suggests methods of controlling the diameter distribution. There is a trade-off here between small diameter SWCNTs and SWCNTs with low defect densities.



INTRODUCTION

For many applications of single-walled carbon nanotubes (SWCNTs), separation by electronic type, diameter, or chirality is important. There are two general procedures that can lead to SWCNT separation: postgrowth processing or high precision control during synthesis. Postgrowth processing has become very effective (see, for example, ref 1.); however, such separation techniques pose challenges as they typically require solution phase manipulations that usually damage carbon nanotubes (CNTs) and are currently only effective for short (<10 μm) CNTs. Most importantly, postgrowth separation can only be successfully performed on solutions that already contain the desired CNTs, and the yield of the separation techniques will always depend on the initial distribution of CNTs in the sample. Ideally, one would be able to grow CNTs of one single specific chirality. Being able to narrow down the distribution of diameters and chiralities is a step toward this goal. To achieve this greater level of control over the distribution of SWCNTs, the underlying mechanisms that lead to selectivity must be understood.

Much research on the mechanisms that determine SWCNT diameter and chirality has been done,[2−12] and various models have been proposed. Importantly, the CNT diameter has been shown to depend on the catalyst nanoparticle diameter.[3] An kinetic growth rate mechanism based on a screw dislocation derived model has been proposed to explain the distribution of chiralities among SWCNTs.[8,12] In the present report, we highlight the effects of the intrinsic thermodynamic stability of the SWCNT lattice on the diameter distribution.

Defect densities are also a defining characteristic of CNT ensembles, as they are for any crystalline material. The presence of defects alters the optical and electronic properties of CNTs. We find a single common activation energy in the D/G ratio (a measure of the defect density) over a wide range of synthesis conditions and produced CNTs. This observation suggests that the defect density is determined primarily by a single activated mechanism, such as the catalytic healing of defects[13−15] as the CNT grows. Moreover, as many different types of defects may be present, the single activation energy suggests that the defect density is determined primarily by the healing of a single type of defect, for example, a simple defect, such as a pentagon/heptagon pair. This has important consequences for the type of material that can be grown.

EXPERIMENTAL METHODS

The CNT forests grown here were produced in a cold-walled chemical vapor deposition (CVD) reactor operated at atmospheric pressure, using dilute acetylene[16,17] (0.1% C_2H_2, 99.9% Ar) as the carbon source gas, water vapor[18] (obtained from a bubbler) and hydrogen gas (2% H_2, 98% Ar) as enhancers, Ar as a carrier gas, and a Co/Al_2O_3 thin film as the

Received: August 31, 2012
Revised: January 21, 2013
Published: January 24, 2013

ACS Publications © 2013 American Chemical Society

catalyst. The catalyst (0.35 nm Co and 50 nm Al_2O_3 layers) is deposited as uniform layers by e-beam evaporation onto a 0.5 mm thick silicon wafer with a 1 μm thermal oxide that is then cleaved into ~90 mm^2 pieces for growth. Upon heating to high temperatures, the thin Co layer breaks into nanoparticles (with a wide distribution of diameters that is greater than 0.35 nm but does depend on the initial thickness of the layer).[19−21] Complete details on the growth procedure can be found in the Supporting Information. Here, we vary both the growth temperature T and the C_2H_2 partial pressure P (through the C_2H_2 flow rate F). The entire range of growth temperatures that produce CNT forests is explored. Outside of this temperature range, either low yield surface CNTs or nothing at all grew. We also analyze previously published data obtained from forests grown using ethanol[22] and acetylene[23] as source gases.

Raman spectra were acquired using a custom built Raman spectrometer[24] with 532 nm excitation. The CNT forests were analyzed ex situ, without any modification or processing, using a 20× objective in plan view, looking orthogonal to the top surface of the forests (parallel to the average CNT axis). All spectra were acquired ex situ at room temperature. For each forest, a minimum of three spectra were acquired, each from a different location on the same forest. Each spectrum consists of five 6 s acquisitions. The power density was kept low enough to prevent burning of the CNTs. We also compare the data acquired in the present report to some of our prior results[22,23] that were obtained at both 532 and 785 nm.

RESULTS AND DISCUSSION

Typical Raman spectra of our CNT forests, normalized to the G^+ peak maximum, are shown in Figure 1. Here, we present only some of the Raman spectra; additional spectra for all other growth temperatures at 20 °C intervals from 700 to 980 °C are available in the Supporting Information (Figures S1 and S2). From Figure 1, it is clear that the D band intensity (~1330 cm^{-1}) decreases with increasing growth temperature T, indicating that the CNTs produced at lower growth temperatures are more defective.

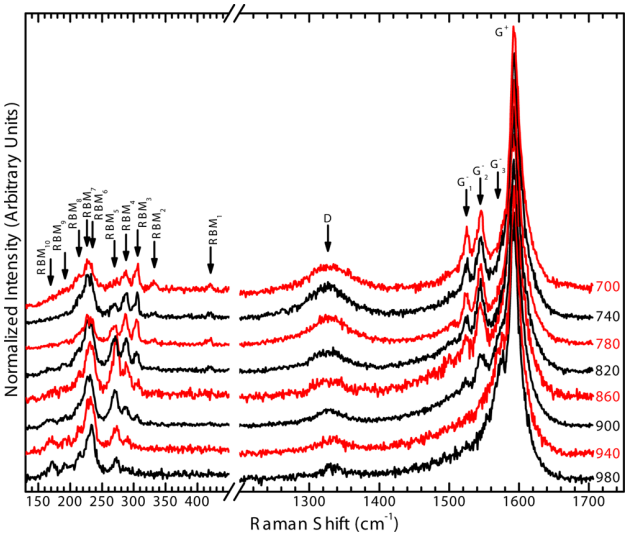


Figure 1. Raman spectra for CNT forest samples with growth temperatures indicated (in °C). Spectra are normalized to 1 at maximum of G band and vertically offset for clarity. Peak labels correspond to Tables 1 and 2.

The Raman spectra also appear to be typical for SWCNT ensembles, with a relatively low D/G ratio and strong and abundant radial breathing modes (RBMs). We, therefore, assume that each RBM is associated with a different diameter SWCNT. This is consistent with the expectation that a sufficiently thin metal catalyst film will favor predominantly SWCNTs, as previously reported for iron.[21] As the growth temperature increases, RBMs at smaller Raman shifts appear, while RBMs at larger Raman shifts disappear, indicating that the diameter distribution is shifting toward larger diameters. The G^- peaks provide further evidence of the same trend. All of these changes will now be discussed in detail.

D/G Ratio. The ratio of the D band intensity I_D to the G band intensity I_G (the D/G ratio I_D/I_G) is indicative of the density of defects in a CNT sample. In the present report, the forests are sufficiently thick that the underlying silicon substrate is generally not visible in the Raman spectra. Because the laser spot size and penetration depth remain constant, the total volume of CNT forest contributing to the Raman signal remains constant, and the D/G ratio provides a meaningful measure of the density of defects.

We calculate the D/G ratio using the integrated intensity of each band obtained from a fitted Lorentzian curve. We observe only a single D band peak and use only the G^+ peak for this calculation (the G^+ peak is fitted simultaneously with the G^- peaks). The D/G ratio is plotted in Figure 2 (black circles and solid black line) as a logarithmic function of $1/k_BT$, where k_B is the Boltzmann constant. A straight line fitted to the data will thus have a slope that gives a characteristic energy $E = 0.82 \pm 0.03$ eV (79 ± 3 kJ/mol) that describes the relationship $I_D/I_G \propto \exp(E/k_BT)$. The proportionality constant is found to be $(4 \pm 1) \times 10^{-5}$.

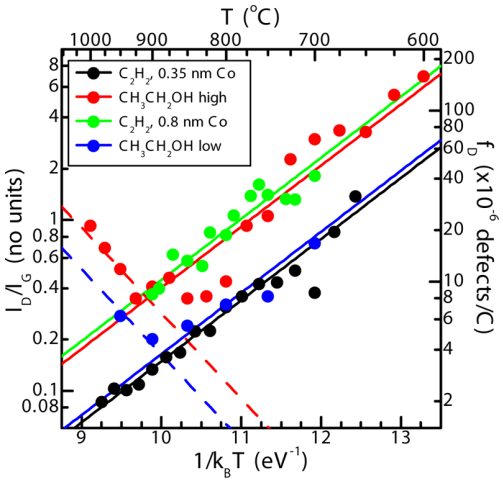


Figure 2. D/G ratio I_D/I_G vs $1/k_BT$ for several data sets grown under different CVD conditions. Fractional defect density f_D calculated from eq 1. Black circles and solid line are the present data and a linear fit. Other data sets come from our previous reports (see text for details). Broken lines are to guide the eye.

Also plotted on Figure 2 are the D/G ratios from previous reports for ethanol CVD with 0.8 nm of Co catalyst (red),[22] acetylene CVD with 0.8 nm of Co catalyst (green),[23] and a lower concentration ethanol CVD (10% of the other, but otherwise identical growth conditions) with 0.8 nm of Co

catalyst (blue). The three lines with a positive slope are all parallel to the 0.82 eV line from the present report and provide a good fit to their respective data sets. The negative slope lines (dashed) are to guide the eye and highlight the critical point at which the temperature dependence changes for the ethanol data sets.

Raman spectra for each of the four data sets in Figure 2 are available in the Supporting Information for growth temperatures of 700 and 900 °C (Figures S3 and S4, respectively). At 700 °C, only the forests grown for the present report (C_2H_2 carbon source and 0.35 nm of Co catalyst) show a significant number of RBMs (therefore, suggesting a significant number of SWCNTs) and a D/G ratio that is significantly less than 1. At 900 °C, all growth conditions have RBMs and lower D bands. The lack of RBMs on the thick catalyst samples with low growth temperatures suggests that there may be multi-walled carbon nanotubes (MWCNTs) present on these samples.

We previously found a characteristic energy of 1.1 ± 0.1 eV (110 ± 10 kJ/mol) for ethanol CVD.[22] There are two reasons why this is different from the present characteristic energy of 0.82 ± 0.03 eV (79 ± 3 kJ/mol). First, the ethanol data have a critical point where the dependence on temperature changes and the exact position of this point is not easy to determine. The slope will change based on which points are included in the fit. Second, the scatter in the ethanol data is rather large. The scatter in the present data is much smaller due to more stringent controls on the acquisition of the Raman spectra. In Figure 2, it appears that these two data sets are parallel.

The exact nature of the mechanisms that generate defects is restricted by the data presented in Figure 2. For each data set, the 0.82 eV slope fits the data quite well. This suggests that the mechanism responsible for this temperature dependence is independent of the source gas, concentration, and catalyst thickness/size (though these all affect the value of the D/G ratio through the intercept in Figure 2). Preliminary D/G ratio data obtained from CNT forests grown with Fe catalyst suggest an activated temperature dependence, but with a noticeably lower activation energy (see the Supporting Information, Figure S6). We have previously reported that the kinetics of ethanol growth and acetylene growth differ significantly,[22,23] despite the fact that their D/G ratios are similar functions of growth temperature T. The Raman spectra for all four data sets shown in Figure 2 (see the Supporting Information, Figures S3 and S4) differ considerably in terms of CNT species (in particular, SWCNTs vs MWCNTs) and quality, suggesting that the defect density is independent of the material produced. Combined, all of the above observations suggest that the mechanism that determines the defect density is intrinsic to the formation of a graphene lattice.

The fact that a single activation energy is seen across all the data sets suggests that a single mechanism is responsible for our observations. The healing of defects[13,15] satisfies the above criteria. Furthermore, the single energy suggests that the healing of a single type of defect may be responsible. We propose that the observed temperature dependence of the D/G ratio is a result of the activated catalytic healing[15] of one single type of simple defect, such as a pentagon/heptagon pair. Although many types of defects may form in the CNT lattice and eventually be integrated into the CNT, the defects with the lowest activation energy for healing will be the most readily healed. Higher growth temperatures make this healing process more effective, thus leading to a lower overall density of defects.

In general, defect healing can have an activation energy much higher than the observed 0.82 eV; a simple low-energy pentagon/heptagon pair can have a formation energy of up to 4.4 eV.[15] The presence of edges, catalytic adatoms, or metal catalyst can lower the energy barrier for healing to values on the order of 1 eV.[15,25,26] This mechanism, therefore, depends on the catalytic material used (as suggested by our preliminary Fe investigation), and this dependence would likely be seen in the magnitude of the characteristic energy.[15,27]

It is also possible that the observed energy (0.82 eV) may be the result of a barrier to carbon surface diffusion. As the temperature increased, more carbon would reach the growth front and potentially lead to fewer defects. The increased rate of carbon diffusion should also lead to an increased growth rate. This explanation appears inconsistent with our data because, in a previous report,[23] we have observed that the growth rate does not increase with temperature in our C_2H_2 CVD process.

The critical point in the ethanol D/G ratio data sets (see ref 22.) shows that there is a second mechanism for ethanol growth that determines the D/G ratio. This mechanism is likely related to the opening of a new defect production pathway at high growth temperatures that may be related to, for example, the onset of the gas phase pyrolysis of ethanol. The critical point may depend on the catalyst material as well, but seems to be unique to ethanol as it is not observed for acetylene over the entire temperature range.

The D/G ratio can be written as being proportional to the defect density n_D, which was determined for graphene to be (for 532 nm laser excitation)[28] $n_D = (2.2 \pm 0.6) \times 10^{-3}(I_D/I_G)_{peak}$ defects/nm^2, where $(I_D/I_G)_{peak}$ is the ratio of the peak intensities, instead of the integrated intensities used in the present report. To account for this difference in I_D/I_G, we include an extra factor of 0.4 ± 0.1 (see the Supporting Information, Figure S7 and related text). The linear defect density (along the length of an SWCNT of diameter d) is $\lambda_D = \pi d n_D$, and the fractional defect density (number of defects per carbon atom) is given by

$$f_D = \Omega n_D = (2.3 \pm 0.6) \times 10^{-5}(I_D/I_G) \text{ defects/carbon} \quad (1)$$

Here, $\Omega = 0.026$ nm^2/carbon is the density of graphene. Note that a single defect may affect many carbon atoms. For an SWCNT with a D/G ratio of 0.1 (which occurs at ~950 °C), we find $f_D = 2.3 \times 10^{-6}$ defects/carbon (or equivalently 1 defect per 4.4×10^5 carbon atoms) and $\lambda_D = 0.28$ defects/μm (for a 1 nm diameter SWCNT). Conversely, this means that it would be possible to grow a 3.6 μm segment of a 1 nm diameter SWCNT without any defects at ~950 °C.

Here, the linear growth rate for C_2H_2 CVD is on the order of 1 μm/s,[23] corresponding to 1.2×10^5 carbon/s added to the CNT (for a 1 nm diameter SWCNT). At this temperature, the D/G ratio is ~0.3, which is equivalent to $f_D = 6.9 \times 10^{-6}$ defects/carbon. This implies that defects are incorporated into the CNT at a rate of ~1 defect/s. The actual defect production rate would be at least this high; however, it is more likely that defects are produced at a much higher rate and then healed.

The synthesis of a graphene lattice (and, therefore, CNTs) from C_2H_2 is thermodynamically spontaneous under experimental conditions up to very high temperatures (~3000 °C; see below). However, it is commonly observed that temperatures above ~550 °C are necessary to grow CNTs in CVD. The defect healing mechanism predicts a minimum temperature for growth: at low temperatures, the lattice is too

defective to grow. If we assume that a certain defect density is sufficient to prevent growth, we can calculate the minimum temperature required for growth using the results presented in Figure 2. For example, if a defect density of λ_D = 1 defect/nm in a 1 nm diameter SWCNT ($n_D \sim 0.32$ defects/nm^2 and $f_D \sim 1$ defect/120 carbon atoms) is sufficient to prevent growth from occurring, we find a minimum growth temperature $T \sim 200$ °C if we extrapolate using the line of best fit in Figure 2.

Here, the observed minimum temperature for CNT growth is ~660 °C. If defect healing was the mechanism determining this temperature and preventing growth, it would correspond to a much smaller defect density of $n_D \sim 2.5 \times 10^{-5}$ defects/nm^2 ($\lambda_D = 8 \times 10^{-5}$ defects/nm in a 1 nm diameter SWCNT). Thus, although the defect healing mechanism does set a minimum temperature for growth, here it is probable that this minimum temperature is determined by a different mechanism, such as a lack of catalyst nanoparticles forming as the temperature becomes too low.[19,20]

The healing of defects also explains why high growth temperatures produce fewer defects, as the higher temperatures promote an increased healing rate. Above, we calculated that it is possible to produce a 3.6 μm segment of a 1 nm diameter SWCNT without any defects at ~950 °C. Extrapolating to a slightly higher temperature (~1200 °C, $I_D/I_G \sim 0.03$), it should be possible to produce a 12 μm segment of a defect-free 1 nm diameter SWCNT. At even higher temperatures (~1500 °C, $I_D/I_G \sim 0.009$), a 40 μm segment of a defect-free 1 nm diameter SWCNT should be possible. Of course, as T increases, other mechanisms, such as gas phase etching, may set in.

Although defects are minimized at high growth temperatures T, here, higher T also have a significantly lower yield (represented by forest height H, as shown in the Supporting Information, Figure S8), thus highlighting a trade-off between the quality and quantity of currently produced CNT forests, as recently reported by Kimura et al.[29] The trend of forest height H as a function of growth temperature T (see the Supporting Information, Figure S8) for the forests in the present report is consistent with our previous report of acetylene growth.[23]

Although using a thin catalyst (0.35 nm in the present report) lowered the D/G ratio (see Figure 2), it also decreased the yield. Decreasing the C_2H_2 flow rate F does slightly improve sample quality, with the D/G ratio changing from 0.3 to 0.2 (at T = 840 °C) as F decreases from 270 to 40 sccm (see spectra in the Supporting Information, Figure S5). Decreasing F likely improves the D/G ratio because the lower flow rate provides a lower growth rate, thus providing more time to heal the defects as the CNT is growing.[14,15] Decreasing F does not have a noticeable effect on the yield, but it does significantly lengthen the growth time required to achieve a similar yield, which is an important consideration by itself.

CNT Diameters. The other main trend seen in the Raman spectra (Figure 1) is that the positions of the RBMs shift toward smaller Raman shifts, and thus larger diameter SWCNTs, as the growth temperature T increases. This is commonly observed in many synthesis processes.[5,9,11,30−38] We identify 10 regular RBMs that consistently show up in our spectra (see Table 1). We calculate the diameters of the associated SWCNTs using the relationship $\omega_{RBM} = 248/d$ cm^{-1} with d in units of nanometers.[39]

We track the intensity of each RBM as a function of growth temperature T in Figure 3a, which shows the intensity of each RBM relative to G^+ (thus normalizing for the amount of carbon) and then normalized to 1 at its maximum. Relatively,

Table 1. Observed RBMs and Calculated Diameters

	ω (cm^{-1})	d (nm)
RBM_1	419 ± 1	0.592 ± 0.002
RBM_2	332 ± 1	0.746 ± 0.002
RBM_3	305 ± 1	0.812 ± 0.003
RBM_4	288 ± 2	0.860 ± 0.005
RBM_5	270 ± 2	0.917 ± 0.005
RBM_6	235 ± 1	1.058 ± 0.005
RBM_7	227 ± 1	1.094 ± 0.005
RBM_8	214 ± 1	1.160 ± 0.008
RBM_9	192 ± 2	1.30 ± 0.01
RBM_{10}	170 ± 2	1.46 ± 0.01

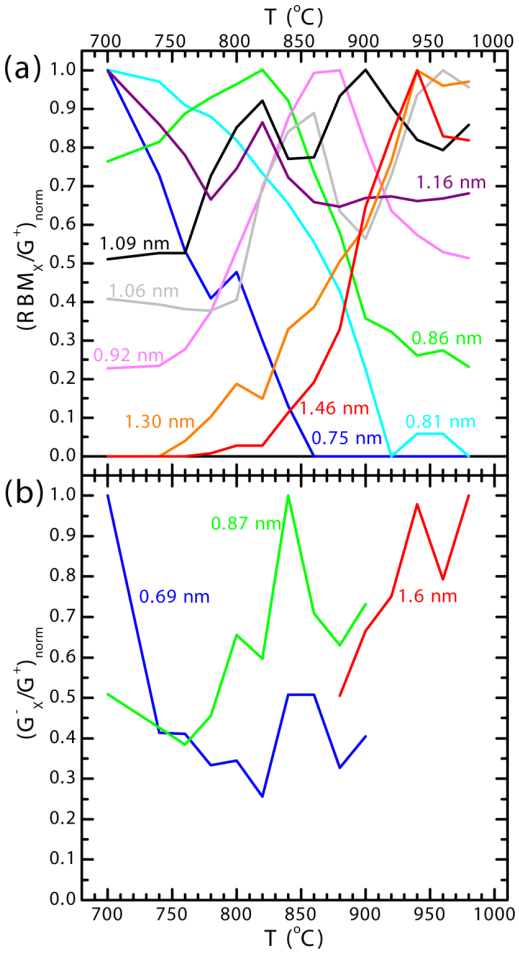


Figure 3. Relative SWCNT abundance as a function of growth temperature T as determined by (a) RBM intensity and (b) G^- intensity. Intensities relative to G^+ intensity and normalized at the maximum for each curve.

smaller diameter SWCNTs become less abundant as T increases while the relative abundance of larger diameter SWCNTs increases. RBM_1 was consistently very weak, and meaningful data of this type could not be extracted.

Smaller diameter SWCNTs have their maximum intensity at lower growth temperatures than the larger diameter SWCNTs. As the growth temperature increases, increasingly larger diameter SWCNTs reach their maximum abundance and then decline. It is interesting to note that some curves in Figure 3a (corresponding to 1.06, 1.09, and 1.16 nm SWCNTs)

have a double peak. This may arise from unresolved doublets in the RBM spectra. If an RBM was really two (or more) unresolved peaks from slightly different diameter SWCNTs, we might expect that each would reach a maximum abundance at a different temperature.

To further quantify this shift toward larger SWCNT diameters d at higher growth temperatures T, we define an average diameter d_{av}, which is taken as a weighted average of the RBMs' peak positions. The weighting is given by the integrated intensity of each RBM relative to the total integrated intensity of all the RBMs. The intensities are determined by fitting the spectra with a series of Lorentzian curves, one for each RBM. This parameter is plotted in Figure 4 (open circles)

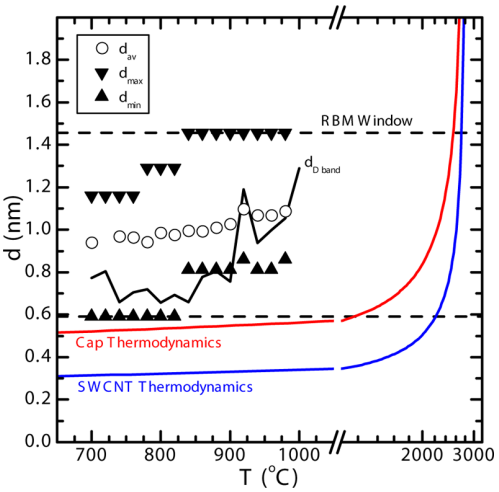


Figure 4. Diameter d vs growth temperature T. Broken lines represent the window in which RBMs were observed. RBM derived results are represented by symbols; D band derived results are given by a solid black line. Colored lines are predictions of the thermodynamic model.

and varies from a minimum of 0.94 nm at 700 °C to 1.09 nm at 980 °C. We note that d_{av} is heavily influenced by resonance effects, and, in particular, the RBMs at 235 and 227 cm^{-1} (corresponding to 1.06 and 1.09 nm diameter SWCNTs respectively), which are consistently intense.

The minimum observed diameter d_{min} and maximum observed diameter d_{max} can also be determined. From Figure 3a, the 0.75 and 0.81 nm diameter SWCNTs disappear completely as the growth temperature increases, whereas the 1.30 and 1.46 nm diameter SWCNTs appear. Although RBM_1 (representing a 0.59 nm diameter SWCNT) is not shown in Figure 3a due to its low signal/noise ratio, it is clearly absent above 820 °C (see the Supporting Information, Figure S2). Using these points, and the overall smallest and largest observed diameters (dashed lines in Figure 4), we can approximate d_{min} and d_{max}, which are shown as the triangles in Figure 4. We see that d_{av} (open circles in Figure 4) seems to track d_{min} and d_{max} quite well, and thus provides a reasonable estimate of the true average.

While the positions of the RBMs are most commonly used to determine SWCNT diameters, the positions of the G^- peaks also depend on the diameter. To supplement the diameter information obtained from the RBMs, we also look at the position of the G^- peaks ω_{G^-}. For semiconducting SWCNTs, this dependence is: $\omega_{G^-} = 1582 - 27.5/d^2$ cm^{-1} with d in units of nanometers.[40] Due to the sharp line shape and nice fit by a single Lorentzian, we assume that the G^- peaks that we observe all correspond to semiconducting SWCNTs.[39] We identify three strong G^- peaks that consistently appear in each spectrum, and we track these peaks as a function of growth temperature T. The positions of these peaks are given in Table 2, along with their calculated diameters.

Table 2. Observed G^- Peaks (for Semiconducting SWCNTs) and Calculated Diameters

	ω (cm^{-1})	d (nm)
G_1^-	1524 ± 1	0.69 ± 0.01
G_2^-	1545 ± 1	0.87 ± 0.01
G_3^-	1571 ± 2	1.6 ± 0.1

As with the RBMs, we track the intensity of each G^- peak as a function of growth temperature T in Figure 3b, which shows the intensity of each G^- peak relative to the G^+ peak and normalized at its maximum. The G^- results in Figure 3b are consistent with the RBM results in Figure 3a: smaller diameter SWCNTs become relatively less abundant as the growth temperature increases, whereas larger diameter SWCNTs become relatively more abundant, with the abundance peaking at higher growth temperatures for larger diameter SWCNTs.

Unlike the RBMs, the G^- peak data are noisier due to increased difficulty fitting the peaks on the sloping background, whereas the RBMs had a relatively flat background. Furthermore, the G^- peaks are not readily visible throughout the entire temperature range for this same reason: they become washed out by the background. The peaks visible at lower growth temperatures (G_1^- and G_2^-) correspond to smaller diameter SWCNTs than the peak visible at higher growth temperatures (G_3^-), which shows a shift to larger diameters at higher T and is consistent with the results derived from the RBMs.

Finally, the SWCNT diameter dependence on growth temperature can be obtained from the position of the D band ω_D, which, at all T, is well fit by a single Lorentzian line shape. For a single SWCNT, ω_D is related to the diameter d: $\omega_D = \omega_D^\circ + C/d$ cm^{-1} with d in units of nanometers.[41] Here, ω_D° and C are equal to 1354.8 cm^{-1} and −16.5 nm/cm, respectively, for 2.41 eV laser excitation and 1309 cm^{-1} and −18.9 nm/cm, respectively, for 1.58 eV laser excitation.[41] To determine the parameters for 2.33 eV (532 nm) laser excitation, we use linear interpolation and find ω_D° = 1351 cm^{-1} and C = −16.7 nm/cm.

For an ensemble of CNTs, as in the forests of the present report, the observed position and width of the D band depend on the distribution of CNTs in the sample.[22,27] As the growth temperature increases, we do see a slight shift in the position of the D band, which can be related to a shift in the average diameter of the SWCNTs toward larger diameters. These data are shown in Figure 4 as the solid black line and is consistent with the temperature dependence determined from the RBMs.

Thermodynamic Model. The shift to larger diameter SWCNTs with increasing growth temperature T is seen in many different CVD processes using a wide variety of source gases and catalysts.[5,9,11,32−35,37,38] Furthermore, such behavior has also been reported in pulsed laser synthesis.[30,31] Given that these processes vary considerably from one another but all show a similar diameter dependence on temperature, it seems probable that there is a common mechanism that determines the SWCNT diameter distribution and that this mechanism is

dx.doi.org/10.1021/jp308672a | J. Phys. Chem. C 2013, 117, 3527−3536

intrinsic to CNT growth, as opposed to being specific to one particular catalyst or source gas.

One potential explanation for the commonly observed diameter dependence is the thermodynamic stability of the CNT lattice[4,5,34,42] or the cap.[43] Previous studies have explored the interactions between the SWCNT cap and the catalyst nanoparticle at the atomic level using models of strain,[2] thermodynamic models,[44] and simulations.[45−48] However, connecting these results directly to CVD process parameters (in particular, source gas pressure and composition) can be challenging. Here, we look at the overall chemistry and thermodynamics of growth in relation to the CVD process parameters (temperature, pressure, and gas composition) and, using a model of this, investigate to what extent the observed temperature dependence of the diameter distribution can be explained by the intrinsic formation thermodynamics of CNTs. For simplicity, we consider only SWCNTs and assume that once one begins growing, its diameter does not change,[24,38] though it remains possible that the nanoparticle diameters may change due to Ostwald ripening.[49]

To understand this intrinsic thermodynamic effect, we suppose that SWCNTs grow using carbon produced in the complete decomposition of the C_2H_2 source gas into graphite and hydrogen:

$$C_2H_2(\text{gas}) \rightleftharpoons 2C(\text{graphite}) + H_2(\text{gas}) \tag{2}$$

Although this is the overall reaction of the C_2H_2 reactant to the CNT product, the reaction itself can be broken down into a series of elementary steps, such as those proposed by Eres et al.[50] and Wirth et al.[51] However, here we are interested in the overall reaction because we are interested in the overall thermodynamics of the reaction.

A chemical reaction is spontaneous when its change in free energy $\Delta G = \Delta H - T\Delta S < 0$ (ΔH is the enthalpy of formation, and ΔS is the entropy). For the above reaction, the thermodynamic parameters are (per carbon atom produced and in the standard state, designated by "°") $\Delta H° = -1.18$ eV/carbon (114 kJ/mol carbon) and $\Delta S° = -0.305$ meV/K/carbon (29.4 J/K/mol carbon).[52] However, in the actual chemical reaction (eq 2), C_2H_2 and H_2 are not in their standard states. The effect of the pressure P of the gaseous chemicals alters the change in free energy, $\Delta G = \Delta G° + \Sigma n_i k_B T \ln(P_i/P°)$, where the n_i are the stoichiometric coefficients (positive for products and negative for reactants) and "°" denotes the standard state. For the above chemical reaction, this makes the overall change in free energy

$$\Delta G = \Delta H° - T\Delta S° - \frac{1}{2}k_B T \ln\left(\frac{P_{C_2H_2}}{P_{H_2}}\right) \tag{3}$$

Here, $P_{C_2H_2} = 90$ Pa and $P_{H_2} = 540$ Pa. Setting $\Delta G < 0$ in eq 3 means that this reaction (eq 2) is spontaneous up to ~3000 °C under experimental conditions.

For an SWCNT, the thermodynamic parameters must be adjusted due to the different crystal structure of CNTs. We consider two possibilities involving the strain in the SWCNT: the strain due to rolling the graphene sheet into an SWCNT and the strain in the formation of the CNT cap. We suppose that this strain energy E changes the enthalpy of formation of graphite $\Delta H°$ to $\Delta H° + E$. There may also be changes in $\Delta S°$, but we assume that these effects are negligible.

The diameter-dependent curvature induced strain energy E resulting from rolling the graphene lattice into an SWCNT can be written, per carbon atom, as a function of SWCNT diameter d:[53,54]

$$E = \frac{Ya^3\Omega}{6d^2} = \frac{A}{d^2} \tag{4}$$

Here, $Y = 1$ TPa is the elastic modulus and $a = 0.34$ nm is the interlayer spacing in graphite, suggesting that $A = 0.97$ eV nm^2. More sophisticated theoretical calculations show the same diameter dependence, but with $A = 0.08$ eV nm^2,[54−64] which we will use here.

The strain energy in the SWCNT cap can also be written as a function of SWCNT diameter if one assumes that the SWCNT cap is half of an approximately spherical fullerene with the same diameter as the SWCNT. On a per carbon atom basis, this energy also has the form $E = A/d^2$, where $A \sim 0.22$ eV nm^2.[57,65,66] This form is only approximately valid for small fullerenes ($d < 1.5$ nm),[57] but since we are primarily considering SWCNTs with diameters in this range, higher diameter deviations are ignored.

The strain energy has the same form for both the CNT lattice stability and the cap stability. One can understand intuitively that the cap stability has a higher energy scale because its curvature is in two dimensions, whereas the rolling of the CNT takes place in only a single dimension.

Initially, adding new carbon to the SWCNT requires the additional energy (relative to graphite), as shown in eq 4, with $A \sim 0.22$ eV nm^2. As the length of the nanotube increases toward infinity, this strain energy per carbon atom decreases rapidly as new carbon atoms are added to the SWCNT lattice according to eq 4 with $A = 0.08$ eV nm^2.

The SWCNT cap energy, as shown in eq 4, should also contain some correction terms to account for the fact that, unlike a free-standing fullerene, the half fullerene of the cap interacts with the catalyst nanoparticle. These interactions have previously been shown to be important.[2,44−48] One correction is an interaction between each carbon atom in the cap and the catalyst nanoparticle. As a first approximation, this is a constant on a per carbon atom basis and should reduce the enthalpy of formation of the cap. The other correction is an interaction between the edge of the cap and the catalyst nanoparticle. This correction depends on the number of carbon atoms around the perimeter of the cap, which is proportional to d. On a per carbon atom basis, this correction is proportional to d^{-1} since the number of carbon atoms in the cap is proportional to d^2. On the basis of previous reports,[45,47,48] these corrections may be on the same order of magnitude as the strain energy.

The overall change in free energy for the complete conversion of acetylene into SWCNTs is given by

$$\Delta G = \Delta H° + \frac{A}{d^2} - T\Delta S° - \frac{1}{2}k_B T \ln\left(\frac{P_{C_2H_2}}{P_{H_2}}\right) \tag{5}$$

To determine the minimum diameter d_{min}, we set $\Delta G = 0$ in eq 5 and solve for d. The results are presented in Figure 4 as the red and blue solid curves for the cap energy and rolling energy, respectively. The higher growth temperature range (with a logarithmic scale) shows the overall trend.

The model predicts a minimum diameter of 0.52 nm at 700 °C, which increases continuously to 0.56 nm at 980 °C. Experimentally, the observed minimum diameter varies from 0.59 nm at 700 °C to 0.86 nm at 980 °C. Comparing the

models' predictions to our results, the stability boundary obtained from the SWCNT formation thermodynamics (blue curve in Figure 4) is lower than the experimental data. On the other hand, the stability boundary obtained from cap formation thermodynamics (red curve in Figure 4) is quite close to the experimental values.

The minimum diameter d_{min} as predicted by the thermodynamics of the SWCNT formation (blue curve in Figure 4) is a firm lower limit on the diameter as it represents the final product of synthesis—a free-standing SWCNT—and the reaction must lead to this product in the end. The thermodynamics of the cap formation, as plotted in Figure 4 (red curve), represent a tighter constraint on d_{min}. If the above-mentioned corrections to the enthalpy of formation of the SWCNT cap result in a cap that is more thermodynamically stable than an SWCNT of a given diameter (in Figure 4, this corresponds to the red curve being lower than the blue curve), this would lead to the situation where a small diameter cap could form, but an SWCNT could not grow. In this case, d_{min} for the produced SWCNTs would necessarily be determined by the thermodynamics of the SWCNT formation (blue curve).

The deviation between predicted and observed minimum diameters is not surprising. First, Raman spectroscopy is a resonant process; it only probes a subset of the SWCNTs present in the sample. The minimum diameter, as measured with Raman spectroscopy, is thus only accurate so long as the smallest diameter in the distribution happens to be in resonance. With only one excitation wavelength, we extract a very rough d_{min} and d_{max} with steplike features larger than the spacing of subsequent diameters. Second, the actual situation during growth is more complex than presented in the model. For example, the interaction between the edge of the cap and the catalyst nanoparticle should also influence the chirality.[67]

This model predicts a dependence on the partial pressure of C_2H_2, P. We test this by varying the C_2H_2 flow rate F (at T = 840 °C) while keeping the other flow rates fixed, thus varying the partial pressure of C_2H_2. Following the same procedure used to analyze the temperature dependence, we do find a change in d_{av} as a function of pressure: a decrease from 1.01 to 0.94 nm as the pressure is increased from 39 to 92 Pa, which is shown in Figure 5 as open circles. The minimum diameter d_{min} and maximum diameter d_{max} are shown as triangles, along with the average diameter as determined from the D band (solid black line) and the theoretical curves (red for cap energy and blue for rolling energy). The dependence of the SWCNT diameter on pressure has been reported by others.[7,11,68−70] Raw spectra can be found in the Supporting Information (Figure S5). The model fits the data as well as it does in Figure 4. Here, the trends are more subtle, but that too is predicted by our model.

Because eq 5 relates the growth temperature T and C_2H_2 pressure P, one can construct a "phase diagram" that describes the spontaneity of SWCNT growth. This "phase diagram" is shown in Figure 6 using A = 0.22 eV nm^2 and P_{H_2} = 540 Pa. SWCNT diameters are only thermodynamically favorable above the indicated lines. In general terms, in order for the formation of very narrow CNTs from C_2H_2 to be energetically favored, one requires either high pressure P or low growth temperature T.

Our data also indicated a maximum diameter d_{max} that varied as a function of T. We now consider the origin of d_{max}. In order for CNT to grow, the lattice, as it forms on the catalyst

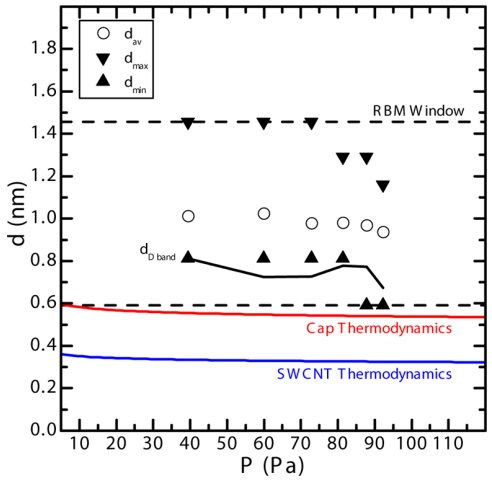


Figure 5. Diameter d vs C_2H_2 pressure P. Broken lines represent the window in which RBMs were observed. RBM derived results are represented by symbols; D band derived results are given by a solid black line. Colored lines are predictions of the thermodynamic model.

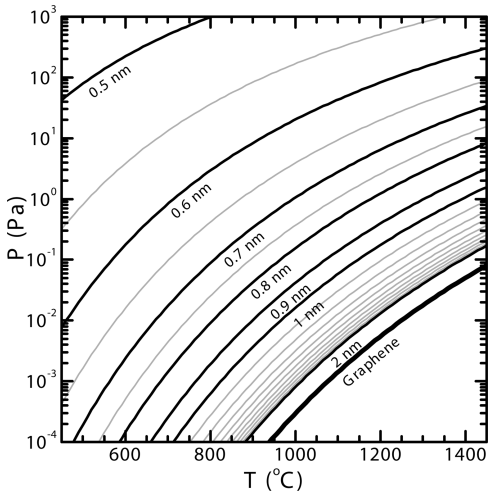


Figure 6. SWCNT "phase diagram" for cap stability. A given diameter SWCNT is stable above the line representing its diameter. This figure assumes a C_2H_2 carbon source and uses thermodynamic parameters from the text.

nanoparticle, must "lift off" from the nanoparticle and break free from the adhesion energy holding it there.[2,45−48] This adhesion energy is otherwise a barrier to growth. It has been shown previously that this adhesion energy is comparable to the cap formation energy.[45] Larger diameter caps have more carbon atoms, and thus greater total adhesion energy. As the growth temperature increases, larger caps are able to lift off, thus producing larger diameter SWCNTs. This may explain the observed temperature dependence of the maximum diameter.

Finally, we outline how our thermodynamic model can be applied to other synthesis processes. Most importantly, the chemical reaction involved in growth must be known, as is shown here for C_2H_2 in eq 2. The pressures of the gases can also be very important because the temperature dependence of d_{min} comes from the term $\Delta S = \Delta S^\circ - \Sigma n_i k_B \ln(P_i/P^\circ)$, where ΔS is the real entropy (corrected for nonstandard conditions) and the n_i are the stoichiometric coefficients (positive for products and negative for reactants). Here, the pressure

dx.doi.org/10.1021/jp308672a | J. Phys. Chem. C 2013, 117, 3527−3536

correction term is small; however, for other carbon sources, it may be large enough to change the sign of ΔS, and thus drastically alter the temperature dependence of d_{min}.

Different carbon sources can yield different trends, depending on the signs of $\Delta H°$ and ΔS (four possible cases exist; see the Supporting Information for further details). As an example, CNT growth from CO has a well-known chemical reaction (disproportionation of CO),[68] and our thermodynamic model can thus be applied. The predicted trend for CNT growth from CO as a carbon source is qualitatively similar to that for C_2H_2, and is generally consistent with experimental results for the temperature dependence[9,33,37] and pressure dependence[68,69] of d_{min}. For the case of ethanol, the chemical reaction that leads to growth is not as certain. One of the possible reactions is the complete decomposition of ethanol:

$$CH_3CH_2OH(gas) \rightleftharpoons 2C(graphite) + 2H_2(gas) + H_2O(gas) \quad (6)$$

This reaction has a change in entropy ΔS with the opposite sign (compared to C_2H_2 and CO), and we find that d_{min} is predicted to *decrease* with increasing T (see the Supporting Information). Our own ethanol data (see ref 22.) is not sufficiently clear to extract d_{min} as a function of T; however, the predicted temperature dependence is contrary to other published results[5,11,32,34] that show that d_{min} increases with increasing T, like the C_2H_2 data in the present report. This difference may be a result of a different mechanism determining d_{min} by setting conditions on growth that are more strict (see the following section on "growth filters"). Furthermore, the above chemical reaction may not be the reaction that leads to growth (and thus determines the diameter). Regardless, whatever reaction does lead to growth (whether or not d_{min} is determined by thermodynamics or another mechanism that is more strict), only CNTs that are thermodynamically favorable can grow.

Growth Filters. Other mechanisms do contribute to determining the diameter distribution of SWCNTs. The most prominent of these mechanisms involves the catalyst nanoparticle, which is known to affect the diameter of the CNTs that they produce.[3] Mechanisms that alter the catalyst nanoparticle shape or diameter distribution thus likely alter the diameter distribution of the grown SWCNTs as well. The "phase diagram" in Figure 6 alone cannot determine the diameters of the SWCNTs that would be produced in a synthesis process. In order for any CNTs to grow, all mechanisms would need to be "properly aligned" in the sense that they must all allow for the formation of CNTs in the same diameter range.

Another way of looking at this is to consider that the observed diameter distribution is the result of a series of "filters" through which all diameters are sorted. In general, the abundance of different CNTs is a result of nucleation, growth, and termination. Each of these three stages represents a very coarse filter. Here, we can go one step further and look at some of the mechanisms involved in each of these coarse steps, each of which includes thermodynamic filters and kinetic filters. For a given species of SWCNT (as defined by its chirality (n,m)) to appear in the final synthesized material, it must be able to pass through each of these different filters.

The nucleation filter can be split up: the formation of each (n,m) SWCNT and its cap must be thermodynamically favorable, as shown in the "phase diagram" in Figure 6. This requires the appropriate combination of growth temperature and gas pressures. Additionally, the size distribution of the catalyst nanoparticles must allow for the growth of each (n,m), whether this is an effect of size, shape, or chemical state of the nanoparticles. Finally, nucleation must occur at an appreciable kinetic rate for each (n,m).

Like the nucleation filter, the growth stage must also be thermodynamically favorable for each (n,m), as well as kinetically favorable for each (n,m) because the SWCNTs must grow at an appreciable rate. One kinetic filter during this stage may include mechanisms such as the screw dislocation growth theory that favors high chiral angles.[8,12] Finally, termination must not occur too quickly for each (n,m) or growth will be limited. One consideration for termination is the effect of neighboring CNTs, which is especially important in CNT forest growth. If the CNTs are all growing at vastly different rates, there will be significant strain in the forest, and this may bring about termination.[23,71] Any (n,m) SWCNT that passes through all of these filters will be observed in the final product. The complete "misalignment" of any of these filters would be sufficient to prevent the growth of CNTs altogether.

One potential general way to produce a limited selection of SWCNT diameters can be proposed based on the above discussion by considering two of the filters that occur during nucleation: the thermodynamics of cap formation and the effect of the catalyst nanoparticles, assuming that the nanoparticles can set a well-defined maximum and minimum diameter for the SWCNTs that they produce. First, one must set the properties of the catalyst nanoparticle (size, shape, and chemical composition), thus setting a maximum and minimum allowable SWCNT diameter with this filter. Although the size of the catalyst nanoparticles is affected by the temperature, the size can also be controlled during the catalyst preparation stage. The growth temperature T can then be tuned, thus setting a minimum (and maximum) thermodynamically allowed diameter with this filter. By properly adjusting the minimum and maximum diameters allowed by each filter, it should be possible to adjust the overlap and thus narrow the diameter distribution.

CONCLUSION

Using Raman spectroscopy, we have analyzed the relative density of defects in our CVD grown CNTs. High growth temperatures favor large diameter SWCNTs with few defects, whereas lower temperatures favor much narrower SWCNTs, but with more defects. We also see not only a trade-off between the quality and quantity of the SWCNTs[29] but also a trade-off in terms of their diameter. The similarities of these results to other CVD processes suggest several constraints on the mechanisms responsible for the production of defects, and, in particular, that this mechanism may be intrinsic to the growth of not just a CNT, but a graphene lattice in general. We propose the healing of defects, in particular a single type of simple defect, such as a pentagon/heptagon pair, as the CNTs grow as a possible mechanism to explain the observed temperature dependence of the defect density.

We have shown that there are clear systematic and reproducible changes in the distribution of SWCNT diameters as a function of growth temperature and C_2H_2 pressure in our CVD process. The diameter-dependent effect of strain induced curvature energy of the bending of the graphene lattice into a CNT and the strain energy of the CNT cap are proposed thermodynamic "growth filters" and may explain our observations. The "phase diagram" for C_2H_2 synthesis suggests

that small diameter SWCNTs are favored at low growth temperatures and high pressures. The overall diameter distribution is determined by several "growth filters", including the intrinsic thermodynamics mechanism discussed here. For growth to occur, all of these mechanisms must allow a common subset of CNTs. This provides guidelines for the controlled synthesis of SWCNTs with specific diameter distributions.

■ ASSOCIATED CONTENT

Supporting Information

The Supporting Information includes details of the experimental procedure for CNT growth, Raman spectra for CNT forests under a variety of growth conditions, and, in particular, functions of growth temperature T and C_2H_2 partial pressure P. It also includes the D/G ratio temperature dependence for Fe catalyst and the relationship between D/G ratio when calculated using peak intensities versus integrated intensities. Finally, there is a discussion of general cases of the thermodynamic model for d_{min} with examples. This material is available free of charge via the Internet at http://pubs.acs.org.

■ AUTHOR INFORMATION

Corresponding Author

*E-mail: [REDACTED].

Notes

The authors declare no competing financial interest.

■ ACKNOWLEDGMENTS

The authors thank the referees for their useful and insightful suggestions. The authors also thank the following individuals for their assistance and support: A. Li-Pook-Than, C. Kingston, H. Tran, and M. Denhoff. P.V. was supported by NSERC, NRC-GSSSP, and P.F.'s NSERC Discovery Grant.

■ REFERENCES

(1) Hersam, M. C. *Nat. Nanotechnol.* **2008**, *3*, 387−394.
(2) Kanzow, H.; Lenski, C.; Ding, A. *Phys. Rev. B* **2001**, *63*, 125402.
(3) Cheung, C. L.; Kurtz, A.; Park, H.; Lieber, C. M. *J. Phys. Chem. B* **2002**, *106*, 2429−2433.
(4) Bachilo, S. M.; Balzano, L.; Herrera, J. E.; Pompeo, F.; Resasco, D. E.; Weisman, R. B. *J. Am. Chem. Soc.* **2003**, *125*, 11186−11187.
(5) Miyauchi, Y.; Chiashi, S.; Murakami, Y.; Hayashida, Y.; Maruyama, S. *Chem. Phys. Lett.* **2004**, *387*, 198−203.
(6) Lin, M.; Tan, J. P. Y.; Boothroyd, C.; Loh, K. P.; Tok, E. S.; Foo, Y.-L. *Nano Lett.* **2006**, *6*, 449−452.
(7) Lu, C.; Liu, J. *J. Phys. Chem. B* **2006**, *110*, 20254−20257.
(8) Ding, F.; Harutyunyan, A. R.; Yakobson, B. I. *Proc. Nat. Acad. Sci. U.S.A.* **2009**, *106*, 2506−2509.
(9) Li, N.; Wang, X.; Ren, F.; Haller, G. L.; Pfefferle, L. D. *J. Phys. Chem. C* **2009**, *113*, 10070−10078.
(10) Chiang, W.-H.; Sankaran, R. M. *Nat. Mater.* **2009**, *8*, 882−886.
(11) Picher, M.; Anglaret, E.; Arenal, R.; Jourdain, V. *ACS Nano* **2011**, *5*, 2118−2125.
(12) Rao, R.; Liptak, D.; Cherukuri, T.; Yakobson, B. I.; Maruyama, B. *Nat. Mater.* **2012**, *11*, 213−216.
(13) Picher, M.; Anglaret, E.; Arenal, R.; Jourdain, V. *Nano Lett.* **2009**, *9*, 542−547.
(14) Page, A. J.; Ohta, Y.; Okamoto, Y.; Irle, S.; Morokuma, K. *J. Phys. Chem. C* **2009**, *113*, 20198−20207.
(15) Yuan, Q.; Xu, Z.; Yakobson, B. I.; Ding, F. *Phys. Rev. Lett.* **2012**, *108*, 245505.
(16) Eres, G.; Puretzky, A. A.; Geohegan, D. B.; Cui, H. *Appl. Phys. Lett.* **2004**, *84*, 1759−1761.
(17) Eres, G.; Kinkhabwala, A. A.; Cui, H.; Geohegan, D. B.; Puretzky, A. A.; Lowndes, D. H. *J. Phys. Chem. B* **2005**, *109*, 16684−16694.
(18) Hata, K.; Futaba, D. N.; Mizuno, K.; Namai, T.; Yumura, M.; Iijima, S. *Science* **2004**, *306*, 1362−1364.
(19) Chhowalla, M.; Teo, K. B. K.; Ducati, C.; Rupesinghe, N. L.; Amaratunga, G. A. J.; Ferrari, A. C.; Roy, D.; Robertson, J.; Milne, W. I. *J. Appl. Phys.* **2001**, *90*, 5308−5317.
(20) Takagi, D.; Homma, Y.; Kobayashi, Y. *Physica E* **2004**, *24*, 1−5.
(21) Zhao, B.; Futaba, D. N.; Yasuda, S.; Akoshima, M.; Yamada, T.; Hata, K. *ACS Nano* **2008**, *3*, 108−114.
(22) Vinten, P.; Lefebvre, J.; Finnie, P. *Chem. Phys. Lett.* **2009**, *469*, 293−297.
(23) Vinten, P.; Marshall, P.; Lefebvre, J.; Finnie, P. *Nanotechnology* **2010**, *21*, 035603.
(24) Finnie, P.; Li-Pook-Than, A.; Lefebvre, J. *Nano Res.* **2009**, *2*, 783−792.
(25) Ewels, C. P.; Heggie, M. I.; Briddon, P. R. *Chem. Phys. Lett.* **2002**, *351*, 178−182.
(26) Karoui, S.; Amara, H.; Bichara, C.; Ducastelle, F. *ACS Nano* **2010**, *4*, 6114−6120.
(27) Picher, M.; Navas, H.; Arenal, R.; Quesnel, E.; Anglaret, E.; Jourdain, V. *Carbon* **2012**, *50*, 2407−2416.
(28) Cançado, L. G.; Jorio, A.; Martins Ferreira, E. H.; Stavale, F.; Achete, C. A.; Capaz, R. B.; Moutinho, M. V. O.; Lombardo, A.; Kulmala, T. S.; Ferrari, A. C. *Nano Lett.* **2011**, *11*, 3190−3196.
(29) Kimura, H.; Futaba, D. N.; Yumura, M.; Hata, K. *J. Am. Chem. Soc.* **2012**, *134*, 9219−9224.
(30) Bandow, S.; Asaka, S.; Saito, Y.; Rao, A. M.; Grigorian, L.; Richter, E.; Eklund, P. C. *Phys. Rev. Lett.* **1998**, *80*, 3779−3782.
(31) Kataura, H.; Kumazawa, Y.; Maniwa, Y.; Ohtsuka, Y.; Sen, R.; Suzuki, S.; Achiba, Y. *Carbon* **2000**, *38*, 1691−1697.
(32) Maruyama, S.; Kojima, R.; Miyauchi, Y.; Chiashi, S.; Kohno, M. *Chem. Phys. Lett.* **2002**, *360*, 229−234.
(33) Alvarez, W. E.; Pompeo, F.; Herrera, J. E.; Balzano, L.; Resasco, D. E. *Chem. Mater.* **2002**, *14*, 1853−1858.
(34) Unalan, H. E.; Chhowalla, M. *Nanotechnology* **2005**, *16*, 2153−2163.
(35) Ago, H.; Imamura, S.; Okazaki, T.; Saito, T.; Yumura, M.; Tsuji, M. *J. Phys. Chem. B* **2005**, *109*, 10035−10041.
(36) Ishigami, N.; Ago, H.; Imamoto, K.; Tsuji, M.; Iakoubovskii, K.; Minami, N. *J. Am. Chem. Soc.* **2008**, *130*, 9918−9924.
(37) Loebick, C. Z.; Abanulo, D.; Majewska, M.; Haller, G. L.; Pfefferle, L. D. *Appl. Catal., A* **2010**, *374*, 213−220.
(38) Li-Pook-Than, A.; Lefebvre, J.; Finnie, P. *J. Phys. Chem. C* **2010**, *114*, 11018−11025.
(39) Dresselhaus, M. S.; Dresselhaus, G.; Saito, R.; Jorio, A. *New J. Phys.* **2003**, *5*, 139.1−139.17.
(40) Telg, H.; Duque, J. G.; Staiger, M.; Tu, X.; Hennrich, F.; Kappes, M. M.; Zheng, M.; Maultzsch, J.; Thomsen, C.; Doorn, S. K. *ACS Nano* **2012**, *6*, 904−911.
(41) Souza Filho, A. G.; Jorio, A.; Samsonidze, G. G.; Dresselhaus, G.; Pimenta, M. A.; Dresselhaus, M. S.; Swan, A. K.; Ünlü, M. S.; Goldberg, B. B.; Saito, R. *Phys. Rev. B* **2003**, *67*, 035427.
(42) Inoue, S.; Kikuchi, Y. *Chem. Phys. Lett.* **2005**, *410*, 209−212.
(43) Reich, S.; Li, L.; Robertson, J. *Phys. Rev. B* **2005**, *72*, 165423.
(44) Kuznetsov, V. L.; Usoltseva, A. N.; Chuvilin, A. L.; Obraztsova, E. D.; Bonard, J.-M. *Phys. Rev. B* **2001**, *64*, 235401.
(45) Ding, F.; Larsson, P.; Larsson, A.; Ahuja, R.; Duan, H.; Rosén, A.; Bolton, K. *Nano Lett.* **2008**, *8*, 463−468.
(46) Amara, H.; Bichara, C.; Ducastelle, F. *Phys. Rev. Lett.* **2008**, *100*, 056105.
(47) Burgos, J. C.; Reyna, H.; Yakobson, B. I.; Balbuena, P. B. *J. Phys. Chem. C* **2010**, *114*, 6952−6958.
(48) Burgos, J. C.; Jones, E.; Balbuena, P. B. *J. Phys. Chem. C* **2011**, *115*, 7668−7675.
(49) Amama, P. B.; Pint, C. L.; McJilton, L.; Kim, S. M.; Stach, E. A.; Murray, P. T.; Hauge, R. H.; Maruyama, B. *Nano Lett.* **2009**, *9*, 44−49.

(50) Eres, G.; Rouleau, C. M.; Yoon, M.; Puretzky, A. A.; Jackson, J. J.; Geohegan, D. B. *J. Phys. Chem. C* **2009**, *113*, 15484−15491.
(51) Wirth, C. T.; Zhang, C.; Zhong, G.; Hofmann, S.; Robertson, J. *ACS Nano* **2009**, *3*, 3560−3566.
(52) Haynes, W. M., Ed. *CRC Handbook of Chemistry and Physics*, 91st ed. (Internet Version 2011); CRC Press/Taylor and Francis: Boca Raton, FL, 2011; pp 5.4−5.42.
(53) Tibbetts, G. G. *J. Cryst. Growth* **1984**, *66*, 632−638.
(54) Robertson, D. H.; Brenner, D. W.; Mintmire, J. W. *Phys. Rev. B* **1992**, *45*, 12592−12595.
(55) Hernández, E.; Goze, C.; Bernier, P.; Rubio, A. *Appl. Phys. A: Mater. Sci. Process.* **1999**, *68*, 287−292.
(56) Sánchez-Portal, D.; Artacho, E.; Soler, J. M.; Rubio, A.; Ordejón, P. *Phys. Rev. B* **1999**, *59*, 12678−12688.
(57) Park, N.; Lee, K.; Han, S.; Yu, J.; Ihm, J. *Phys. Rev. B* **2002**, *65*, 121405.
(58) Gülseren, O.; Yildirim, T.; Ciraci, S. *Phys. Rev. B* **2002**, *65*, 153405.
(59) Cabria, I.; Mintmire, J. W.; White, C. T. *Phys. Rev. B* **2003**, *67*, 121406.
(60) Peralta-Inga, Z.; Boyd, S.; Murray, J. S.; O'Connor, C. J.; Politzer, P. *Struct. Chem.* **2003**, *14*, 431−443.
(61) Popov, V. *New J. Phys.* **2004**, *6*, 1−17.
(62) Barnard, A. S.; Snook, I. K. *J. Chem. Phys.* **2004**, *120*, 3817−3821.
(63) Xiao, C.; Chan, H. S. O.; Xu, G. Q.; Lim, K. T.; Lin, J. *Appl. Phys. Lett.* **2004**, *84*, 1677−1679.
(64) Li, Y.; Peng, S.; Mann, D.; Cao, J.; Tu, R.; Cho, K. J.; Dai, H. *J. Phys. Chem. B* **2005**, *109*, 6968−6971.
(65) Adams, G. B.; Sankey, O. F.; Page, J. B.; O'Keeffe, M.; Drabold, D. A. *Science* **1992**, *256*, 1792−1795.
(66) Barnard, A. S.; Russo, S. P.; Snook, I. K. *J. Chem. Phys.* **2003**, *118*, 1594−1597.
(67) Liu, Y.; Dobrinsky, A.; Yakobson, B. I. *Phys. Rev. Lett.* **2010**, *105*, 235502.
(68) Nikolaev, P.; Bronikowski, M. J.; Bradley, R. K.; Rohmund, F.; Colbert, D. T.; Smith, K. A.; Smalley, R. E. *Chem. Phys. Lett.* **1999**, *313*, 91−97.
(69) Carver, R. L.; Peng, H.; Sadana, A. K.; Nikolaev, P.; Arepalli, S.; Scott, C. D.; Billups, W. E.; Hauge, R. H.; Smalley, R. E. *J. Nanosci. Nanotechnol.* **2005**, *5*, 1035−1040.
(70) Wang, B.; Wei, L.; Yao, L.; Li, L.-J.; Yang, Y.; Chen, Y. *J. Phys. Chem. C* **2007**, *111*, 14612−14616.
(71) Han, J.-H.; Graff, R. A.; Welch, B.; Marsh, C. P.; Franks, R.; Strano, M. S. *ACS Nano* **2008**, *2*, 53−60.

Chapter 9

General discussion and conclusions

9.1 Summary of results

Before discussing the general implications of the work contained in this thesis or discussing how the results fit together with one another and the big picture, this section briefly summarizes the previous chapters.

Chapter 2 detailed the correlations between the characteristic energy scales of growth, termination of growth, and number of defects present (as determined by the D/G ratio) for ethanol sourced chemical vapour deposition (CVD). All of these parameters have the same activated form as a function of growth temperature, and the same energies are often present. Additionally, all of these parameters share a critical point in their temperature dependence where the characteristic energy changes. These observations suggest two conclusions: first, the kinetics and Raman parameters are intimately linked, and, second, more than one mechanism is responsible for the observations. Furthermore, the activated temperature dependence suggests a possible chemical origin for the mechanisms responsible for growth, termination, and defect density. The height of the forests appears to be comparatively short, which brings up the question of whether or not ethanol is the best carbon source. This chapter also serves to demonstrate the methods used to extract *in situ* data using optical microscopy.

The question of the carbon source was addressed in Chapter 3 by using acetylene CVD to grow the nanotubes. The acetylene source gas produced much taller forests. These taller forests manifested several different final morphologies, which suggest that there are significant interactions between the individual nanotubes in the forest and that these interactions may be a source of termination. The exact termination morphology is dependent on the balance of forces within the forest. This chapter also identified an abrupt termination that deviates from the underlying smooth exponential decay kinetics, again showing that several mechanisms control the growth and termination of carbon nanotube (CNT) forests. This chapter proposes that a growth rate difference between different nanotubes in the forests may be a cause of the strain. This growth rate difference is an important part of the next few chapters. Chapter 3, like Chapter 2, also saw an activated temperature dependence for the kinetic parameters and the D/G ratio, with the D/G ratio following the same trend seen in the previous chapter. This correlation between the D/G ratio for two different carbon sources is revisited in Chapter 8.

Chapter 4 provided some further details about the interactions between the individual nanotubes in the forests and discussed the overall shape and structure (morphology) of the forests. It again addressed the growth rate difference and suggests, based on *in situ* observations, that the growth rate difference may possibly be due to gas phase

diffusion. The growth rate difference is featured prominently in subsequent chapters and the proposed gas phase diffusion as the cause is revisited in Chapter 7.

Chapter 5 and Chapter 6 analyzed a microscale rippling morphology, and several other *in situ* and *ex situ* observations that together suggest that not all nanotubes grow at the same rate. These chapters reported a diffraction grating effect occurring as a result of reflection from carbon nanotubes, which are well known for being very black [1]. The work contained in these chapters was motivated by the differences seen in Chapter 3 as function of catalyst island size, when smaller catalyst islands were first analyzed.

Having now identified a clear difference in two different catalyst island sizes, Chapter 7 contained a thorough study of this effect. It explained the results of the catalyst island size dependence, as well as the non-uniform growth rate seen in previous chapters, using a gas phase diffusion model in which all parameters were based on real physical quantities and were measured or estimated from known values. These parameters include the efficiency at which the acetylene source gas is converted into CNTs and the density of the CNT forests.

Finally, Chapter 8 looked at the composition of the actual material produced in these synthesis processes using Raman spectroscopy. By using a thinner catalyst the quality of the nanotubes (measured through the D/G ratio) and the number of single-walled carbon nanotubes (SWCNTs) in the forests of this chapter were greatly increased compared to the forests grown in previous chapters. In addition, the dependence of the D/G ratio on temperature was found to be the same for a large variety of growth parameters, including ethanol (from Chapter 2) and acetylene carbon sources (from Chapter 3), catalyst thickness, and the species of carbon nanotubes produced. This suggests that the number of defects as a function of temperature is intrinsic to the growth process of not just carbon nanotubes, but the graphene lattice in general. It was proposed that the defect density is determined by the healing of defects that initially form in the lattice structure. Defects are healed as the nanotube lattice coalesces into its final structure, with many disappearing before they are incorporated into the final nanotube lattice. The healing of defects necessarily involves the breaking and reforming of bonds, and is thus chemical in nature, as expected from Chapter 2. Higher temperatures lead to lower defect densities.

To explain the observed diameter dependence in Chapter 8, a thermodynamic model was introduced. This model is intrinsic to the growth of carbon nanotubes and suggests that the route to narrower diameter nanotubes (at least for acetylene CVD) lies in the regime of high pressure and low temperature. This chapter concludes that not all growth outcomes can be optimized at once. For example, the D/G ratio is not minimized simultaneously with maximum yield. This is consistent with a previous report [2], but

Chapter 8 also adds the nanotube diameter as another factor that cannot be simultaneously minimized with a maximum yield and crystallinity. In general, optimization will depend strongly on what is required from the synthesis process.

9.2 General discussion

This section serves the purpose of uniting many of the ideas presented in this thesis (and summarized above). The following discussion builds upon the conclusions of each chapter, brings them together and discusses some of the other results of this thesis that are not necessarily the focus of any of the preceding chapters, such as the experimental methods that were developed over the course of this research. Furthermore, several broad conclusions are drawn from all of the above results.

9.2.1 Experimental methods

Experimentally, this thesis clearly demonstrated the utility of *in situ* optical microscopy for the study of carbon nanotube growth. Several variations of this technique were being reported in the early days of this research, and a few even before this research began [3–7]. This thesis has further developed *in situ* optical microscopy as a technique and has used it to observe not simply the quantitative growth kinetics, but also the qualitative aspects of the forest morphology.

The are four main observations that this technique has provided: (1) high resolution growth curves of forest height as a function of growth time (Chapter 2 and subsequent chapters), (2) changes in forest morphology as a function of time including termination morphologies (Chapter 3) and concavity changes, (3) optical diffraction occurring *in situ* (Chapter 6), and (4) the non-uniformity in the initial growth rate (Chapter 4 and subsequent chapters). Each of these observations contributed significantly to some aspect of this thesis, and without these observations, much of this work would not have been possible.

In particular, it was the *in situ* data in Chapter 3 that were able to show that there was a weak exponential decay in the growth curve prior to the abrupt termination, consistent with Ref. 8. The *in situ* data had a relatively short time scale and a low uncertainty to allow this observation. Previous methods (see for example Ref. 9) generally involved growing several different forests for different periods of time and measuring the height of each one *ex situ* after the growth was intentionally terminated at the given time. The resolution and uncertainty of these methods did not allow the same observations.

Qualitative observations of similar *in situ* optical microscopy data in Chapter 3 revealed a two-stage growth curve that was explained by strain driven termination.

The observation in Chapter 6 of the diffraction grating effect occurring *in situ* as the forests were growing provided very direct evidence that the ripples form as the nanotubes are growing and do not change afterward. To the author's best knowledge, this is the first concrete evidence that these ripples do indeed form as a result of growth and not as a post-growth effect. The non-uniform growth rate that was observed with *in situ* optical microscopy was critical in explaining the origin of the ripples and a major motivation to analyzing the gas phase diffusion in Chapter 6.

One of the other benefits that the optical monitoring provided is not mentioned in any of the preceding chapters but nevertheless contributed to the results presented in this thesis. This benefit is the almost immediate feedback that can be obtained with this *in situ* method. By simply watching the growth occurring on live camera, it is possible to quickly evaluate the results. For instance, when roughly optimizing the CVD reactor for maximum height during acetylene growth, the effect of large changes in any CVD control parameter can immediately be determined. Of course this optical monitoring method only works because carbon nanotube forests are large enough to be easily visible to the camera.

This thesis also shows that a relatively basic CVD reactor using simple and safe to handle gases and a straightforward optical monitoring system can produce good quality SWCNTs. CVD systems like this are quite attractive for industrial production of SWCNTs because of their simplicity (and hence cost) and ability to be scaled up to meet the higher output demands of industrial scale production.

In terms of actually producing carbon nanotubes, this thesis confirms previous observations that acetylene is a better carbon source than ethanol [10] for producing tall forests, and therefore high yield. Using a thinner catalyst produces more single walled carbon nanotubes (possibly due to smaller diameter catalyst nanoparticles) and reduces the number of defects, but also decreases yield. Although this was only tested for acetylene, the forests produced are still taller than the ethanol forests on the thicker catalyst. If the ethanol forests similarly decreased in height when grown from a thin catalyst layer, they would be very short and provide a very low yield. Unpatterned, uniform catalyst layers on large area substrates tend to produce taller forests than patterned samples.

Finally, the specific growth process and the CVD reactor procedures have been developed significantly during this thesis in terms of optimizing the output (whether it is quality, quantity, or a specific diameter distribution that is desired), improving the reproducibility, and streamlining the process. The effect of the CVD control parameters

(in particular the temperature and flow rate/pressure of the carbon source gas) on the growth rate, yield (height of the forest), quality (D/G ratio), and diameter have been determined and are broadly consistent with the large number of other processes described in the literature.

In general, lower growth pressures tend to slightly improve the D/G ratio. Pressure and flow rate do not affect the yield very much, but lowering them does dramatically increase the amount of time required to grow the nanotubes, which is a very important consideration for commercial production. Lower growth temperatures produce more defective CNTs, and also narrower diameter SWCNTs, but will also produce highly defective MWCNTs at low enough temperatures. The yield is generally maximized between 750°C and 800°C and decreases as the temperature moves away from this maximum. Higher temperatures lead to faster growth and faster termination.

Because many growth parameter changes have opposite effects on the quality and quantity of material, the definition of "optimizing" the growth process thus depends significantly on the particular application of the CNTs being synthesized and whether a high yield of slightly defective nanotubes is better or worse than a low yield of highly crystalline nanotubes.

9.2.2 Multiple mechanisms

One of the main conclusions of this thesis is that the growth of carbon nanotube forests is not a simple straightforward process: many different mechanisms are involved and must all work together to provide a final outcome. Here, the first indication of multiple mechanisms was first seen immediately in Chapter 2 when the critical point in the temperature dependence highlighted the changeover from one mechanism to another in both the growth kinetics and Raman parameters. Multiple mechanisms were seen again in Chapter 3 when the different termination morphologies suggested that, depending on the growth conditions, different termination mechanisms were dominant. Furthermore, the growth curves in Chapter 3 showed an abrupt termination superposed over a steady exponential decay, which again suggests that two different mechanisms are responsible for termination.

In the ethanol CVD (Chapter 2), only the uniform termination mechanism (see Chapter 3) is seen. No signs of even minor cracking or delamination are observed, and the growth curves show only a single exponential decay. The abrupt termination that may be caused by strain within the forest does not manifest itself in ethanol CVD. This is likely a result of the short final height of these forests that does not provide the necessary

conditions for abrupt termination to manifest.

Another example of multiple mechanisms that differs from the previous examples is the possibility of multiple reaction pathways being available to the acetylene source gas. For example acetylene is converted into carbon nanotubes but it also appears to play a role in the termination mechanism. In Chapter 7 it was observed that the termination time was a function of the carbon concentration, which suggests that a carbon consuming chemical reaction may lead to termination. Although the exact termination mechanism is not known, the fact that it depends on the acetylene concentration suggests that it is indeed a chemical reaction that happens in parallel to growth. This reaction may be, for example, the conversion of acetylene into a build up of amorphous carbon on the catalyst nanoparticle or a chemical reaction with the nanoparticle such as the formation of a carbide. The conversion efficiency of acetylene to carbon nanotubes was measured to be ∼30% (see Chapter 7) and although much of the gas will simply bounce of the substrate surface, it is certainly possible that at least some of it will also be consumed in the parallel parasitic reaction, either in the gas phase or at the catalyst nanoparticle.

Chapter 6 and Chapter 7 presented a unified picture (see Chapter 7, Foreword) of how many of the observed strain relief mechanisms (concavity, sidewall curvature, and rippling) function together during the growth of a carbon nanotube forest.

The final chapter (Chapter 8) again presented the idea of multiple mechanisms, this time while considering the diameter selectivity of carbon nanotube growth, particularly in the discussion regarding "growth filters". All filters (mechanisms) occur simultaneously during growth. Chapter 8 identified one specific filter: an intrinsic process that can lead to diameter selectivity. Chapter 8 also discussed a few other filters based on other reports. In order for a specific nanotube (as determined by its chirality) to grow, it must be allowed by each of the filters. If it is blocked by even one filter, it will not grow. This idea is illustrated in Fig. 1. In Fig. 1, 3 filters are represented and superposed over a schematic of all SWCNT chiralities for $d < 1.37$ nm. The filter that represents the thermodynamically allowed nanotubes is shown in Fig. 1a, represented by the green area that spreads outward from 0.7 nm. The filter that represents the SWCNTs that are allowed by the catalyst nanoparticle size is represented by the shaded blue region between 0.5 nm and 1.2 nm that is shown in Fig. 1b. Finally, a filter that allows only large chiral angles to appear is represented by the red wedge shaped region between 15° and 30° that is shown in Fig. 1c. This growth filter may be due to a mechanism similar to the screw dislocation growth theory[11] (see Section 1.3.2).

All of these filters are illustrated together in Fig. 1d, where there are various areas of overlap between different filters. These filters are essentially a Venn diagram [12] where

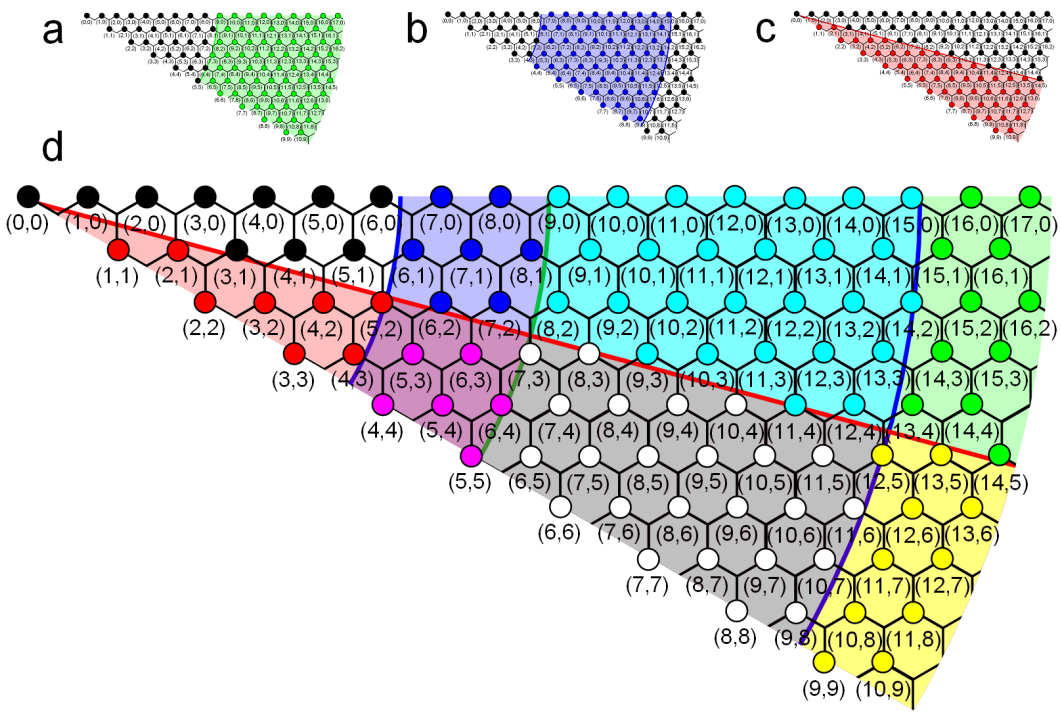


Figure 1: Schematic illustration of the "filters" that lead to chiral and diameter selectivity, superposed over a grid of CNT chiralities. Three filters are illustrated by the (a) green, (b) blue, and (c) red shaded regions which correspond (a) the thermodynamics filter of Chapter 8, (b) a catalyst nanoparticle size filter, and (c) a filter allowing only large chiral angles. The region where all three filters overlap (d) represents the SWCNTs that can grow; these are represented by white circles.

the allowed nanotubes are in the region of the mutual intersection of all three filters (represented as the gray area with the white points in Fig. 1d). The nanotubes that appear in this region have their lower diameter limit set by the green thermodynamics filter, their upper diameter limit set by the blue catalyst nanoparticle filter, and their chiral angle range set by the red filter. If there is no mutual overlap between the filters, then no nanotubes will be produced at all. In the context of Fig. 1d, this could occur, for example, if the blue and green regions did not overlap such that all diameters allowed by the catalyst nanoparticle were smaller than the minimum diameter that was thermodynamically allowable.

The concept of multiple mechanisms coexisting (but perhaps not all manifesting at the same time) also serves the purpose of uniting many diverse theories about how nanotubes grow and how they terminate.

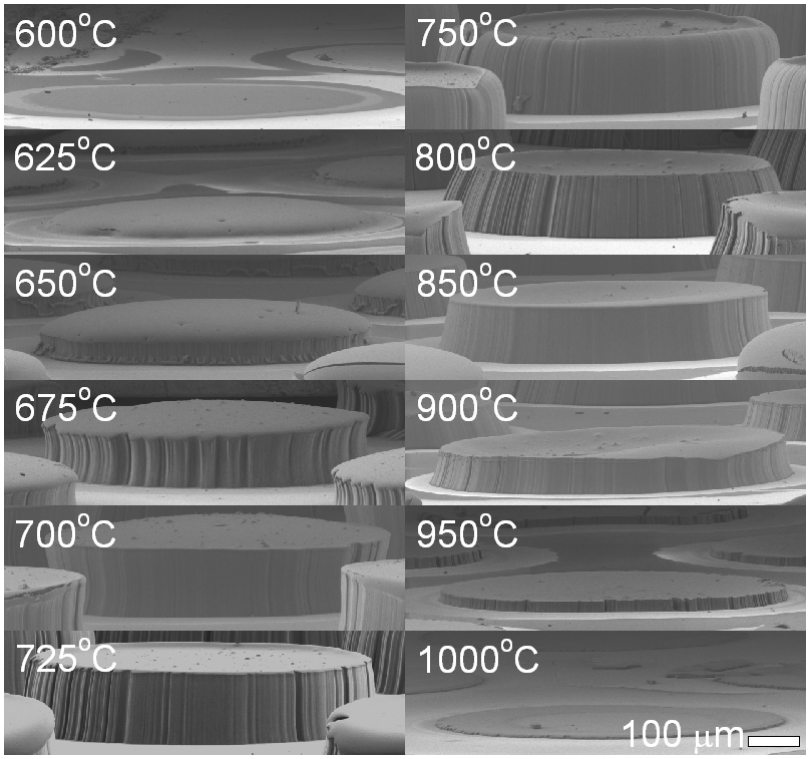


Figure 2: Concavity of the top surface of CNT forests as a function of growth temperature T (indicated) for ethanol CVD.

9.2.3 Gas phase diffusion

The gas phase diffusion model of Chapter 7 predicts a non-uniform gas distribution. With the observation of a supply limited growth regime, the non-uniform distribution of acetylene leads to a non-uniform growth rate across the patterned catalyst island. This non-uniform growth rate not only nicely explains many of the results presented in this thesis, but can also explain some other results. For example, some of the ethanol grown forests in Chapter 2 had convex top surfaces. Not only did these forests have convex top surfaces, but the concavity of a forest depends on the growth temperature. Forests have convex top surfaces at low growth temperatures which change to concave top surfaces as the growth temperature increases. The changeover occurs at approximately 725°C, a temperature at which the top surface is essentially flat. This temperature dependence is shown in Fig. 2.

In the case of convex top surfaces, the extra gas that is received around the edges is detrimental to growth, which occurs in the regime where the system is significantly overfed and increases in the amount of gas have no effect on the growth rate. This is unlike the situation in Chapter 7, where more gas resulted in a faster growth rate. Recall that in Chapter 2, it was concluded that at the low temperatures, there was likely an

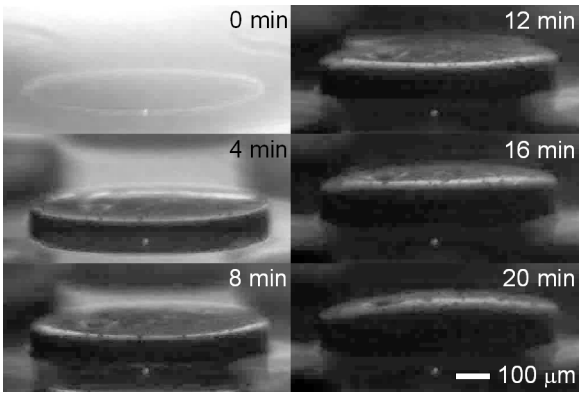


Figure 3: Frames from an *in situ* video (changed to black and white and contrast enhanced) of a forest growing at 675°C during ethanol CVD synthesis (times indicated). The forest initially grows with a flat top surface, but gains a convex top surface as it approaches its termination. An SEM image of the final forest is shown in Fig. 2.

excess amount of gas in the CVD chamber. When the growth process is significantly overfed, parasitic reactions become relatively more important as less gas is being used up in the growth process. These parasitic reactions can increase the termination rate, thus causing the growth rate of the outer nanotubes to slow down sooner and more rapidly than the inner nanotubes. The inner nanotubes thus grow taller and for a longer period of time, leading to a convex top surface that forms toward the end of growth.

Indeed, *in situ* optical microscopy shows that this is the case and that the forests with a convex top surface initially start to grow with a flat top surface, but gain their convex top surface near the end of their growth, just prior to termination. This is a direct contrast to the forests with concave top surfaces, which gain their concavity during the initial stages of growth. Figure 3 shows frames (with times indicated) from an *in situ* video (changed to black and white and contrast enhanced for better viewing) of a forest growing at 675°C during ethanol CVD. The forest shown in Fig. 3 is the same forest that is shown in the scanning electron microscope (SEM) image in Fig. 2 (675°C).

The prediction of the gas phase diffusion model of a non-uniform gas distribution (which leads to non-uniform growth rate in the supply limited growth regime seen at present) is thus versatile in that it can explain many of the morphological features seen in this thesis: the concave and convex top surfaces, the curvature and rippling of the forest sidewalls, and the observation that the outer nanotubes in the forests often delaminate. The non-uniform gas distribution can also explain the observed dependence of the growth kinetics on the size of the patterned catalyst islands. Finally, the gas phase diffusion model also suggests that, for different gases, the diffusion length of the gas will be different and will thus cause a difference in the observed morphologies.

9.2.4 Inter-nanotube interactions

A growing carbon nanotube forest is not simply a collection of individual nanotubes growing, but is instead the collective growth of many nanotubes that interact with one another. In the discussion of termination mechanisms (see Chapter 3), one of the main outcomes of this work is proposing just how significant the interactions between the individual nanotubes within a forest really are. These inter-nanotube interactions are a likely cause of the termination of forest growth (by causing strain within the forest) and most definitely contribute to the morphology of the forests. The cracking of the forest demonstrates one situation where the cohesion energy is overcome while delamination shows a situation where the cohesion of the forest keeps it intact. Conversely, delamination provides evidence of the adhesion to the substrate being broken while cracking provides evidence of the adhesion to the substrate remaining intact.

Another consequence of inter-nanotube interactions is the rippling morphology that was discussed in detail in Chapter 5 and Chapter 6. This phenomenon in particular demonstrates the importance of these interactions. Here the cohesion energy between the nanotubes and the strain energy that results from bending the nanotubes play a role in the observed rippling pattern. Likewise, the smoothness of the observed concave top surfaces provides good evidence for long range inter-nanotube interactions, primarily the induced strain and cohesion. The gas phase diffusion model of Chapter 7 provides further insight: a non-uniform growth rate among the nanotubes (due to a non-uniform source gas distribution), coupled with the nanotube-nanotube interactions within the forest, can cause the strain that leads to the observed morphological features. In cases where the difference in growth rate (and hence strain) between the inner and outer nanotubes is negligible, no rippling will be observed, and the observed concavity will be considerably less.

In Chapter 3, an analogy was made to crystal growth, and in particular the Stranski-Krastanov (SK) growth mode of heteroepitaxy [13]. Here, it is important to remember that growth of CNT forests occurs at the base, whereas growth in heteroepitaxy is occurring from the top. In the analogy, the picture of the SK growth mode (Fig. 13 of Chapter 1) should be flipped upside down to make a proper comparison to the growth of a CNT forest. Initially, the forest that grows is uniform and has no cracks (as observed in Chapter 3), but after a certain critical thickness, a transition to "island growth" (as seen in the SK growth mode) occurs. In the sense of carbon nanotube forests, island growth would imply cracks between adjacent regions of the forest. The top of the forest is still well held together, but the base is not. Eventually, these cracks can propagate through to the top of the forest and it can rip open, as seen in the cracking morphology.

The adhesion energy is strong enough to anchor each piece of the forest to the substrate.

Another way of thinking about this is to consider the idea of strained epitaxial layers that crack apart under tensile strain and delaminate from the substrate under compressive strain [13]. In the cracking of carbon nanotube forests, the pieces of the forests that crack apart tend to be deflected outward (see Chapter 3), which suggests that this may possibly be the result of the release of some tensile strain in the forest. A possible origin of the tensile strain is the same as the origin of the convex forests. If the outer nanotubes were to terminate before the inner nanotubes, yet remain anchored to the substrate, they would pull the still growing inner nanotubes toward the edge of the forest, thus providing the tensile strain that rips the forest apart. Going one step further, this analogy would suggest that delamination in a carbon nanotube forest might occur due to the release of compressive strain. The observation that cracking and delamination are essentially mutually exclusive lends further support to this analogy. Furthermore, in epitaxial growth, the critical thickness for delamination is often greater than that for cracking [13], which is, at the very least, consistent with the observation that delaminated forests are generally taller than cracked forests.

One important conclusion of Chapter 7 is that larger catalyst islands (the limiting case of which is unpatterned growth substrates) produce taller forests than smaller islands. This is surprising since one might initially expect that smaller islands would reduce long range strain in the forests. The unpatterned samples may yield taller forests by providing more uniform CVD conditions due to an increased uniformity of the concentration of source gas (and thus a more uniform growth rate and less strain). This links the effects of strain, caused by the non-uniform growth rate, back to the height of the forests and provides a very simple way of increasing the yield. Not only do the forests grow taller, but using the unpatterned substrates necessarily produces more nanotubes per substrate area than the patterned samples (because all of the substrate area on the unpatterned substrates is covered with catalyst).

One of the important outcomes of all of this research is that in order to reach greater final heights, it is important to not only increase the growth rate of the individual nanotubes in the forest, but also to make sure that the distribution of growth rates among these nanotubes is as narrow as possible. Broad distributions of growth rates will lead to significant strain building up in the forest, causing deformations, as well as nanotubes being ripped off the substrate or anchoring the forest to the substrate and thus potentially causing the overall termination of the forest.

9.2.5 Control over diameter distribution and defect density

The final chapter of this thesis (Chapter 8) provided explanations for the observed diameter distribution and defect density of SWCNT samples. Chapter 8 provided both a physical description for what was occurring at the microscale and how some general CVD control parameters affect the diameter and defect density.

The defect density was explained as a result of the healing [14–16] of a single type of simple defect in the nanotube lattice. This is intrinsic to the formation of carbon nanotubes and is not a result of a specific carbon source or catalyst. Furthermore, this mechanism is not specific to carbon nanotubes, but can also be extended to the CVD growth of graphene. In the same way that earlier research on carbon fibers and fullerenes can be applied to carbon nanotube research, so too can carbon nanotube research be applied to the newer field of graphene research [17, 18]. By understanding this mechanism and what factors control it, it will be possible to better control the CVD growth of carbon nanotubes and tailor the output to the desired crystallinity.

The minimum diameter for SWCNTs may depend on the thermodynamic stability of the formation energy associated with the strain in the hemispherical cap. A "phase diagram" of diameter stability was proposed in Chapter 8 (see Fig. 6 in Chapter 8) for acetylene CVD. This phase diagram shows that narrow diameter SWCNTs can be achieved at low growth temperatures and high carbon source pressures (for acetylene CVD and carbon monoxide CVD). The HiPCO® (high pressure carbon monoxide) CVD synthesis method [19] can produce narrow diameter SWCNTs by using, as the name suggests, high pressures. Similarly, the CoMoCAT® synthesis process [20] also produces narrow diameter SWCNTs by using pressures greater than atmospheric pressure. The fact that these processes produce narrow SWCNTs at pressures greater than atmospheric pressure is completely consistent with the findings of this thesis.

The fact that this model is consistent with considerably different synthesis methods shows its generality and applicability to carbon nanotube research as whole. The physical insight that it provides should help guide future research toward being able to exert further control over the synthesis process in terms of the nanotube diameter distribution.

9.3 Conclusions

To summarize, the main conclusions of this thesis are:

1. *In situ* data provide insightful information on the carbon nanotube growth process, both quantitatively and qualitatively.

2. Raman spectra obtained *ex situ* can yield information that correlates well with the CVD growth conditions.
3. The effects of the various CVD control parameters have been studied such that the reliable production of CNT forests with a specific height, defect density, diameter distribution, and to a lesser degree morphology is possible. However, when "optimizing" a CVD reactor, there is a trade off between high yield, low defect density, and narrow diameter SWCNTs.
4. In most aspects of CNT forest growth, there are competing mechanisms that dominate under different growth conditions; some of these mechanisms were analyzed in this work. These multiple mechanisms are particularly noticeable in the termination of growth and the diameter selectivity that occurs during the growth process.
5. The interactions between individual carbon nanotubes and strain within a forest are not negligible. They play a significant role in determining the morphology of the forest and in termination. Any complete model of carbon nanotube forest growth must include these interactions. Maximizing the yield by maximizing forest height requires that individual CNT growth is maximized. Simultaneously, differences in growth rates must be minimized to reduce strain.
6. A model of gas phase diffusion was developed to explain the observed morphology and catalyst island size dependent growth kinetics. Coupled with the high efficiency of C_2H_2 as a carbon source, gas phase diffusion can be a very important factor in CVD synthesis of CNTs.
7. The temperature dependence of the defect density can be explained by a defect healing mechanism, which is independent of many CVD parameters and intrinsic to the growth of carbon nanotubes and even graphene.
8. A thermodynamics model was developed in order to explain the observed diameter distribution of a SWCNT sample produced by CVD: the minimum diameter of a SWCNT is determined by its thermodynamics of formation and in particular the strain energy involved in "rolling" a sheet of graphene into a carbon nanotube.

The mechanisms identified and studied here are: strain induced termination, rippling, non-uniform growth rates due to gas phase diffusion, defect healing, and the intrinsic thermodynamic stability of carbon nanotubes that contributes to diameter selectivity. In the context of the growth of forests in the CVD reactor used in this research, these are the most important mechanisms in play and are sufficient to describe the growth process of carbon nanotube forests and to provide guidance on how to optimize the reactor.

Other similar CVD reactors may produce slightly different results, even with the same substrate, catalyst, gas composition, flow rate, and growth temperature. The reasons for this are fairly straightforward. In the reactor used in this thesis, not all of the gas that is flowed into the reactor reaches the substrate. Changing the way the gas is delivered may change the amount of gas that reaches the substrate. Likewise, a different heating system or chamber design may create a slightly different thermal gradients. These slight changes could change the results somewhat, but the overall trends would likely be the same. Although these slight differences would be difficult to measure, if one could account for them, it would be possible to reproduce the results completely on any CVD system that has the same overall properties.

For any synthesis process, it is important to consider which mechanisms are most important for each specific CVD process (as it was done in this thesis for this specific CVD reactor) and include the important contribution in the description of the growth, while leaving negligible contributions out. The nanotube-nanotube interactions, defect healing mechanism, and thermodynamic minimum diameter model are sufficiently robust that they are always important considerations in the growth of forests, and, for the two latter, SWCNTs in general. By carefully considering what aspects of the growth are most important to include, one can provide an accurate model for any specific process, which can be reused and further adapted for slightly different processes as the situation warrants.

The mechanisms, techniques, and concepts proposed in this thesis will assist others in describing observations of their growth process and will aid them by providing direction to their research and optimizing their synthesis process to produce the best nanotubes for their specific intended application. In an ideal carbon nanotube synthesis process, one will be able to make carbon nanotubes in a specific configuration and tailored to a specific template of a set number of walls, length, crystallinity, and diameter. The results and conclusions of this thesis represent a step toward this ideal synthesis process and into a future where carbon nanotube synthesis is fully understood and many of the exciting applications are a reality.

References

[1] Z-P Yang, L Ci, J A Bur, S-Y Lin, and P M Ajayan. *Nano Lett.*, 8:446–51, 2008.

[2] H Kimura, D N Futaba, M Yumura, and K Hata. *J. Am. Chem. Soc.*, 134:9219–24, 2012.

[3] K Kaminska, J Lefebvre, D G Austing, and P Finnie. *Nanotechnology*, 18:165707, 2007.

[4] I Gunjishima, T Inoue, and A Okamoto. *Appl. Phys. Lett.*, 91:193102, 2007.

[5] A A Puretzky, G Eres, C M Rouleau, I N Ivanov, and D B Geohegan. *Nanotechnology*, 19:055605, 2008.

[6] C Mattevi, C T Wirth, S Hofmann, R Blume, M Cantoro, C Ducati, C Cepek, A Knop-Gericke, S Milne, C Castellarin-Cudia, S Dolafi, A Goldoni, R Schloegl, and J Robertson. *J. Phys. Chem. C*, 112:12207–13, 2008.

[7] S Yasuda, D N Futaba, M Yumura, S Iijima, and K Hata. *Appl. Phys. Lett.*, 93:143115, 2008.

[8] E R Meshot and A J Hart. *Appl. Phys. Lett.*, 92:113107, 2008.

[9] D N Futaba, K Hata, T Yamada, K Mizuno, M Yumura, and S Iijima. *Phys. Rev. Lett.*, 95:056104, 2005.

[10] G Eres, A A Kinkhabwala, H Cui, D B Geohegan, A A Puretzky, and D H Lowndes. *J. Phys. Chem. B*, 109:16684–94, 2005.

[11] F Ding, A R Harutyunyan, and B I Yakobson. *Proc. Nat. Acad. Sci.*, 106:2506–9, 2009.

[12] R V Hogg and E A Tanis. *Probability and Statistical Inference, 6^{th} Edition.* Prentice-Hall, USA, 2001.

[13] J E Ayers. *Heteroepitaxy of Semiconductors.* CRC Press, USA, 2007.

[14] M Picher, E Anglaret, R Arenal, and V Jourdain. *Nano Lett.*, 9:542–7, 2009.

[15] A J Page, Y Ohta, Y Okamoto, S Irle, and K Morokuma. *J. Phys. Chem. C*, 113:20198–207, 2009.

[16] Q Yuan, Z Xu, B I Yakobson, and F Ding. *Phys. Rev. Lett.*, 108:245505, 2012.

[17] D Tománek, A Jorio, M S Dresselhaus, and G Dresselhaus. In A Jorio, G Dresselhaus, and M S Dresselhaus, editors, *Carbon Nanotubes: Advanced Topics in the Synthesis, Structure, Properties and Applications*, pages 1–12. Springer, Germany, 2008.

[18] C Mattevi, H Kim, and M Chhowalla. *J. Mater. Chem.*, 21:3324–34, 2011.

[19] P Nikolaev, M J Bronikowski, R K Bradley, F Rohmund, D T Colbert, K A Smith, and R E Smalley. *Chem. Phys. Lett.*, 313:91–7, 1999.

[20] D E Resasco, W E Alvarez, F Pompeo, L Balzano, J E Herrera, B Kitiyanan, and A Borgna. *J. Nanopart. Res.*, 4:131–6, 2002.

Appendix A

Supplementary material for: Kinetic critical temperature and optimized chemical vapor deposition growth of carbon nanotubes (Chapter 2)

as published* in *Chemical Physics Letters*, Volume 469, Pages 293–297, 2009.
http://dx.doi.org/10.1016/j.cplett.2008.12.095

* This material has been reformatted for printing in this thesis, though the figures themselves are unchanged. An expanded caption has also been added to Video S1. Only the printable version of this material is reproduced here. The multimedia portion of this material is available from the University of Ottawa's thesis repository (uO Research) as indicated in the List of videos, as well as the article's publisher's website, which can be accessed using the above hyperlink.

Supplementary material for: Kinetic critical temperature and optimized chemical vapor deposition growth of carbon nanotubes

P. Vinten, J. Lefebvre, P. Finnie

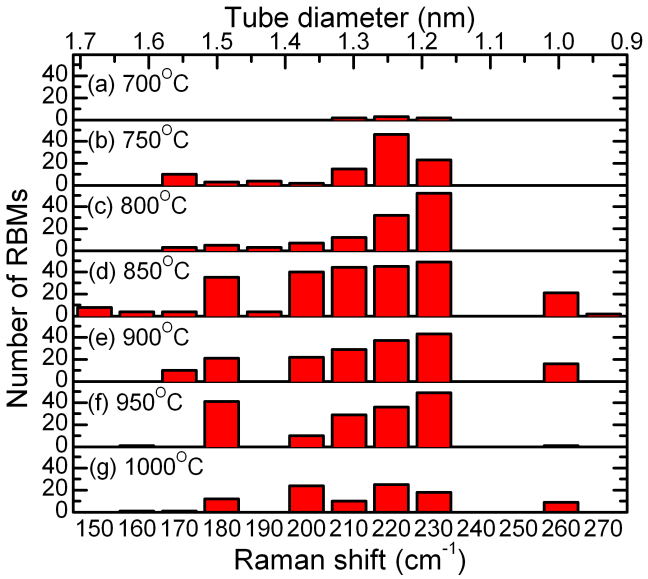


Figure S1: A histogram of the detected RBMs, binned in intervals of 10 cm^{-1}. ω [cm^{-1}]= $248/d$ [nm] (see Chapter 2 ref. 35). Below 700°C, we did not detect any RBMs.



Video S1: Video of growing carbon nanotubes. Video runs in real time and is cropped from the original: frame width corresponds to ∼1 mm.

Appendix B

Supplementary material for: Distinct termination morphologies for vertically aligned carbon nanotube forests (Chapter 3)

as published* in *Nanotechnology*, Volume 21, Article 035603 (7 Pages), 2010.
http://dx.doi.org/10.1088/0957-4484/21/3/035603

Copyright notice: ©2010 IOP Publishing Ltd.

* Only the printable version of this material is reproduced here. The multimedia portion of this material is available from the University of Ottawa's thesis repository (uO Research) as indicated in the List of videos, as well as the article's publisher's website, which can be accessed using the above hyperlink.

Supplementary material for: Distinct termination morphologies for vertically aligned carbon nanotube forests

P Vinten, P Marshall, J Lefebvre and P Finnie

1. Raman Acquisition Parameters

Raman acquisition parameters were identical to our previous report. From our previous report (reference [21] in main article):

"Raman spectra were obtained *ex situ* using a commercial confocal Raman system (Jobin Yvon Labram) with a 300 line/mm grating and 50X extra-long working distance microscope objective. We used 785 nm and 1 mW excitation on a spot of $\sim$1 μm in diameter and a confocal hole of 100 μm. At this power density, there was no damage to the forests, however if the power was increased by even less than an order of magnitude, irreversible damage was done to the forests. The total laser exposure was identical for all points with a total of 9 s acquisition composed of three 3 s acquisitions at each data point. We scanned each sample across a 5 $\times$ 5 grid covering a 120 μm $\times$ 120 μm area. This was done twice for a total of 50 spectra per sample. The samples were analyzed [in plan view] from the tops of the forests (90° to the substrate), and the laser was linearly polarized parallel to the substrate surface (perpendicular to the average nanotube axis, which was vertical)."

2. Figures

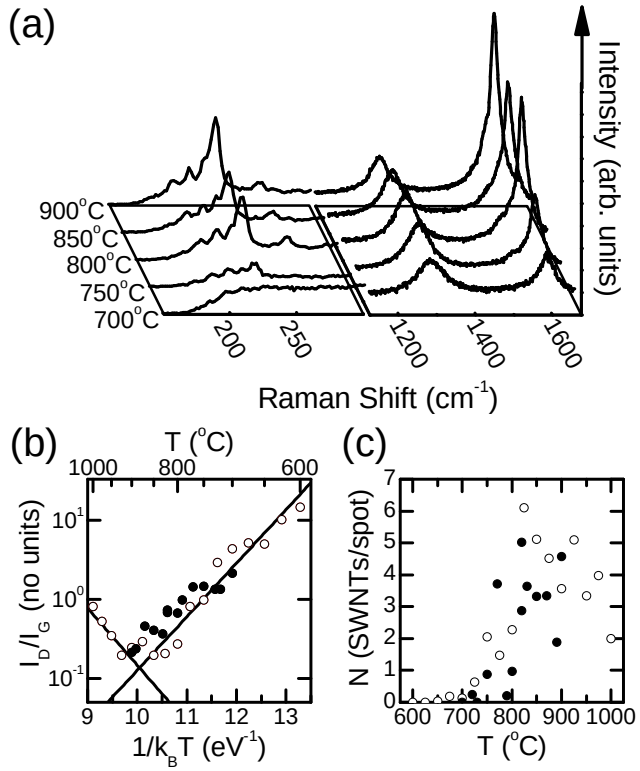


Figure S1. (a) Raman spectra in RBM and D and G band regions for various growth temperatures T. (b) Integrated D/G intensity ratio I_D/I_G vs $1/k_BT$ and (c) average number of resonant RBMs N vs T. Solid circles are current acetylene data and, for comparison, open circles are ethanol data from our previous report (reference [21] in main article). Linear fits to ethanol data have characteristic energies -1.1 ± 0.1 eV (below 860°C) and 1.1 ± 0.1 eV (above 860°C).

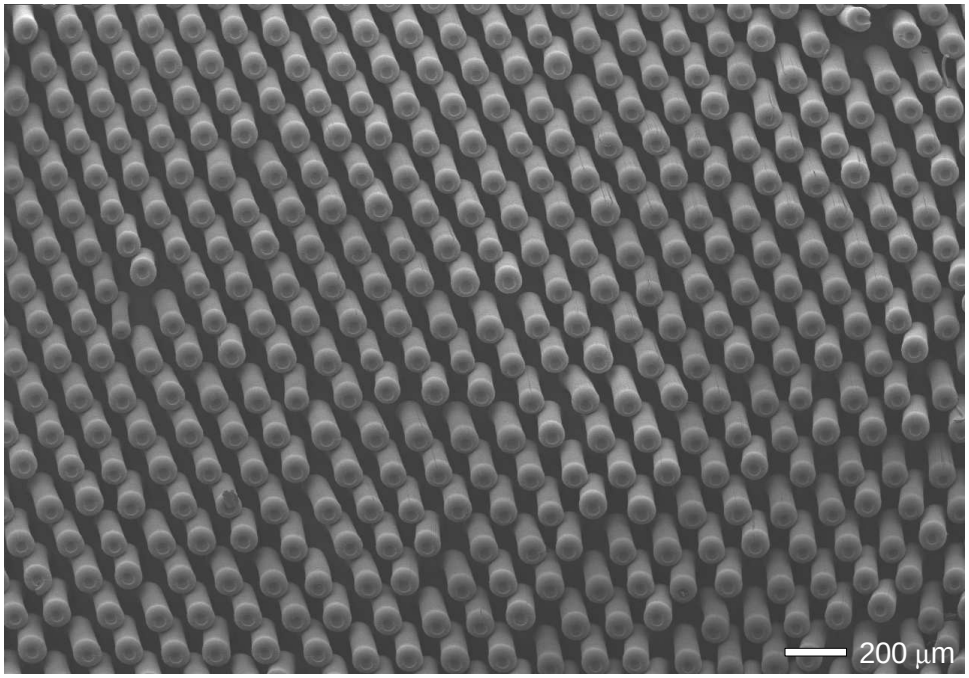


Figure S2. SEM image showing that the concavity of the forests is almost always centered. These forests were grown on 100 μm catalyst islands using the same experimental procedure as in the main article.

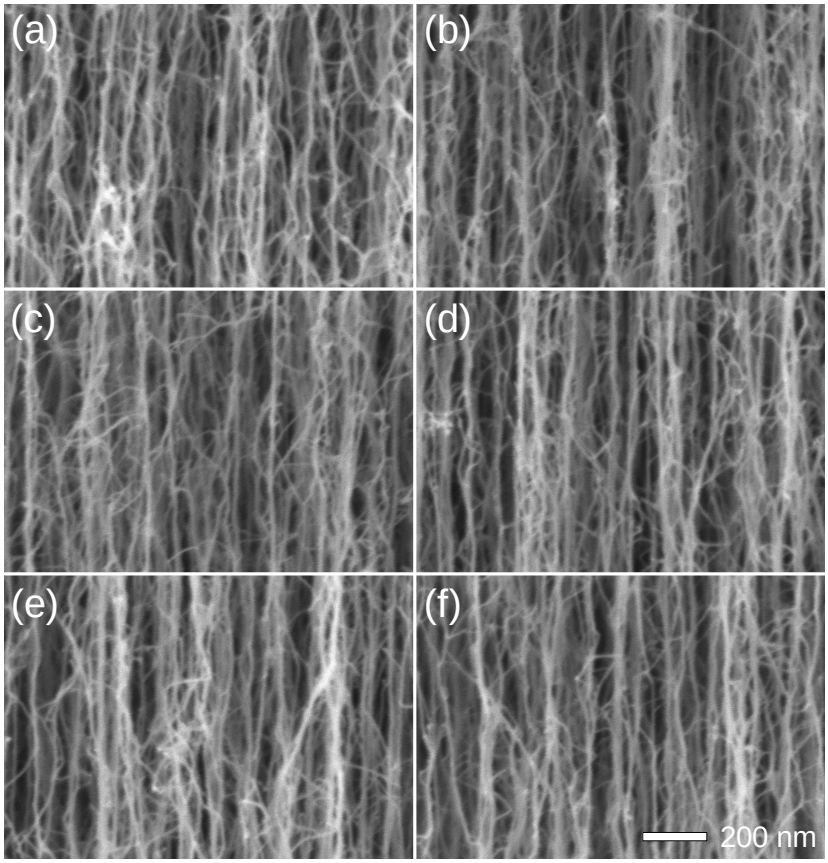


Figure S3. High magnification SEM images showing the microscopic organization of nanotubes on the side walls of a forest grown on a 800 μm catalyst island. These images were taken edge on to the substrate for a side view of the forest from near the top (a) to near the base (f).

3. Videos

`videoS1.avi`

Video S1. Forest growth and uniform termination at 900°C. This is the movie from which figure 1(a) in the main article is derived. Movie cropped and frame rate increased. 2.9 second runtime corresponds to ∼5 minutes of real elapsed time. Frame width corresponds to 875 μm.

`videoS2.avi`

Video S2. Forest growth and delamination at 730°C. This is the movie from which figure 1(b) in the main article is derived. This video also shows the outer nanotubes peeling from the bulk of the forest. Movie cropped and frame rate increased. 6.6 second runtime corresponds to ∼11 minutes of real elapsed time. Frame width corresponds to 925 μm.

`videoS3.avi`

Video S3. Forest growth and cracking at 720°C. This is the movie from which figure 1(c) in the main article is derived. Movie cropped and frame rate increased. 4.2 second runtime corresponds to ∼7 minutes of real elapsed time. Frame width corresponds to 900 μm.

`videoS4.avi`

Video S4. Forest growth on an unpatterned catalyst sample completely curling up on itself and delaminating. Movie cropped and frame rate increased. 16.5 second runtime corresponds to ∼108 minutes of real elapsed time. Initial frame width corresponds to ∼7.5 mm.

Appendix C

Supplementary material for: Origin of periodic rippling during chemical vapor deposition growth of carbon nanotube forests (Chapter 6)

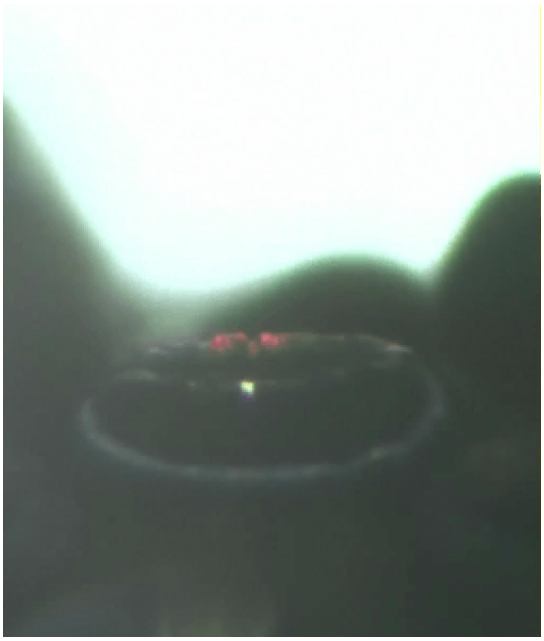
as published* in *Carbon*, Volume 49, Pages 4972–4981, 2011.
http://dx.doi.org/10.1016/j.carbon.2011.02.017

* Only the printable version of this material is reproduced here. The multimedia portion of this material is available from the University of Ottawa's thesis repository (uO Research) as indicated in the List of videos, as well as the article's publisher's website, which can be accessed using the above hyperlink.

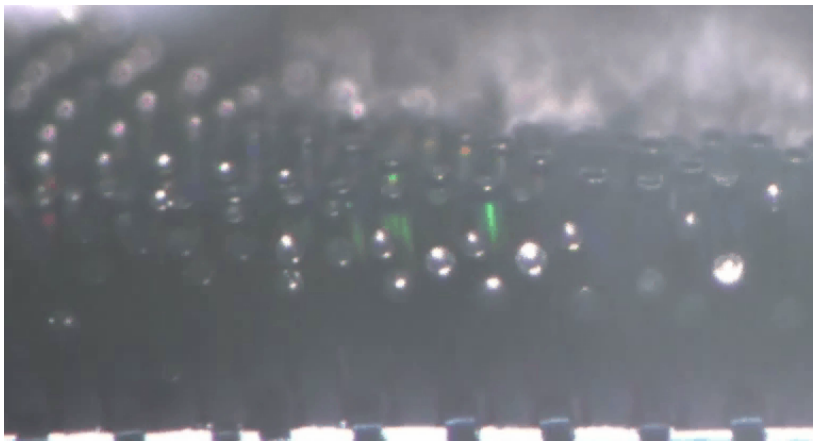
Supplementary material for: Origin of periodic rippling during chemical vapor deposition growth of carbon nanotube forests

P. Vinten, J. Bond, P. Marshall, J. Lefebvre, P. Finnie

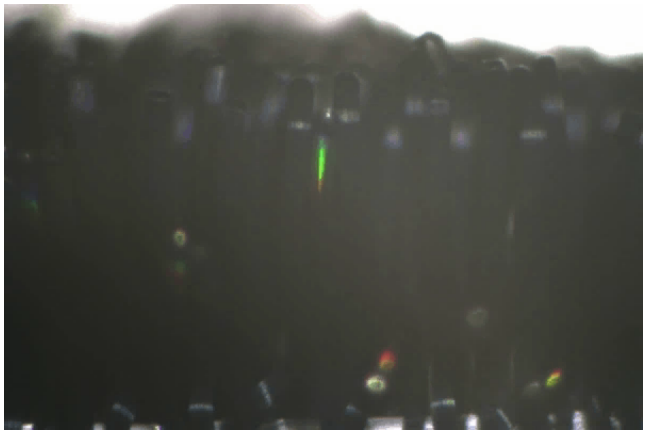
Videos



Video S1. Iridescence (red) as seen *in situ* from the forest shown in Fig. 3 (SEM) and Fig. 4a. Figure 4a is a frame from the raw video from which this video is based. Forest grown at 760°C using 220 sccm C_2H_2 flow rate on a 700 μm diameter catalyst island. Movie cropped and frame rate increased. 5.0 second runtime corresponds to ∼30 minutes of real elapsed time. Frame width corresponds to ∼840 μm.



Video S2. Iridescence as seen *in situ* from multiple 100 μm diameter forests as shown in Fig. 4b. Figure 4b is a frame from the raw video from which this video is based. Forests grown at 760°C using 180 sccm C_2H_2 flow rate on 100 μm diameter catalyst islands that were evenly spaced on a hexagonal grid. Movie cropped and frame rate increased. 3.1 second runtime corresponds to ∼90 seconds of real elapsed time, near the termination time of forest growth. Frame width corresponds to ∼2.7 mm.



Video S3. Iridescence not changing due to post-growth cooling in reactor from $T = 760$°C to $T < 100$°C. The whole sample moves because the metallic heater supports warp as the temperature changes. Forests grown at 760°C using 180 sccm C_2H_2 flow rate. Movie cropped and frame rate increased. 3.0 second runtime corresponds to ∼5 minutes of real elapsed time. Frame width corresponds to ∼2.2 mm.

Appendix D

Supplementary material for: Critical role of gas phase diffusion and high efficiency in vertically aligned carbon nanotube forest growth (Chapter 7)

This appendix is based on the supplementary material included with the article upon which Chapter 7 is based. That article is accepted for publication (4 April 2013) in the journal *Carbon*. That article (and the corresponding supplementary material) can be accessed via the following hyperlink:
`http://dx.doi.org/10.1016/j.carbon.2013.04.007`

* Only the printable version of this material is reproduced here. The multimedia portion of this material is available from the University of Ottawa's thesis repository (uO Research) as indicated in the List of videos, as well as the article's publisher's website, which can be accessed using the above hyperlink.

Supplementary material for: Critical role of gas phase diffusion and high efficiency in vertically aligned carbon nanotube forest growth

P. Vinten, P. Marshall, T. Quance, J. Lefebvre, P. Finnie

1 Experimental procedures

The substrate pattern is laid out such that all four sizes of catalyst island can be in the same focal plane, and the pattern can be flipped horizontally in the reactor by rotating the sample. Rotating the pattern had no noticeable effect. The pattern itself is shown in Fig. 1a in Chapter 7. Additional substrates with a slightly different pattern were prepared using photolithography for the Auger electron spectroscopy (AES) investigation.

The carbon source was dilute acetylene gas (0.1% C_2H_2, 99.9% Ar), assisted by hydrogen (2% H_2, 98% Ar), and water vapour obtained from a bubbler. The reactor was operated at atmospheric pressure. Before each growth run, the reactor was purged for 10 min with the Ar/H_2 mixture flowing at 2500 sccm. Samples were heated to the growth temperature T (measured with a two-colour infrared pyrometer) in an Ar/H_2 environment with a flow rate of 320 sccm. After 5 min, water vapour was introduced by passing part of the Ar/H_2 mixture through the bubbler such that the water concentration reached 1000 ppmv at the reactor exhaust (GE Panametrics Moisture Monitor Series 35). 5 min after the water was first introduced, dilute acetylene (0.1% C_2H_2, 99.9% Ar) was introduced (at 225 sccm) to initiate growth, while turning the total Ar/H_2 flow rate down to 95 sccm, to maintain an overall flow rate of 320 sccm and a water concentration of 1000 ppmv. After the growth was determined to have halted via self-termination (by visual inspection with the camera), the chamber was purged for 5 min with the Ar/H_2 mixture flowing at 2500 sccm. The heater was then shut off and the Ar/H_2 was allowed to flow for another 5 min before it was shut off. All samples remained in the Ar/H_2 environment inside the reactor for at least another 30 min prior to removal to atmosphere. More information can be found in our previous reports (References 14, 15, and 17 in Chapter 7). Kinetics data were acquired *in situ* using a long focal length optical microscope and digital camera as described in our previous reports.

When the C_2H_2 flow rate was varied, the water concentration remained at 1000 ppmv, and the Ar/H_2 flow rate remained at 95 sccm. We did not vary the water concentration along with the carbon supply because we wanted to see the true effect of varying the carbon supply. Had we varied the water concentration simultaneously with the carbon supply, we

would have changed the etching rate since the supposed role of water is to etch amorphous carbon from the catalyst nanoparticle, thereby prolonging growth (see Ref. 2 in Chapter 7). Regardless, we do not see much variation in the kinetics as a function of water concentration: forests grown with 500 ppmv and 3000 ppmv H_2O (in otherwise identical environments) had no apparent differences in terms of morphology or kinetics.

2 Results and discussion

2.1 Kinetic observations

Figure S1a-f and Video S1 show the growth of carbon nanotube forests from the pattern shown in Fig. 1a in Chapter 7, with the four forests at the front in the video corresponding to the bottom of Fig. 1a (diameters: 200 μm, 100 μm, 400 μm, and 800 μm). Heights are indicated for three forests on Fig. S1c-f. This video (and Video S2) are captured at a 5° glancing angle to the substrate. A scanning electron microscope (SEM, Hitachi S-4700) image of the same forests is shown in Fig. 1b in Chapter 7, at an angle of 45° to the substrate. Growth curves (height H as a function of growth time t) for the four forests are shown in Fig. S2. The growth curve for the 200 μm diameter forest does not show its termination because the forest tilted sideways, out of view of the camera. The terminal height H_T of this forest is determined *ex situ* using SEM. In Fig. S1a-f and Video S1, the smallest forest initially grows the fastest (Fig. S1c), but then terminates first (Fig. S1d), while the largest forest grows much slower, but for a longer duration, and ultimately reaches a taller final height (Fig. S1f).

`videoS1.avi`

Video S1: Simultaneous growth of forests from four different catalyst island sizes as shown in Fig. S1. The video has been cropped and its frame rate has been increased. The 15 s runtime corresponds to ∼25 min of real elapsed time. The frame width corresponds to ∼2.4 mm.

`videoS2.avi`

Video S2: The initial moments of growth and the non-uniform initial growth rate as shown in Fig. 5 in Chapter 7. The video has been cropped but runs in real time. The frame width corresponds to ∼840 μm.

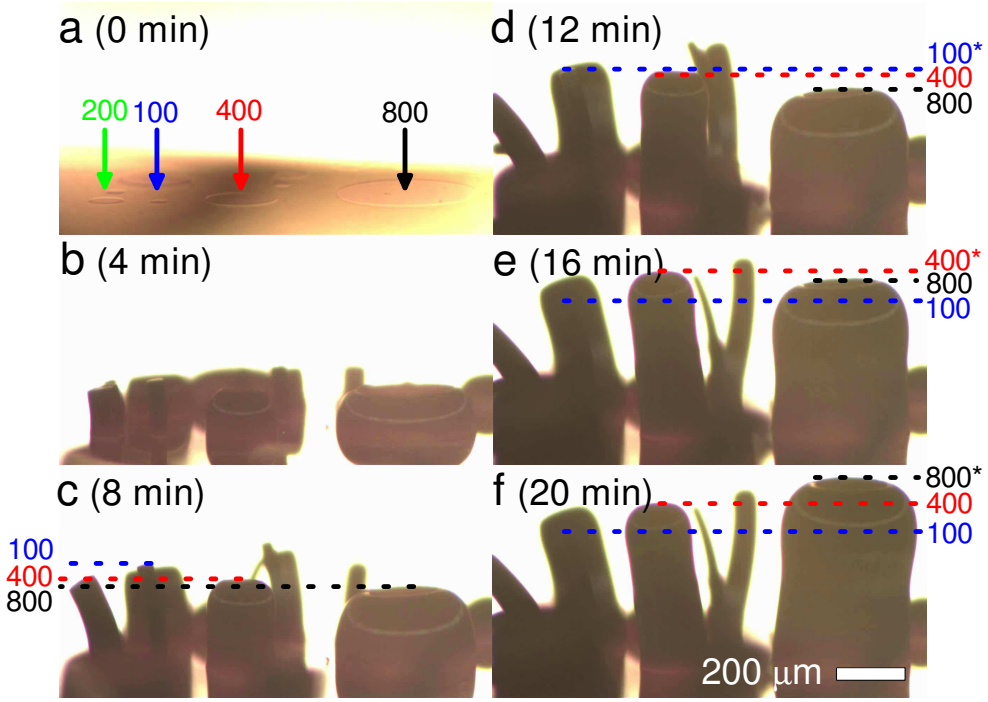


Figure S1: (a-f) Frames from an *in situ* video (Video S1) of growing CNT forests of four different sizes at 820°C (viewed at ∼5° angle to the substrate). The forests from left to right have diameters 200 μm, 100 μm, 400 μm, and 800 μm (indicated). Growth times are indicated, and heights for three forests are indicated in frames (c-f). * denotes that the relevant forest has terminated (approximate). Growth curves for these forests are shown in Fig. S2.

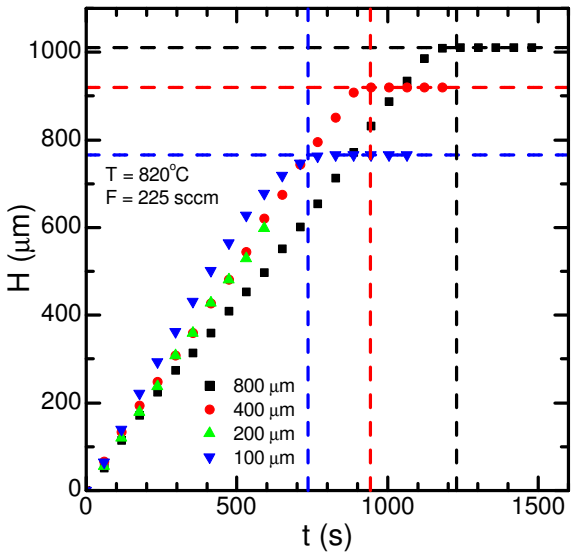


Figure S2: Growth curves. Height H vs growth time t for four forests grown simultaneously at 820°C from catalyst islands of different sizes. Termination height H_T and termination time τ_T are indicated by dashed lines (horizontal and vertical respectively). These growth curves correspond to Fig. S1, Video S1, and Fig. 1b in Chapter 7.

2.2 SEM observations

Figure S3 shows an SEM image of forests grown at 760°C, viewed at ∼45° to the substrate. Some forests are bent, some bend two ways, while others are straight. Of interest, two of the 100 μm diameter forests bent over and touched the nearby 400 μm diameter forests which kept growing after the 100 μm forest stopped growing. This resulted in the smaller forests being ripped of the substrate by the larger forests and serves to illustrate the forces involved (see Ref. 26 of Chapter 3). Figure S4a is an SEM image of the base of a forest, showing the forest partially delaminated from the substrate near the edge of the catalyst island and good alignment of the CNTs even near the base. Figure S4b shows extensive delamination on a different forest.

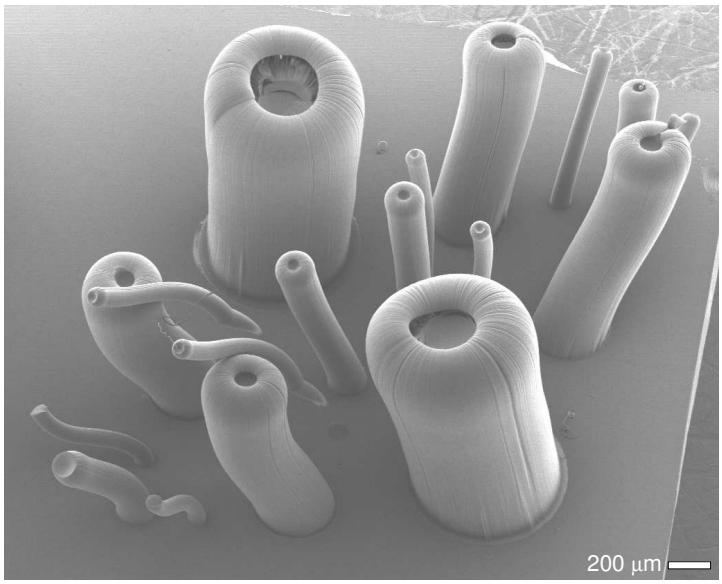


Figure S3: An SEM image of forests grown at 760°C, viewed at ∼45° to the substrate.

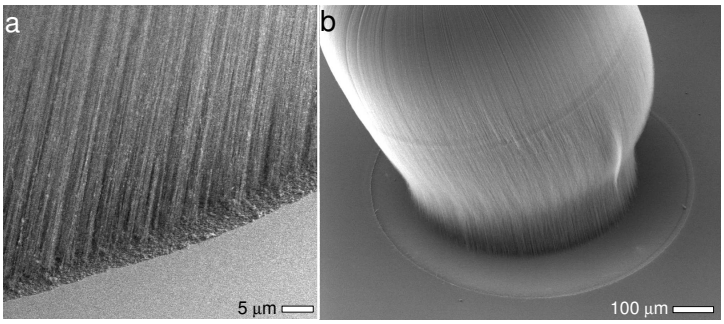


Figure S4: SEM images of the base of CNT forests. (a) Good alignment, but some delamination around the edges of a forest grown from a 400 μm diameter catalyst island at 740°C. (b) Extreme example of delamination around the edges of a forest grown from an 800 μm diameter catalyst island at 760°C.

2.3 Auger electron spectroscopy

Auger electron spectroscopy (AES) was performed *ex situ* using a PHI 700 Scanning Auger Nanoprobe, a scanning Auger microscope (SAM). This instrument can perform highly localized AES. Here we used μm lateral resolution and performed line scans to generate thickness profiles of the Co layer. Although the AES does not give the absolute value of the thickness of the Co layer, it can easily detect changes in the thickness of the layer by a change in the strength of the signal. We expect the 0.8 nm layer of Co to be, on average, 2-3 monolayers thick. One very important point is that AES is able to evaluate just the deposited Co layer without simultaneously measuring changes in the thickness of the underlying Al_2O_3 layer. We observe that Al_2O_3 layers of either 250 nm or 50 nm produce essentially the same forests, so the alumina layer thickness variation is likely insignificant.

The underlying Al_2O_3 layer was always visible underneath the 0.8 nm Co layer, though the SiO_2 underneath the 250 nm Al_2O_3 was not visible. Even a 10 nm layer of Al_2O_3 was enough to block the signal from SiO_2. AES is very surface sensitive, with a penetration depth α typically on the order of a few nm (here, $\alpha < 10$ nm). Spectra were acquired over the expected energy ranges of Si, O, Al, Co, C and differentiated (a standard procedure in AES). The difference between the maximum and minimum differential Co signal are presented here in Fig. S5. The signals have been normalized with respect to their maximum and minimum. Scans consisted of 32 or 64 points to generate a line. The line followed the radial direction of the round catalyst island, across the edge of the catalyst island (left side of Fig. S5) and over an equal sized portion of the SiO_2 substrate (right side of Fig. S5). In addition to the as-prepared samples (black) used in Chapter 7, scans were also performed on samples annealed at 760°C in an $Ar/H_2/H_2O$ environment for 10 min (blue) and 40 min (red), and as-prepared photolithographic samples (green).

Figure S5a shows 10 μm line scans (normalized on both sides) near the edge of the island to analyze the edge effects. The photolithographic samples have much sharper edge effects. Despite this, they produced forests with the same physical features as the shadow mask samples: concave top surfaces with curved and rippled sidewalls. For both sample types, the edge effects do not have the same scale as the observed concavity of the top surface of the forest. The edge effects do not change with heating and no Co was observed outside of the patterned area, which suggests that the Co catalyst does not diffuse onto the surrounding SiO_2. Furthermore, we rarely see any nanotubes on the surface outside of the patterned area, which further suggests that no Co is present outside of the intended area.

Larger 200 μm line scans across the edge of the catalyst island (Fig. S5b) show the uniformity of the 0.8 nm Co layer. The scale of this uniformity makes it unlikely that the catalyst deposition is the cause of the observed growth non-uniformity across the catalyst island.

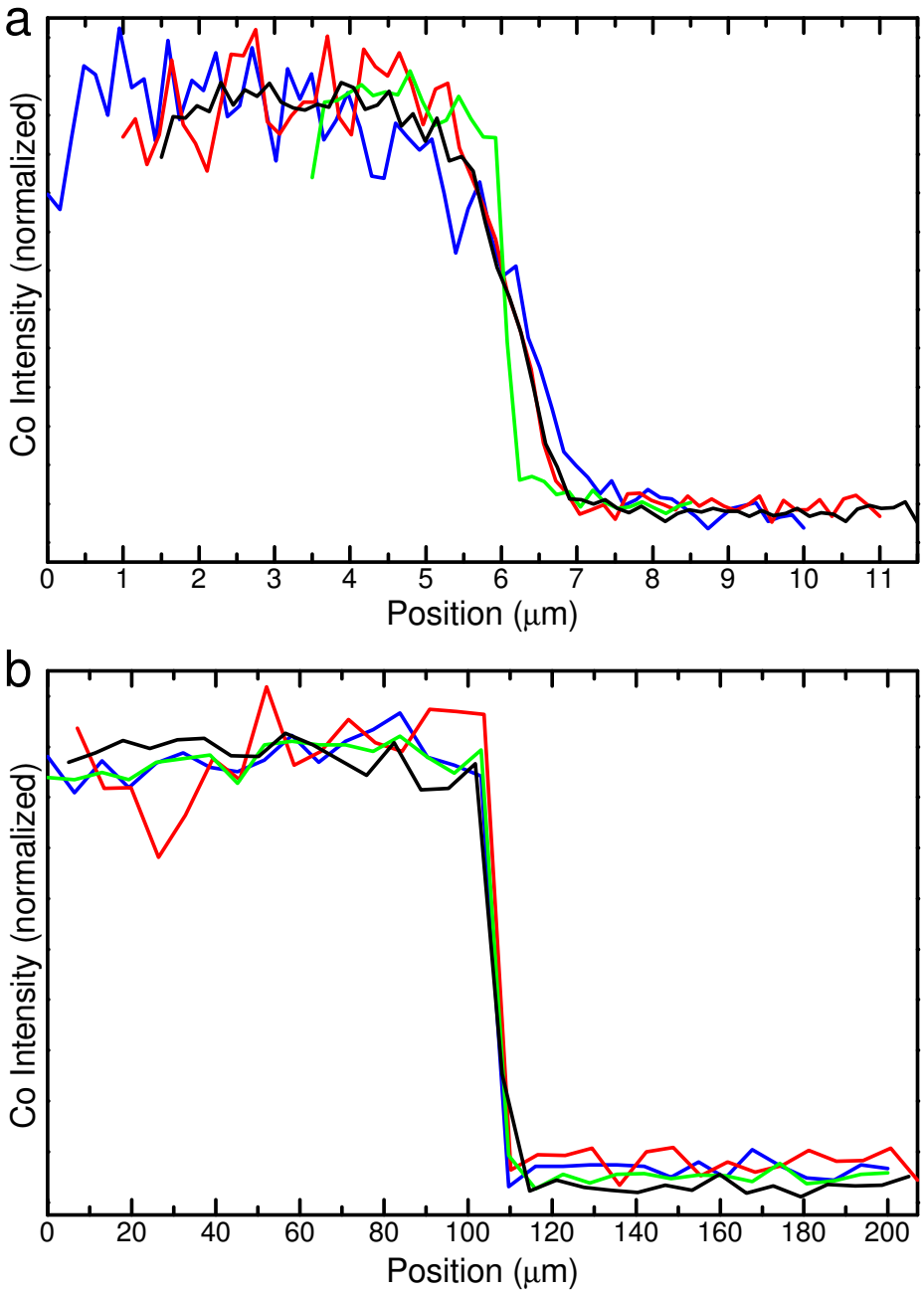


Figure S5: Auger electron spectroscopy line profiles of Co catalyst island. (a) Co line profiles showing the short range edge effects on the shadowmasked (annealed and un-annealed) and photolithographic samples. (b) Co line profiles showing the long range edge effects on the shadowmasked (annealed and un-annealed) and photolithographic samples. Colours represent different samples: black, as-prepared shadowmask sample; blue, shadowmask sample after 10 min anneal; red, shadowmask sample after 40 min anneal; green, as-prepared photolithographic sample. Actual length scales are given on the axes.

2.4 Raman spectroscopy

Raman spectra were acquired using a 532 nm laser with the Raman system described in Chapter 1, Section 1.6.3. Each spectrum consists of ten 3 s acquisitions. The samples were analyzed in plan view from the tops of the forests (90° to the substrate), and the laser was linearly polarized parallel to the substrate surface (perpendicular to the average nanotube axis, which was vertical). Spectra were acquired *ex situ* at room temperature for forests grown at a variety of temperatures and for all island sizes at each temperature. Spectra (normalized to the G-band peak) of forests grown at 860°C are shown in Fig. S6. A minimum of four spectra were acquired for each island size, each at a different location, but all from the same sample.

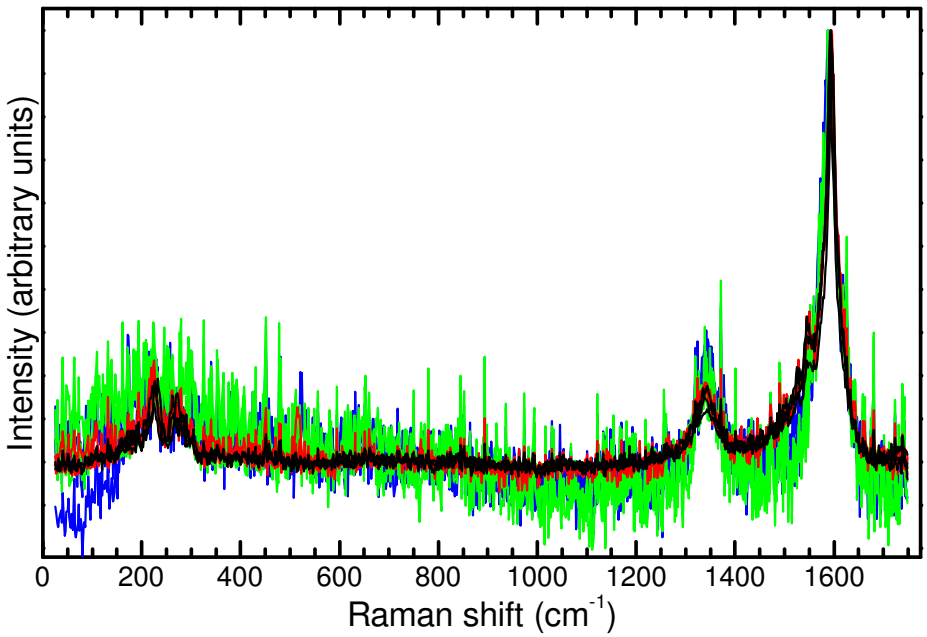


Figure S6: Raman spectra for 4 different catalyst island sizes. Colours represent forest diameters: 100 μm, 200 μm, 400 μm, and 800 μm and are represented by blue, green, red, and black respectively.

2.5 Gas diffusion model

The geometry used to solve Equation (1) in Chapter 7 is shown in Fig. S7.

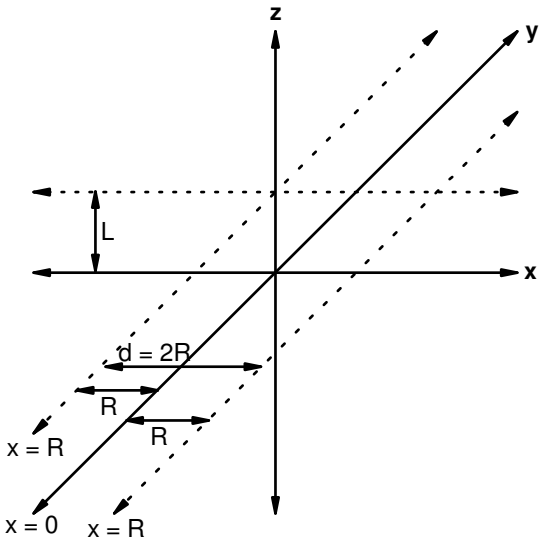


Figure S7: Sketch of the boundary conditions used to solve Equation (1) in Chapter 7.

The forms of A and B are:

$$A^{-1} = 1 + \frac{1}{\sqrt{1-\epsilon}} \tanh\left(R/\sqrt{D\left(1-\epsilon\right)\tau_d}\right)$$
$$B^{-1} = 1 + \sqrt{1-\epsilon} \coth\left(R/\sqrt{D\left(1-\epsilon\right)\tau_d}\right) \tag{S1}$$

While solving Equation (1) in Chapter 7, we define $1/\tau_{eff} = 1/\tau_d + 1/\tau_g$. A and B are calculated using the conditions that $n\left(x\right)$ and $\partial n\left(x\right)/\partial x$ must be continuous at $x = R$.

To determine the relationship between the efficiency ϵ and the time constants τ_d and τ_g, we begin by assuming that ϵ is independent of location and is constant in time. We thus consider a simplified version Equation (1) in Chapter 7 for an unpatterned forest:

$$\frac{\partial n}{\partial t} = I - \frac{n}{\tau_d} - \frac{n}{\tau_g} \tag{S2}$$

In this case, the steady state solution is independent of position and is simply $n = I\tau_{eff}$. Furthermore, in this case we can define the instantaneous efficiency as:

$$\epsilon = \frac{\text{gas used for growth}}{\text{gas flowed into reactor}} = \frac{n/\tau_g}{I} \tag{S3}$$

Combining this equation with the solution to Equation (S2), the efficiency for a uniform forest can be written as $\epsilon = \tau_{eff}/\tau_g = \tau_d/\left(\tau_g + \tau_d\right)$. Thus, the parameter τ_g can be calculated from τ_d through the expression $\tau_g = \tau_d\left(1-\epsilon\right)/\epsilon$. Equation (S3) is the instantaneous efficiency whereas Equation (3) in Chapter 7 is the overall average efficiency; these are the same due to

the assumed steady state conditions. The measured values of M, τ_T, and γ used to calculate ϵ (Equation (3) in Chapter 7) are shown in Table S1. The flow rate F was 225 sccm of 0.1% C_2H_2 in Ar.

Table S1: Values of M, τ_T, and γ used to calculate ϵ. M_g is the denominator of Equation (3) in Chapter 7.

M [mg]	τ_T [s]	γ	M_g [mg]	ϵ [%]
2.2	3030	0.48	6.7	33
1.2	1850	0.36	3.1	39
1.5	2530	0.42	4.9	31
1.4	2740	0.53	6.7	21
3.9	7200	0.52	17.1	23

2.5.1 Bessel functions

In Chapter 7, for simplicity, a linear (1D) solution to model edge effects was presented (Equation (2) of Chapter 7). The linear solution is simple to work with, captures the essential processes and is sufficient to estimate the magnitudes of various effects and the critical parameters such as length scales. In reality however, the islands are circular with a finite radius. To better capture the effects of this geometry, a cylindrical solution in the form of Bessel functions could be used. However, for the sizes of islands used here, the results obtained from the cylindrical solution do not differ significantly from the linear solution. The systematic difference introduced by using a 1D solution instead of Bessel functions ranges from 1% for the smallest catalyst islands to 7% for the largest. This difference considers the difference in the predicted concentration of gas at the center of the catalyst islands. The effects of the nearest neighbour islands is likely more significant than the shape of the island itself (see, for example, the effect of catalyst island spacing in Fig. 6 of Chapter 7 and the related discussion in Section 3.2 of Chapter 7). Nearest neighbour effects would be simpler to model in the linear solution than the cylindrical solution, though these effects were not considered here.

The overall general shape of the gas distribution across the catalyst island remains the same as depicted in Fig. 7c of Chapter 7. The trend of smaller catalyst islands receiving more gas than the larger catalyst islands is also still present. The solution to Equation (1) of Chapter 7 in the form of Bessel functions is:

$$\begin{aligned} n(x) &= U\ \mathrm{I}_0\Big(r/\sqrt{D\tau_{eff}}\Big) + I\tau_{eff}\ ; \qquad x < R \\ n(x) &= V\ \mathrm{K}_0\Big(r/\sqrt{D\tau_d}\Big) + I\tau_d\ ; \qquad x > R \end{aligned} \tag{S4}$$

where I_0 and K_0 are modified Bessel functions of zeroth order. The constants U and V are analogous to the constants A and B for the linear solutions and can be solved for using the same boundary conditions.

2.6 CNT areal density

We directly measured the areal density of bundles σ_b in the forests, which was then used to determine the areal density of CNTs in the forest σ. Forests were grown at 760°C for 2 min. After growth, the forests were gently removed from the growth substrate using two sided tape, exposing the bottom surface in cross section (see Fig. S8). The tips of nanotube bundles are clearly visible in SEM and can be counted directly. Several forests were used for this purpose and all SEM images were taken near the center of the circular forests. All SEM images were first adjusted to the same brightness level (as presented in Fig. S8), and then a threshold was applied to highlight the tips of the bundles, which were counted using *ImageJ*. For several images, the bundles were actually counted in order to verify that *ImageJ* was generating accurate counts.

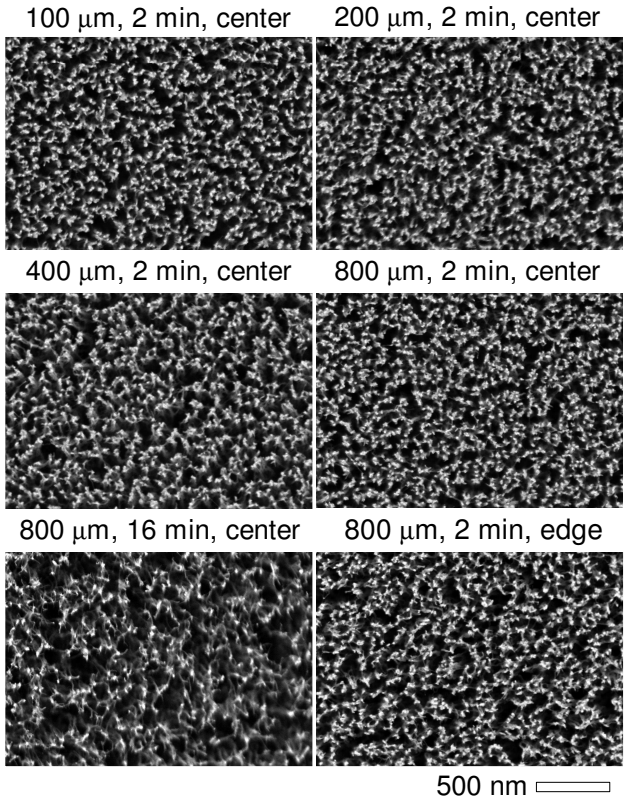


Figure S8: SEM images of the bottom cross section of forests for each catalyst island diameter and for the 800 μm diameter forest upon natural termination (τ_T = 16 min) and near the edge. Scale bar applies to all frames. Densities are given in Table S2.

At least 5 images were acquired for each catalyst island size, involving several forests of each size. The averages for each size are shown in Table S2. The quoted error reflects the standard deviation. There is no obvious systematic variation within error. We find an overall average of $\sigma_b = (2.0 \pm 0.4) \times 10^{10}$ bundles/cm^2. The density was visibly less when the forests naturally terminated (16 min for the 800 μm diameter forest). There was no measurable difference in the density between the center and the edge of the 800 μm diameter forest.

Table S2: Measured values of σ_b for CNT forests grown under different conditions.

d [μm]	t [min]	σ_b [bundles/cm^2]
100, center	2	$(2.1 \pm 0.4) \times 10^{10}$
200, center	2	$(2.1 \pm 0.4) \times 10^{10}$
400, center	2	$(1.6 \pm 0.3) \times 10^{10}$
800, center	2	$(2.2 \pm 0.4) \times 10^{10}$
800, center	16	$(1.4 \pm 0.6) \times 10^{10}$
800, edge	2	$(2.1 \pm 0.4) \times 10^{10}$

Appendix E

Supporting Information for: Thermodynamic and Energetic Effects on the Diameter and Defect Density in Single Walled Carbon Nanotube Synthesis (Chapter 8)

as published* in *The Journal of Physical Chemistry C*, Volume 117, Pages 3527–3536, 2013.
http://dx.doi.org/10.1021/jp308672a

Copyright notice: Reproduced with permission from [*J. Phys. Chem. C*, **2013**, *117* (7), pp 3527–3536.] Copyright 2013 American Chemical Society.

*In accordance with University of Ottawa regulations, the contact email address has been removed from this document.

Supporting information for:

Thermodynamic and Energetic Effects on the Diameter and Defect Density in Single Walled Carbon Nanotube Synthesis

Phillip Vinten,[†,‡] Paul Marshall,[†] Jacques Lefebvre,[†] and Paul Finnie[*,†,‡]

National Research Council Canada, Building M-50, 1200 Montreal Road, Ottawa, ON, K1A 0R6, Canada, and Department of Physics, University of Ottawa, 150 Louis Pasteur, Ottawa, ON, K1N 6N5, Canada

E-mail: [REDACTED]

[*]To whom correspondence should be addressed
[†]National Research Council Canada
[‡]University of Ottawa

Experimental Methods

The carbon source was dilute acetylene gas (0.1% C_2H_2, 99.9% Ar). Hydrogen was also diluted with argon (2% H_2, 98% Ar). The water vapour was obtained by passing the Ar/H_2 mixture through a bubbler.

Prior to each growth run, the reactor was purged for 10 min with the Ar/H_2 mixture at a flow rate of 2500 sccm. The substrate was then heated to the growth temperature T (measured with a two-colour infrared optical pyrometer) with a resistive heater under a flow of 320 sccm of the Ar/H_2 mixture. After 5 minutes, water vapour was introduced into the reactor by passing part of the Ar/H_2 mixture through the bubbler (but still maintaining a 320 sccm total flow) to reach a steady water concentration of 1000 ppmv at the reactor exhaust (measured with a GE Panametrics Moisture Monitor Series 35). After another 5 min (since the introduction of the water vapour), the dilute acetylene gas (0.1% C_2H_2, 99.9% Ar) was introduced into the reactor at 225 sccm to initiate growth, while reducing the total Ar/H_2 flow rate to 95 sccm in order to maintain an overall flow rate of 320 sccm and a water concentration of 1000 ppmv.

Once the growth was determined to have halted (via self-termination) by visual inspection with a long focal length optical microscope and digital camera, the reactor was purged for 5 min with the Ar/H_2 mixture flowing at 2500 sccm. The heater was then shut off and the Ar/H_2 was allowed to flow for another 5 min before it was shut off. All samples remained in the Ar/H_2 environment inside the reactor for at least another 30 min prior to removal to atmosphere.

In the pressure variation experiments, the C_2H_2 flow rate was varied while the water concentration remained at 1000 ppmv and the Ar/H_2 flow rate remained at 95 sccm (and thus varying the partial pressure of C_2H_2).

Raman Spectra

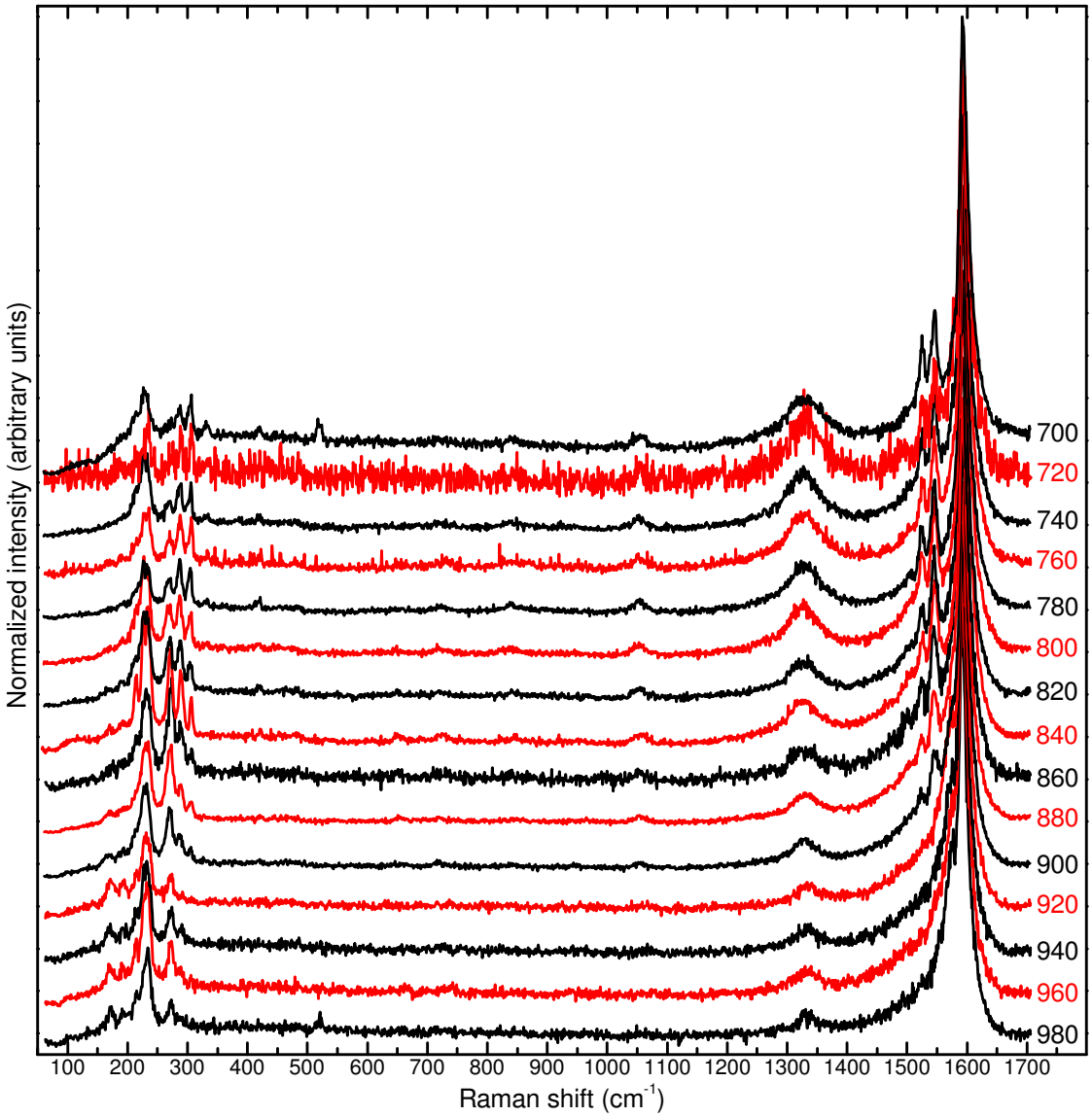


Figure S1: Raman spectra for CNT forest samples. Spectra are normalized to 1 at maximum of G band and vertically offset for clarity. Growth temperatures indicated (in units of [°C]).

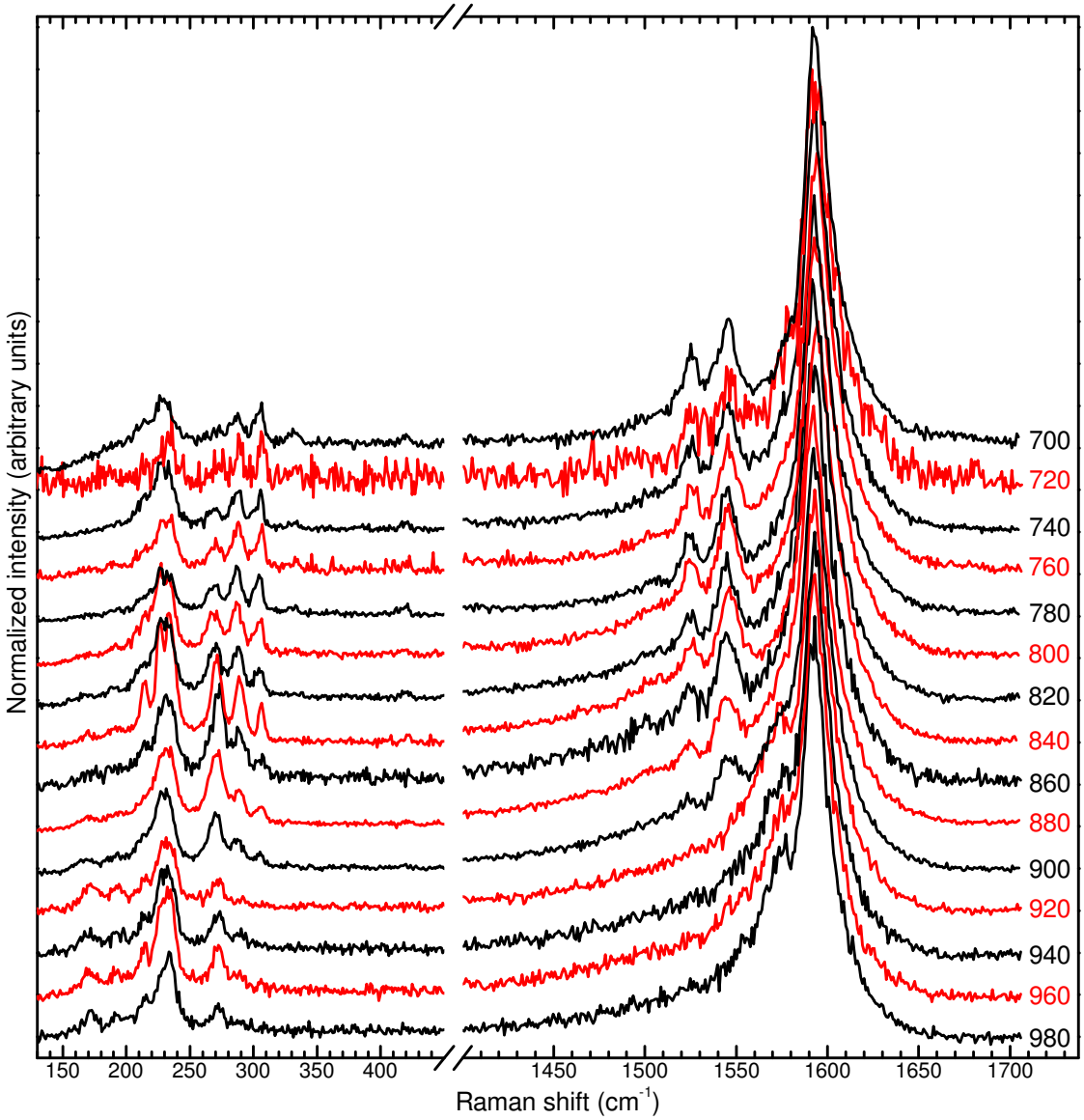


Figure S2: Raman spectra for CNT forest samples (from Fig. S1) in RBM and G band regions. Spectra are normalized to 1 at maximum of G band and vertically offset for clarity. Growth temperatures indicated (in units of [°C]).

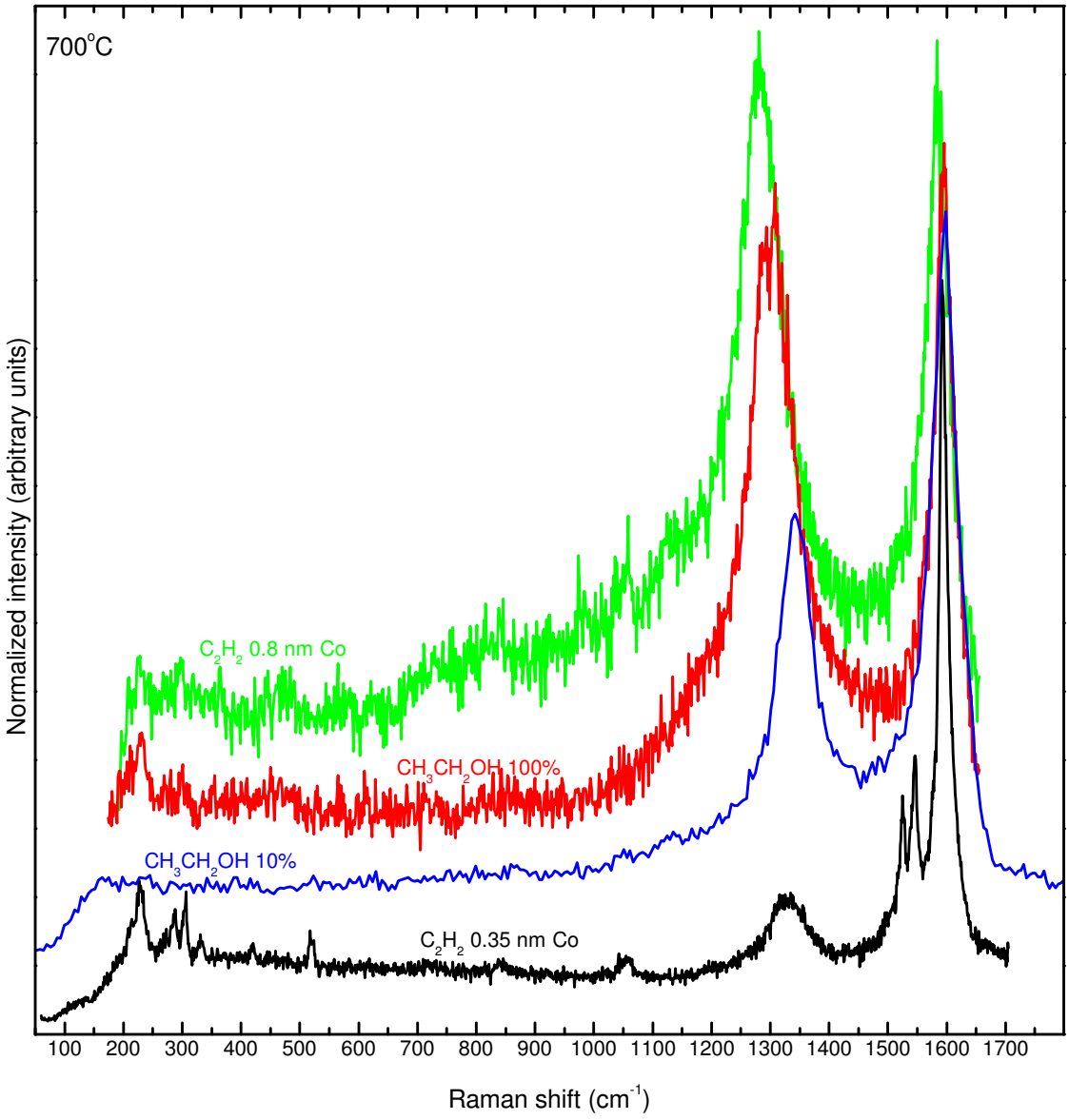


Figure S3: Raman spectra for CNT forest samples grown at 700°C for various growth conditions (indicated). Spectra are normalized to 1 at maximum of G band and vertically offset for clarity. Blue spectrum acquired with low resolution grating. Shift in D band position is due to different excitation wavelengths (532 nm for black and blue, 785 nm for red and green).

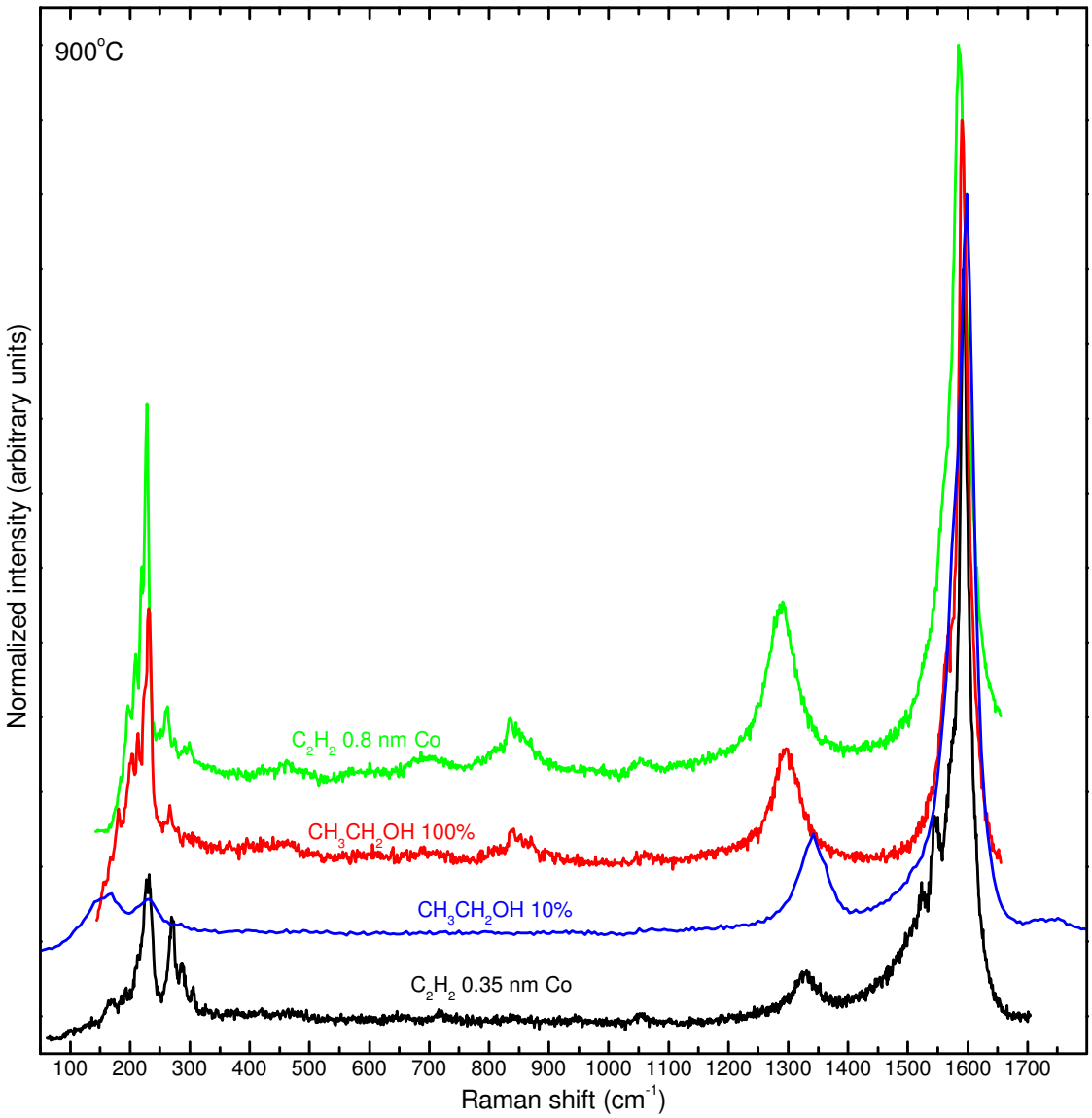


Figure S4: Raman spectra for CNT forest samples grown at 900°C for various growth conditions (indicated). Spectra are normalized to 1 at maximum of G band and vertically offset for clarity. Blue spectrum acquired with low resolution grating. Shift in D band position is due to different excitation wavelengths (532 nm for black and blue, 785 nm for red and green).

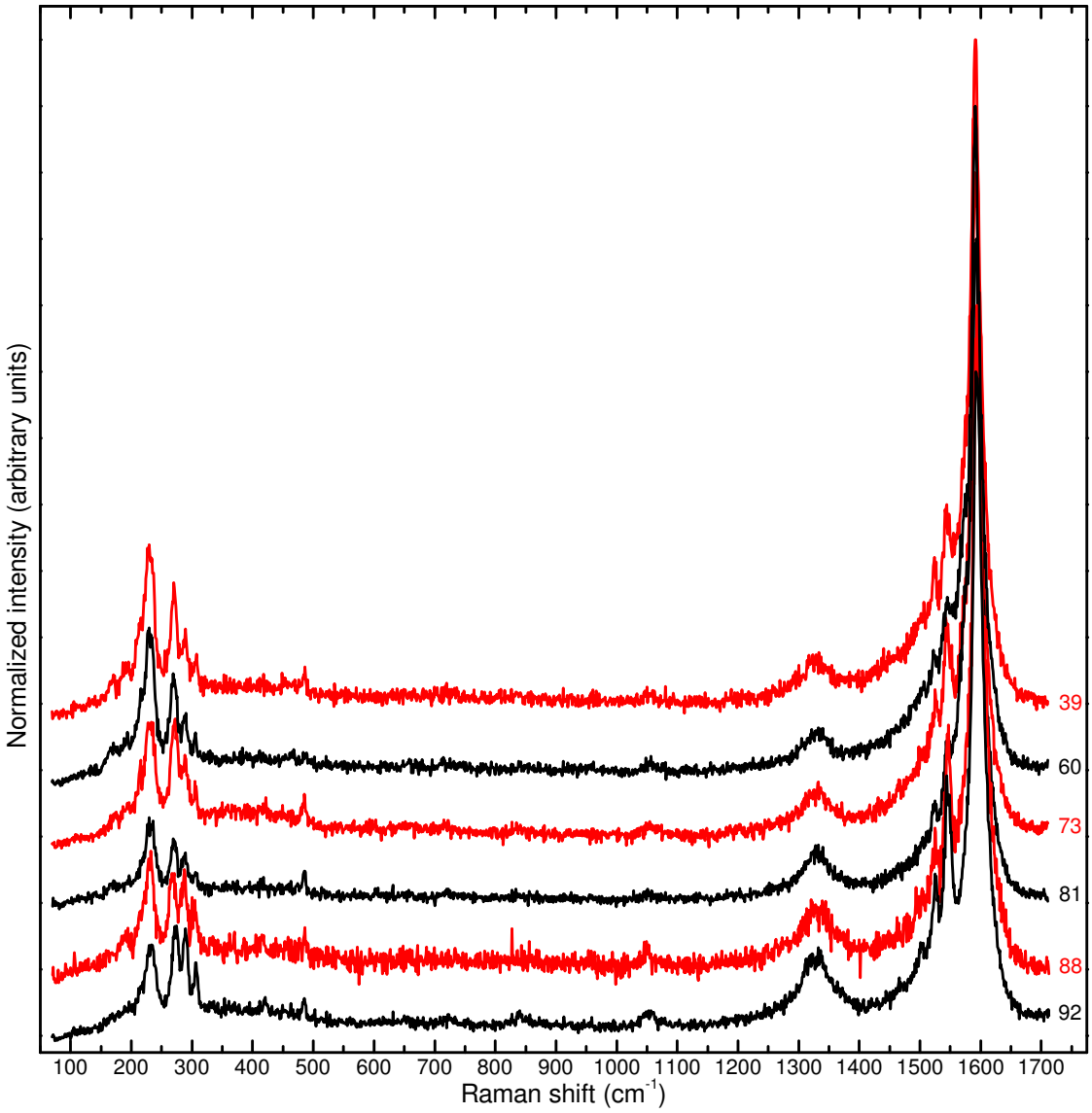


Figure S5: Raman spectra for CNT forest samples. Spectra are normalized to 1 at maximum of G band and vertically offset for clarity. Growth pressures indicated (in units of [Pa]).

D/G Ratio for Fe CVD

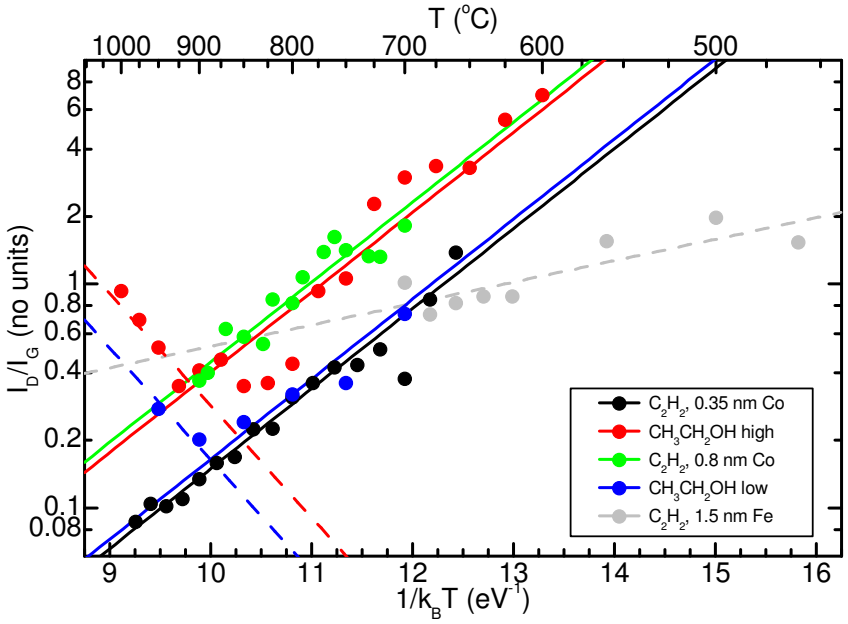


Figure S6: D/G ratio I_D/I_G vs $1/k_BT$ for several data sets grown under different CVD conditions (see Fig. 2 in main text). Gray circles and solid line are preliminary data from C_2H_2 CVD on 1.5 nm thick Fe catalyst. Broken lines are to guide the eye.

D/G Ratio From Peak vs Integrated Intensities

Cançado et al. (Ref. 27 in main text) used the peak intensities of the D band and G band to calculate their D/G ratio. In the present report, we have used the integrated intensities. To perform a proper comparison, we calculated our D/G ratio while considering the peak intensities as determined by the fitted Lorentzian line shapes. A comparison of the D/G ratio of the present report, calculated by both methods, is shown in Fig. S7. We find that the two D/G ratios are related with a simple direct proportionality: $(I_D/I_G)_{peak} = (0.4 \pm 0.1)\,(I_D/I_G)_{integrated}$.

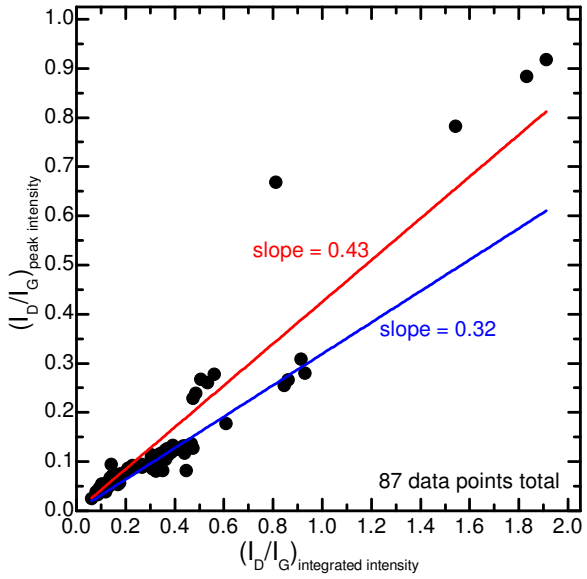


Figure S7: D/G ratio as determined by peak intensity vs D/G ratio as determined by integrated intensity for the present data set.

The exact relation between the two parameters is somewhat more complex than the simple direct proportionality shown in Fig. S7, however, this simple form is sufficient for the purpose of the estimations that it is used for in the main text (especially given the ∼25% error on the constant reported by Cançado et al.). A more precise comparison of the peak vs integrated intensity ratios would consider the Lorentzian line shape:

$$y(x) = y_o + \frac{2A}{\pi}\frac{w}{4(x-x_o)^2 + w^2} \tag{S1}$$

Here, y_o is the base line of the curve, x_o is the peak position, A is the integrated area under the curve, and w is the full width at half maximum (FWHM). The peak intensity of the Lorentzian is:

$$h = y(x_o) - y_o = \frac{2A}{\pi w} \tag{S2}$$

Therefore, the peak intensity D/G ratio is:

$$(I_D/I_G)_{\text{peak}} = h_D/h_G = \frac{w_G}{w_D}\frac{A_D}{A_G} = \frac{w_G}{w_D}(I_D/I_G)_{\text{integrated}} \tag{S3}$$

Thus, the 0.4 slope determined in Fig. S7 is the average ratio of the width of the G band to the width of the D band. From Fig. S7, it is clear that this ratio is likely not exactly constant, but can be approximated as such within a $\sim$25% error bound.

Yield

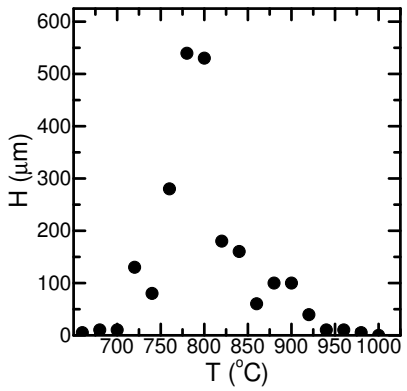


Figure S8: Forest height H as a function of growth temperature T.

Thermodynamic Model

The general chemical reaction for the complete conversion of a carbon source gas into SWCNTs is:

$$n_{\mathrm{R}}\{\text{Reactants}\} \rightleftharpoons \mathrm{C}(\text{SWCNT}) + n_{\mathrm{P}}\{\text{Products}\} \tag{S4}$$

Here, the n_i are the stoichiometric coefficients. For this reaction, the change in free energy is given by (see main text):

$$\Delta G = \Delta H^{\circ} + \frac{A}{d^2} - T\Delta S^{\circ} + \sum n_i k_B T \ln\left(P_i/P^{\circ}\right) \tag{S5}$$

In the summation, the n_i are positive for products and negative for reactants. If we define $\Delta S = \Delta S^{\circ} - \sum n_i k_B \ln\left(P_i/P^{\circ}\right)$ and solve for d_{min} (by setting $\Delta G = 0$), Eq. S5 becomes:

$$d_{min} = \frac{A^{1/2}}{\sqrt{T\Delta S - \Delta H^{\circ}}} \tag{S6}$$

There are 4 general cases for $d_{min}(T)$, depending on the signs of ΔH° and ΔS:

1. $\Delta H^{\circ} < 0$ and $\Delta S < 0$: Only case with d_{min} increasing with increasing T. Spontaneous below a certain temperature. Example (at standard and experimental pressures):

$$\mathrm{C_2H_2(gas)} \rightleftharpoons \mathrm{2C(graphite) + H_2(gas)} \tag{S7}$$

2. $\Delta H^{\circ} < 0$ and $\Delta S > 0$: Always spontaneous. Example (at standard pressure):

$$\mathrm{CH_3CH_2OH(gas)} \rightleftharpoons \mathrm{2C(graphite) + 2H_2(gas) + H_2O(gas)} \tag{S8}$$

3. $\Delta H^{\circ} > 0$ and $\Delta S > 0$: This case may give a lower T limit for growth. Spontaneous above a certain temperature. Example (at standard pressure):

$$\mathrm{CH_4(gas)} \rightleftharpoons \mathrm{C(graphite) + 2H_2(gas)} \tag{S9}$$

4. $\Delta H^\circ > 0$ and $\Delta S < 0$: Never spontaneous (and gives values for d_{min} that are not real numbers).

These cases are illustrated in Fig. S9 for $|\Delta H^\circ| = 1$ eV/carbon, $|\Delta S| = 0.4$ meV/K/carbon, and $A = 0.22$ eV nm^2. It is important to note that these curves are not static for a given reaction, but will shift in response to changes in the pressure of gaseous products and reactants. The above examples are potential reactions that could lead to SWCNT growth. The thermodynamic quantities used to calculate ΔH° and ΔS in the above examples come from Ref. 51 in the main text.

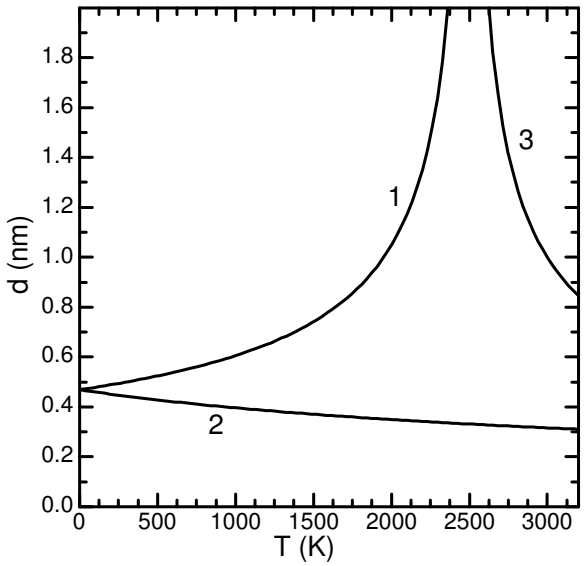


Figure S9: d_{min} as a function of T for $|\Delta H^\circ| = 1$ eV/carbon, $|\Delta S| = 0.4$ meV/K/carbon, and $A = 0.22$ eV nm^2.